

Department of Earth and Environmental Sciences (DISAT)

PhD program in Chemical, Geological and Environmental Sciences,

Cycle XXXI Geological Sciences curriculum

# **Geological analysis and numerical modelling of La Saxe landslide (Courmayeur) to improve understanding of geomorphological and geotechnical mechanisms and of the potential landslide evolution**

Alberti Stefano

Registration number: 718499

Tutor: Prof. Giovanni Battista Crosta

Coordinator: Prof. Maria Luce Frezzotti

ACADEMIC YEAR 2017-2018

Stefano Alberti

*Geological analysis and numerical modelling of La Saxe landslide (Courmayeur) to improve understanding of geomorphological and geotechnical mechanisms and of the potential landslide evolution*

©Milan, October 2018

e-mail: [s.alberti11@campus.unimib.it](mailto:s.alberti11@campus.unimib.it)

Funding for this thesis comes directly from the Regione Autonoma Valle d'Aosta.



*Ma tu non facevi frane?*

*(F.A.)*





## ABSTRACT

Rockslides are characterized by slow to extremely slow displacement rates in their initial phases or for their entire evolution. They frequently occur in foliated metamorphic rocks (e.g. schist, phyllite, paragneiss series). Field and monitoring evidence show that deformation is predominantly localized along a shear zone. Mineralogic, grain size and fabric characteristics of the shear zone control its behavior and the possible evolution of the rockslide from a slow creeping to a fast moving one. In this thesis we investigate the shear zone behavior and evolution through conventional (direct shear, standard triaxial) and unconventional laboratory testing (with an LHV low-to-high-velocity shear ring apparatus). We try to merge mineralogic data with material degradation and their role in the transition from slow to fast evolution due to creep phenomena, the change in material behavior with shear displacement and velocity and, finally, the understanding of the influence of pore-water pressure regime on material behavior. The tests were carried out on samples collected from boreholes through cataclastic shear zones within the Mont de La Saxe (MLS) rockslide (Western Italian Alps), Valle d'Aosta region, Italy, at the extreme termination of a Deep-seated Gravitational Slope Deformations. The rockslide volume is of about  $8 \times 10^6$  m<sup>3</sup>, and it extends between 1400 and 1870 m a.s.l., over area of 150,000 m<sup>2</sup>. This landslide is located close to Entrèves and La Palud (Courmayeur municipality) villages and to the Mont Blanc highway that connects Italy to France through a tunnel. Laboratory tests were also performed on samples from the Chervaz rockslide (Valle d'Aosta region) located in a different rock suite (e.g. serpentine schist with high portion of phyllosilicates).

The MLS shear zone contained both phyllosilicates (at least 20%) and graphite minerals (about 10%) which can control frictional properties. Furthermore, grain size reduction has been observed during slow ring shear testing together with particles rearrangement. Frictional and viscous characteristics, such as the tangential displacement increment before the steady state and the tertiary creep behavior, have been derived.

The long-term monitoring of this instability started on 2009 and during the following years has been improved. The monitoring system is composed by ground surface (GB-InSAR, optical targets, TLS surveys, GPS network) and deep-seated equipment (inclinometers, piezometers and DMS probes). Such an extensive monitoring is – probably – a unique case in the Alps. A clear seasonal behavior has been observed, especially during snow-melt season when the rockslide shows a massive increment of displacements (e.g. 2012, 2013 and especially 2014).

An additional case study was selected, the Ruinon rockslide (upper Valtellina, Italian Alps) because of the long-term available dataset (since 2006). A statistical analysis of monitoring data has been completed, in order to characterize the behavior of the rockslides through time and to propose a new approach to define Early Warning displacement rate thresholds.

Finally, after the experimental campaign and the deep analysis of monitoring data, a mathematical model, based on the Perzyna's delayed plasticity theory, in which the hardening rule considers the degradation process, has been developed. The material parameters were calibrated on the experimental

results previously obtained and using the monitoring data. The numerical simulations through this model give the evolution of the kinematic variables (displacement, velocity and acceleration) during the experimental results.

The results contribute new knowledge regarding the shear zone development and evolution and provide an improved understanding of these mechanisms by developing one of the first high quality data sets that combines new laboratory tests and field data able to develop a model for the landslide forecasting. Finally, the study provides a new approach to define Early Warning displacement rate thresholds for slope failures.

**Keywords:** Rockslide, LHV, experimental test, ring shear apparatus, shear zone, numerical modeling, Perzyna, MIBSA, Mont de La Saxe, Aosta Valley, Italy, Ruinon, Chervaz

## FOREWORD

The present research was focused on Mont de La Saxe rockslide, which represents – probably – the present-day case with the highest natural hazard on the Alps, and, consequently, the most extensively monitored site.

Funding for this thesis comes directly from the Regione Autonoma Valle d’Aosta (RAVA), thanks to Geological Survey of RAVA.

The research focused on entire processes strictly linked with this slope instability was started by the University of Milano – Bicocca under supervision of Prof. G.B. Crosta and his research group.

All the work here presented was conducted under his supervision and thanks to his advices, most of analyses have been performed using equipment provided directly by the research group.

The current research was carried out by means of a multidisciplinary approach, including different techniques. Several experts were involved and gave their contribution to the present work.

Dott. Geol. Davide Bertolo and Ing. Patrick Theugaz from Regione Autonoma Valle D’Aosta, Ing. Carlo Rivolta and Ing. Davide Leva from Ellegi s.r.l., and – finally – Dott. Geol. Mario Lovisolo and Geol. Luigi Foglino from C.S.G. s.r.l. that they provided useful data regarding the study area and about the investigation conducted before and during the research project.

Finally, the research included two periods abroad. Both, financed directly by Regione Autonoma Valle d’Aosta, were conducted at the Disaster Prevention Research Institute of Kyoto University (Japan). Under the supervision of Prof. Toskitaka Kamai and Prof. Gonghui Wang, several laboratory tests were conducted to analyze the behavior of shear zone materials from study area, during this period we developed a new type of test in collaboration with PhD. G. Dattola.

## RESEARCH AIM AND OBJECTIVES

The primary aim of this research was to study the relationship between landslide motion and its causes, with reference to large ( $>1\text{Mm}^3$ ), deep-seated (slip surface typically  $> 10$  m below ground level), reactivated complex landslides, that typically move at rates varying from extremely slow to very fast. The selected case study, a complex landslide located in upper Aosta Valley (Italy), and called Mont de La Saxe (Italy), focusing on both surface movement and mechanical behavior at depth. Especially concerning the investigation of properties and behavior of shear zones, where accommodate most of the landslide displacement. Mineralogic, grain size and fabric characteristics of the shear zone control its behavior and the possible evolution of the rockslide from a slow creeping to a fast moving one.

The analyses were extended to other case studies, i.e. Chervaz (Aosta Valley) and Ruinon (Upper Valtellina, Italy) rockslides to test the proposed approach under different conditions.

Pursuant to the primary objective, a second task is improving numerical model based on visco-plastic formulation proposed by Perzyna (Perzyna, 1963, 1966; Olszak and Perzyna, 1969) and developed by Secondi et al. (2011, 2013), Crosta et al. (2014) and Castellanza et al. (2015). The main feature of this model is that the rate-independent yield function used for describing the visco-plastic strain can become larger than zero, which effect is known as *overstress*. The model is calibrated using the characterization of geo-materials comes from shear band. Use of this model can help to refine the scenarios for the evolution of the landslide.

The third key objective of this thesis is focused on analyses of monitoring data, collected from different case studies (i.e. MLS and Ruinon rockslides). A statistical analysis is used in order to characterize the behavior of the rockslides through time and to propose a new approach to define Early Warning displacement rate thresholds.

Main research topic can be summarized as follow:

- **Mechanical characterization of shear zone material:** aims of this study consisted of using and developing conventional (direct shear and triaxial tests) and unconventional (LHV ring shear tests under different control conditions) laboratory testing to characterize the frictional and viscous behavior of shear zone materials, and to verify how these could be related to grain comminution and content of platy minerals (e.g. phyllosilicates and graphite). Samples mineralogy then, was characterized by XRD, XRF and SEM analyses whereas the shear zone fabric was examined before and after shearing by grain size, SEM and micro-CT analysis.
- **Integration of available monitoring data:** the MLS rockslide is deeply monitored since 2009 with different systems, like manual and automatic inclinometers, DMS<sup>®</sup> columns (Differential Monitoring of Stability by CSG), manual and automatic GPS and robotized total station, GB-InSAR and Terrestrial Laser scans, full coring borehole survey and piezometers network. Data integration and fusion are requested to improve the knowledge of kinematics and the geological and geomorphological settings of this landslide, and to develop models to forecast landslide evolution.
- **Improve and develop landslide models:** a visco-plastic numerical model has been developed (Secondi et al., 2011, 2013; Crosta et al., 2014; Castellanza et al., 2015) and tested on this landslide and here improved in collaboration with PhD Giuseppe Dattola to refine the scenarios for the evolution of the landslide.
- **Statistical analyses of monitoring data:** have been performed to examine their distribution and to propose a new approach to define Early Warning displacement rate thresholds. The analyses have been performed using data averaged with different time intervals so to study the effects of noise on the threshold values. Analyses of false alarm triggered by the choice of different threshold values (i.e. different percentiles) have been implemented and analyzed.
- **Comparing analyses and results to other case studies:** the investigations performed on Mont de La Saxe rockslide samples and on monitoring data, have been extended to two different case studies. First one, also located in the Aosta Valley, the Chervaz rockslide, and another one, the Ruinon rockslide, ubicated in upper Valtellina (Italy) and both characterized by different involved lithologies and displacement patterns but affected by a similar creep behavior.

# FRAMEWORK

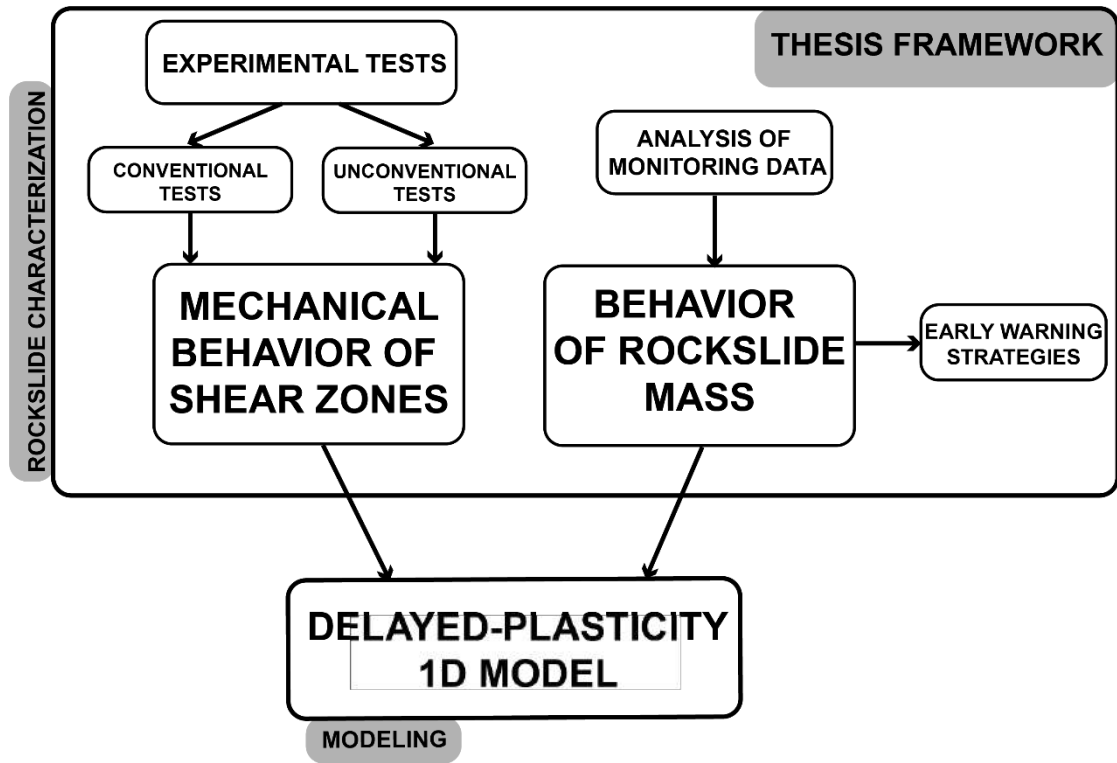


# TABLE OF CONTENTS

	Introduction .....	1
1	Landslide Processes .....	7
1.1	Definitions and classifications .....	7
1.2	Principles of slope stability .....	9
1.2.1	Landslide movements .....	9
1.2.2	Creep .....	13
1.3	Properties of materials .....	17
1.4	The shear strength of the slip surface .....	19
1.4.1	Rate and state friction (RSF) .....	20
1.5	Behavior of Shear Zones .....	25
1.6	Dynamic Viscosity .....	33
1.7	Landslide triggering .....	35
1.8	Landslide investigation and monitoring .....	36
1.9	Displacement measurements .....	37
1.10	Hydrological measurements .....	39
1.11	Landslide Modeling .....	40
1.12	Landslide Early Warning Systems .....	43
2	Investigation sites .....	48
2.1	Mont de La Saxe Rockslide .....	48
2.1.1	Geomorphological Setting .....	50
2.1.2	Climatic Setting .....	61
2.1.3	Geological Setting .....	63
2.2	Structural Setting .....	70
2.3	Main Instability Events .....	72
2.4	Hydrogeological Setting .....	74
2.5	Monitoring System .....	76
2.5.1	Ground-based network: displacement data .....	78
2.5.2	Ground-based network: piezometric data .....	82
2.5.3	2D groundwater flow model .....	90



2.6	Sliding surface .....	93
2.7	Chervaz Rockslide .....	96
2.8	Ruinon Rockslide .....	98
3	Experimental Tests .....	101
3.1	Shear zone sampling .....	103
3.2	Mechanical Characterization .....	106
3.2.1	Conventional geotechnical tests .....	106
3.2.2	Unconventional tests: Ring Shear Apparatus (RSA) .....	106
3.3	Results.....	110
3.3.1	Grain Size Distribution and Consistency limits .....	110
3.3.2	Uniaxial compression tests.....	111
3.3.3	Standard triaxial and direct shear tests .....	112
3.3.4	Force Control test.....	113
3.3.5	Shear Speed test .....	114
3.3.6	Pore-Water Pressure Control test .....	115
3.3.7	Aging test .....	117
3.4	Discussion .....	120
4	Fabric Characterization.....	125
4.1	Mineralogical, textural and structural characterizations .....	128
4.1.1	XRD and XRF analyses .....	128
4.1.2	SEM analysis .....	128
4.1.3	Micro-CT analysis .....	129
4.2	Results.....	130
4.2.1	XRD and XRF analyses .....	130
4.2.2	SEM analysis .....	131
4.2.3	Micro-CT analysis .....	143
4.3	Discussion .....	148
5	1D Block visco-plastic modeling .....	159
5.1	Multi Interacting Blocks Slope Analyses (MIBSA model) .....	163
5.1.1	Single block motion .....	163
5.1.2	The shear band model.....	166

5.1.3	Compatibility condition and the final system .....	168
5.1.4	Calibration and improvements .....	168
5.1.5	Results and discussion .....	172
5.2	Conclusions.....	184
6	Statistical Analyses of Monitoring Data .....	185
6.1	Normal Probability Plots (NPP).....	187
6.1.1	Results and discussion .....	188
6.1.2	GB-InSAR data.....	188
6.1.3	DMS® columns data.....	191
6.1.4	Piezometric data.....	195
7	The Ruinon rockslide.....	200
7.1	Monitoring system .....	200
7.1.1	Ground-based geotechnical network .....	200
7.1.2	Ground-based radar interferometry .....	201
7.1.3	Definition of rockslide sub-areas: early warning domains .....	204
7.2	Objective definition of early warning criteria .....	208
7.2.1	Landslide sensitivity to hydrological triggers: selecting early warning strategies .....	208
7.3	Predicting landslide collapse: early warning velocity thresholds .....	212
7.3.1	Fukuzono-Voight Approach .....	212
7.3.2	The Statistical Approach .....	214
7.4	Combining the approaches and minimization of false alarms .....	217
7.5	Conclusions.....	222
8	Conclusions .....	223
8.1	Key findings .....	223
8.2	Limitations.....	225
8.3	Recommendations for further research.....	226
9	References .....	230



# INTRODUCTION

*No matter where you are going,  
the road is uphill and against the wind.*

A *landslide* is the movement of a mass of rock, debris, or earth down a slope, under the influence of gravity (Nemčok *et al.*, 1972; Varnes, 1978; Hutchinson, 1988; WP/WLI, 1990; Cruden, 1991; Cruden and Varnes, 1996). Landslides are one of the most dangerous hydro-geological hazards causing damages to natural and human environments. They can involve flowing, sliding, toppling or falling phenomena and most of them exhibit a combination of two or more types of movement (Varnes, 1978; Crozier, 1986; Hutchison, 1988; Cruden and Varnes, 1996; Dikau *et al.*, 1996). Landslides are observed both at the Earth's continental surfaces and in submarine environments, also on other planets (e.g. Mars; Crosta *et al.*, 2018).

The range of landslide phenomena is extremely large, making mass movements one of the most diversified and complex natural hazard (Figure 2). Landslides have been recognized in all continents, in the seas and in the oceans. On Earth, the area of a landslide spans nine orders of magnitude, from a small soil slide involving a few square meters to large submarine landslides covering several hundreds of square kilometers of land and sea floor. The volume of mass movements spans sixteen orders of magnitude, from a single cobble falling from a rock cliff to gigantic submarine slides. Landslide velocity extends at least over fourteen orders of magnitude, from creeping failures moving at millimeters per year (or even less) to rock avalanches travelling at hundreds of kilometers per hour. Mass movements can occur singularly or in groups of up to several thousands. Multiple landslides occur almost simultaneously when slopes are shaken by an earthquake or over a period of hours or days when failures are triggered by intense or prolonged rainfall. Rapid snow-melt can trigger slope failures several days after the onset of the triggering meteorological event. An individual landslide-triggering event (e.g., intense or prolonged rainfall, earthquake, snow-melt) can involve a single slope or a group of slopes extending for a few hectares or can affect thousands of square kilometers spanning major physiographic and climatic regions. Total landslide area produced by an individual triggering event ranges from a few tens of square meters to hundreds of square kilometers. The lifetime of a single mass movement ranges from a few seconds in the case of individual rock falls, to several hundreds and possibly thousands of years in the case of large dormant landslides.

Between 2004 and 2016, 4,862 fatal landslides were recorded worldwide, causing a total of 55,997 fatalities (Froude and Petley, 2018). Most of human losses occurred in Asia (Figure 1). In August 2014, the Yunman earthquake (Mw = 6.1, China) triggered valley-blocking landslides which killed 589 people and injured more than 2,300 others in landslide-prone region of China. In 2015 a mixed rock and ice avalanche destroyed a small village called Langtang in northern part of Nepal killing over 250 people. During 2016 a series of landslides triggered by the monsoon in Nepal led to over 30 fatalities. In August 14<sup>th</sup>, 2017, a significant mudflow events occurred in and around the capital city of Freetown in Sierra Leone killing 1,141 people and leaving more than 3,000 homeless. In 2018, a series of debris flows in northwest part of Los Angeles in Santa Barbara County (California, USA) have been 21 reported death and a damage quantified in over 200 M USD. In July 2018 a heavy rainfall events in southwestern Japan causing widespread flooding and different landslides with over 100 casualties.



*Figure 1 - Spatial distribution of fatal landslides over the period 2004-2016, each black dot representing a single event (Froude and Petley, 2018)*

In addition to loss of life landslides have an important impact on key infrastructures. These include transport links (roads, railways, etc.) (e.g. Griffiths et al., 2004; Bromhead and Ibsen, 2007; Winter et al., 2007; Hearn and Massey, 2009); commercial and residential properties (e.g. Eisbacher and Clague, 1980; Mill et al., 2007; Wong and Ko, 2006); power generation and supplies such as oil and gas pipeline (e.g. Couperthwaite and Marshall, 1989; Lee et al., 2009) and the disruption of key lifelines such as lakes, rivers and reservoirs (e.g. Dunning et al., 2006).

The impact of landslides can further lead to secondary hazards such as the damming of rivers and subsequent outburst floods (e.g. Costa and Schuster, 1987; Korup, 2005; Hancox et al., 2005; Dunning et al., 2006, Petley et al., 2010) and the transfer of debris into river systems creating flood hazards and impacting water quality (McCahon et al., 1987).

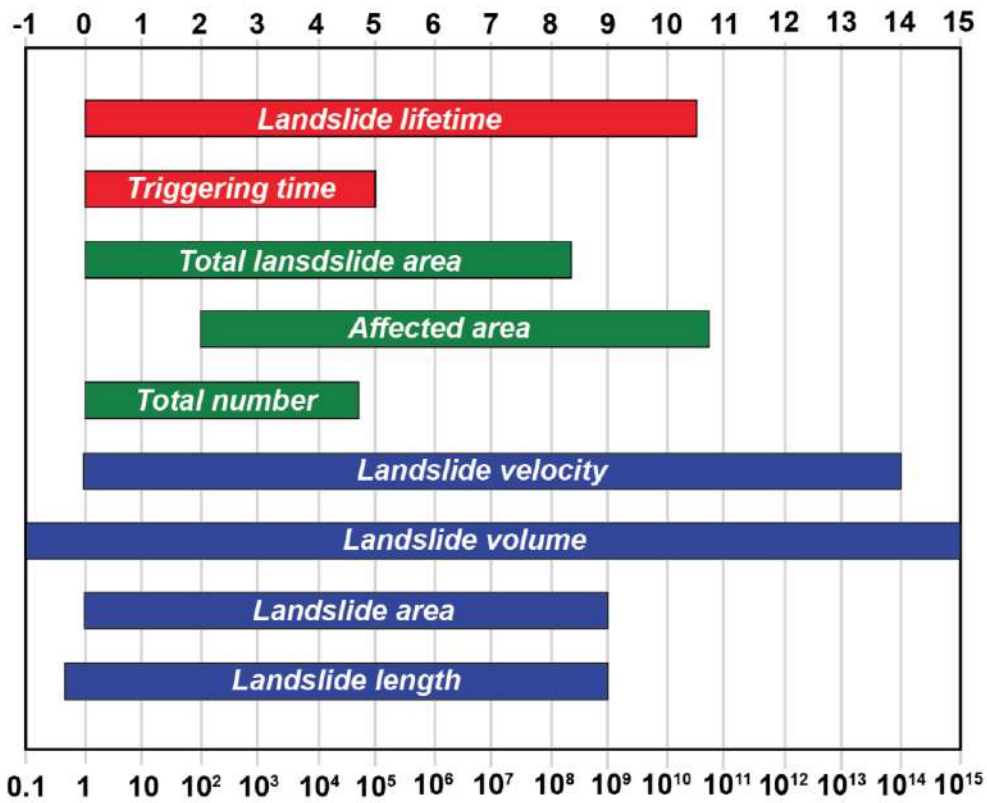


Figure 2 - The large spectrum of landslide phenomena. x-axes show order of magnitude (logarithmic scale). Landslide length, in meter, landslide area, in square meters, and landslide volume, in cubic meters, refer to a single slope failure. Landslide velocity is in meters per second. Total number is the number of landslides triggered by an event. Affected area is the territory affected by the triggering event, in square meters. Total landslide area is the cumulative landslide area produced by a triggering event, in square meters. Triggering time is the period of a landslide triggering event, in seconds. Lifetime is the lifetime of a landslide, in seconds. Figures in the graph are approximate and for descriptive purposes (modify after Thiebes, 2011)

The movement of a landslide is mainly controlled by mechanical behavior of the slope material and of the shear zone. The investigation of shear bands and other material instability phenomena have become of considerable interest because of its importance in predicting failure of materials.

Shear zones are controlled by their mineral composition and mechanical properties of materials which can result in a combination of frictional and viscous properties. Deep-seated rockslides are frequently found in foliated metamorphic rocks (e.g. phyllite, schist or paragneiss; Straühal et al. 2017) with shear zones which can be localized in a few centimeters or can reach even metric thickness. The slope kinematics can be affected by deformation in one or several discrete shear zones characterized by a large deformation with respect to these occurring within the remaining part of the landslide mass (e.g.; Zangerl et al. 2007, 2010, Crosta et al. 2014; Straühal et al. 2017).

The thickness and the grain size of these shear zones (from sandy to silty-clayey material) can control both the mechanical behavior and the hydraulic regime of the slopes causing strain localization and hydraulic compartmentalization (Crosta et al., 2017). Therefore, considering also the other influencing parameters (e.g. pore-water pressure, in situ stress, internal deformation), the rockslide stability is consequently dominated more by shear zone characteristics than by overall rock mass properties.

Given that the basal shear zones are produced during the rockslide evolution, data about their petrographic and mineralogic composition and the geomechanical properties can clarify both their evolution and that of the rockslide stability with displacement, velocity and time.

Quantifying the presence of minerals and evaluating their influence on the rockslide system behavior, represents a major step in landslide understanding. The comprehension of the effects of graphite and platy minerals (e.g. phyllosilicates) on the shear zone behavior and on the rockslide system in the post-peak shear strength range has always been considered hard. Several authors have investigated the changes occurring within both faults and landslide shear zones. Fukuoka et al. (2006) analyzed the shear zone thickness, Storti et al. (2003) dealt with grain size distribution evolution, whereas alignment of platy minerals (i.e. phyllosilicates) was treated by Yamasaki and Chigira (2011). These parameters may strongly influence the mechanical behavior and its evolution (e.g. Buffington 1992; Wen et al. 2007; Engl et al. 2010; Henderson et al. 2010). Therefore, a comparison of shear zones with different total displacements can be helpful in analyzing the possible evolution of an early-stage rockslide, passing from peak to post peak and residual strength. According to Lupini et al. (1981), the displacements necessary to reach the residual shear strength increase with the amount of platy minerals (i.e. phyllosilicates). As shown by Kenney (1967), Tiwari et al. (2005) and Hu et al. (2017) mineralogical composition has a major influence on the residual shear strength. Their studies demonstrated that soils with large amounts of clay minerals (or in general the presence of phyllosilicates, e.g. talc) are characterized by low residual friction angles. The occurrence of clay minerals in rockslides shear zones is common (e.g. Jaboyedoff et al., 2004; Bonzanigo et al. 2007) and can be caused by the chemical weathering of crushed and fragmented host rock due to contact with groundwater. Consequently, these clay minerals can adversely affect the activity and stability behavior of a rockslide.

Various authors have shown similarities between shear zones in rockslides and in fault zones (Zulauf et al., 1990; Craw, 2002; Nakamura et al., 2015; Straühal et al., 2017) asserting that there is no discernible

difference in structure, mineralogical composition or geomechanical properties between brittle tectonic fault zones and rockslide shear zones). Oohashi et al. (2011) reported that a dry graphite fault gouge has a very low coefficient of friction ( $\mu \approx 0.1$  over slip rates ranging from 50  $\mu\text{m/s}$  to 1.3  $\mu\text{m/s}$ ). Consequently, graphite may reduce the fault strength effectively likewise as other fault lubricants, depending on its abundance and distribution within the fault zone. Laboratory experiments (Oohashi et al., 2012) revealed how specific minerals (so called 'fault lubricants') such as chrysotile, smectite (montmorillonite) and talc have low coefficient of friction ( $\mu < 0.2$ ) under water-saturated conditions when compared with most rock-forming minerals. To characterize the behavior of shear zones and to measure the residual shear strength, direct shear, triaxial and ring shear tests have been performed (e.g. Skempton and Petley, 1967; Hutchison, 1969; Bromhead and Dixon, 1986; Sassa et al., 1997, Wang et al., 2003). The behavior of graphite-rich layers in pelitic schists was recently analyzed by Yamasaki et al. (2016) by performing back-pressured direct shear testing on artificial rock samples both with and without graphite layers.

For the analysis of time-dependent failure in materials, such as the shear banding and creep in geomaterials (Desai and Zhang, 1987; Cristescu, 1994; Samtani et al., 1996; Cristescu and Cazacu, 2000), various visco-plastic material models have been proposed.

Nowadays, one weakness is the lack of correlation between observations of movement in real landslide systems and the understanding of the deformation processes occurring in the basal shear zone (Martel, 2004).

Numerous authors have developed methods of landslide prediction based on the pre-failure movement of unstable slopes (e.g. Salt, 1988; Fukuzono 1985, 1989, 1990; Hayashi et al., 1989) based on the Saito (1965) method of assessing patterns of linearity in  $1/v - t$  space. Such methodologies have shown some success as predictors of slope failure (e.g. Voight, 1988, Petley et al., 2002). The relative merits of these methodologies have been questioned (e.g. Hutchinson, 2001) as they fail to consider the geotechnical parameters or potential variations in pore-water pressures that may impact on the time and behavior of a landslide at failure. Furthermore, assessment of landslide failure movement patterns (e.g. Petley et al., 2002; Petley et al., 2006) has demonstrated that two distinct movement patterns in  $1/v - t$  space can occur. These patterns have subsequently been linked to the deformation properties of the materials at the shear zone, through a series of specialist pore pressure reinflation tests that replicate rainfall or groundwater induced landslide failure.

To link movement patterns in both first-time landslides and reactivation failures to the patterns and mechanics of shear surface development in different materials, if accurate landslide failure prediction and behavior forecasting methodologies can be established have been used models.

One of the most simply and suitable model is based on 1D pseudo-dynamic visco-plastic approach (e.g. Angeli et al., 1996; Secondi et al. 2011, 2013; Crosta et al., 2014; Castellanza et al., 2015), based on Perzyna's theory (Perzyna, 1963). This model has been successfully applied to different landslide (e.g. Bindo-Cortenova landslide, Vallcebre landslide, Vajont landslide and Mont de La Saxe rockslide) and due to the extreme simplicity of the model, a real-time calibration and prediction process can be implemented in order to continuously refine the values of the model parameters. This step could be implemented in the



Early Warning System via collection of a consistent and comprehensive dataset and could be able to update in near-real time the displacement rate thresholds. Currently, the limitations of this kind of approach is related to inability of this model to predict a possible sudden collapse of the entire mass or of one of the sub-blocks, and this is part of the ongoing research effort. Consequently, the displacement-rate threshold values, adopted in the EWS for the case of a rapid collapse scenario, are based on Fukuzono-Voight approach (Saito, 1965; Voight, 1988; Fukuzono 1988, 1990). Contemporaneous overpassing of these threshold values at multiple measuring points, both at the surface and at depth, is a requirement to initiate any civil protection action and allows either to avoid false alarm or to differentiate among the various possible scenarios (i.e., rock falls or slides of limited volume).

Due to the multidisciplinary approach of the research project, the results presented in this thesis could be constrained and verified by comparing the results obtained using different investigation techniques, as applied to the surface monitoring network data or the interpretation of borehole displacement data. Similarly, the combination of geological data, the analysis of monitoring data, the performed tests data and numerical modelling, such that the results constrained each other, proved to be necessary to better understand the processes acting on the investigated complex rockslide.

# LANDSLIDE PROCESSES

*Someday you will find me  
Caught beneath the landslide*

## **1.1 Definitions and classifications**

A very basic but widely accepted and used definition for landslide was established by Cruden (1991) and Cruden and Varnes (1996) and defines a landslide as *"the movement of a mass of rock, debris or earth down a slope"*. Cruden and Varnes (1996) note that it describes all kinds of mass movements and it is not limited to granular soil or a sliding movement. The term landslide is well established in the research community and will therefore also be used in this thesis as an overarching term referring to all movement types and material properties. Further on, the term mass movement is used interchangeably with landslide.

The most common classification for landslides is based on material properties and process types (Figure 3). Besides the main types of movement processes there is one complex class which contains movement processes with two or more different processes acting in space and time along downslope movement of the landslide mass.

A second widely acknowledged classification of landslides is based on movement velocity (Cruden and Varnes, 1996), which ranges from extremely fast to extremely slow (Figure 4). Moreover, landslides can be distinguished regarding their state of activity. Cruden and Varnes (1996) established eight groups, namely active, suspended, reactivated, inactive, dormant, abandoned, stabilized and relict mass movements. Further on, single, multiple and successive movements are distinguished. Other differentiations can be based on, for example, the water content of involved materials (Cruden and Varnes, 1996).

Type of Movement	Type of Material		Velocity scale	
	Bedrock	Unconsolidated sediment or soil	slow	rapid
		 Coarse >20%      Fine >80%	1   2   3   4   5   6   7	16 mm.yr <sup>-1</sup> 13 m.month <sup>-1</sup> 5 m.sec <sup>-1</sup>
<b>Fall / topple</b>	 Rock fall Block topple Flexural topple	Debris fall / topple	Earth	6-7
<b>Flow</b>	 Rock flow (deep creep)	Debris flow Avalanches Soil creep Soilfluxion	Earth Loess flow Mass creep	5-7
<b>Spread</b>	 Rock spread		Earth spread	4-5
<b>Slide</b>				
- Translational	 Rock block slide Rock slide	Debris block slide / slide	Earth	6-7
- Rotational	 Rock slump	Debris slump Multiple rotational slide	Earth Successive rotational slide	4-5
<b>Complex</b>	Combination of two or more types of movements			4-7

Figure 3 - Landslides classification according to the type of movement, the type of material and the velocity scale (modified after Cruden and Varnes, 1996)

AGE	RETURN PERIOD	MORPHOLOGIC CHANGES	ACTIVITY	
Present	1 day	 Fresh morphology, distinct from the surroundings. Cracks are clearly visible.	 Continuous	ACTIVE
			 Suspended      Reactived	
Historical 150 BP	1 year	 The morphology remains different from the surroundings. However, the forms are softer than before.	 Dormant	INACTIVE
			 Abandoned      Stabilised	
Holocene 10,000 BP	> 1000 yr	 The surface is modified by water erosion. The landslide becomes covered with vegetation.	 Relict	INACTIVE
Pleistocene 20,000 BP		 The morphology is slightly noticeable, there are only morphological traces of the phenomenon.		

Figure 4 - Classification of landslide activity levels in function of the geomorphological features (modified after McCaipin, 1984 and Thiery et al., 2007)

## 1.2 Principles of slope stability

### 1.2.1 Landslide movements

All landslide events result from gravitational forces that cause the materials to fail and move downslope from an unstable to a more stable position, they are a sign of slope instability which is defined as the "propensity for a slope to undergo morphologically and structurally disruptive landslide processes" (Glade and Crozier, 2005b). Glade and Crozier (2005b) visualize slope stability as a dynamic spectrum (Figure 5). On one end, there is a stable slope which is subject to preparatory factors which convert the slope to a marginally stable state. At this point, dynamic triggering factors exceeding certain thresholds can alter the state of the slope to actively unstable which leads to continuous or intermittent movement. During the described transformation from stable to actively unstable slope conditions the margin of stability is continuously decreasing. Precondition or predisposing factors are thought as static factors that influence the margin of stability and allow dynamic factors. Preparatory factors are dynamic which change the stability margin over time without initiating slope failure. Typical examples for preparatory factors are weathering, deforestation, tectonic uplift or environmental change. Triggering factors actively shift the state of stability to an unstable condition. Common triggers for landslides are intense rainstorms, seismic shaking or slope undercutting (Glade and Crozier, 2005b). Inherent in this concept is the theory of extrinsic and intrinsic thresholds (Schumm, 1979). Sustaining factors control the behavior of the actively unstable state and therefore dictate the duration of movement, form and run out distance of slope failure. A similar concept is described by Leroueil (1996) who distinguishes four stages of landslide movement: a pre-failure stage including deformation process leading to failure, the onset of failure characterized by the formation of a continuous shear surface through the entire soil mass, a post failure stage starting from failure until the mass stops, and a reactivation phase when sliding occurs on a pre-existing shear surface.

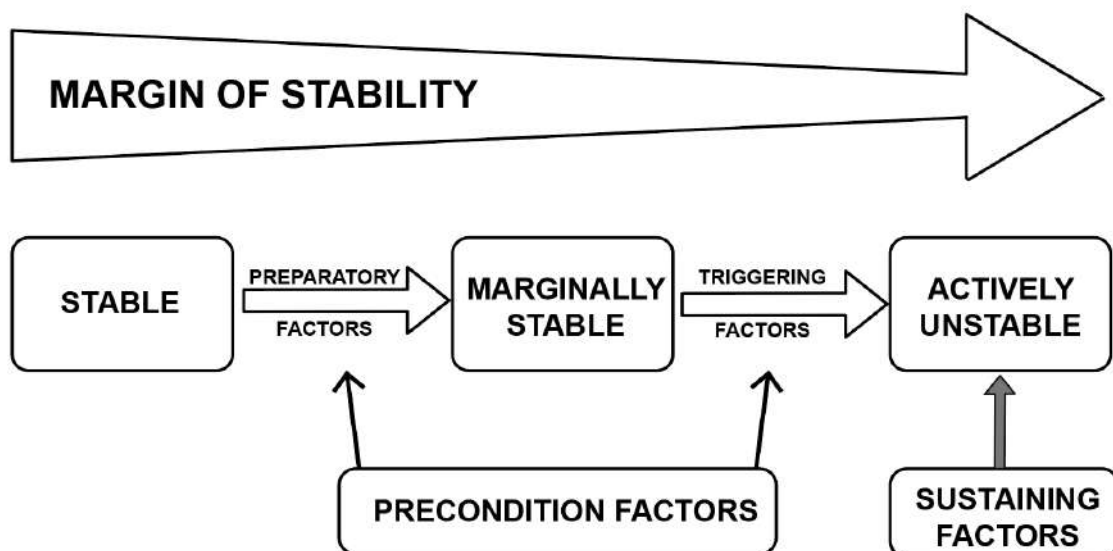


Figure 5 - Stability states and destabilizing factors (after Glade and Crozier 2005b, based on Crozier 1989)

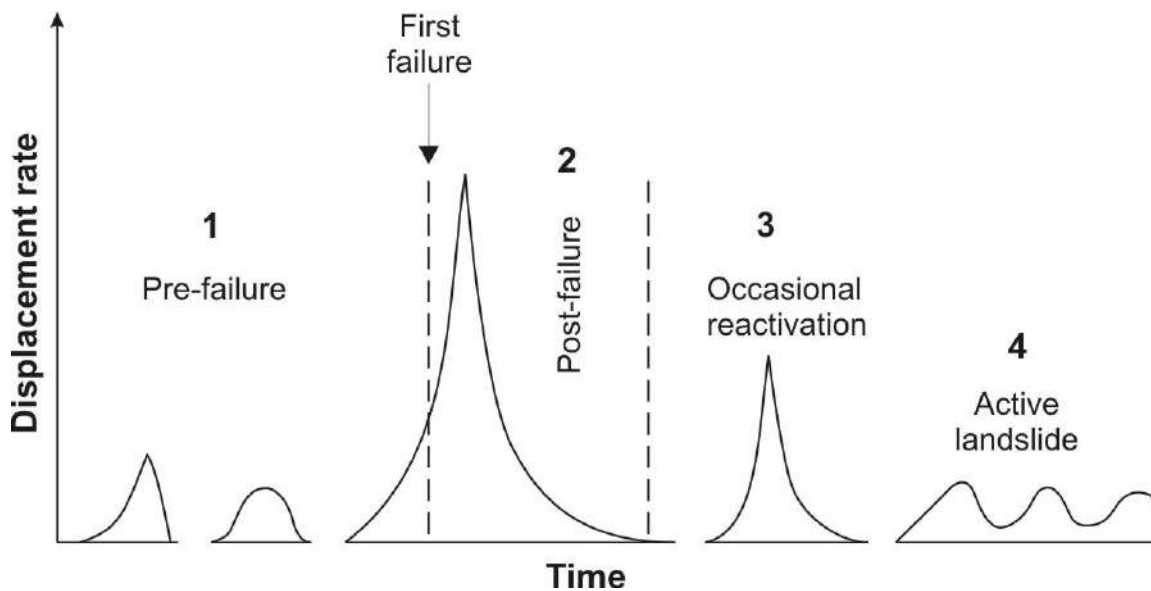


Figure 6 – The different stages of slope movements (from Leroueil,1996)

Stresses acting within a slope can be illustrated by vectors (Figure 7), where a mass ( $m$ ) is subject to acceleration of gravity ( $g$ ) which can be differentiated into a downslope component ( $\tau$ ) and a force acting perpendicular to slope surface ( $\sigma$ ). Distribution of stresses depends on slope angle ( $\beta$ ) and downslope force increases with higher slope angles.

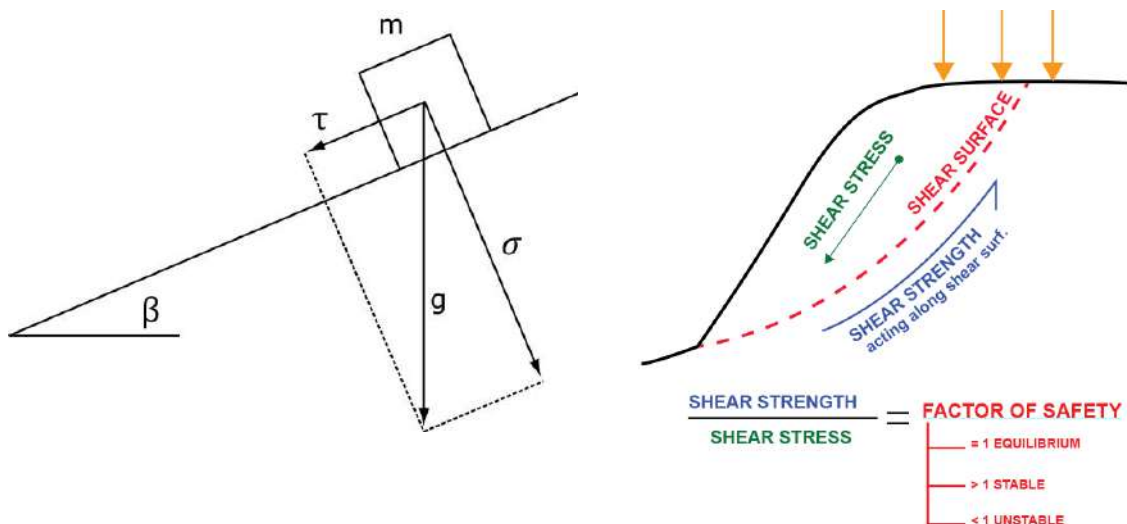


Figure 7 - Stress vectors within a slope on left (based on Ahnert 2003); the balance of forces in landslide development on right

The potentially destructive effects of slope instability led to early research in prediction of slope failures. Calculation of slope stability dates to Coulomb (1776) and his work on stability of retaining walls and determination of the most likely shear surfaces with a wedge method, which are still valuable today (Ahnert, 2003). Another important advance of slope stability calculation was made by Terzaghi (1925), who

established the fundamental concept of effective stress. Therein, the effects of porewater pressure in slope stability are acknowledged. Pore-water pressure is the pressure of water in the voids between solid particles of the soil (Terzaghi, 1953). As water cannot sustain shear stress, only the skeleton of solid particles at their contact points can, slope stability decreases with a higher pore-water pressure. The stability of slope can be assessed by calculating the Factor of Safety (FoS) for an infinity slope, which is the ratio of driving and resisting forces within a slope (Crozier 1989):

$$FoS = \frac{\text{shear strength}}{\text{shear stress}} = \frac{c + (\sigma - u)\tan\phi'}{\tau} = \frac{c + \left(\frac{W}{A}\cos\beta - u\right)\tan\phi'}{\frac{W}{A}\sin\beta}$$

where

- $\tau$  = shear stress
- $c$  = cohesion with respect effective normal stress
- $\sigma$  = total normal stress
- $u$  = pore-water pressure
- $\sigma'$  =  $\sigma - u$
- $\phi'$  = angle of internal friction with respect to effective normal stress
- $W$  = weight of the material; that is  $\gamma =$  bulk density multiplied by  $V$
- $A$  = Area  $\rightarrow$  Force =  $W/A$
- $\beta$  = angle of shear surface

In theory, a slope with FoS equal to 1 represents a slope in a state in which the forces are acting in equilibrium. In this case the slope is considered to be at the failure point. When the shear forces acting in the slope exceed the forces acting to promote failure, the slope can be considered to be stable ( $FoS > 1$ ). Conversely, when shear forces are sufficiently reduced, or the forces acting to promote failure are increased such that the shear strength is exceeded (i.e.  $FoS < 1$ ), the slope will fail. In this respect landslides may be viewed as a dynamic geomorphological process acting to rebalance the forces within a slope from an unstable to more stable state. To fully understand landslide failure conditions an appreciation of the key strength operating within, and the stress components acting upon, a slope is needed.

Examination of shear parameters and the stress-strain behavior of materials are primarily experimental, because of the technical difficulties to study the processes in nature. Shear parameters are generally determined in the laboratory by undertaking, triaxial and direct shear tests (Wu, 1996). A relatively undisturbed soil sample is placed into a specific box (e.g. shear box) and stress is applied until the material fails. Applied loads and subsequent strains are recorded. Idealized stress-strain curves for brittle and ductile failure regimes are given in Figure 8.

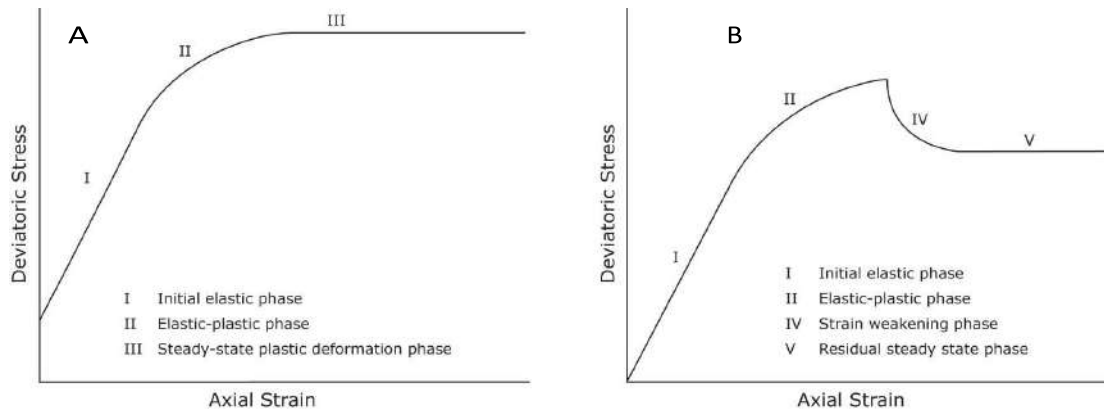


Figure 8 - Idealized stress-strain curves for brittle (A) and ductile (B) deformation (Petley and Allison 1997)

Most geological materials and engineering soils can display both brittle and ductile failure modes depending on their confining pressure (Cristescu, 1989). However, brittle failure is dominant at low confining pressures representative for shallow failures (Petley and Allison, 1997). As stress or load is applied soil materials generally display an initial phase of elastic and recoverable strain. The applied stress is loaded on the grain-bonds within the material which deform but do not break. An increase of stress causes the material's weakest bonds to break and an elastic-plastic phase can be observed which is characterized by increasing strain rates. As more and more bonds break, peak strength is exceeded, and shear strength is significantly reduced. The shear surface fully develops in the strain weakening phase in which shear strength steadily reduces to a residual value. During this phase shear zone contraction or dilation may occur which affects pore pressures and therefore strain rates (Vardoulakis., 2002; Wang and Sassa, 2002; Helmstetter, et al., 2004; Petley et al., 2005; Iverson, 2005).

Thereafter, strains primarily occur as displacement along the shear surface. Ductile behavior can be observed at high effective stresses prevalent in very deep-seated landslides and in materials with little or no inter-particle bonding like weathered clays (Petley and Allison, 1997). The initial phases of elastic and elastic-plastic strain are similar to the brittle failure regime. However, due to the high confining stress no shear surface can develop. Increased load results in purely plastic deformation at constant stresses as the material reforms. Moreover, a transition between ductile and brittle behavior was observed by (Petley and Allison, 1997) at very high pressures (order of MPa), which are present in very deep-seated landslides.

## 1.2.2 Creep

As mentioned above the term creep does not describe a certain landslide type but may be used to describe deformation that continues under constant stress (Varnes, 1984; Cruden and Varnes, 1996; Terzaghi et al., 1996). A general definition describes the creep as a time dependent deformation under a constant application of stress, exclusive of hydrodynamic effects (Watts, 1981). In the literature, creep has been generally investigated in the laboratory by using both the odometer (Augustesen et al., 2004) and triaxial apparatuses (Figure 10 and Figure 11). Creep deformations occur if the stress level is kept constant, and hence the strains continue to increase.

This phenomenon has been studied under different disciplines including geomorphology (e.g. Selby, 1993), engineering (e.g. Varnes, 1984), materials science (e.g. De la Cruz-Reyna and Reyes-Dávila, 2001), and rheology (e.g. Ranalli, 1995). A comprehensive classification of creep in landslides has been given by Hutchinson (1988) namely: (i) 'superficial, predominantly seasonal creep or mantle creep', (ii) 'deep-seated, continuous creep or mass creep', (iii) 'prefailure creep or progressive creep', and (iv) 'post-failure creep' (Table 1).

Table 1 - Definitions of creep (modified after Hutchinson, 1988; Ng, 2007 and Massey, 2013)

Type	Key approach	Type of creep described	Key characteristics	References
1	Geomorphology	Superficial, predominantly seasonal creep; mantle creep	Confined to surface layer (less than 1 m deep); involves changes of volume due to changes in water content and temperature	Terzaghi (1953); Carson and Kirkby (1972); Selby (1993)
2	Engineering	Deep-seated, continuous creep; mass creep	Occurs at constant stress below the maximum strength of the material	Terzaghi (1953); Varnes (1978, 1983); Selby (1993); Fell <i>et al.</i> (2000)
3	Materials science	Pre-failure creep; progressive creep	Accelerating displacements towards shear failure; involves progressive development of shear structures from discrete shear zones to continuous displacement shears	Terzaghi (1950); Bjerrum (1967); Ter-Stipanian (1980); De la Cruz-Reyna and Reyes-Dávila (2001)
4	Rheology	Post-failure creep	Involves small renewals of failure on a pre-existing slip surface	Van-Asch (1984); Ranalli (1995)

Engineering (Type 2) and material science (Type 3) definitions consider deformation below maximum shear stress/strength prior to failure. The key distinction between these two creep types is that the former emphasizes the time-dependent dimension of the deformation, while the latter involves the dynamic nature of pre-failure movement, highlighting the changing stress distribution within materials (Ng, 2007). Rheological (Type 4) creep is a post failure mechanism as it involves reactivation by sliding along an existing shear surface. This definition, therefore, relates to the velocity of motion (i.e. creeping) and not to the mechanism, which should not be confused with type 2 and 3 definitions. For the purpose of this research the term "creep" is used to describe the post-failure pattern of landslide velocity (Type 4) with no reference



to the mechanism of displacement, the term “plastic deformation” is used to describe pre-failure Type 2 and 3 creep.

Some creep takes place in almost all soil earth and rock slopes and may concentrate along pre-existing or potential slip surfaces or distribute evenly across the landslide profile (Fang, 1990). Creep movements in landslide can be continuous or may vary seasonally with hydrological conditions (Petley and Allison, 1997). Creep can be maintained for long periods; however, creep gradually decreases shear strength and a slope's margin of stability (Fang, 1990) and eventually the slope may fail.

If the movement has radically reduced the resistance properties of the sliding mass causing a change in the movement mechanism, i.e. a translational block-slide transforms into a debris or earth flow (Cruden and Varnes, 1996 and Panet, 1969), acceleration could continue until the landslide fails catastrophically (Terzaghi, 1950). However, periods of rapid acceleration e.g. Type IV movements, or rapid surge events could be followed by periods of equally rapid deceleration and rest (Allison and Brunsden, 1990; Angeli et al., 1996). Several authors suggest that in large deep-seated translational slides, different types of post-failure creep motion (reactivations) can occur with varying frequency and at different times within the seasonal record (Allison and Brunsden, 1990; Crosta and Agliardi, 2003; Corominas et al., 2005, and van Asch et al 2007). This repetition of landslide displacement patterns through time is well represented in the literature, e.g. Iverson (1985); Allison and Brunsden (1990); Bracegirdle et al. (1991); Angeli et al. (1996); Petley et al. (2005); Matsuura et al. (2008); Ranalli et al. (2009); Schulz et al. (2009a, 2009b). The frequency and magnitude of these post-failure motion events will depend upon the frequency and magnitude of the destabilizing events, such as pore pressure increases, earthquake-induced ground accelerations, changing material properties e.g. strain softening of the shear-surface clay and changes in load (e.g. loss of toe support).

A widely acknowledged concept of creep distinguishes between the phases of creep movement (Okamoto et al., 2004; Petley et al., 2005b, 2005c; 2008): the primary, secondary and tertiary stages where the strain rate is observed to be decreasing, constant and increasing until failure, respectively. When constant stress lower than peak strength is applied to a soil mass subsequent strains are time-dependent and can be visualized as displacement versus time plot (Figure 9). In the primary creep stage strains are initially high due to elastic deformation but decrease with time. During the secondary creep phase, the material suffers diffuse damage, but strains are generally slow or almost steady (Okamoto et al. 2004), or may even stop altogether (Petley et al., 2008). When diffuse micro-cracks start to interact to form a shear surface, the critical point into the tertiary phase is reached (Reches and Lockner, 1994; Main, 2000). This phase is characterized by a rapid acceleration of displacement until final failure.

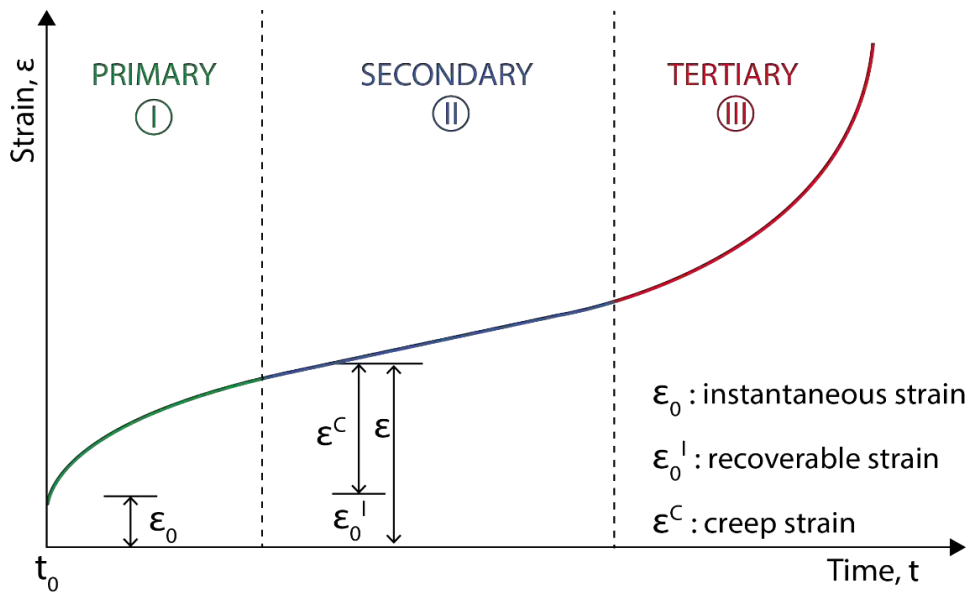


Figure 9 - Idealized strain curves for the three stages of creep (after Leroueil, 1978)

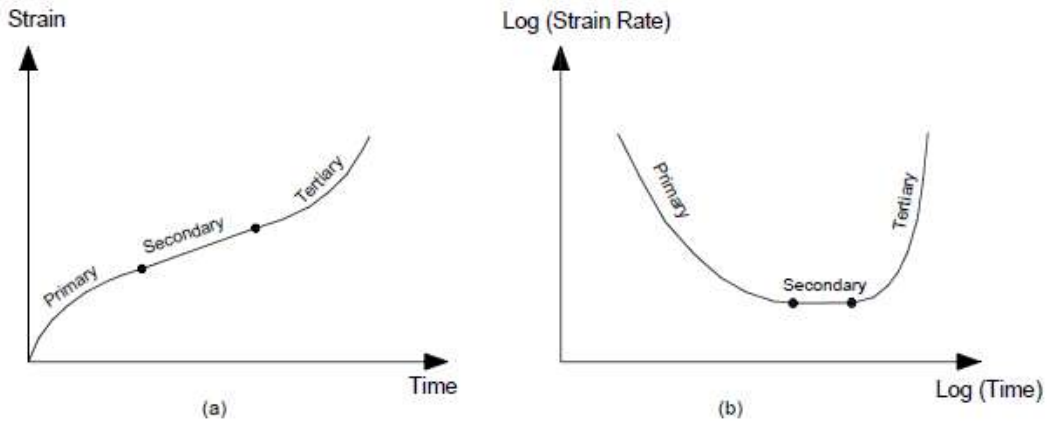


Figure 10 - Primary, secondary, and Tertiary creep stages from a typical triaxial test shown on both: (a) arithmetic and (b) logarithmic scales (modified after Augustesen et al., 2004)

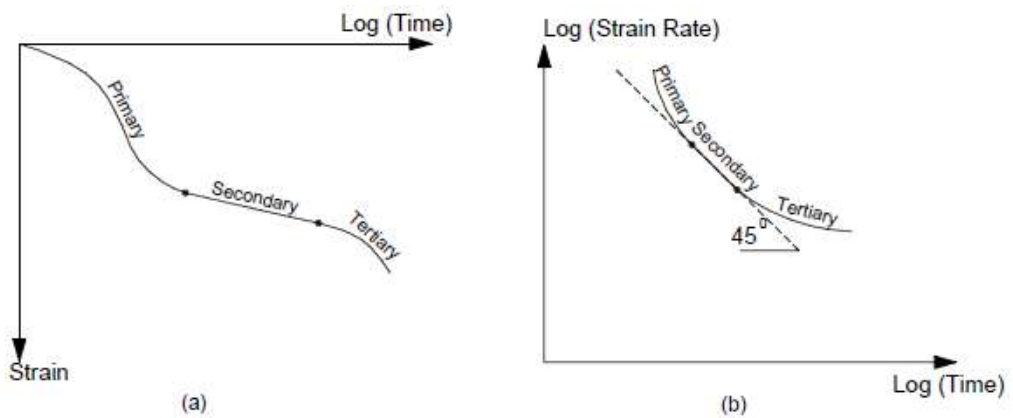


Figure 11 - Primary, secondary and Tertiary compression stages in an odometer test; (a) strain-logarithm of time plot, and (b) logarithmic of strain rate-logarithmic of time plot (modified after Augustensen et al., 2004)

The increasing displacement rates associated with rupture growth and micro-crack interactions during the tertiary creep stage have been subject to research for a long time in order to predict final failure (Saito 1965; Bjerrum, 1967; Saito, 1969; Voight, 1989; Fukuzono, 1990) and volcanic eruptions (Voight, 1988). The concept is frequently termed progressive failure analysis and usually employs examination of movement patterns by plotting movement in  $\Lambda - t$  space, where  $\Lambda = 1/v$  ( $v$  is velocity and  $t$  is time; Figure 12) (Petley et al., 2002).

It has been observed in many shear experiments and real landslides that linear trends in acceleration occur if failure is imminent. This was the case for first-time failures and for failures in which brittle behavior was dominant in the basal shear zone. However, reactivated landslides and failures where ductile deformation is dominant display asymptotic trend in  $\Lambda - t$ , space which has been observed in several landslides (e.g., in Italy, New Zealand, California, Japan and the UK) (Petley et al. 2002; Carey et al. 2007; Massey, 2010, Massey et al., 2013).

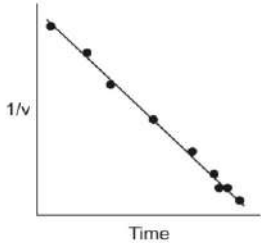
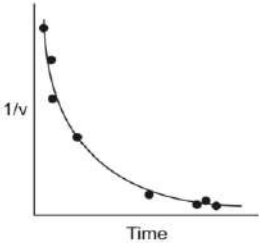
Landslide Movement styles/patterns	Type I	Type II
Landslide acceleration behaviour (1/velocity against time)	<ul style="list-style-type: none"> <li>Linear trend</li> </ul>  <p>The graph shows a series of data points connected by a straight line, indicating a linear relationship between the inverse of velocity (1/v) and time. The y-axis is labeled 1/v and the x-axis is labeled Time.</p> <ul style="list-style-type: none"> <li>Bulk Movement accelerates <i>linearly</i> with time</li> </ul>	<ul style="list-style-type: none"> <li>Asymptotic trend</li> </ul>  <p>The graph shows a series of data points connected by a curve that levels off as time increases, indicating an asymptotic relationship between the inverse of velocity (1/v) and time. The y-axis is labeled 1/v and the x-axis is labeled Time.</p> <ul style="list-style-type: none"> <li>Bulk Movement accelerates <i>exponentially</i> with time</li> </ul>
Dominant basal (at depth) deformation process	<ul style="list-style-type: none"> <li>Crack propagation/growth</li> <li>New cracks join together (micro-cracking process)</li> <li>Development of discrete shear/rupture surface</li> <li>Shear surface generation</li> <li>Brittle failure mechanisms</li> </ul>	<ul style="list-style-type: none"> <li>Crack nucleation</li> <li>New cracks remain isolated</li> <li>Sliding on existing planes of weakness</li> <li>Reactivation of existing landslide systems</li> <li>Ductile deformation processes</li> </ul>
Material behaviour Stress-strain relationship	<ul style="list-style-type: none"> <li>Brittle</li> <li>Commonly occurs in bonded or cemented materials at relatively low confining pressures</li> </ul>	<ul style="list-style-type: none"> <li>Ductile/plastic/non-brittle</li> <li>Shown by materials with little or no interparticle bonding at high confining pressures</li> </ul>
Failure	<ul style="list-style-type: none"> <li>First-time failure</li> <li>Catastrophic</li> <li>Sudden and rapid displacement</li> </ul>	<ul style="list-style-type: none"> <li>Landslide reactivation</li> <li>Non catastrophic/not intrinsically dangerous</li> <li>Continual, slow, creep-like movement</li> </ul>

Figure 12 - Summary of the L-t analyses and their implications on landslide behavior (from Ng, 2007)

### **1.3 Properties of materials**

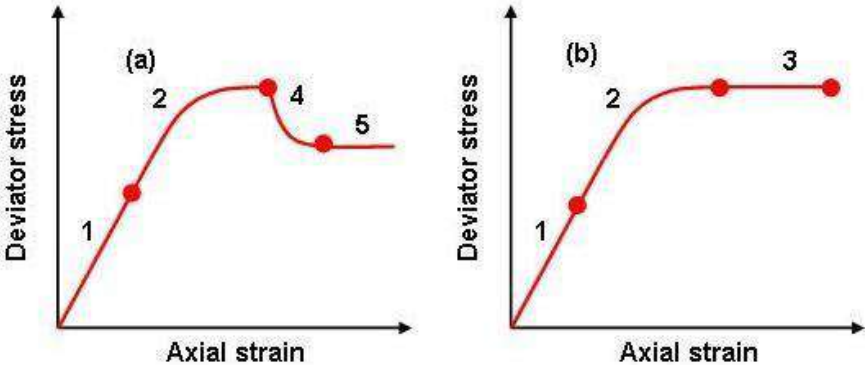
Several laboratory studies conducted on remolded clays (e.g. Parry, 1960; Schofield and Wroth, 1968; Bishop and Lovenbury, 1969) have revealed that at any given mean effective stress, shear failure of the material occurs at constant deviator stress irrespective of strain. In such conditions the material is theoretically able to deform at a constant pore volume to infinite strain. In real systems, however, this is likely to occur only until geometric changes force a change in the stress system or magnitude. The sediment in such conditions is behaving as a perfectly plastic material in the sense that it is undergoing a permanent change in shape without fracturing or without hardening or softening. This form of material behavior is commonly referred to as ductile deformation (e.g. Petley and Allison, 1997) and can be illustrated by a standard stress strain curve (Figure 13a). Plastic deformation in the context of this study refers to the deformation of slope materials under constant shear stress prior to failure. In material science this process is usually referred to as creep and occurs prior to the development of an unstable mechanism e.g. formation of a surface along which sliding could occur.

Ductile deformation has been identified to occur in most geological materials at high effective stresses and may also be characteristic of materials with little or no interparticle bonding. Critically, under these conditions strains are not able to localize to form a shear surface and therefore the material is not able to either sustain an increase in load or to strain-weaken, resulting in a phase of purely plastic, or cataclastic, deformation at constant stress (Petley and Allison, 1997). The mechanism of internal deformation is thus an internal restructuring of the material, at constant porosity. Such deformation is considered to occur at a 'critical state'.

Strictly, this critical state concept applies only to homogenous materials that behave in a perfectly plastic manner. Most natural sediments exhibit an initial shear strength that is greater than that of the critical state due to the presence of interparticle (cohesive) forces. This higher shear strength is generally referred to as the peak strength. Once the peak strength is exceeded, the deviator stress sustained by the sediment decays until the critical state (residual strength) is attained. As the shear force is constant but the shear resistance is reducing, the material must respond by deforming and thus developing strain. Under these conditions sediments will continue to deform until either the shear forces reduce, or until changes in geometry or deformation mechanism promote a change in either the stress state or the sediment's strength. Thus, in conventional soil mechanics theory, stress and strain can be seen to be a coupled phenomenon, with the state of stress, and its inter-relationship with the properties of the material, defining the strain, and vice-versa.

During brittle deformation resulting from increased stress, the material initially undergoes a short phase of elastic (recoverable) strain caused by the bonds, which result from grain-grain adhesion between particles, being loaded but not breaking (Figure 13b). Eventually the load will become sufficiently large that the weakest or most intensely stressed bonds will begin to break (Petley and Allison, 1997). At this point the material is undergoing a combination of elastic and plastic deformation, characterized by a decrease in the gradient of the stress-strain curve. Eventually, the material will reach a point at which so many bonds have been broken that it is unable to bear the applied load or stress. At this point a shear surface will develop as

a consequence of strain weakening, and strength will decrease. Thereafter, deformation in the material will occur primarily as displacement across the shear surface, with the friction across it determining the material strength. Typically, the strength of the material decreases towards the critical state.



	Deformation phase	Description
1	Initial elastic	Bonds resulting from grain-grain adhesion between particles within a material are loaded but not breaking.
2	Elastic-plastic	Weakest most intensely stressed bonds break. Material is undergoing both elastic and plastic deformation characterised by steady decline in stress-strain curve.
3	Plastic-steady state	Strain does not localise along a singular shear surface and therefore material gradually destructured as purely plastic deformation without strain weakening.
4	Brittle cracking	Sufficient bonds are broken that the material is no longer able to bear the applied load/stress. Shear surface develops as a result of strain weakening.
5	Residual-steady state	Shear surface has fully developed and movement has reduced to residual value controlled by frictional resistance along the fully deformed shear surface.

Figure 13 - Idealized deformation patterns (a) Ductile deformation (b) Brittle deformation

Brittle failure commonly occurs in bonded, cemented or cohesive materials at relatively low confining pressures. At a confining pressure in the range of 1250 kPa, most engineering soils will display brittle behavior (Petley and Allison, 1997). Consequently, it is logical that these distinctive forms of material behavior will have key control of the movement patterns recorded at the earth’s surface during landslide initiation.

## 1.4 The shear strength of the slip surface

Most of displacements are usually concentrated along one or more shear zones, that develop in the strain weakening phases, in which shear strength is reduced to a residual value (Massey, 2010). Behavior of shear zones is governed by the Mohr-Coulomb failure criterion, in particular by the ratio of shear force to normal force on the sliding surface, with slip occurring when the Mohr-Coulomb failure criterion is met (Terzaghi and Peck, 1948). The shear strength ( $\tau_f$ ) of a soil at a point on a particular plane was originally expressed by Coulomb as a linear function of the normal effective stress ( $\sigma'$ ) on the plane at the same point (Craig, 1997) where  $c'$  (apparent cohesion) and  $\phi'$  (friction angle) are the shear-strength parameters in terms of effective stress (Figure 14):

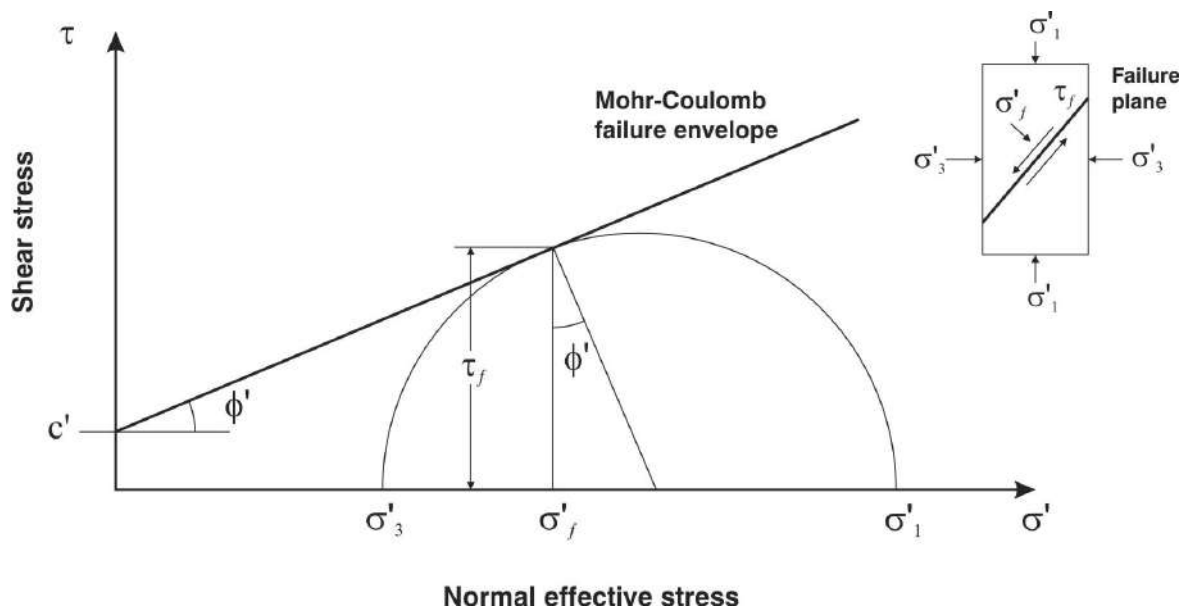


Figure 14 – The Mohr-Coulomb failure envelopes (after Craig, 1992)

$$\tau_f = c' + \sigma' \tan \phi'$$

Failure will occur at any point where a critical combination of shear stress and effective normal stress develops or is exceeded (Craig, 1997). Under pseudo-static conditions, the shear stress operating along the slip surface, and therefore landslide acceleration, depends on variations in the resisting force caused by pore-pressure induced changes (including changes in seepage forces) of effective stress (Picarelli 2007), and changes in material properties (Terzaghi and Peck, 1948; Lupini et al., 1981; Skempton, 1985). As these landslides displace along a pre-existing shear surface, it is assumed in most cases that the materials on the slip surface are remolded and at post-peak or residual values. Skempton (1985) found that for both normally-consolidated and over-consolidated clays, the post-peak drop in drained shear strength to residual values is due entirely to destruction of the original soil structure and particle reorientation. A Keynote paper prepared by Morgenstern (1995) suggests that the movement of slow landslides is regulated by a combination of factors. He states: 'In addition to rate dependence of residual strength of clay, it was noted that the velocity of sliding would also be influenced by the geometrical complexity of the landslide mass. Thickness, water pressure distribution, slope of slip surface, lateral restraint due to channelization and

other factors vary from place to place in all but the simplest landslides. Hence not all locations within a landslide would be mobilized simultaneously and the velocity would be moderated’.

#### 1.4.1 Rate and state friction (RSF)

Most of the studies aimed to characterize the frictional behavior of the rock materials are oriented on the natural and induced seismicity related to the reliable seismic hazard assessment. Most commonly, the laboratory friction data are described in the framework of rate-and-state (RSF), which provides empirical relations between the measured coefficient of friction ( $\mu$ ), rate of deformation ( $V$ ), and ‘state’ ( $\theta$ ). While some variations exist, the most widely used functional form reads (Dieterich, 1978, 1979, 1981; Ruina et al., 1983):

$$\mu(V, \theta) = \mu^* + a \ln\left(\frac{V}{V^*}\right) + b \ln\left(\frac{V^* \theta}{D_c}\right) \quad (\text{eq. 1.})$$

where  $\mu^*$  is a reference coefficient of friction measured at sliding velocity  $V^*$ . The parameters  $a$  and  $b$  are proportionality constants for the magnitudes of the instantaneous ‘direct’ and time-dependent ‘evolution’ effects, respectively, and are thought to represent material properties. The characteristic slip distance  $D_c$  controls the slip distance over which the evolution towards the new steady-state takes place. The evolution of the state parameter  $\theta$  is formulated either by the ‘ageing law’ (eq. 2; Dieterich, 1979) or ‘slip law’ (eq. 3); Ruina, 1983):

$$\frac{d\theta}{dt} = 1 - \frac{V\theta}{D_c} \quad (\text{eq. 2.})$$

$$\frac{d\theta}{dt} = -\frac{V\theta}{D_c} \ln\left(\frac{V\theta}{D_c}\right) \quad (\text{eq. 3.})$$

At steady-state, both state evolution laws reduce  $\theta$  to  $\frac{D_c}{V}$ , so that the steady-state coefficient of friction can be simply expressed as:

$$\mu_{ss}(V) = \mu^* + (a - b) \ln\left(\frac{V}{V^*}\right) \quad (\text{eq. 4.})$$

The parameter  $(a-b)$  now describes the velocity-dependence of  $\mu$  at steady-state, with positive values (i.e.  $a>b$ ) resulting in velocity strengthening, and negative values resulting in velocity-weakening behavior. It has been demonstrated by Ruina (1983) that a material characterized by a negative  $(a-b)$  is prone to frictional instabilities, i.e. stick-slip behavior.

Various authors (e.g. Brace and Byerlee, 1966; Ruina, 1983, Scholz, 1998; Nakatani, 2001; Kato and Tullis, 2001) demonstrate a stick-slip movement on faults behavior, thus, the earthquake is the *slip*, and the *stick* is the inter-seismic period of elastic strain accumulation. In the standard model of stick-slip friction it is assumed that sliding begins when the ratio of shear to normal stress on the surface reaches a value  $m_s$ , the static friction coefficient (Figure 15). Once sliding initiates, frictional resistance falls to a lower dynamic friction coefficient,  $\mu_d$ , and this weakening of sliding resistance may, depending on the stiffness of the system, result in a dynamic instability (Scholz, 1998). First, it was found that  $\mu_s$  depends on the history of the sliding surface. If the surfaces are in static contact under load for time  $t$ , then  $\mu_s$  increases slowly as  $\log t$ . Second, the dynamic friction, when measured in the steady-state sliding regime, depends on the sliding

velocity,  $V$ . This dependence, which goes as  $\log V$ , may be either positive or negative, depending on the rock type and certain other parameters (e.g. temperature).

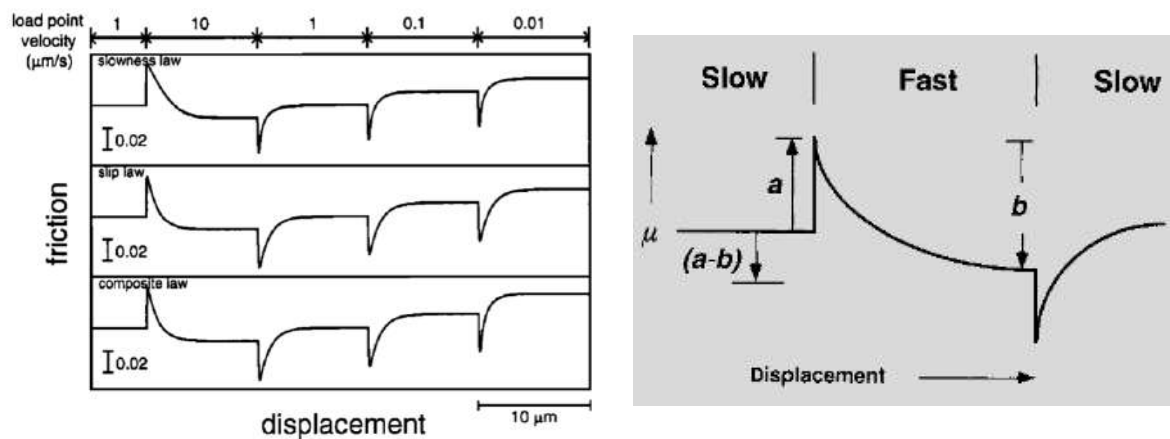


Figure 15 – on left, numerical simulation for a velocity stepping test, the variations of friction coefficient are shown for the slowness (top), slip (middle) and composite (bottom) laws (from Kato and Tullis, 2001); on right, experimental observation on frictional response to a suddenly imposed increase and then decrease in sliding velocity (from Scholz, 1998).

Similarly, these concepts concerning the faults can be applied to landslide and shear zones behavior.

Rates of landslide displacement on pre-existing shear surfaces can vary by many orders of magnitude from extremely slow to extremely rapid (< 16 mm/year to > 5 m/second, Cruden and Varnes 1996). For several large reactivated rock slides in Tertiary-age sedimentary materials of New Zealand, the recorded average landslide speeds vary between 0.3 to 0.5 mm/day for the Taihape landslide, 1 to 27 mm/day for the Utiku landslide, 10 to > 400 mm/day for the Abbotsford landslide (Hancox et al., 1980) and up to 430 mm/day for the Deans landslide (McSaveney and Griffiths 1987). Changes in the residual shear strength of the slide surface materials could be caused by changes in movement (shear) rate. Rate induced changes in shear strength could therefore be an important control on landslide movement.

Skempton (1985) using the results from ring-shear tests on clays carried out by Petley (1966) and Lupini et al. (1981), found that when sheared at slow rates the average change in strength is less than 2.5% per order of magnitude variation in shear rate, and that variations in strength within the usual range of slow laboratory tests (0.0001 to 0.01 mm/minute or 0.1 to 14.1 mm/day) are negligible (Figure 16). From ring-shear tests on clays sheared at higher rates, an increase in strength becomes pronounced at rates exceeding 100 mm/minute, when a qualitative change in behavior occurs (Figure 17). Lupini et al. (1981) and Skempton (1985) suggested that this behavior was probably associated with the disturbance of the originally ordered structure and termed it 'turbulent shear'. Some disturbance appears plausible, as when sheared at rates of ~ 300 mm/minute followed by re-imposed lower rates of shear, a peak in strength is observed, with resistance falling to the residual only after considerable further displacement (Skempton, 1985). However, this process cannot involve turbulence. Nieuwenhuis (1991) and Angeli et al. (2004) suggest that once residual strength has been achieved and shearing has stopped, consolidation of the shear band may lead to strength regain, attenuating the likelihood of reactivation (van Asch et al., 2007) (i.e. following the consolidation theory).



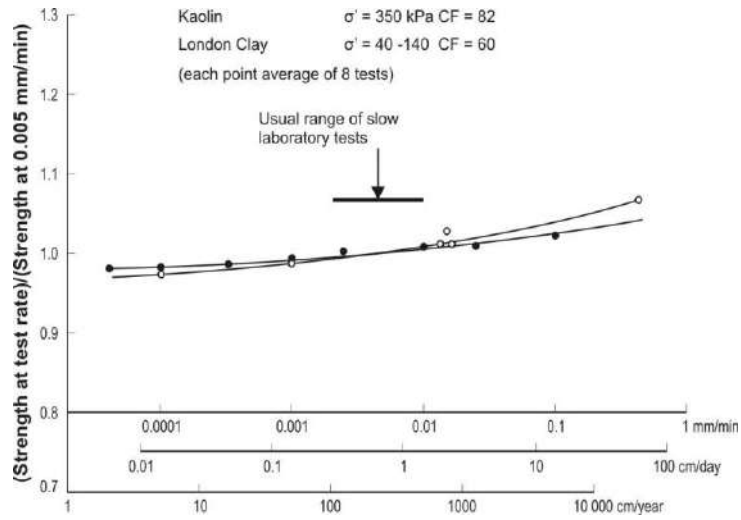


Figure 16 - Variation in residual strength of clays at slow rates of displacement (from Skempton, 1985)

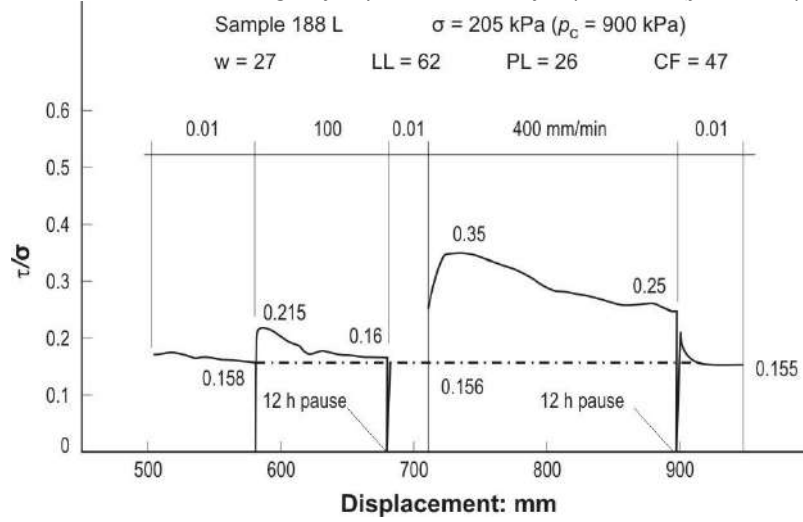


Figure 17 - Kalabagh Dam ring-shear test, August 1983. (from Skempton, 1985)

Tika and Hutchinson (1999) investigated through a ring shear apparatus the mechanical behavior of shear zone of Vajont landslide, the tests were carried out at slow and fast rates of shearing defining the coefficient of friction. The observed behavior at slow rates (0.0145 mm/min) and fast rates (2,600 mm/min) have been significantly different (Figure 18), especially when sheared at fast rates of displacement showed initially an increase in strength above the slow residual value followed by a significant drop in strength below the slow residual value at rates greater than a critical value (negative rate effect). The minimum fast strength was as low as 60% of the slow residual value at rates greater than 100 mm/min.

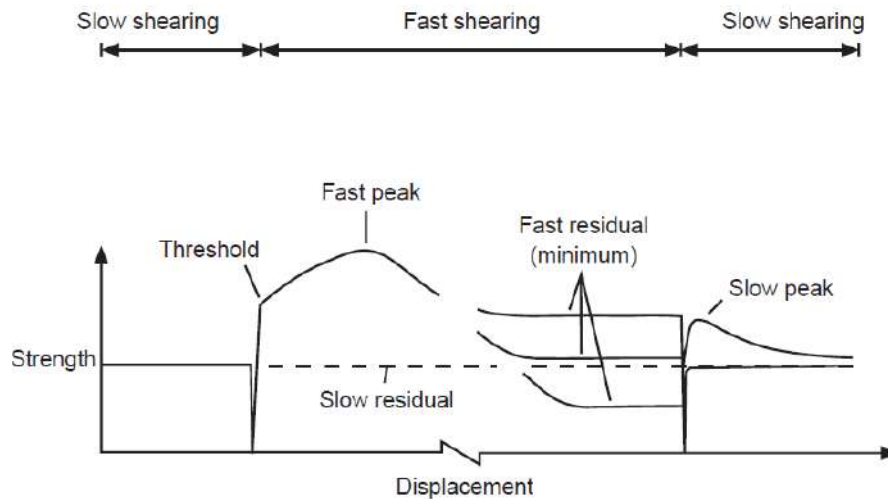


Figure 18 – summary of the observed rate-dependent phenomena for the residual strength (from Tika and Hutchinson, 1999)

Ferri et al. (2011) performed a series of experiments on the clay-rich gouges from Vajont basal detachment providing evidence that their frictional properties were controlled by (i) the frictional properties of smectite, (ii) the water content of the clays, and (iii) the imposed slip rate. They found that the formation of a continuous film of liquid water in the slipping zone reduced the coefficient of friction to almost zero (Figure 19). In particular, at room humidity the friction coefficient increases at low velocity (velocity strengthening behavior). At higher slip rates (Figure 19), the friction coefficient decays, due to the efficient shear heating which is responsible of a temperature increasing. At such high slip rates (1.31 m/s equivalent velocity), the measured dilatancy of the slipping zone, the presence of decomposition products of smectites which might result from grain rolling, support the hypothesis that powder lubrication processes were triggered; at wet conditions, the frictional behavior is always velocity weakening and friction evolves to almost zero when velocity increases. They also demonstrated that, shearing localizes along the water layers among particles or at the clay-rich gouge/wall rock boundary.

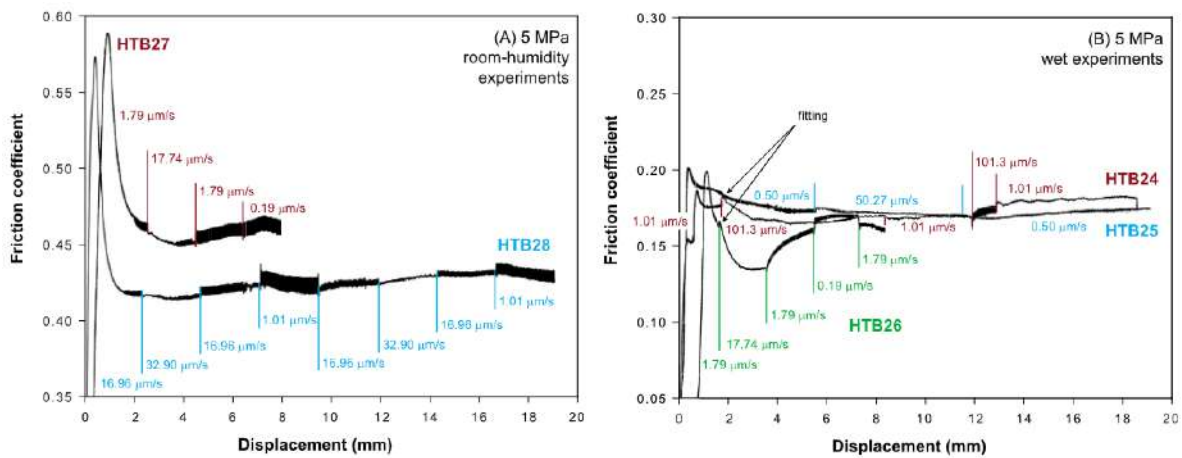


Figure 19 - Friction coefficient versus displacement in representative biaxial experiments at constant normal stress: (a) room humidity conditions and (b) wet conditions (from Ferri et al., 2011)

## 1.5 Behavior of Shear Zones

Given that the shear zones are the result of the rockslide evolution, and most of displacements are usually concentrated along one or more of these, that develop in the strain weakening phases (e.g. schistosity), in which shear strength is reduced to a residual value, their characterization is fundamental. Investigation about their petrographic and mineralogic composition and the geo-mechanical properties is essential to predict the future rockslide behavior, including stability with displacement, velocity and time. To measure these parameters were used both conventional (uniaxial compression, triaxial and direct shear tests; e.g. Straühal et al., 2017) and unconventional tests (LHV tests; e.g. Sassa, 1997, Tika and Hutchinson, 1999, Wang and Sassa, 2002; Wang et al., 2003, Agung et al., 2004; Wang et al., 2007; Wang et al., 2010; Ferri et al., 2013; Schulz and Wang, 2014; Yamasaki et al., 2016; Schulz et al., 2018). The most important works related to shear zones, were conducted on faults slip movement (as presented further on) by Direct Shear, Ring Shear Apparatus (RSA) or similar testing machines (e.g. biaxial, rotary shear).

Most of the studies (e.g. Skempton, 1964; Shimamoto and Logan, 1981; Lupini et al., 1981; Tiwari et al., 2005; Collettini et al., 2009, 2011; Wenk et al., 2010; Moore and Locker, 2011; Di toro et al., 2011 Oohashi et al., 2011, 2012, 2013; Yamasaki and Chigira, 2011; Ferri et al., 2014) demonstrate that weakening of slip zone (for faults and landslides) can occur in cases where weak mineral phases (Figure 20, e.g. phyllosilicates and graphite) constitute even a small percentage of the total fault rock and that low friction results from slip on a network of weak phyllosilicate- and graphite-rich surfaces within the rock fabric. Samples with well-developed foliation are extremely weak compared to their powdered equivalents.

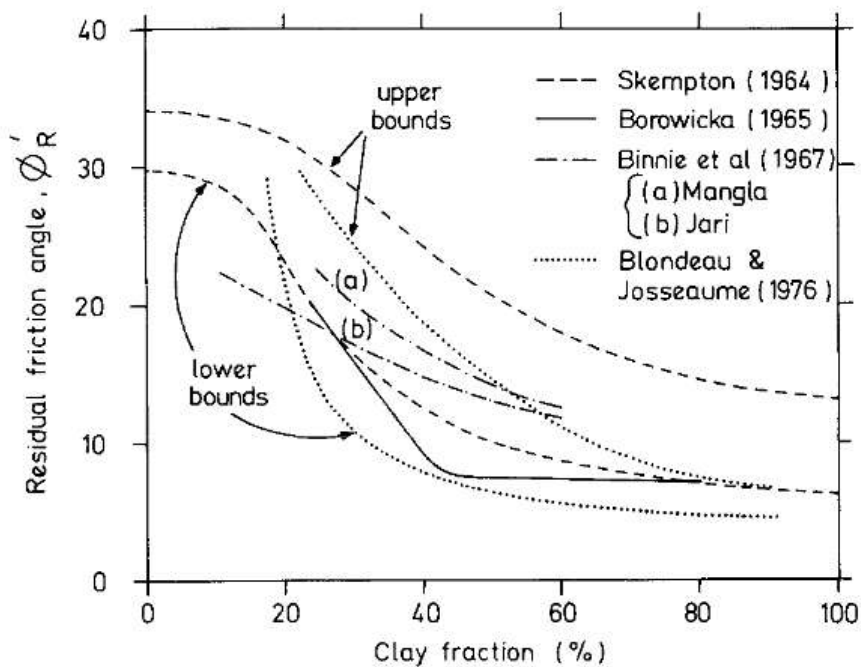


Figure 20 - Residual strength: correlation with clay fraction (from Lupini et al., 1981). In general view, has been demonstrated that residual friction angle decreases with increasing clay fraction.

Dynamic weakening mechanisms can explain some observations; however, creep and aseismic slip are thought to occur on weak layers, and quasi-static weakening mechanisms are required to initiate frictional slip (Collettini et al., 2009).

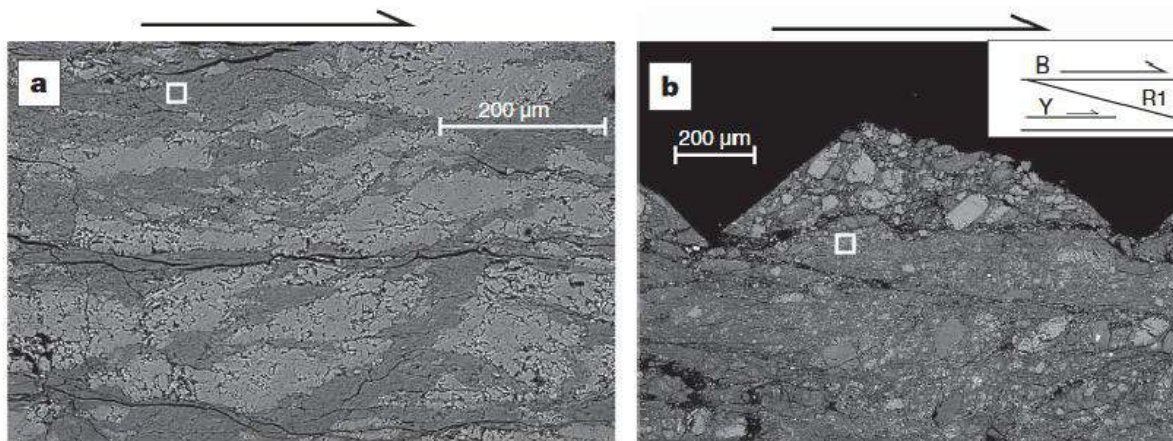


Figure 21 - Comparison between solid-foliated and powder sliding surfaces. a) the calcite sigmoid are interspersed within a fine-grained foliation made of tremolite and phyllosilicates (smectite, chlorite and talc). The slipping processes occur along planes localized within the foliation) The fault rock shows a cataclastic texture with zones affected by grain-size reduction (from Collettini et al., 2009)

Some experiments were conducted on artificial samples with graphite (e.g. Yamasaki and Chigira, 2011; Oohashi et al., 2013; Yamasaki et al., 2016) and they demonstrate that the shear strength of these decreased abruptly with increasing areal extent of the graphite layer along the shear surface, from which it can be inferred that the continuity of a graphite layer in natural pelitic schist has a considerable effect on shear resistance, suggesting that even comparatively low dip angles of schistosity in pelitic schist could initiate microscopic slip along the graphite-rich layers.

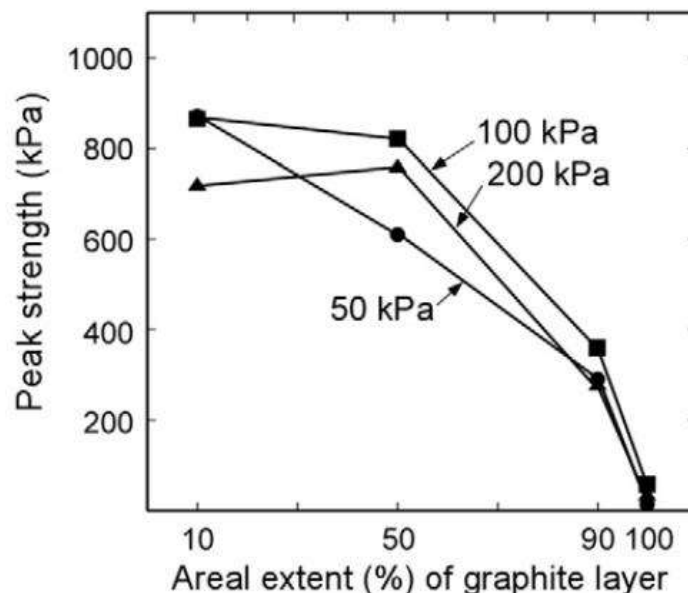


Figure 22 - Relation of peak frictional strength with areal extent (percent of area of shear plane) of graphite layer embedded in the shear plane of artificial rock samples at various normal stresses (from Yamasaki et al., 2016).

Other studies (e.g. Wibberley et al., 2008; Oohashi et al. 2012, 2013) investigated the presence and influence of graphite and amorphous carbon in natural environment (fault zones), demonstrating that a low concentration (up to 12%) is high enough to affect frictional properties at wide range of slip rates (Figure 23) and also demonstrated that the coefficients of friction of the gouges decrease nonlinearly with increasing graphite fraction for any given shear strain and slip rate (Figure 24).

Graphite is a well-known solid lubricant, and the friction coefficient of graphite powder was very low over a wide range of slip rates whereas that of amorphous carbon became low only at slip rates greater than a few centimeters per second, similar to other rock-forming minerals.

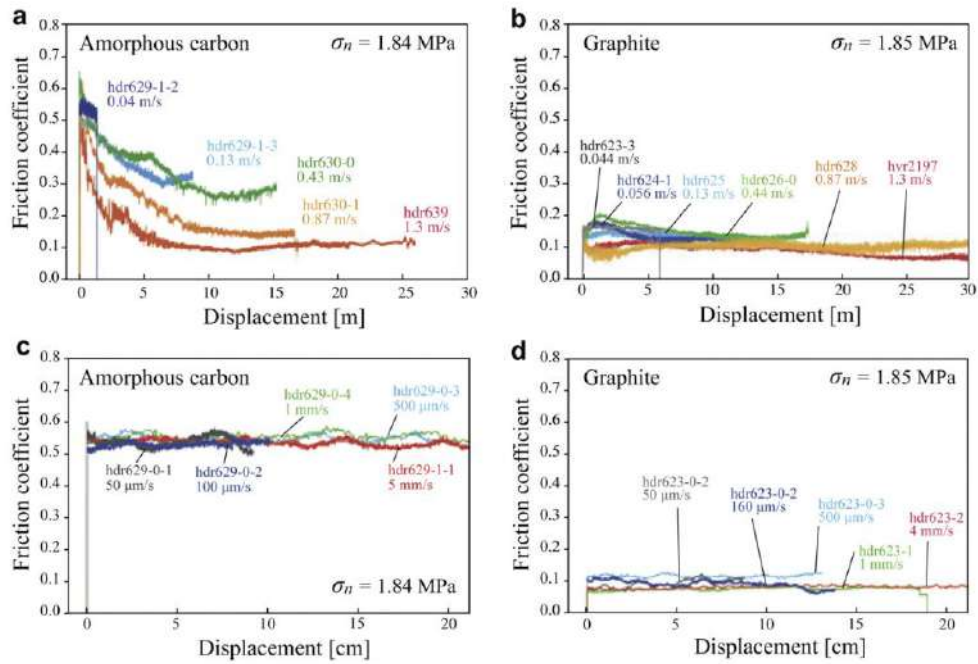


Figure 23 - Frictional behaviors at various slip rates on amorphous carbon gouge (a, c) and graphite gouge (b, d) at a normal stress in an intermediate to high-velocity regime; (a, b) and a low to intermediate-velocity regime (slip rate of 50 m/s to 5 mm/s) (c, d) (from Oohashi et al., 2012)

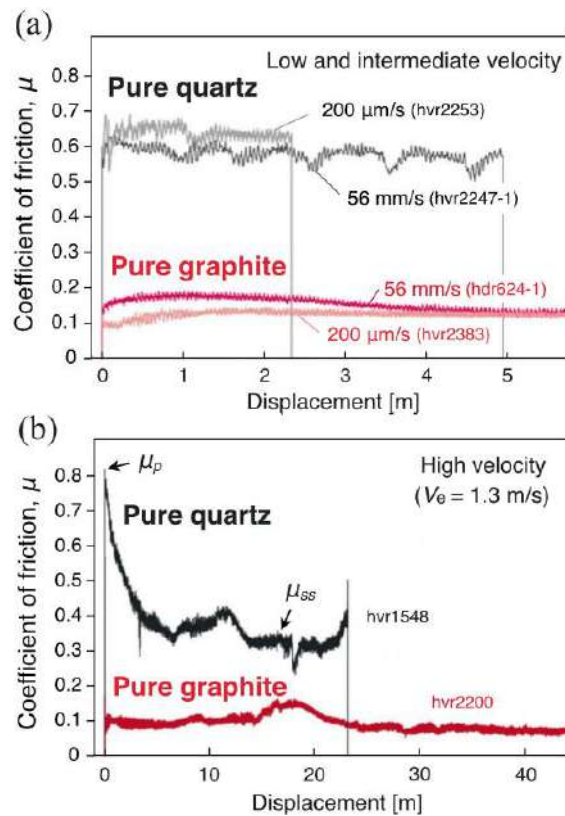


Figure 24 – Coefficient of friction plotted against fault displacement for pure quartz and pure graphite gouges deformed under dry conditions (with room humidity) at a normal stress and at (a) low, intermediate, and (b) high velocities, as specified on each curve (from Oohashi et al., 2013)

Other studies (e.g. Schulz et al., 1982; Morrow et al., 2000; Moore and Locker, 2004, Morrow et al., 2017) investigated the influence of water on frictional strength and was observed a decrease in frictional resistance of gouge materials (e.g. talc, serpentine series, chlorite, graphite, quartz; Figure 25) with saturation, found that certain near-surface creep events across active faults were correlated with rainfall and the associated *swelling and softening* of fault gouge (Schulz et al., 1982). Conversely, they observed that a drawdown of the water table due to a lack of rain dewatered the slip zone and led to an increase in the failure strength of gouge materials, causing a delay in near-surface creep events until a threshold stress was reached.

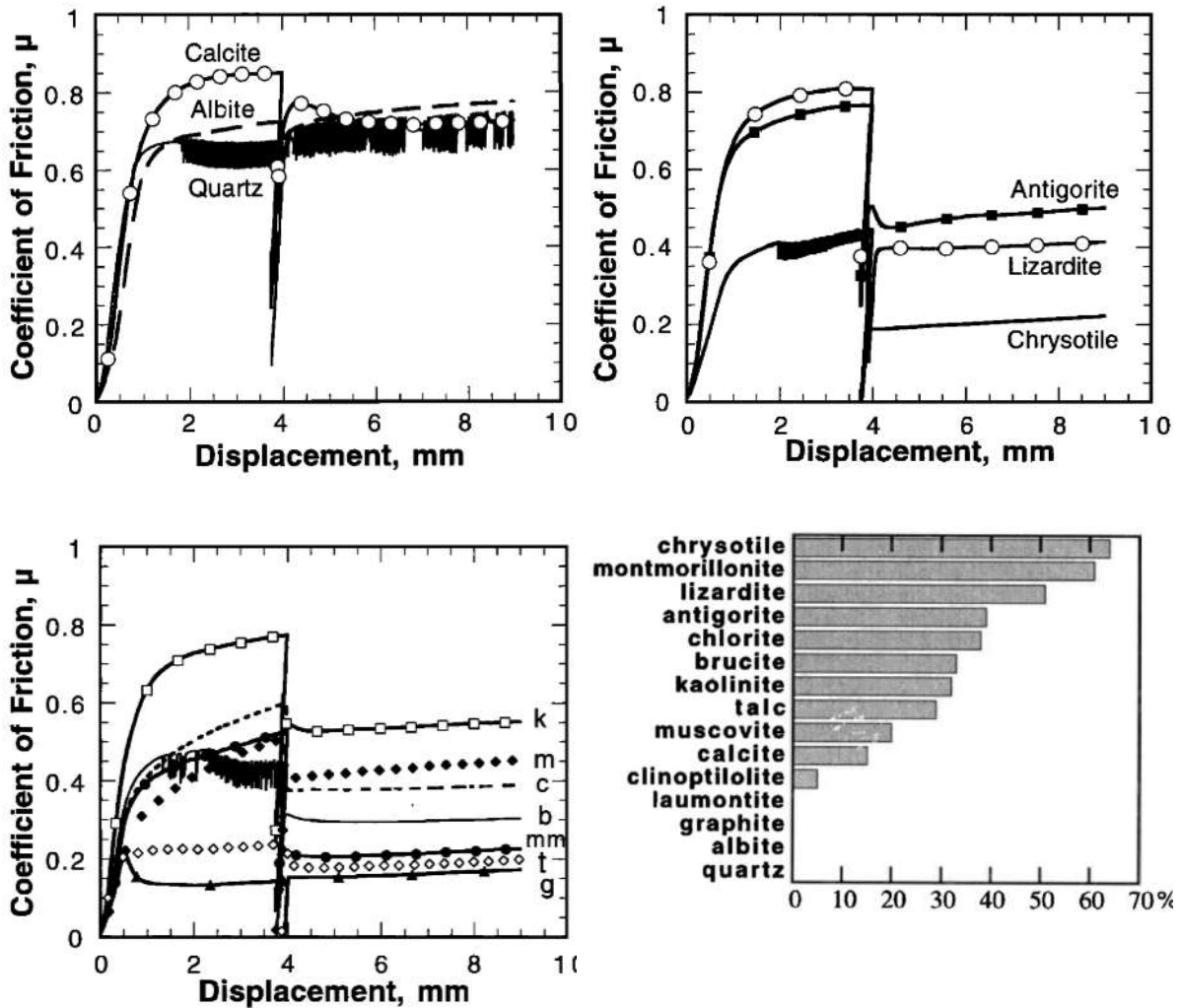


Figure 25 – coefficient of friction versus axial sliding displacement for fault gouge minerals. In the lower left corner graph the letters refer to: kaolinite (k), muscovite (m), chlorite (c), brucite (b), montmorillonite (mm), talc (t) and graphite (g). Fourth graph represent the percentage decreasing of friction strength for gouge minerals after saturation (from Morrow et al., 2000)

Most of the studies on landslide shear zone material was conducted through use of ring shear apparatus (e.g. Sassa et al., 1997; Tika and Hutchinson, 1999; Wang and Sassa, 2002; Sassa et al., 2004; Wang et al., 2010; Schulz and Wang, 2014). Sassa et al. (2004) simulated a landslide triggered by the gradual increase of ground-water level during heavy rainfall. Sliding surface liquefaction resulted with the progress of shearing even in the naturally drained condition corresponding to the gradual increase of pore-water pressure in the debris-flow materials. An undrained ring-shear test was carried out simulating the undrained loading process that takes place in the pre-existing deposits and the weathered surface soils on the valley slopes. This revealed that only a small increment in the shear stress due to the impacting by the displaced soil mass could have caused shear failure of these deposits/soils with the generation of high pore-water pressure (Figure 26).



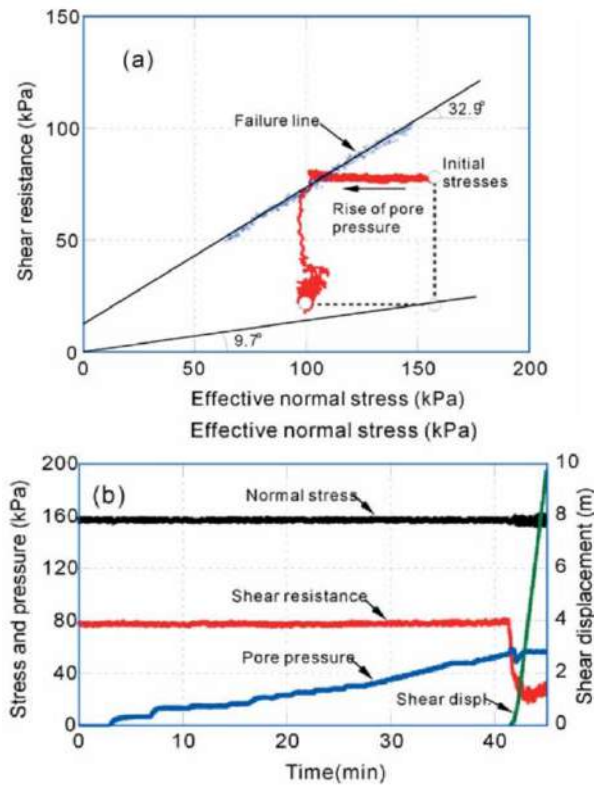


Figure 26 – results of ring shear tests to simulate the increment of pore-water pressure as in rainfall-induced landslides (from Sassa et al., 2004)

Wang et al. (2010) characterized the shear behavior of weathered serpentinite samples from Shiraiishi landslide (Japan). They performed a series of tests at different normal stresses and shear displacement rates. These tests showed that samples with different clay minerals showed different shear behavior (with more clayey showing larger decrease in friction angle) and the samples near the shear zone were characterized by a lower friction angle if compared with samples from landslide body. Furthermore, they been demonstrated that the residual shear strength increased significantly with shear rate (Figure 27). Schulz and Wang (2014) using the same apparatus (RSA #5 at Disaster Prevention Research Institute, Kyoto University) performed a series of seismic loading tests at constant displacement rate. They revealed that failure characteristics resulted from decreasing strength with displacement and increasing strength with displacement rate. Invariant strength was observed at low displacement rates and during tests for which shear stress was gradually increased until failure occurred, which supports implications of constant strength from monitoring observations of the landslide seasonal reactivations.

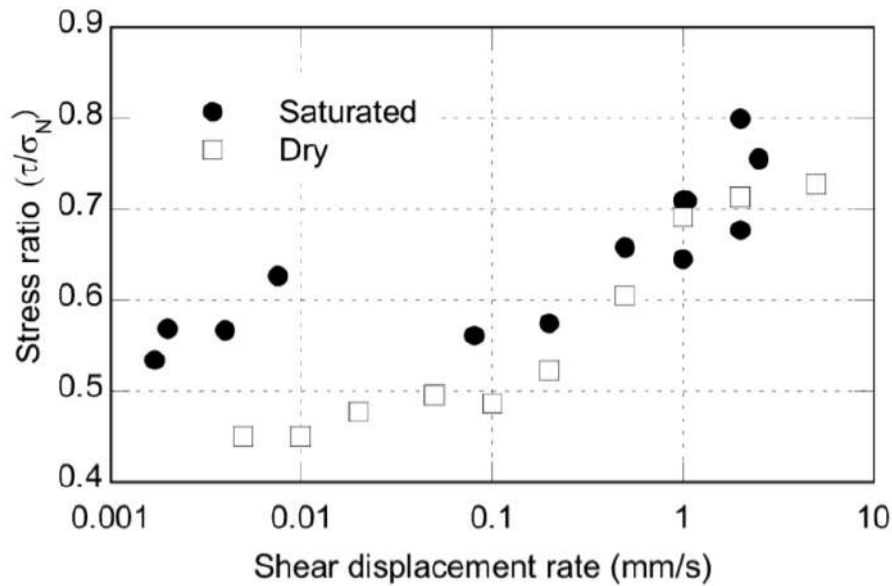


Figure 27 - Residual shear strength against shear rate (from Wang et al., 2010)

The investigation of the structure, the mineralogical composition and geomechanical characteristics (residual friction angle, grain size distribution) of the shear zones of deep-seated rockslides was presented in Straühal et al. (2017). They found a large amount of biotite, muscovite and chlorite, but no strength-sensitive swelling clay minerals. The residual friction angles of the analyzed samples vary between 19° and 28°, with the higher value from tectonic shear zones. A trend of decreasing residual friction angle with increasing clay and silt fractions and increasing phyllosilicate content was observed. Nevertheless, a clear correlation between the grain size distribution or the mineralogy and the friction angle was not present, given that the residual friction angle depends on several additional characteristics (e.g. uniformity, roundness). Furthermore, a strong influence on the friction angle to the specific testing procedure used (i.e. upper grain size limit, displacement rate; Figure 28) have been observed.

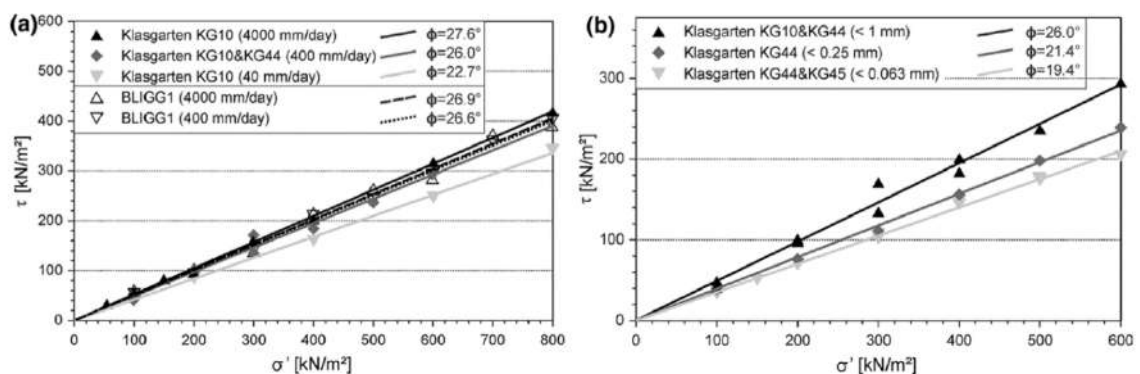


Figure 28 – a) Influence of the displacement rate on the residual shear resistance. All tests were performed with an identical maximum grain size of 1 mm; b) influence of the maximum grain size on the residual shear resistance (from Straühal et al., 2017)

For the tests at a high displacement rate (4000 mm/day), a trend of increasing laboratory residual friction angles with higher displacement rates could be observed according to previous works. Finally, a discernible difference in structure, mineralogical composition or geomechanical properties between the brittle tectonic fault zones and the shear zones of rockslides located in low-strength metamorphic rock (Figure 29).

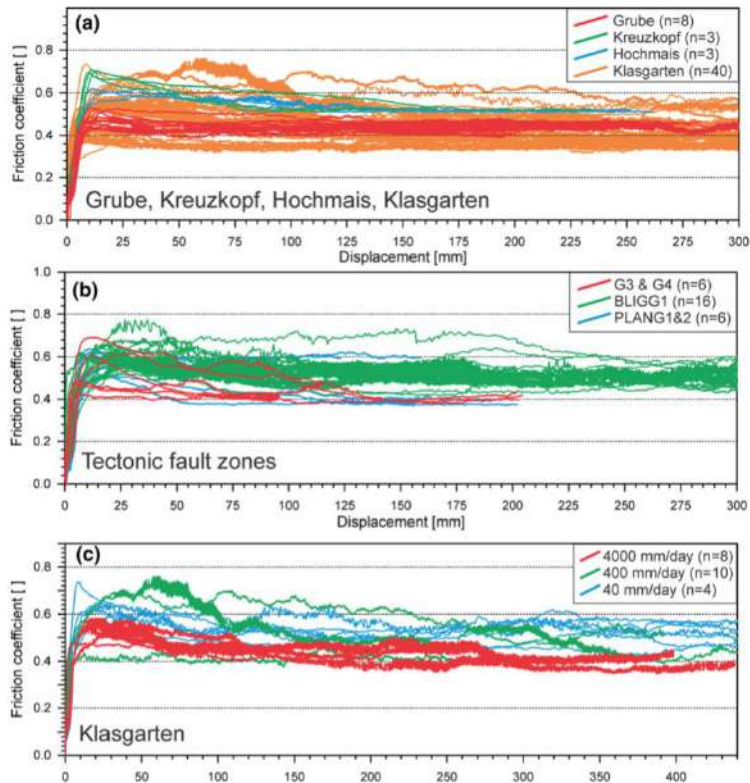


Figure 29 – The coefficient of friction versus the shear displacement obtained from the ring shear tests. A) Rockslide shear zone samples; b) tectonic fault zone samples; c) rockslide samples with varying shearing rates and identical maximum grain size of 1 mm (from Straühal et al., 2017)

## 1.6 Dynamic Viscosity

To investigate these differences, several authors have modified the Mohr-Coulomb failure criterion to include a viscosity component, assuming that the material along the *slip surface* is a layer with a finite thickness and behaves as a visco-plastic material (fluid) during periods of landslide acceleration (e.g. Bertini et al., 1984; Angeli et al., 1994; van Asch, 2007; Picarelli, 2007; Gonzalez et al., 2008; Secondi et al., 2013; Crosta et al., 2014; Frigerio et al., 2014; Castellanza et al., 2015). However, displacement occurs by slip along a large number of shear surfaces within the material forming the shear zone, and the material between these shear surfaces is also likely to deform plastically. Therefore, not all the material forming the zone of deformation has to deform during a period of displacement; instead, the width of the shear band mobilized during a particular displacement period can change and may do so as a function of the applied stress. Unlike Coulomb friction which ignores the thickness of the shear zone, viscosity takes the shear-zone thickness into account.

Viscosity is defined as the resistance of a liquid to shear forces (Newton). In any flow, there is generally a gradient in shear across the flow and the fluid viscosity (which determines the shear gradient) arises from the shear resistance across the flow. Several flow models have been proposed to describe the mobility of slow-moving landslides. Flow models based on Bingham's law are frequently used (e.g. Yen, 1969; Van Genuchten, 1988; van Asch, 1990; Angeli et al., 1996; Corominas, 2005; Delbridge et al., 2016):

$$\frac{dV}{dZ} = \frac{1}{\eta} (\tau - \tau_0)$$

$$\tau_0 = (\sigma - u) \tan \phi'_r$$

$$\tau = \sigma \sin \alpha \cos \alpha$$

The second equation is the Mohr Coulomb failure criterion.  $V$  is the relative velocity (m/s),  $Z$  is the depth,  $\eta$  is the dynamic viscosity (Pa s),  $\tau$  is the shear stress (kPa),  $\tau_0$  is the threshold shear stress (kPa) (or residual shear strength) calculated using the Mohr-Coulomb failure criterion,  $\sigma$  is the normal stress (kPa),  $u$  is the pore pressure (kPa),  $\phi'_r$  the residual friction angle ( $c' = 0$  when relative motion is occurring), and  $\alpha$  is the angle of the slip surface (Corominas et al., 2005; van Asch et al., 2007). For narrow shear bands < 5 cm, van Asch et al. (2007), found that one could assume a straight velocity profile (Newtonian viscosity) and thus a linear relationship between the velocity and depth, giving:

$$V = \frac{h_m}{\eta} (\tau - \tau_0)$$

where  $h_m$  is the thickness of the slip surface (m).

For large ranges of excess stress ( $\tau - \tau_0$ ) it has been found that the relationship is non-linear (Bertini et al., 1984; Salt, 1988; Bracegirdle et al., 1991; Cornforth and Vessely, 1991):

$$V = \frac{h_m}{\eta_0} (\tau - \tau_0)^b$$

The exponent  $b$  can be interpreted as a non-Newtonian viscosity and can be derived from back analyses, while  $\eta_0$  (the apparent viscosity at zero shear) can be considered as the *intrinsic viscosity* of the material (van Asch et al., 2007).

These concepts have been applied to several flow-type landslides to predict their movement patterns (e.g. van Asch et al., 2007), using both laboratory ring-shear tests and back-analyses. Some authors have applied them to translational slides but with limited success (Picarelli, 2004; Corominas et al., 2005). Van Asch et al. (2007) found that there were significant discrepancies between laboratory-scale and field-scale viscosity parameters. These variations were thought to have been due to one or a combination of:

- Errors in calculating the excess shear stress and that the excess shear stress may not be constant over the landslide, and that the infinite-slope model used to calculate these values was too simplistic;
- Apparent viscosity can be generated by negative as well as positive pore pressures and confound the truly intrinsic viscous behavior of the material;
- The intrinsic viscosity changes with effective stress and is therefore a function of pore pressure and seepage forces;
- Identifying and measuring the thickness of the shear band, and testing techniques used to determine its parameters.

Other models, such as Voight's semi-empirical time-dependent failure criterion (Voight, 1989), have been used as a tool to forecast the failure of large rock slides using monitoring data, however, it can only be applied to data characterized by continuous acceleration and constant external conditions (Crosta and Agliardi, 2002), severely limiting its application to reactivated landslides.

## **1.7 Landslide triggering**

Even though landslides can occur without the impact of external factors, generally their occurrence is connected to some kind of triggering event. Many factors can act as triggers for landslides. The most common natural triggers are either related to geological events, such as seismic shaking due to volcanic eruptions or earthquakes, or hydrological events such as intense rainfall, rapid snowmelt or water level changes in rivers or lakes at the foot of slopes (Wieczorek, 1996). Moreover, human interaction in the form of loading or slope cutting can trigger landslide events. The most important trigger, however, in both shallow and deep-seated landslides is intense rainfall (Crosta and Frattini, 2008). Infiltrating rain percolates within the soil, thus increasing pore pressures at hydrologic boundaries, which subsequently decreases shear strength. Positive pore-water pressure may occur directly caused by infiltration and percolation (saturation from above) or may be the result of perched ground water tables (saturation from below) (Terlien, 1998). Important factors determining the evolution of saturation are soil permeability and stratification, preferential flow paths, as well as mechanical characteristics (Berardi et al., 2005).

Prediction of landslide triggering thresholds is one of the key issues in landslide research (Berardi et al., 2005), and established thresholds have an important role in early warning (Terlien, 1998). One of the most influential works in this field was published by Caine (1980) who worked on landslide triggering rainfall thresholds based on rainfall intensity and duration analyses. Since then, many research projects worked on defining rainfall thresholds which trigger landslides. Triggering thresholds are predominantly expressed as rainfall intensity and duration, or cumulative and antecedent rainfall, and can be defined as the line fitting the minimum intensity of rainfall associated with the occurrence of landslide in different areas (Caine, 1980).

Landslide triggering thresholds differ from one region to another based on hydro-climatological and geophysical properties, such as regional and local rainfall characteristics and patterns, slope morphometry, soil characteristics, lithology, morphology, climate (e.g. snow depth) and geological history (Crosta, 1998). Further on, landslide triggering thresholds may also vary with time (Crozier, 1999), for example due to seasonal changes of vegetation (Wieczorek and Glade, 2005).

Most case studies of rainfall thresholds relate to shallow landslides or debris flows. Triggering of these landslides types generally refers to short and intense rain storms, while the occurrence of deep-seated landslides is more affected by long-term rainfall trends (Terranova et al., 2007).

Deep-seated landslides share a more complex hydrology compared to shallow landslides and simple correlations between rainfall and deep-seated landslide triggering cannot be determined (Terlien, 1998). To establish triggering thresholds in deep-seated landslides it is necessary to include rainfall, snow-melting, water infiltration and percolation, generally by means of modelling subsurface hydrology (Ekanayake and Phillips, 1999; Crosta et al., 2014), and to determine the location of shear surface, as well as the hydrological triggering mechanism (Terlien, 1998).

A common procedure is to calculate pore pressures conditions required for slope instability which are then compared to observed pore pressures and checked for reasonability. Based on multiple regression analysis of piezometric measurements Matsushi and Matsukura (2007) established rainfall intensity duration thresholds. Godt et al. (2006) applied a similar approach and derived rainfall thresholds by comparing rainfall data with measurements of volumetric water content. Other authors utilize models to predict pore pressure in response to rainfall events. Wilson (1989) presented a simple numerical model to investigate the build-up of saturation and establish rainfall thresholds. The model represents soils as leaky barrels, where additional water is added at one rate, while water is lost by another rate. Wilson and Wieczorek (1995) combined the model with measurements of piezometric levels and data on antecedent rainfall to derive rainfall thresholds. A related approach has been performed by Terranova et al. (2007) who derive critical rainfall situation for landslide triggering based on modelled infiltration and comparison with piezometer data. Moreover, several other case studies also applied hydrological models to predict pore pressure evolution in response to rainfall events to establish landslide triggering rainfall thresholds (Reid, 1994; Crosta, 1998; Terlien, 1998; Ekanayake and Phillips, 1999; Iverson, 2000; Frattini et al., 2009). Coupled hydrology and stability models have been widely applied to predict the effects of rain storms, and to define critical situations. Examples for local scale (Buma, 2000; Brooks et al., 2004; Berardi et al., 2005; Pagano et al., 2008), and regional scale (Dhakal et al., 2002; Crosta and Frattini, 2003) approaches can be found in the respective literature.

## **1.8 Landslide investigation and monitoring**

The occurrence of landslides is sometimes surprising for humans as they seem to occur without previous warning signs. However, Terzaghi (1950) noted that if a landslide comes as a surprise to eyewitnesses, it would be more accurate to say that the observers failed to detect the phenomena which preceded the slide. Therefore, dedicated landslide analyses and monitoring methods have to be applied to be able to recognize potential slope failures.

Many methodological approaches have been developed to reveal the occurrence of landslides in space and time, to investigate processes acting within mass movements and to monitor ground displacements. The wide range of possible methodological approaches for landslide research stretch from field or desk-based mapping, to measurements of surface and subsurface movement in field or by remotely acquired data sources, recordings of triggering factors like rainfall or hydrological parameters, and the use of simulation models.

Landslides can be assessed on various spatial scales (Glade and Crozier 2005a), but a general distinction between local and regional approaches can be made. The initial step of regional approaches is to define the spatial occurrence of landslides, commonly by preparing landslide inventories (Wieczorek et al. 2005). For local analyses Nakamura (Nakamura 2004) argues that one of the first steps to understand the landslides under investigation are field investigations and boreholes to define the slip surface. Regarding rockslides, but also applicable to other landslide phenomena, (Glawe and Lotter 1996) stated that when instabilities can be expected geotechnical investigations, displacement monitoring and modelling techniques are generally applied. Following (Cornforth and Mikkelsen 1996) ideal features of a landslide monitoring system

are continuous measurements of pore-water pressure in the shear zone by automated sensors in order to correlate these with rainfall data.

Regarding monitoring it should be made clear, that there is no obvious threshold that determines what time intervals between repeated measurements are necessary for it to be classed as monitoring. Olalla (2004) points out that monitoring can range from, for example, inclinometer measurements carried out once in a year, or automatic measurements in intervals of seconds. Therefore, every repeated measurement could be defined as monitoring. Automatic monitoring systems are however more convenient than manual measurements as they do not require humans to regularly go to study sites which may be remote or difficult to access (e.g. Spreafico et al., 2015). Another advantage of automated monitoring system is the ability to control measures by time intervals, thresholds or user input. Besides this, questions of data storage, transmission and security arise with such automatic systems. Moreover, data should automatically be processed and checked to prevent inconsistencies (Olalla, 2004). However, issues of managing automatic monitoring systems will not be discussed here.

## **1.9 Displacement measurements**

Many field methods exist to measure ground displacements due to landslide movements. A simple but convenient field method is the use of quadrilaterals (Keaton and DeGraff, 1996) which consist of four stakes that are fixed inside and outside the landslide body. Distances between the stakes can then be measured manually by tape. Quadrilaterals have been applied within several research applications (Baum and Fleming, 1991; Bogaard, 2000; Giraud, 2002; Fernandez-Merodo et al., 2004; Keaton and Gailing, 2004).

The Global Positioning System (GPS) is a method that is often used to monitor landslide movements (Bonnard et al., 1996; Wasowski et al., 2004; Mills et al., 2005; Webster and Diasm 2006; Yin et al., 2008; Zhang et al., 2008). Precision of measurements is in the range of cm to mm. However, the applicability of this method depends on the visibility of satellites which may not be the case in narrow valleys, densely forested areas or on steep cliffs.

The methods described above are applicable to measure and monitor ground deformation at the surface. In order to understand landslide behavior subsurface measurements are necessary. Basic approaches are pits and trenches which can be used to investigate e.g., the depth of a landslide and the position of shear surfaces or to take undisturbed material samples. Generally, pits and trenches can only be established on shallow movements. Examples are given by Bromhead et al. (2000), Clark et al. (2000) and Topal and Akin (2008). Penetration tests can also be performed to investigate stiffness of subsurface materials. More often, drillings are utilized to investigate landslide bodies. An ample variety of drilling devices is available on the market from simple handheld sounding poles to truck-sized rotary drilling machines. Besides the advantage of directly probing the landslide body and having the opportunity to take core samples, sensors can be applied within the boreholes to further investigate subsurface movement and hydrological processes.

In many cases inclinometers are used to determine subsurface movement of landslides (Bonnard et al., 2008; Bressani et al., 2008; Jongmans et al., 2008; Mihalinec and Ortolan, 2008; Yin et al., 2008). General



remarks on the use of inclinometers for landslides research are provided by Stark and Choi (2008). Inclinometers consist of a flexible riled pipe which is placed vertically into a drilled borehole. A high-precision probe is inserted, and the inclination of the pipe is measured in even distances, for example, every e.g., 50 cm. Repeated measurements give information of the occurred inclination changes in downslope and horizontal direction for the entire length of the pipe. However, it is important that inclinometers are fixed into the stable ground beneath the shear surface to prevent data bias. Automated inclinometers are commercially available and usually consist of several inclinometer probes connected to each other to a chain, or automatic systems where the probe automatically moves within the pipe. Within landslide monitoring the use of automatic inclinometer and inclinometer chains has been described by for example, Lollino et al. (2002) and Olalla (2004), Volkmann and Schubert (2005) and Wienhöfer (2009). However, inclinometers can only withstand a certain amount of displacement before pipes break. This makes them especially applicable for monitoring of slow-moving landslides, but also for detection of shear processes in faster moving landslides.

The mentioned field-based methods only give information on ground displacements for points or along lines. However, spatial methods are also available that give information on displacement for entire slopes.

In recent years many studies utilized Terrestrial Laser Scanning (TLS) for monitoring of geomorphological processes. The technique is similar to LiDAR, but ground-based. In contrast to LiDAR it is appropriate for steep cliffs and rock faces as the scanner can be placed in front of it. TLS scans are used to create three dimensional DTM which can further be analyzed quantitatively within GIS or CAD environments to assess e.g., the volume of displaced material between measurements. Precision of TLS is heavily dependent on distance to the target and ranges from centimeters to mm, as well as environmental conditions such as rain or vegetation. General remarks on TLS and its usage for monitoring geomorphological processes are provided by (Prokop and Panholzer, 2009) and (Schaefer and Inkpen, 2010). Many case studies applied TLS for landslide monitoring (e.g., Mikoš et al., 2005; Rosser et al., 2005; Rosser and Petley, 2008; Avian et al., 2009; Baldo et al., 2009; Oppikofer et al., 2009; Abellán et al., 2010).

SAR methods can also be applied in ground-based studies, which are frequently termed Slope Stability Radar (SSR) (Van Westen, 2007). The major advantages of this method are that they provide high precision data in sub-millimeters range without being affected by weather conditions and without the need to install reflectors or ground marks. However, vegetation drastically decreases accuracy. Luzi et al. (2005) used a ground-based DinSAR system to monitor displacement on the Italian Tessina landslide and compared the measurements to regular theodolite surveys. Based on comparable displacement results by both methods they conclude that InSAR is also applicable for landslide early warning systems. Several other research projects installed SSR systems to monitor displacements of landslides (Canuti et al., 2002; Antonello et al., 2004; Eberhardt et al., 2008; Bozzano et al., 2010; Casagli et al., 2010; Di Traglia et al., 2014, Canuti et al., 2018).

## **1.10 Hydrological measurements**

Given the great importance of rainfall and slope hydrology for landslide triggering, these factors are frequently analyzed and monitored within landslide research. Climatic factors such as rain, snowfall, temperature and wind are usually measured at climate stations, which are commercially available or in many cases provided by meteorological agencies. Measurement of ground-water conditions such as pore pressures and soil water suction are usually accomplished by using piezometers and tensiometers. An overview on different types of these sensors can be found in (Kneale, 1987). Piezometers are probably the most common hydrological sensor utilized for landslide research (e.g., Wu et al. 2008; Yin et al. 2008; Calvello et al., 2008; Yin et al., 2010) and come as simple standpipe or more advanced vibrating wire piezometers. Piezometers measure the pressure of water in saturated soils and therefore give information on the height of the groundwater table within a soil. Tensiometers measure matrix potentials and are frequently utilized to assess the soil suction in the vadose zone (Rinaldi et al. 2004; Montrasio and Valentino, 2007; Greco et al., 2010). Piezometers and tensiometers are usually installed within boreholes or directly into the soil at trenches.

The chemical properties of ground and pore-water have a widely acknowledged effect on shear strength and affect slope stability (Di Maio and Onorati 2000; Angeli et al. 2004) by for example, influencing the mechanical behavior of clays (Leroueil, 2004). However, monitoring of ground water composition is only rarely included in landslide monitoring systems (Sakai and Tarumi 2000; Montety et al. 2007; Sakai 2008).

## 1.11 Landslide Modeling

Landslide modelling is, along with experimental subsoil exploration and experience driven safety assessment, one of the main tasks of slope stability practice (Janbu, 1996). Models are applied to analyze current stability status and to predict slope behavior under certain conditions such as rainfall events or scenarios for environmental change. Moreover, models are used for the back analyses of already failed slopes and for assessment of effectiveness of geotechnical stabilization measures (Barla et al., 2004). However, when dealing with modelling it is important to keep in mind, that all models are necessarily simplified generalization and approximations of processes which are occurring in nature (Favis-Mortlock and De Boer, 2003).

Modelling of landslide failures can be either qualitative or quantitative (Carrara et al., 1999). Qualitative approaches integrate descriptive prediction and the opinion of experts, while quantitative applications are based on numerical simulations. Landslide modelling approaches can broadly be separated into models that are focusing on single landslide processes (i.e. local models), and models with greater spatial extent (i.e. regional models) (Crozier and Glade, 2005).

Local approaches to landslides have a long tradition within geotechnical engineering slope stability practice, while regional applications have increasingly emerged since the wide availability of powerful computers and GIS.

Regional landslide modelling methods generally focus on either landslide susceptibility or hazard, or eventually landslide risk. Landslide susceptibility is defined as the *"probability of spatial occurrence of slope failures, given a set of geo-environmental conditions"* (Guzzetti et al., 2005). Therefore, landslide susceptibility modelling seeks to delineate the terrains' potential for landslide processes. In contrast, landslide hazard is defined as *"the probability of occurrence within a specified period of time and within a given area of potentially damaging phenomenon"* (Varnes 1984). The term hazard therefore also requires definition of magnitude of potential events, that is, affected area, volume and velocity of expected landslide events (Reichenbach et al. 2005). The term landslide risk refers to the outcomes of landslide events and is defined as *"the expected degree of loss due to a landslide and the expected number of lives lost, people injured, damage to property and disruption of economic activity"* (Varnes 1984). While landslide susceptibility and hazard concentrate on the causes and properties of landslides, risk also refers to the consequences and outcomes of such processes, which are strongly dependent on the vulnerability of the effected people and infrastructure.

Local models are used for the analysis of single slope failures, i.e. local models, have a long tradition in geotechnical slope stability practice. These models have frequently been applied to assess the stability of human-made or natural slopes, and the design of slopes, such as embankments, road cuts, open-pit mines etc. Moreover, physically-based models for single slopes allow detailed investigation of failure processes, assessment effects of triggering events, and assessment of the effectiveness of remedial measures and stabilization works.

Today, a wide range of computer calculation programs are available for numerical slope stability assessment. Despite the development of more sophisticated numerical models, limit-equilibrium methodology is still widely applied (Abramson, 2002). In the following a short overview of local landslide modelling methods and techniques is presented. It is beyond the scope to review the theoretical background and mathematical and mechanical derivation of local stability calculation (e.g. Bromhead, 1998; Abramson, 2002; Eberhardt 2003).

Limit-equilibrium methods provide a mathematical procedure to determine the forces within a slope that drive and resist movement. Limit-equilibrium analysis usually calculates stability for discrete two-dimensional slices of a slope and for assumed or known potential shear surfaces (Figure 30), but three-dimensional approaches have also been developed. Shear strength of materials along shear surface is assumed to be governed by linear or nonlinear relationship between shear strength and normal. The result of limit-equilibrium analysis is a global FoS for shear surface, which provides a snapshot on stresses and resisting forces relationship. Several numerical methods are available today which assist in locating critical shear surfaces, this is, where the lowest FoS is prevalent. The most widely applied methods are Bishop's simplified approach, which accounts for circular slip surfaces, and Janbu's method for con-circular, i.e. polygonal shear surfaces. Other methods like the infinite-slope wedge method, ordinary slice method, general slice method, Spencer's method, Morgenstern and Price's method, and some others are reviewed elsewhere (Graham, 1984; Anderson and Richards, 1987; Nash, 1987). Given the wide use of numerical limit-equilibrium methods for slope stability analysis in geotechnical practice, most available models allow assessment of effects of e.g., external loads or remedial stabilization structures, such as soil nails or other reinforcements.

However, these methods also comprise some drawbacks. The resulting FoS represents a global value for a two-dimensional slope profile, where movement occurs if the  $FoS < 1.0$ . However, (Bonnard, 2008) notes that limit-equilibrium methods only provide an approximation of force balance within landslides and that in reality displacements may occur with a FoS between 1.0 and 1.1 - 1.15. Moreover, the FoS is an average value for an assumed critical failure surface and provides no information about the actual distributions of stresses or the progressive development of unstable state (Eberhardt et al. 2004).

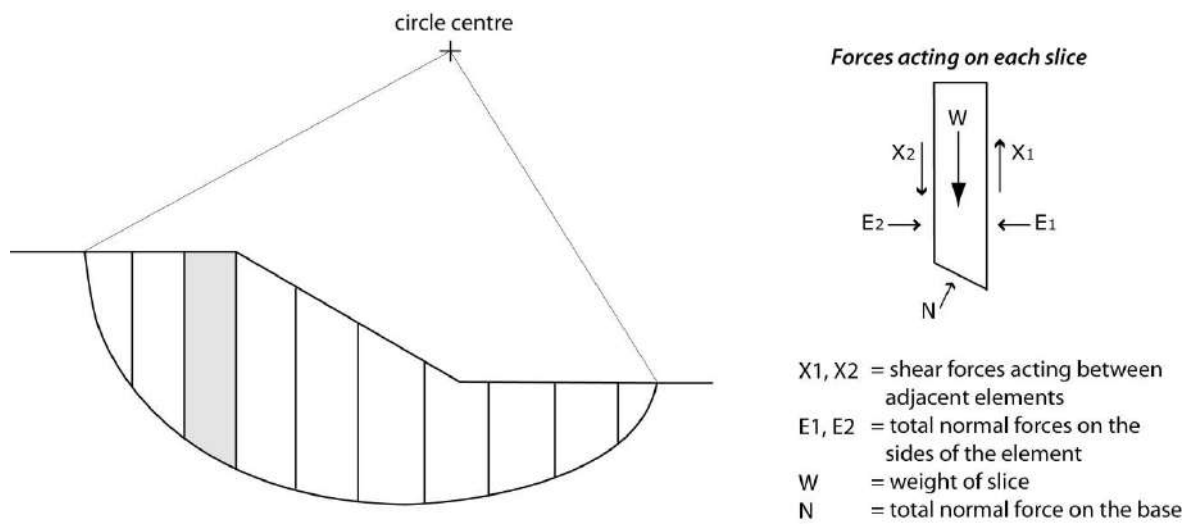


Figure 30 – Simplified illustration of method of slices (based on Conolly, 1997)

A second family of stability models on a local scale is concerned with continuum modelling. The entire slope mass is divided into a finite number of elements and represented as a mesh. Continuum approaches include finite-difference and finite element methods. Finite-difference methods provide numerical approximations of differential equations of equilibrium, strain-displacement relations or the stress-strain equations (Eberhardt, 2003). In contrast, finite-element procedure exploits approximations to the connectivity of elements, and continuity of displacements and stresses between elements (Eberhardt, 2003). However, in both methods the problem domain is discretized into a set of sub-domains or elements. In contrast to limit-equilibrium analysis, continuum modelling software allows for complex time-dependent landslide analysis by including constitutive models such as elasticity, elasto-plasticity and strain softening.

A third family of local landslides models are discontinuum methods, where slopes are represented by distinct blocks which dynamically interact during movement or deformation. The underlying concept of these methods is that limit-equilibrium is repeatedly computed for each block, so that complex non-linear interaction can be accounted for (Eberhardt, 2003).

Three variations of discrete-element variation can be distinguished. Distinct-element methods are based on a force-displacement law to describe interaction between deformable elements, and a law of motion to numerically simulate displacements. Discrete element methods are computationally intensive as many case studies involve a very high number of interacting discrete objects. More detailed information is provided by (Hart, 1993) and (Jing, 1998). Discontinuous deformation analysis simulates interaction of independent blocks along discontinuities, such as fractures and joints. In contrast to distinct-elements methods, discontinuous deformation analysis accounts for displacement instead of simulating forces (Cundall and Strack, 1979). Particle flow methods represent slopes with spherical particles that interact through frictional sliding contacts (Eberhardt, 2003).

## **1.12 Landslide Early Warning Systems**

In the following an introduction to early warning and the challenges of early warning systems is presented. Therein, general aspects on social and technical aspects of early warning are demonstrated. The focus, however, is put on landslide early warning. In addition, a review of existing landslide early warning systems worldwide is presented. It is beyond the scope to give a complete summary of all existent systems, but to illustrate a wide range of technical applications and to highlight integration of social components into early warning process.

Early warning can broadly be defined as the timely advice before a potentially hazardous phenomenon occurs. Dikau and Weichselgärtner (2005) add that the effective use of information for early warning is an important element of general risk management which includes activities such as hazard zoning and prediction, warning communication, disaster prevention and evacuation planning (Figure 31). Good early warning systems therefore comprise identification and estimation of hazardous processes, communication of warnings and adapted reaction of local population. Moreover, early warning systems have to be embedded into local communities to ensure effectiveness of the entire system.

A more pin-pointed definition is used by UNISDR (2009) where early warning system are described as *"the set of capacities needed to generate and disseminate timely and meaningful warning information to enable individuals, communities and organizations threatened by a hazard to prepare and to act appropriately and in sufficient time to reduce the possibility of harm or loss"*.

Early warning systems have been developed for a wide range of natural hazards of which extreme weather events, floods and tsunamis are maybe the best known. However, also for processes such as volcanic eruptions, droughts, snow avalanches, earth- quakes and landslides early warning systems have been installed.

Within the UNISDR a Platform for the Promotion of Early Warning Systems (UNISDR-PPEW) has been founded to stimulate the advance of early warning. UNISDR puts an emphasis on social aspects of early warning and promotes the development of people-centered early warning systems (UNISDR 2006). Four essential key parts for effective early warning can be defined (UNISDR 2006):

1. Knowledge about the risks that threaten a community
2. Monitoring and warning service for these risks
3. Dissemination and communication of warning messages in a way that is understood by the local population
4. Response capability of involved people, who need to know how to react appropriately in case of a warning

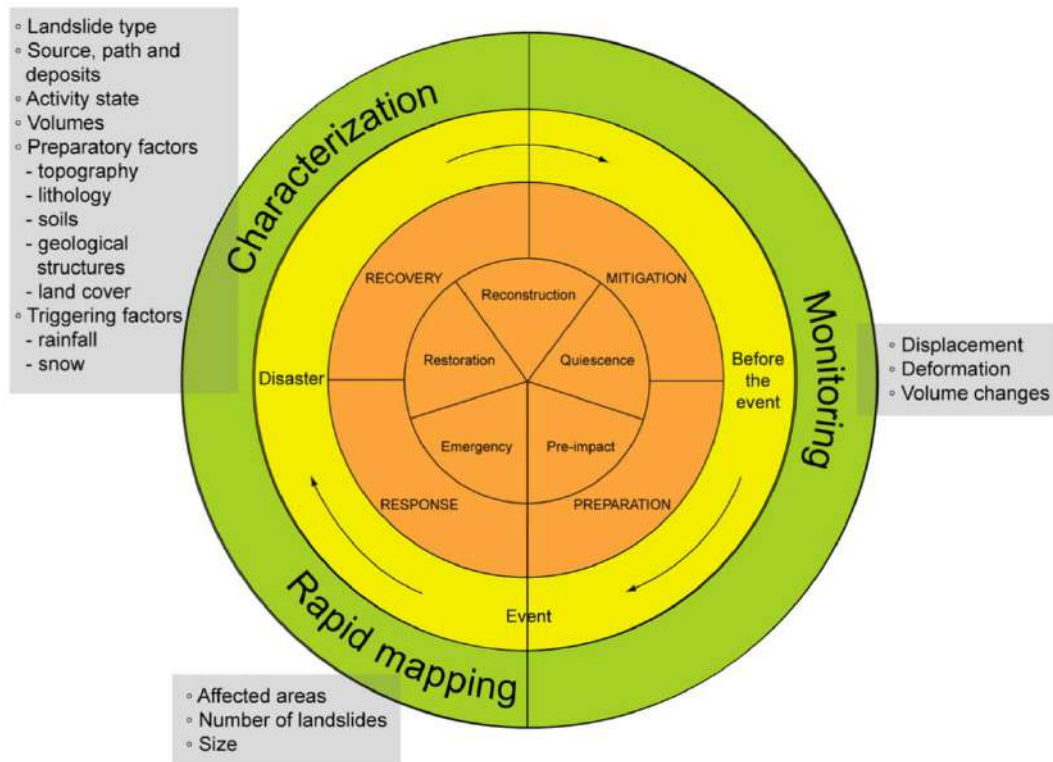


Figure 31 - Rapid mapping, characterization and monitoring as stages of landslide remote sensing in the risk management cycle (modified after Alexander, 2002 and Glade et al., 2005). Priority tasks for landslide investigations (green circle) are shown in relationship to the temporal course of disasters (yellow circle) and the corresponding phases in the risk management cycle (orange circle). Relevant information that can be gathered at each stage with remote sensing techniques are listed within the grey boxes.

Uncertainties always prevail in hazard prediction and are also a major challenge for early warning (UNISDR 2006). Storms may change their track, or lose their strength over time, earthquakes may be expected for a large area, but no exact location can be determined. For many hazard events, only statistical forecasts, such as an El Niño event probability for the next year of 60% can be made. In addition, uncertainties within the social components complicate the prediction of the hazard consequences. These include the reaction of the population to warnings and hazardous events, and the functioning of evacuation plans and general disaster management. Others misunderstand the warning and believe that if a warning is issued by for example the Department of Forestry it only relates to areas with actual logging activities.

Moreover, the costs of unnecessary evacuations due to false alarms are a major concern for decision makers. False alarms are a problem of early warning systems as they can substantially compromise the credibility of early warning systems (Larsen, 2008). The number of false alarms can be reduced by pursuing a conservative strategy and by issuing generalized warnings. However, the use of generalized warnings decreases with the size of the geographic area (Larsen, 2008).

An interesting example of consequences of false warning took place in Italy in 2009 where a scientist had been measuring the emissions of radon gases which are associated with earthquakes. Based on his measurements he was expecting a major earthquake for the city of Sulmona two days before the devastating L'Aquila earthquake (5.8 magnitude on Richter scale) which is located 70 km north-west. As his prediction did not turn out to be accurate, he was accused for creating panic but later absolved.

Given the variety of hazards for which early warning systems have been installed it is difficult to define clear categories. Some basic distinction, however, can be made (Bell et al., 2010):

- Monitoring systems are primarily installed to increase the understanding of natural processes but can also be utilized to plan further actions. These monitoring systems differ by technologies applied, time intervals between measurements and degree of automation.

- Experts- or control-systems provide information on potentially hazardous events and are chiefly implemented to gain information on critical developments and with the aim to guide scientists and decision makers.

- Alarm systems are based on monitoring systems and provoke an automatic warning if, for example, a predefined threshold is exceeded. Further differentiation of alarm systems can be made between pre- and post-event systems and the forewarn time provided by the system. Moreover, these systems differ in their degree of integration of social aspects between purely technical applications and integrative early warning systems.

Early warning systems have also been applied for landslide processes, e.g. rotational and translational slides, debris flows and rock slides. Landslide early warning systems can be installed for single slopes, but also for entire regions. Also, global landslide early warning systems have been proposed by applying methods such as rainfall intensity and duration thresholds (Guzzetti et al., 2008) or satellite-based InSAR monitoring and progressive failure analysis (Petley et al., 2002).

Regional landslide early warning systems can only issue warnings, such as a 70% probability of debris occurrence for a certain region; single slopes cannot be identified (Wieczorek and Glade, 2005). However, local or site-specific landslide early warning systems provide another quality of information. Exceedance of critical thresholds may automatically lead to protective actions, such as alarms, road and bridge closures, evacuation and further disaster management actions. Local landslide early warning systems have been frequently applied, partly because they can sometimes replace structural measures of slope stabilization while providing enough protection. Site-specific systems generally apply monitoring systems for slope movement or landslide triggering factors such as rainfall and pore-water pressure as the early basis of warning.

The Åknes rockslide in Norway is one of the most intensely investigated and monitored landslides worldwide (e.g., Derron et al. 2005; Ganerød et al. 2008; Kveldevik et al. 2008; Kveldevik et al. 2009; Eidsvig et al. 2009; Heincke et al. 2010; Grøneng et al. 2010). The rockslide itself does not pose direct threat to a community, however, slope failure is supposed to trigger a tsunami affecting ships and towns along the fjord. The rockslide mass has a volume of 30-40 million m<sup>3</sup> and displacements vary with seasons and reach 3-10 cm/year with daily movements up to 1 mm (Blikra, 2008). The technical monitoring system includes extensometers, inclinometers, crack-meters, tiltmeters, geophones, piezometers, automated measurements by theodolites, laser and GPS and ground-based radar, and a climate station. All data is available in a web-based database and supervised by experts 24 hours a day. Threshold values for displacement velocity have been established which relate to five alert levels color-coded from green to red.



In case of imminent slope failure sirens warn the population in potentially affected towns. Other topics of the project include development and implementation of warning routines and evacuation planning (Blikra, 2008).

Another example of an intensely monitored rock slide is the Frank Slide at Turtle Mountain, Canada, which exhibited a catastrophic failure in 1903 causing 70 fatalities (Froese et al., 2005). A landslide monitoring and early warning program was launched in 2003 and commenced with detailed site investigations using InSAR, microseismic surveys, ground penetrating radar, drilling and core sample analysis. Within the actual early warning system tiltmeters, extensometers and crack meters are used as primary sensors as they provide high detail displacement data (Froese et al. 2006). Secondary sensors include differential GPS and automatic theodolite measurements which have higher fluctuations but improve understanding of the overall situation. Background information is gained by tertiary sensors, i.e. climate station data and microseismic monitoring. The early warning system comprises four elements (Froese et al., 2005). A monitoring procedure was established to determine responsibilities for measurements and their frequencies, which might change in response to trends and anomalies in the data. Within the threshold development procedure value-based and velocity-based thresholds two standard deviations above noise level were established. Development of alert levels and notification protocols comprise the third element of the early warning system. A standardized terminology and appropriate response to trends in monitoring data were determined. Moreover, action advice was developed for emergencies including procedures for communication and evacuation. The current alert level is accessible on the internet and is presented in four colors. The green alert level indicates normal situations where measurements are in the range of background noise but may exhibit seasonal fluctuation. The watch level is active if multiple sensors display unusual trends and leads to direct communication between technical experts and local decision makers and municipal officials). The warning level is initiated if multiple sensors demonstrate acceleration trends exceeding pre-defined thresholds. If several sensors indicate accelerations and final failure is imminent (one to three days to failure) then the alarm level is issued, and the emergency response procedure is executed. More detailed information on monitoring, modelling (Froese et al., 2009) and the information platform (Froese et al., 2006) is given in the respective literature.

Others two example of landslide early warning system are two the case studies presented in this work. Concerning the Mont de La Saxe (for monitoring system see section 2.5), starting from the management system of the monitoring network, has been defined a specific communication strategy aimed at supporting the decision makers during the critical phases of the landslide evolution, and to share the information with all the stakeholders. The main goals of the communication strategy are: (i) update all LMT members in near-real-time with essential information; (ii) deliver specific periodic (or on-demand) reports for each LMT role, summarizing the evolution of the large slope instability in a defined time period; (iii) fully exploit the potential of the data available, and provide the correct information on the landslide evolution to all people involved in the emergency scenario. In the following, has been described the details of the strategy, as well as how applied it to the management of the La Saxe emergency (Giordan et al., 2015; Manconi and Giordan, 2015).

Regarding Ruinon rockslide, the early warning system has been improved in this work (see section 2.8 and chapter 7, Crosta et al., 2017.).

In conclusion, innovative landslide early warning systems try to integrate sophisticated slope stability models and real time modelling of landslide initiation. Concerning deep-seated landslides and failures in rock more complex monitoring is applied to measure displacements and processes related to movement triggering. Warning thresholds may account for displacement or critical parameter values of triggering factors. Modelling of slope behavior by complex slope stability models is an important part of landslide prediction and is frequently applied for landslide early warning. Most landslide early warning system are not fully automated but leave judgment of the current situation and final warning to experts. Existing landslide early warning systems differ substantially regarding the integration of social aspects. In some cases, landslide early warning is integrated into larger schemes for slope safety, risk management, disaster prevention and hazard awareness, while other systems constitute simple technical approaches (e.g. Mont de La Saxe, Chervaz and Ruinon rockslides).

*Desot l'ève la fan.  
Desot la neilo pan.*

### **2.1 Mont de La Saxe Rockslide**

The Mont de La Saxe rockslide is located in the upper part of Valle d'Aosta region, at the extreme South-West termination of a DSGSD (Figure 33), which occupies the terminal sector of the left-hand side of the Ferret Valley (Ratto et al., 2007; Broccolato et al., 2011; Crosta et al., 2012, 2014). The rockslide dimension is more of  $8 \cdot 10^6$  m<sup>3</sup> in volume, and it extends between 1400 and 1870 m a.s.l., over in area of 150,000 m<sup>2</sup> with a horizontal length of about 750 m, maximum width of 600 m, and average slope gradient of 37° (Figure 32).

A previous analysis about aerial photos since 1988 until now, shows that before 1988, the entire slope was intensely vegetated, and no debris scree was detectable at the already existing small headscarp, and only in middle of nineties the upper scarp activity became evident.

This instability represents one of the most monitored phenomena on Alps, as such its activity could generate a very high social and economic consequences, has been quantify the values of infrastructures involved is over one billion of euros (Figure 33). The landslide is located close to Entrèves and La Palud villages (within Courmayeur municipality) and nearness to the Mont Blanc highway that connects Italy to France (basics for road transport) and related tunnel. The population involved is quantify in 1,200 people. Moreover, during the summer and winter season the local population increases due to the large numbers of tourists.

In order to understand the hydro-mechanical behavior of the landslide, the pre-existing monitoring system was improved since 2009 adding different kinds of surface and sub-surface instruments which allow to record the evolution of the landslide displacement at the ground surface and at depth and the water-table level oscillations.



Figure 32 – geographical position of the Mont de La Saxe rockslide (on left, up) and view from Torino Hut (1958) of Mont de La Saxe; the left-hand flank of the Ferret valley. The photo is taken from the Mt Blanc massif and shows the deep-seated gravitational slope deformation and the Mont de La Saxe rockslide, at the valley outlet above the Entrèves village (on right)

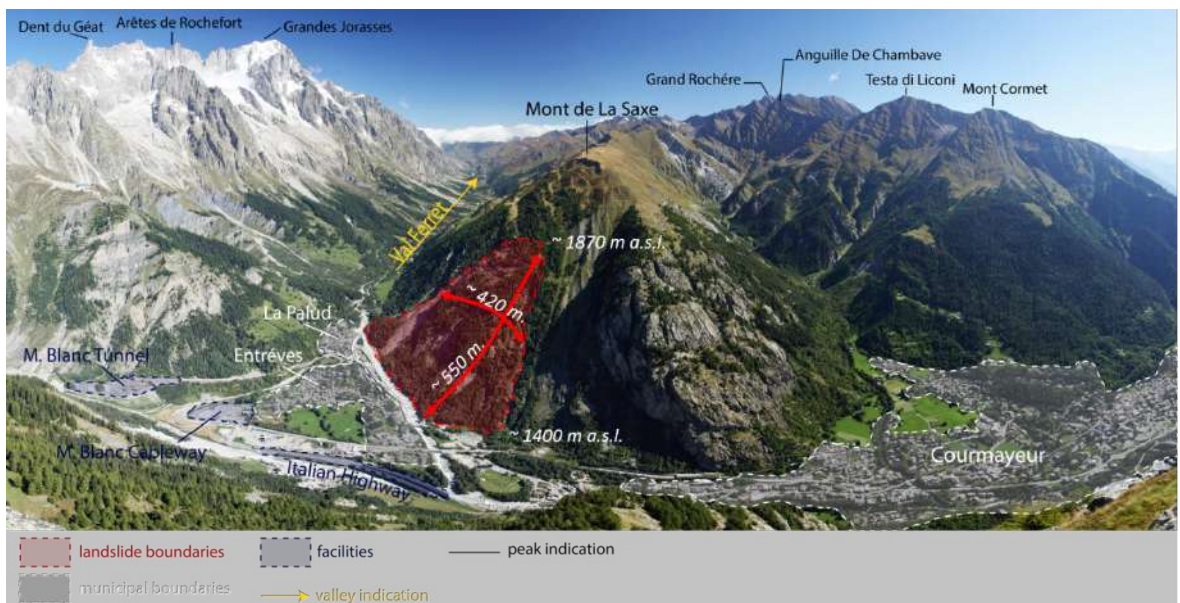


Figure 33 – The Ferret valley taken from the Mont Chetif and shows the deep-seated gravitational slope deformation and the Mont de La Saxe rockslide, at the valley outlet above the Entrèves and La Palud villages (Courmayeur municipality) and near to Mont Blanc Tunnel.

### 2.1.1 Geomorphological Setting

The Valdigne is the upper part of the Aosta Valley in north-west Italy and it extends from La Salle to Courmayeur, including La Thuile Valley, and the side valleys Val Veny and Val Ferret. Especially, the last-mentioned valley is affected by widespread landslide phenomena (Figure 37), including different types as DSGSD, rockfalls, debris and slow earth flows, and complex landslide (Ratto et al., 2007).

The Mont de La Saxe rockslide occupies the terminal sector of the left-hand side of the Ferret Valley (Ratto et al., 2007; Broccolato et al., 2011; Crosta et al., 2012, 2014; Figure 34). Here, rockslide deformations clearly displace gravitational morpho-structures (scarps, counterscarps, trenches) related to the DSGSD (Figure 34 and Figure 38) whose SW-NE rectilinear trend appears strongly disturbed or obliterated inside the rockslide area (Figure 35). This observation may be relevant to the definition of structural constraints for landslide geometry modeling and stability analysis setup (e.g., pre-existing occurrence of weakness zones with different physical mechanical properties with respect to the other slope sectors).

The landslide head is quite irregular and characterized by a rapid evolution with opening and closing tension cracks and intensely broken rock mass. The downhill limit of the head is formed by a steep and irregular rocky wall, some of tens of meters high, below which a gentler slope continues almost up to the slope toe (almost 500 m wide) where an irregular and intensely broken rocky cliff develops. This is connected to the valley bottom by a well-developed scree slope locally more active and interested by rock falls.

At regional scale, the Pleistocene glacial history has left the most pervasive imprints in the geomorphological landscape: large glacial masses have repeatedly occupied the Valle d'Aosta valley system during the middle and upper Pleistocene; in the area of Mont. Blanc there are evidence of the last glacial expansion (LGM, about 14,000 years BP, Porter & Orombelli, 1982) during which the great glacier that descended from the massif covered the reliefs up to an altitude of about 2700 m (referred to the current topography). This occupation, albeit to a lesser extent, persisted for the late-glacial phases (about 10,000 BP years) during which the glacial languages were attested to Courmayeur reaching an altitude between 1600 m and 2000 m in Val Ferret (Porter & Orombelli, 1982).

At the scale of the left watershed of Val Ferret (the Mont de la Saxe represents the southern end) the elements relating to the gravitational dynamics, which guided the modeling of the mountain relief throughout the Holocene (and probably at least during the late-glacial phases), as highlighted by the numerous evidence of gravitational deformation along the whole watershed. As a whole, the relief is presented in a state of *relaxing*, characterized by an extension that is transversal to its major direction, as evidenced by the distribution of the molding forms, which is accompanied by a general fracturing/disarticulation of the rocks (Giardino et al., 2004). This situation of gravitational instability is pre-determined by the proximity of the Penninic Front and the neotectonic cutting area at the edge of the Mont Blanc along the Veny and Ferret valleys; at the same time also from the significant energy that has been increasing in Val Ferret for the glacial deepening of the valley bottom and from the tension release linked to the deglaciation phases.

The structural and geomorphological conditioning have determined for the relief in question a deformative evolution according to a flexural toppling mechanism. The deformation state extensively affects the left side of the Val Ferret, and is such that it has been interpreted as Deep Gravitational Deformation of the Versant (DGPV) in the Inventory of Landslides in Italy (IFFI Project, Trigila et al., 2007). The distinctive surface elements of this deformation are represented by the numerous elongated depressions parallel to the watershed, accompanied by slopes in counter-tendency and interpreted as the surface effect of the incipient overturning; furthermore, the crest sector is subject to large doublings, superficial evidence of the extent to which the survey is subject.

The deep-gravitational deformation of the relief in general is accompanied by local but clear phenomena of superficial gravitational instability, prevalently distributed at the foot of the slope. In particular, it should be noted the activation of the main scarp that borders the Mont de Saxe relief towards the valley, which mainly gives rise to landslides of collapse and dripping; this situation appears favored by other concomitant geomorphological and hydrogeological phenomena, such as: 1) the marked erosive activity induced by the tendency towards the left (SE) migration of the Dora di Ferret, (due to the continuous and abundant feeding of the fluvio-glacial originate from the glacial basins of Mont Blanc) and 2) the water circulation on the slope, which is now carried out in superficial conditions now in depth depending on the permeability characteristics of the covering deposits and the rock masses, exploiting the structural discontinuities and lithological characters and locally determining the deposition of travertine coulters. The tendency towards gravitational instability was probably established with the deglaciation of the LGM and had phases of activity differentiated by magnitude and duration during the Holocene.



*Figure 34 - The left-hand flank of the Ferret valley. The photo is taken from the Mont Chetif and shows the deep-seated gravitational slope deformation and the Mont de La Saxe rockslide. Dotted line represents the main scarp.*





*Figure 35 – the upper part of Mont de La Saxe DSGSD, its evident the presents of main scarp, trenches and counter-scarps.*



Figure 36 – close-up of Mont de La Saxe DSGSD main scarp



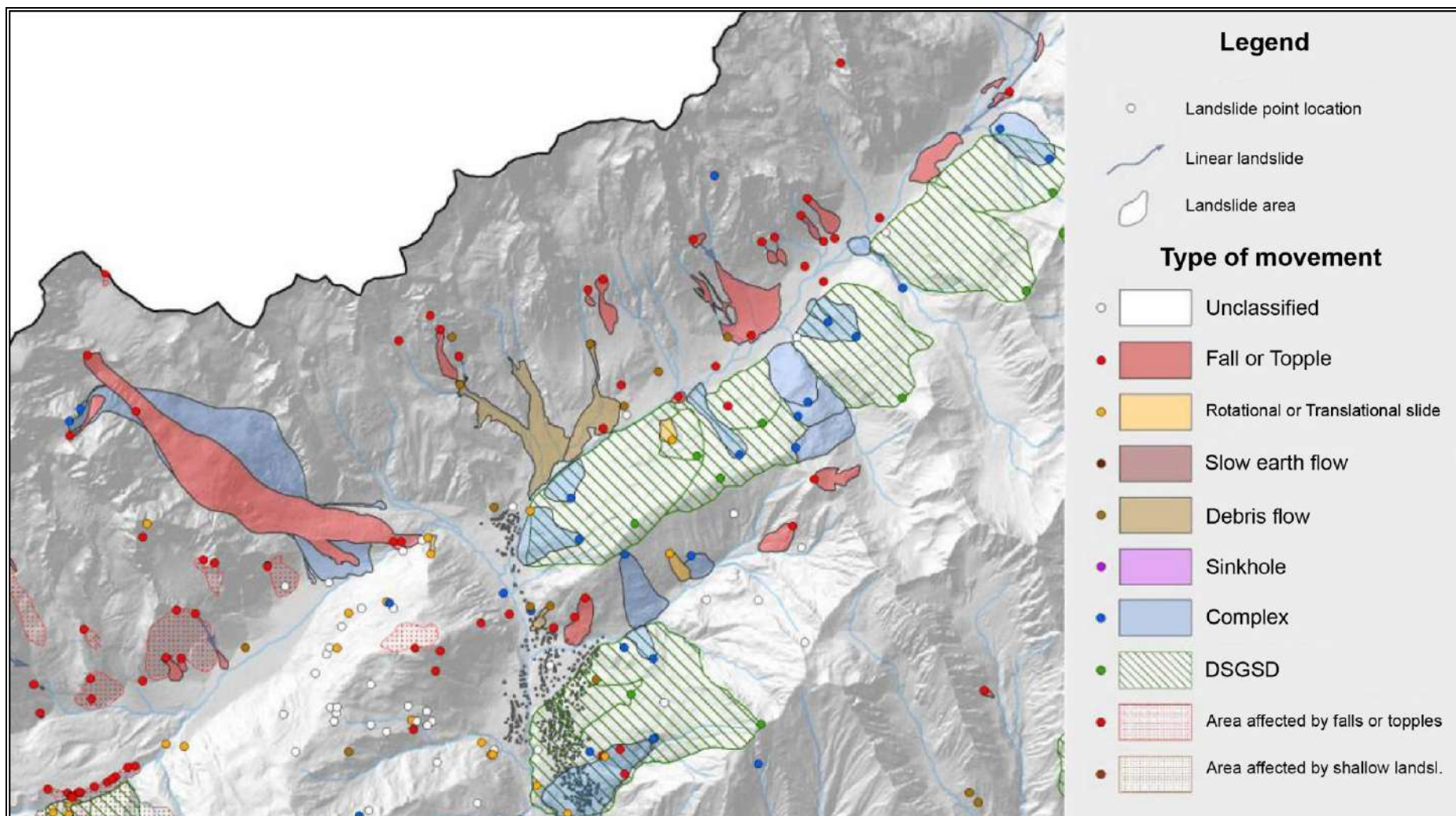


Figure 37 – Overview of IFFI inventory focused on Val Ferret (from Trigila et al., 2010)



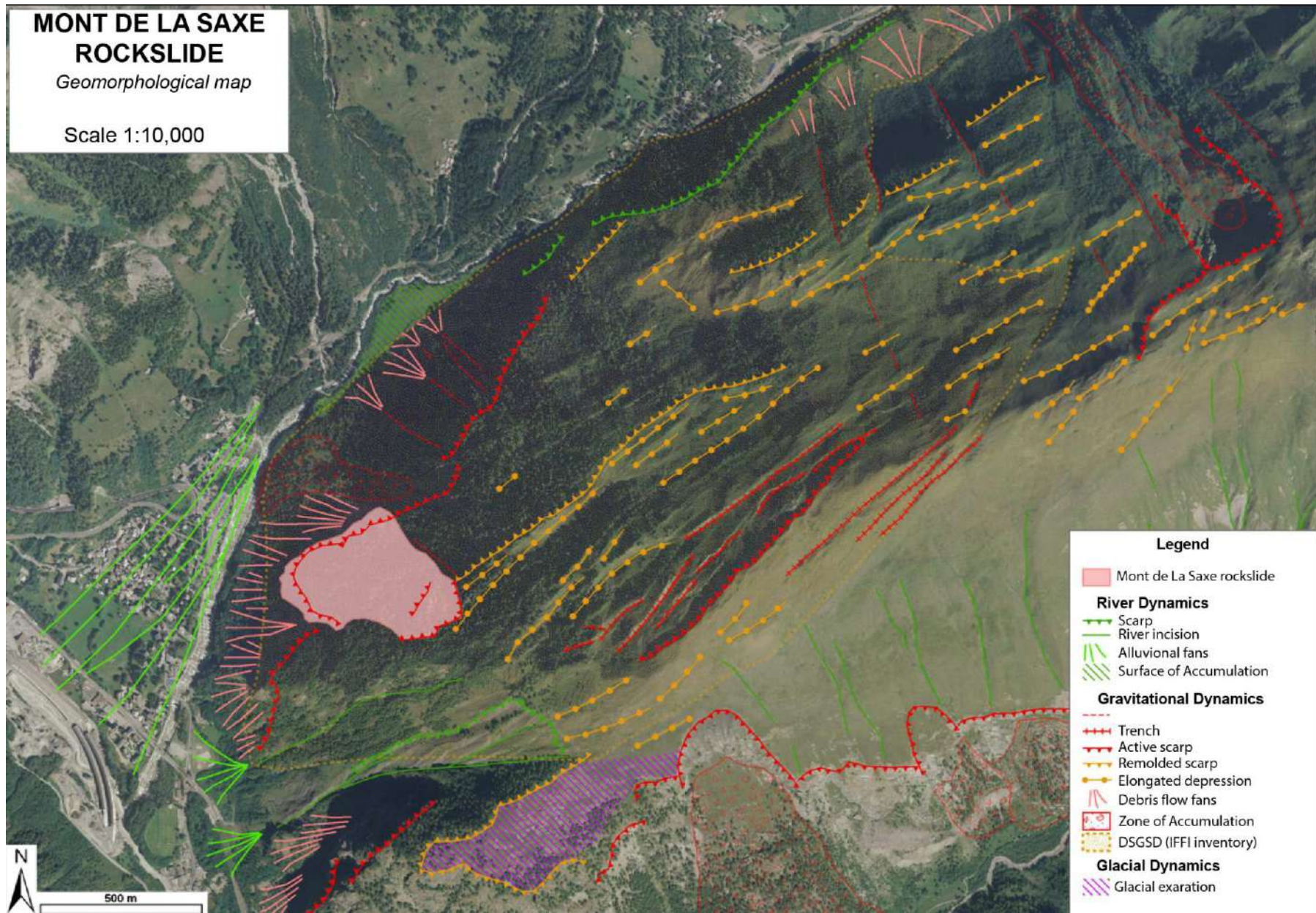


Figure 38 – Geomorphological map of DSGSD that affected the Mont de La Saxe



The area of the Mont de la Saxe landslide is affected by structural (sub-vertical schistosity) and geomorphological (glacial debuttressing) conditioning on a regional scale. According to the general model it can be considered that the landslide derives from a deformation for flexural toppling of entire relief. Furthermore, it is possible consider that in the investigated sector the state of relaxation and extension can be explained both towards Val Ferret (towards NW) and towards W, due to the presence of the main valley crack. The detailed geomorphological characteristics of the individual landslide sectors are described below:

#### **2.1.1.1 Crown**

In the upper sector, the landslide body is characterized by the presence of two main scarps. Upper one ( $\approx 1850$  m; Figure 39) represents the crowning, while the second ( $\approx 1800$  m) represents a further superficial expression of the wide extension that involves the entire slope. In the crowning sector, the directions of the deformation elements (slopes and trenches) assume a bimodal distribution, (NS and EW), according to the main systems of fragile discontinuity of the rocky substrate of the area. Further towards the valley, the shapes take on an intermediate orientation (NE-SW), according to the combination of the two previous systems and along the direction of the landslide evolution.

The scarps are characterized by rock outcropping of carbonate schists (calcareous and clayey) with a persistent foliation, with a schistosity varies from sub-vertical ( $\approx 60^\circ$ N) with immersion towards SE; the substrate is well fractured along the crown, while more inside the landslide body it presents with open fractures and with completely disjointed portions.

At the foot of the scarps there are debris accumulations of varying size, from coarse to fine; the first ones represent the extreme evolution of the most disjointed portions of rock outcropping; the latter, instead, represent the product of colluvium of the schists (probably in its more clayey sectors). The colluvial bodies, where they are thicker, evolve locally in slow debris flow that tend to cover the pre-existing forms and deposits on the slope.



*Figure 39 – main scarp in the upper part of Mont de La Saxe rockslide*

### 2.1.1.2 Left and right flanks

The left flank of the landslide is discontinuous and oriented around E-W; this is not always recognizable either because it is discontinuous or because it is completely vegetated. It is characterized by a series of scarps and trenches oriented on average in the NE-SW direction, which accommodate an extension movement towards NW. The visible extension along each slope of the left limit is usually quantifiable within a few meters. The limit ends near the foot escarpment at an altitude of about 1650 m, where this is articulated by a deep incision.

The right flank is more continuous than the left and is oriented in the NW direction; this limit is articulated in a succession of scarps and trenches that give it a graded appearance.

The evidence of the margin is represented, in the upper part, by a morphology of the more depressed landslide compared to the slope and the opposite situation below 1800 m, where the accumulation of main landslide is particularly swollen.

This situation is also highlighted by the presence, along the right-hand margin of the landslide, of a wide drain canal extended between 1775 and 1575 m of altitude, in which slow debris flow develop; although the slip surface is not exposed, the geometries of the bodies and scarps that originate the debris flows to believe that these involve only the superficial portion, consisting of predominantly fine material of colluvial origin from the substrate and partly also glacial. The drain canal ends abruptly at altitudes between 1600 m and 1575 m close to the slope at the foot of the slope.



*Figure 40 – stepped appearance at right-flank of the rockslide*



### 2.1.1.3 Central sector

The central sector of the landslide body is characterized by a softer morphology, by the absence of rock outcrops and in general by the absence of morphological traces of deformation; this situation can be interpreted as due to the presence of a thick colluvial body originating from the disintegration of the schistose substrate that covers the pre-existing morphologies. The lower-northern portion of the central sector is also characterized by the widespread presence of undifferentiated glacial deposits and its colluvial products; these are outcropped by heterometric, sub-rounded blocks of granitic lithotypes (probably originated from the Mont Blanc massif), whose matrix is generally not visible.



*Figure 41 - Glacial till and its colluvial products present in the lower portion of the central sector of the rockslide*

#### 2.1.1.4 Toe sector

The foot of the landslide is characterized by the presence of a wide and continuous scarp, with an arched shape, oriented in the NNW-SSE direction, this is set along the shale substrate and develops for thick of 50-75 m. The base is covered with debris material accumulated for the withdraw of the scarp itself; these debris fans reach the valley floor extensively.

The slope instability is highlighted by the presence of detachment phenomena, characterized by variable volumes, which can sometimes reach the valley floor. Along the scarp, discontinuity surfaces have been identified in the substrate that separate intact portions (below) from highly fractured portions (above). These have been interpreted as the outcropping of slip surfaces of the landslide.



*Figure 42 – toe sector of the Mont de La Saxe rockslide*



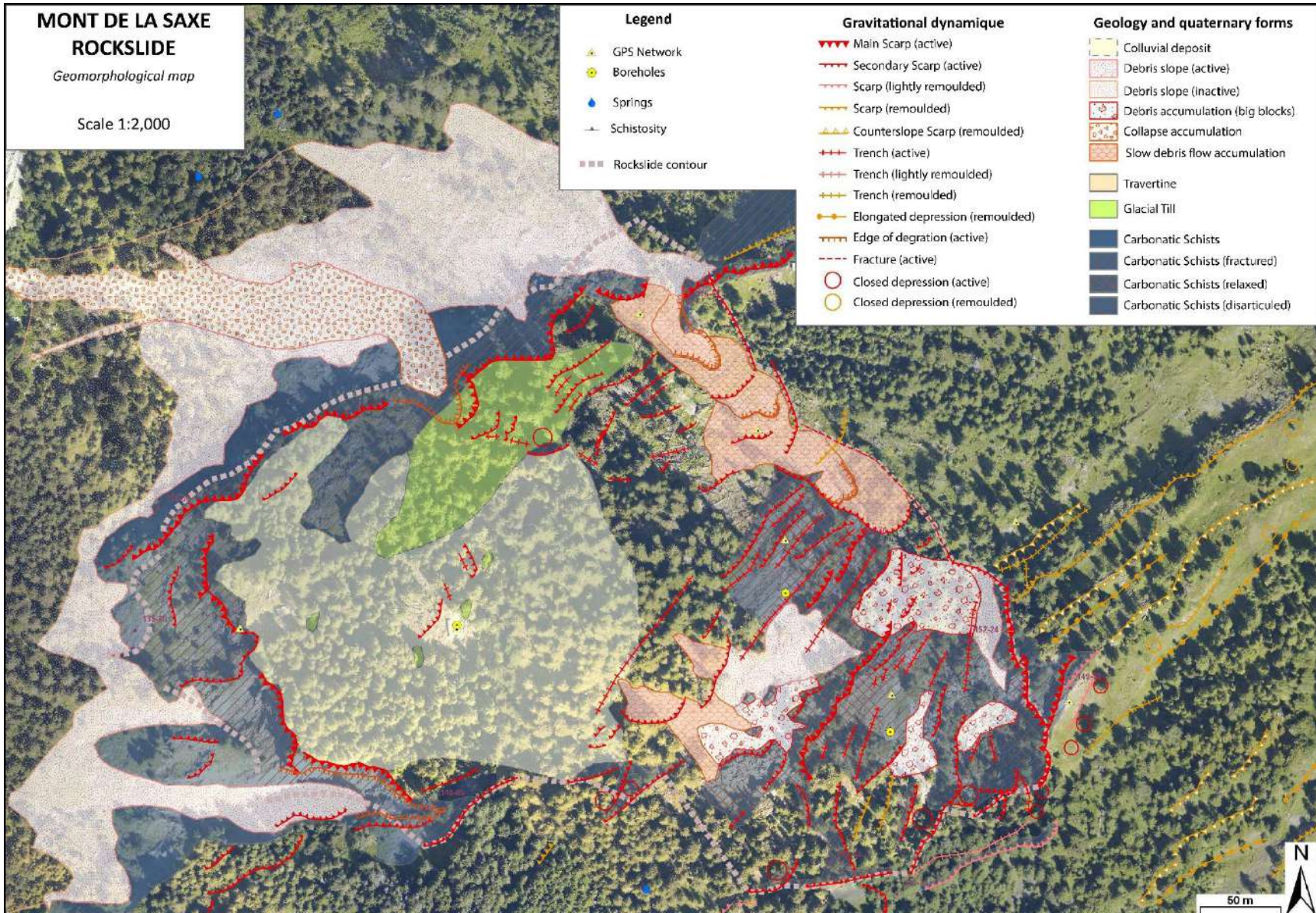


Figure 43 – geomorphological map of Mont de La Saxe rockslide

### 2.1.2 Climatic Setting

The area is subjected to snow fall during the winter (average equivalent rainfall 810 mm ca., data from Mont de La Saxe weather station at 2,076 m a.s.l.) with a total average precipitation of about 1,470 mm (at the rock slide crown area) and a real evapo-transpiration of about 370 mm. The highest snow cover in the last ten years has been recorded on April 2010 with over 3 m thick. Ever since, the rockslide activity is increased until to 2014 when it occurred a critical crisis during late spring (since end of March to June) in concurrence of snow melt and with superficial displacement patterns that have reached the tens of meters.

Since 2009, the Mont de La Saxe rain gouge (Figure 57) has recorded the lowest temperature of -21.6°C and the highest of 26.1°C, and an average annual temperature comprised between 4.5 and 7.0°C. During the period considered the coldest month of the year is February with an average of about -4.0°C, while the warmest month is July with a temperature over 12°C (Figure 44).

According to Köppen-Geiger climate classification (e.g. Peel et al., 2007) its class is *Cfb* with significant with precipitation even during the driest month. In May, the precipitation reaches its peak, with an average of 99 mm (Figure 45).

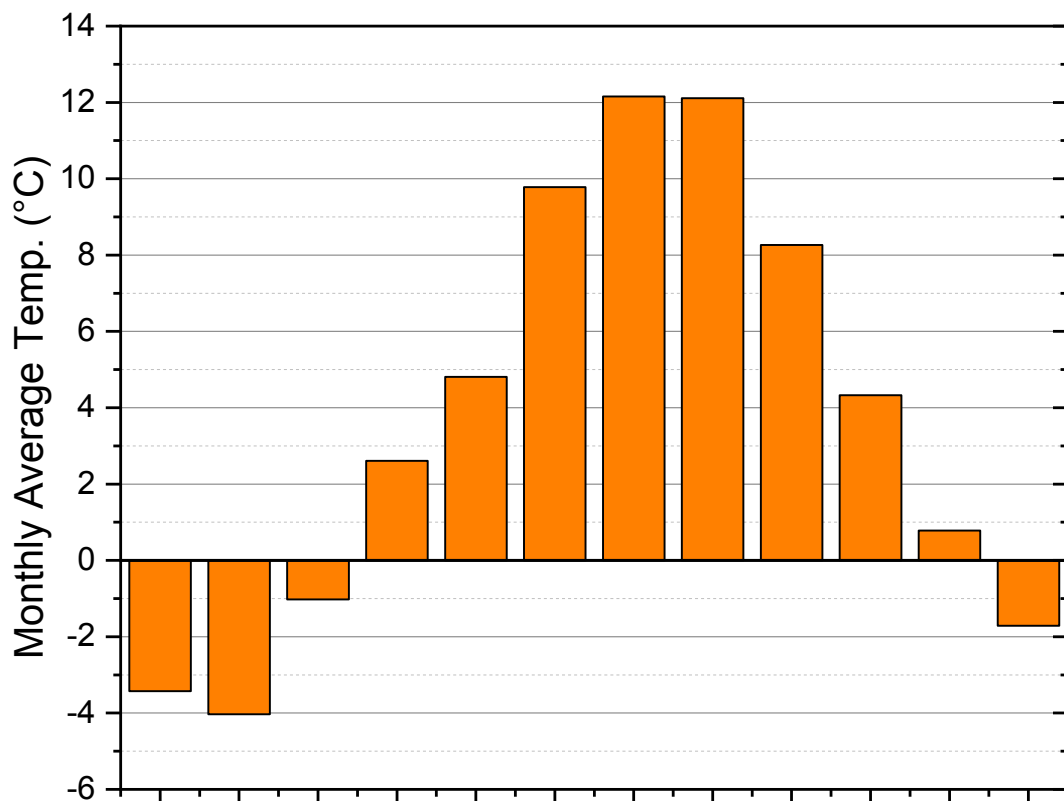


Figure 44 – Monthly average Temperature (2009-2017) for Mont de La Saxe rain gouge (2076 a.s.l. m)



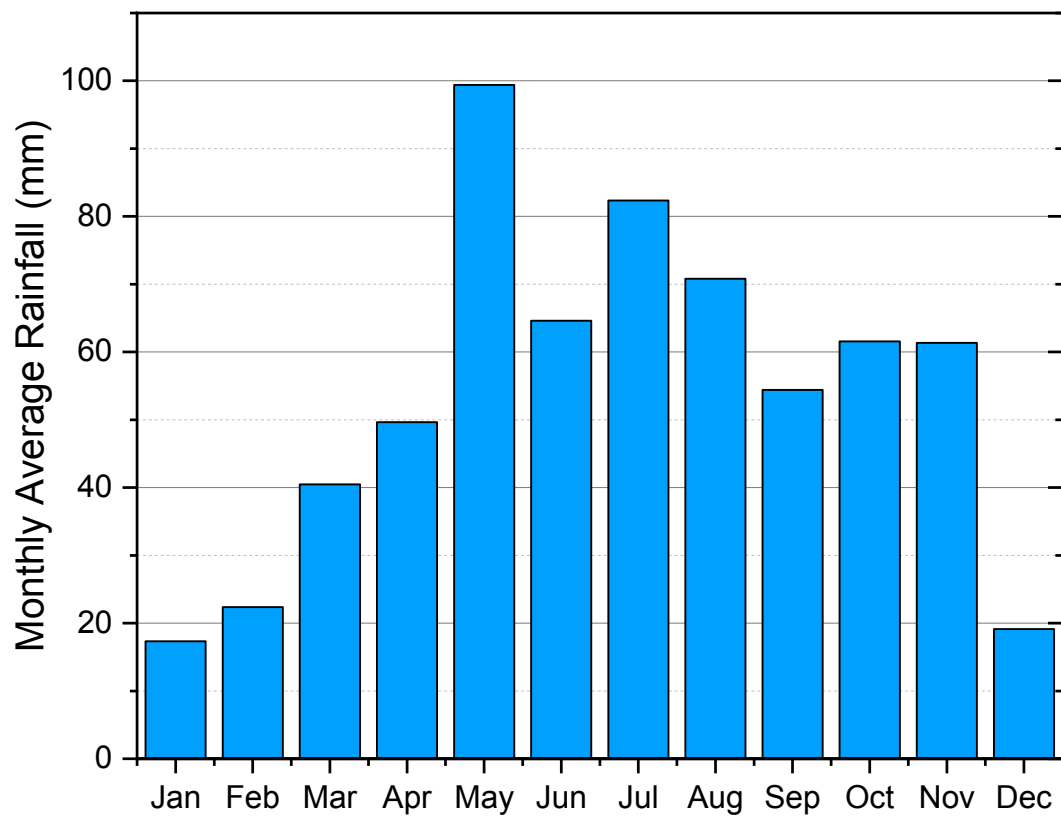


Figure 45 - Monthly average rainfall (2009-2017) for Mont de La Saxe rain gauge (2076 a.s.l. m)

### 2.1.3 Geological Setting

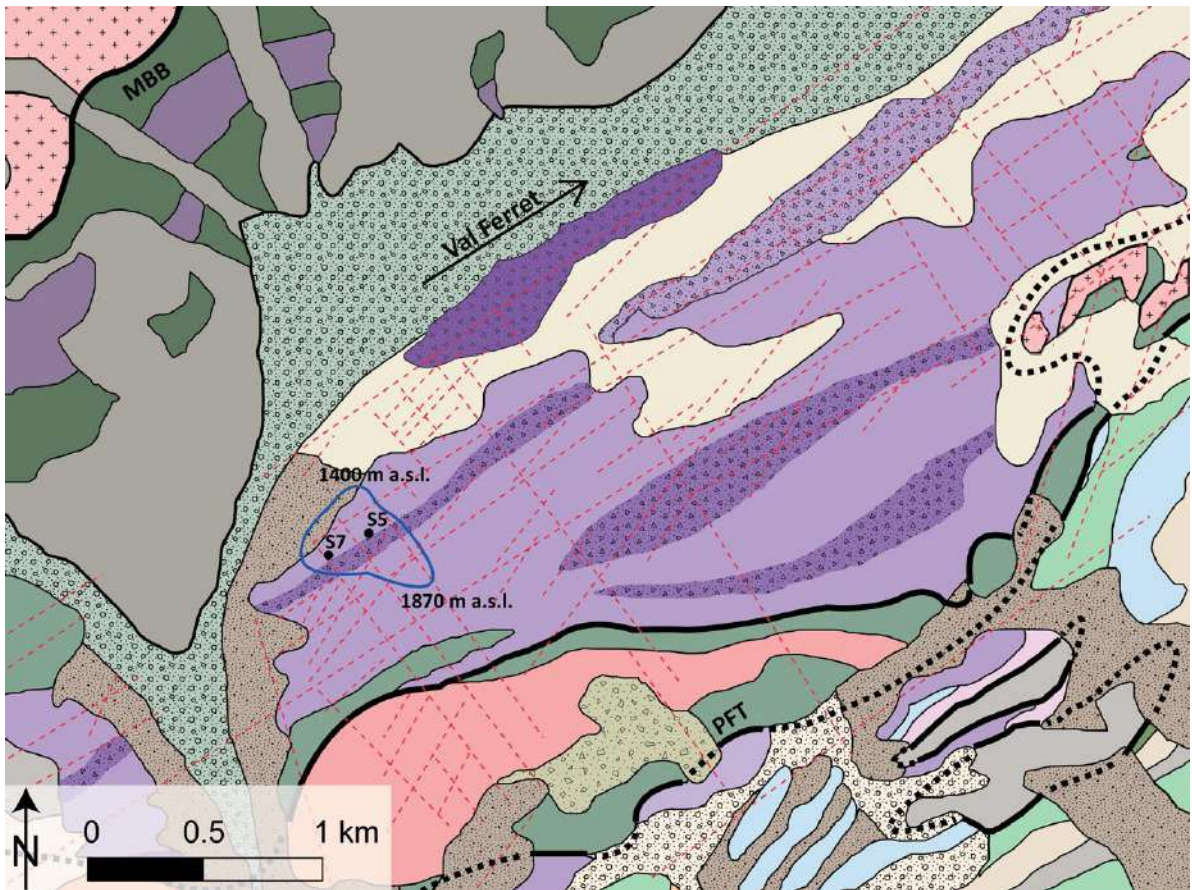
The Mont de La Saxe rockslide is located in meta-sedimentary sequences that belong to Ultra-Helvetic Basal Decollement units and sited close to south of the Mt. Blanc crystalline Massif (an example of Alpine External Massif, that forms a discontinuous belt along the Alps edge), in the Italian Western Alps. It is characterized by rocks of metamorphic very low-grade, intensely deformed during the Middle Jurassic and including marls, argillaceous schists (Figure 49), black schists, mica-schists and calc-schists with quartz-arenite and graphite rich levels (Figure 48) (Antoine et al., 1975; Guermani and Pennacchioni, 1998; Leloup et al., 2005).

Southwards these rocks are found in tectonic contact with the Ultra Helvetic Mt. Chetif Unit, characterized by meta-granite and meta-rhyolite. Just a few kilometers south of the rockslide area there is a main tectonic lineament called Frontal Penninic Thrust (Argand, 1916) that splits the internal (Sion-Courmayeur zone units) and the external (Helvetic and Ultra-Helvetic) part of the Alps. This is a major fault zone around the bend of the western Alps e.g. (Schmid et al., 2004) and it does not simply separate two paleo-geographically different domains but also marks a metamorphic boundary between the HP-LT Sion-Courmayeur Zone and the low-grade Helvetic meta-sediments e.g. (Perello et al., 1999; Figure 47).

In the area interested by the movement, the argillaceous schists mainly dip to the SE are leading black into the slope with dip angles ranging between 20° to 60°, due to the effect of tectonic deformation events at the outcrop scale. The rock fabric seems to be more controlled by pre-existing sedimentary features (bedding) rather than by the development of an axial plane foliation. The Val Ferret morphology and superficial deposits were reshaped during the Last Glacial Maximum (LGM, 25,000-15,000 BP) and subsequent readjustment by gravitational processes.

In fact, at least four glacial pulsations of decreasing intensity have been recognized, each associated with different entities of erosional depth. The last two pulsations would be responsible for the morphogenesis of the narrow valley incision at Mont Chetif. Porter and Orombelli (1982), based on soil evidence, reconstruct the topography and profiles of the glacial masses during the Last Glacial Maximum, concluding that in Val Veny and Val Ferret there was a glacial cap located at an altitude between 2600 and 2900 m above sea level.

The corresponding slopes are widely covered by discontinuous till deposits reworked by gravity and colluvial processes, while significant talus and landslide deposits are found at the slope toe. As it was above mentioned, a large sector of the valley flank is affected by a DSGSD (Deep-seated Gravitational Slope Deformation) characterized by SW-NE trending morpho-structures (associations of gravitational scarps and counterscarps) conditioned by persistent inherited brittle tectonic features, including sub-vertical, dextral strike-slip faults reactivated by slow rock slope instability. These structures also exert a strong conditioning on the SW-trending pattern of superficial drainage axes, which are almost parallel to the slope direction in the upper part of the slope.



### Quaternary deposits

- alluvial deposit
- talus deposit
- reworked glacial dep.
- landslide deposit
- glacial deposit

### Helvetic Units

- Mont Blanc granite

### Ultra Helvetic Units

- Mont Chetif Unit*
- limestones
  - ryolitic porphyroids and microgranites

### Basal decollement Units

- calcschists, argillaceous schists and limestones
- limestones
- black argillaceous schists
- arenaceous limestones

### External Penninic Units

*Courmayeur-Sion zone  
(Tarantaise Flysch)*

- limestones and conglomerates
- black schists with quartzites
- calcareous and argillaceous schists
- limestones and breccias
- dolostones and limestones
- quartzites and conglomerates
- black schists and sandstones

lineaments

certain

inferred

MBB = Mont Blanc Backthrust

PFT = Penninic Frontal Thrust

Figure 46 – geological map for Val Ferret area (modify after Crosta et al., 2014)

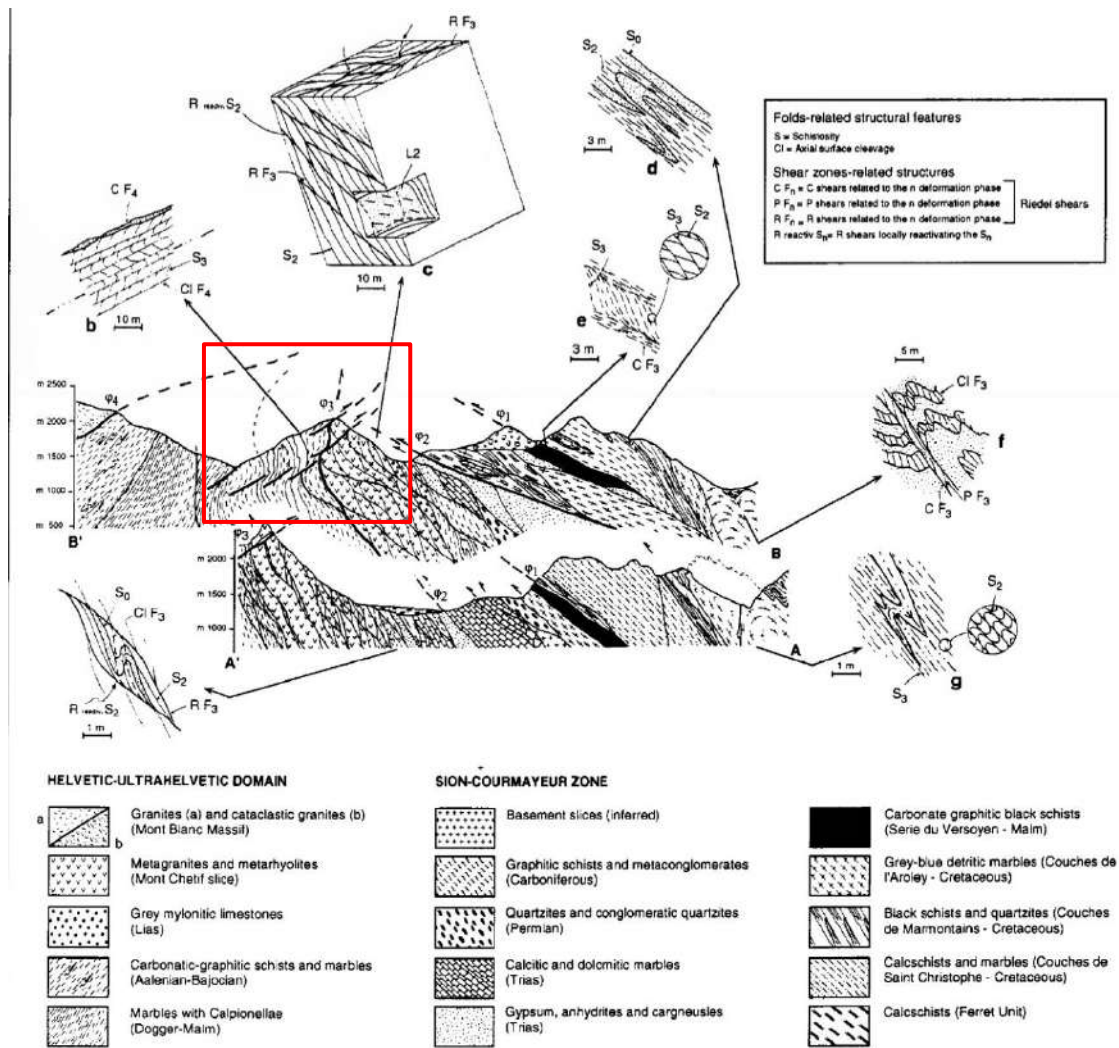


Figure 47 – Cross section of Val Ferret (from Perello et al., 1999): the shear zones  $\psi_1$ ,  $\psi_2$ ,  $\psi_3$ , constitute the Deformation Zone of Courmayeur (NW), which overlaps the Courmayeur- Sion Zone and the Ultraelvetic domain. The shear zone  $\psi_4$  (SE), corresponds to the Pavillon Thrustof, which overlaps the crystalline base of Mont Blanc on the roofs of the Ultraelvetic Domain. In the red box, the detail of the left side of the Val Ferret near its outlet in the main valley floor: the retroflexed structures parallel to the Pavillon Thrust are well recognizable

### 2.1.3.1 Lithostratigraphy

The study area includes the three different tectonic units separated by metamorphic contacts averaging immingering towards SE. From N to S the units are: the Helvetic-Ultraelvetic Unit, the Mont Chetif Unit and the Sion-Courmayeur Zone.

#### Helvetic-Ultraelvetic Unit

The Helvetic-Ultraelvetic Unit includes four main lithotypes with a transitional stratigraphic contact. They have been distinguished:

- shales, characterized by dark gray grained consist mainly of quartz + muscovite + graphite + sulfides; locally they have graphite enrichments or preserve fine-grained arenaceous texture. Carbonatic levels within them have rarely been observed. They mainly outcrops are in the south-western part of the study area;
- graphitic phyllites, from dark gray to very fine-grained black formed by phyllosilicates + quartz + graphite + sulfides and are characterized by a presence of quartz veins (Figure 48). They predominantly

outcropping on the northern slope of the Mont de la Saxe or constitute intercalations within the schists with transitional contacts;

- calc-schist, from gray to hazel, composed of calcite + muscovite + quartz + sulfides (Figure 49).

Impure levels of gray color are locally showed;

- phylladic calc-schist, gray-colored and characterized by fine grain, consisting of muscovite + graphite + quartz + calcite + sulfides (Figure 49). The sulfur content is sometimes higher than 5% and the sulfides are generally characterized by dimensions even close to the centimeter; sometimes there are very rich levels in graphite and white carbonate levels. Contact with the calc-schists is transitional;

- gray marbles, characterized by low presence of phyllosilicates. These rocks emerge sporadically on the left side of the Valle di Armina interspersed with the phyllites and constitute a body of about 80 m thick on the right side of the valley.

### **Mont Chetif Unit**

The Mont Chetif Unit consists of the following lithotypes:

- orthogneiss, composed by meta-granites of light gray color with magmatic structure sometimes well preserved, from meta-rhyolites of gray-green color that locally preserve the porphyritic structure and from meta-haplites of white color. This lithostratigraphic association indicates the presence of a continental base consisting of a hypabyssal intrusive magmatic complex;

- impure marbles and marble calc-schists, they represent the stratigraphic coverage of the continental base and consist of gray-beige colored carbonatic rocks with different percentages of phyllosilicates.

### **Courmayeur-Sion Zone**

The Courmayeur-Sion Zone consists of several tectonic nappes. In this sector it is also known as the Breccias of Tarantasia Unit and consists of the following lithotypes:

- carbonatic phyllites, pelitic rocks of dark gray color due to the presence of abundant graphite. Locally they contain levels with low amounts of carbonates and are generally rich in sulfides;

- quartz-mica-schists, white-gray color made of very rich quartz shales with local levels of meta-conglomerates with quartz clasts. The main outcrops are at the Col du Sapin;

- mica-schists, characterized by gray color, and generally associated and intercalated with the previous ones;

- marbles, gray-blue-colored includes meta-calcarenes alternated with subordinate levels of carbonatic meta-breccias; the main body outcropping in correspondence of Tete de La Tronche and Val Sapin;

- calc-schists, consisting of alternations of levels rich in carbonates and levels rich in quartz-pelitic component. They are medium-grained gray rocks with an arenaceous appearance. They constitute the west wall of the Tete Entre Duex Sex on the orographic right of the Armina Torrent and the wall between the Tete de Bernarde and the Tete de La Tronche on the orographic left.





*Figure 48 - graphitic phyllites belonging to Helvetic-Ultraelvetic Unit*



*Figure 49 – calc-schist belonging to Helvetic-Ultraelvetic Unit*

### 2.1.3.2 Quaternary deposits

Quaternary deposits consist of the following sediments and lithotypes:

- Eluvio-colluvial deposits, sediments sandy matrix-supported constituted by angular clasts; they are formed mainly remolding the bottom glacial deposits and the superficial chemical-physical alteration of the rocky outcrops. They are particularly widespread in the upper-middle part of the slope. On the northern side of the ridge are widely colonized by shrub vegetation (rhododendrons, alders), while on the southern side they are colonized by herbaceous species;
- Travertine, the main body outcropping in the southern sector of the study area in correspondence of an impluvium called 'Sources du Plan-Cereux' and forms a rather continuous outcrop, with a maximum outcropping thickness of about 4 m, which cements eluvio-colluvial deposits, debris deposits and glacial deposits and locally rests on mountain rocks. Other travertine bodies are present in Val Sapin at W of Tete de la Tronche and in the Valle di Armina, on the orographic right, at SSE of the Armina Damon alpine pasture;
- Fluvial deposits, consisting predominantly of rounded and heterometric clasts of prevalent granitic rocks in sandy-gravelly matrix, emerge along the whole riverbed of the Dora di Ferret;
- Mixed-origin deposits, consisting predominantly of rounded and heterometric clasts of prevalent rocks in sandy-gravelly matrix, they are outcropping along the whole riverbed of the Dora of Ferret forming conoids of mixed origin, sometimes coalescent. They are particularly common on the right side of the Armina Valley;
- Debris deposits, consisting of heterometric blocks; they are particularly widespread in the medium-low part of the slope, where they form extensive layers of debris that mask the substrate;
- Landslide deposits, originates by chaotic deposits with clast-supported texture with blocks heterometric in a gravelly-sandy matrix. The matrix is generally lack where involved lithotypes are involved (orthogneiss, marbles, calc-schists) and more abundant in case of less competent lithotypes (phyllites and schists);
- Fluvial-glacial deposits, they are compositional and texturally similar to deposits of mixed origin but have been deposited by proglacial fusion waters. They occupy the valley floor of the Valle di Armina and Val Sapin;
- Lake-glacial deposits, they are identifiable morphologically in correspondence of the valley bottom of Val Ferret to the East of Mayencet where they constitute a flat marsh environment;
- Ablation glacial deposits, they consist of clast-supported deposits with a poor matrix consisting of gravel and sand. They mainly surface in the Vallone di Armina;
- Till glacial deposits, consisting of sediments matrix-supported with rounded heterometric clasts, mainly consisting of granites in a silty and silty-sandy matrix. Locally, are presents glacial erratic up to 10 m<sup>3</sup>.

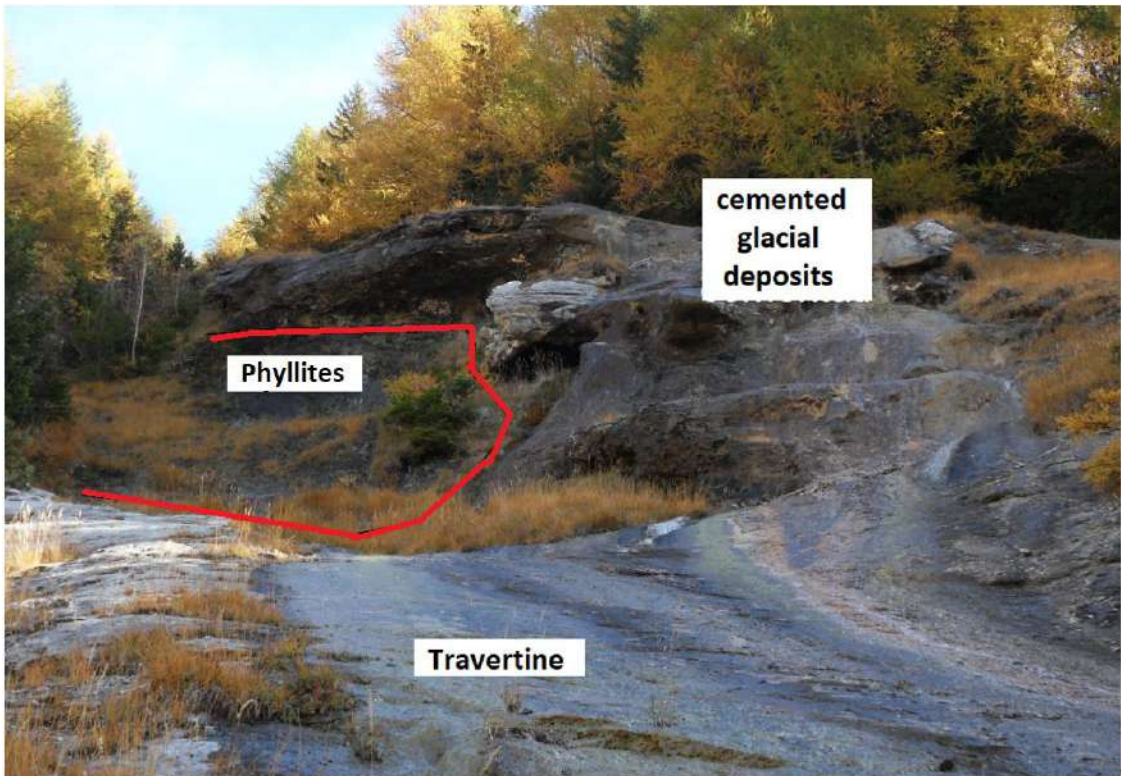


*Figure 50 – travertine deposit posed on glacial till and phyllites outcrop*



## 2.2 Structural Setting

The structural setting here presented derived for study conducted by Regione Autonoma Valle d'Aosta (RL. 1170 – February 2013).

The study area is considered complex due to presence of at least two different late syn-metamorphic tectonic contact and five different deformation phases. The first two identifiable phases have a transposing character and have given rise to the regional schistosity that plunges on average towards SE with an inclination  $> 45^\circ$ . Furthermore, the area underwent a complex quaternary evolution, syn- and post- glacial, which locally masked the macroscopic relationships between the tectonic units and the deformation phases.

Has been recognized 5 different syn-metamorphic deformation phases D1-D5 within the 3 units presents in the study area. Deformation phase D1 is preserved as a metamorphic foliation relict in correspondence with the deformation phase D2. The axes A1 of this deformation phase are locally distinguishable from those relative to the phase D2 only in the hinge zones of the latter, where an angle is generally observed between the two bending axes. The rare visible mesoscopic folds show asymmetric folds with pointed hinges (Figure 51).



Figure 51 - Hinge of deformation phase D2 that preserves S1 and S1 asymmetric folds

Deformation phase D2 is a pervasive deformation phase with isoclinal folds in all lithotypes. The A2 axes show a high dispersion and, at the mesoscale, intersection lines on S2 with non-rectilinear trend have been observed. An intersection line represents the direction of the bending axis responsible for the development of the surface on which it lies, therefore the bending axes A2 are not rectilinear. From the comparison of the average position of the structural elements of the three tectonic units, it can observe how the elements, especially the schistosity, have different positions, both in orientation and in inclination.

Tectonic units are separated by shear zones characterized by the presence of mylonite rocks, which testify to their development in late metamorphic conditions. Based on macroscopic data, two generations of tectonic contacts can be distinguished. Deformation phase D3 is a deformation phase with folds from closed to open which generates locally a crenulation/dissolution cleavage. The folding axes A3 are generally very inclined ( $>60^\circ$ ) and dispersed. Cleavage S3 has direction about NNE-SSW and consists of immersion surfaces both towards W and towards E with inclination generally higher than  $65^\circ$ . At phase D4 two generations of cleavages have been attributed that differ only with respect to the inclination of the surfaces. D4 develops asymmetrical folds from closed to open with NW-SE direct axes with inclination  $<30^\circ$ . S4 surfaces consist of a spatial crenulation cleavage, which develops only in the richest levels of phyllosilicates. The medium-low-angle surfaces plunge to NW with an inclination of  $25-50^\circ$ , while the high-angle surfaces generally immerse towards NW and subordinate to SW with inclination  $>65^\circ$ . The D5 phase deforms the S3 surfaces, but its geometric ratios were not observed with the D4 phase. Develops asymmetrical folds with immersive axes towards ENE at low angles (inclination  $<30^\circ$ ) and immersive axial planes generally towards NE with inclination of  $25-40^\circ$ .

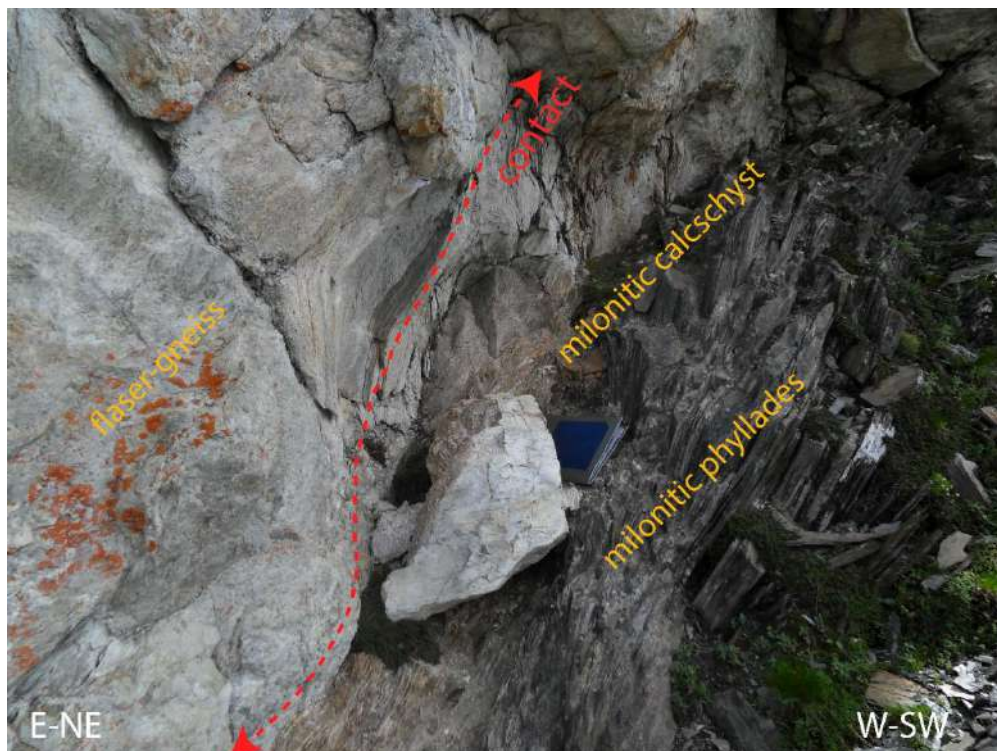


Figure 52 - Tectonic contact between Mont Chetif Unit and Helvetic Unit characterized by the presence of mylonitic rocks

### 2.3 Main Instability Events

Since installation of a widespread monitoring system in 2009, the first time that the system identifies a dangerous movement is on May 2012 (Figure 53), and after about one month the alarm stopped, the involving mass in the instability recognized is about 650,000 m<sup>3</sup>. Various evidences on terrain appeared, as trenches and scarps has been recognized like neo-formed, and further it results strictly linked with a clear evolution of the slope.

At the end of March 2013, the snow-melting triggered a main activation of the instability, and since to April to June has been evacuated about hundred people and has been closed the access to Ferret Valley. This emergency state is lasted about 40 days.

As in the previous year, at the end of March 2014, during the snow-melting season the right flank of the instability has become instable and reached the highest displacement rate never recorded before, over 500 mm/h and the highest total displacement measured in over 1 m per day. During April 17th and April 21th of that year two rock mass collapse involved about 400,000 cubic meters of that sector (Figure 54). In the end of June of the same year, what remained of that sector have collapsed with a debris flow rheology and not involving the facilities and population considering also the civil protection actions put in place d by Geological Survey of Aosta Valley.

After 2014, every year coinciding with the snow-melting season (usually in late Spring) a cyclic and strong acceleration happen but until now has not repeated or reached the values as that year. During 2017 has been recorded the lowest acceleration since monitoring start, and this year, 2018, a small reactivation has been observed during snow-melt season.

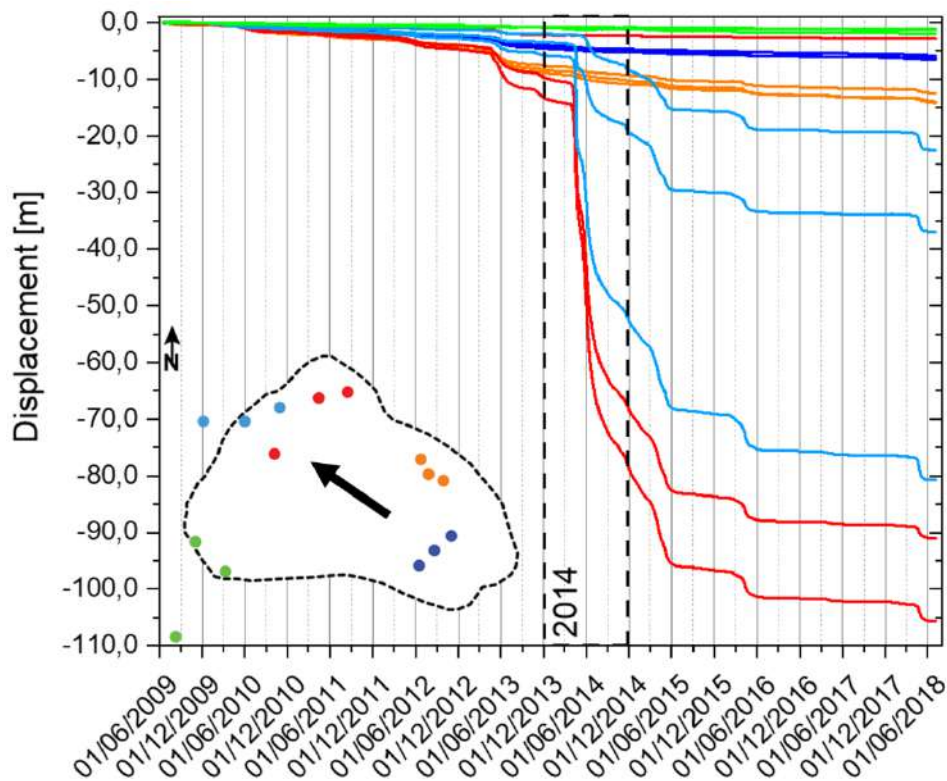


Figure 53 – displacements of GB-InSAR Points-of-interest since 2009 to June 2018





Figure 54 – images from webcam before and after the 2014 collapse, on right-flank of the instability

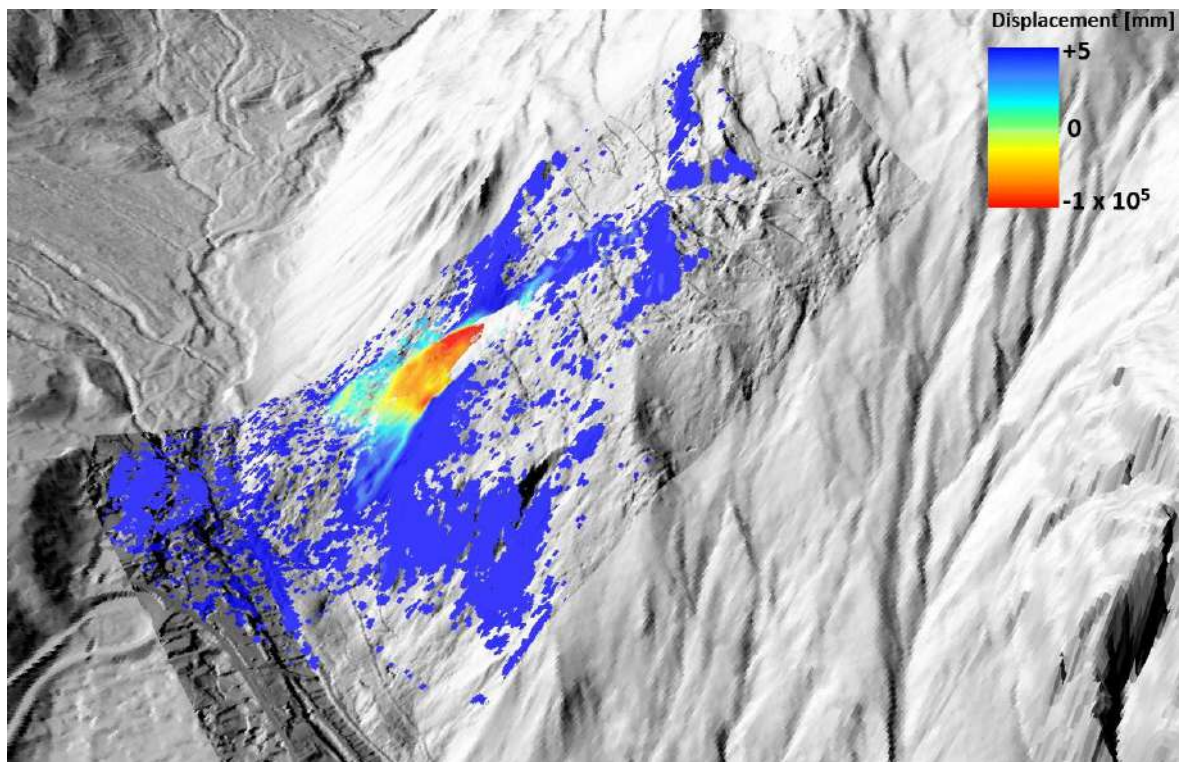


Figure 55 - displacement map from GB-InSAR monitoring since June 2009 up to December 2015. Most of displacements involves the right flank of the instability.

## 2.4 Hydrogeological Setting

The detailed cartography of the Mont de La Saxe ridge allowed to reconstruct the geometry of the geological bodies on the slope.

The area consists of alternating rocks that act as relative raincoats (shales and phyllites) and permeable rocks for karst phenomena (calcareous and marbles). The direction of the geological bodies is about NE-SW (Figure 56). Moreover, there are metamorphic late-cut zones consisting of poorly permeable lithotypes (milonic schist) and other permeable for karst (marble and gypsum in depth). Numerous sources associated with travertine bodies have been mapped in the area, or in any case characterized by the presence of water that precipitates calcium carbonate, therefore encrusting waters. The formation of travertine bodies and the presence of carbonate incrustations occurs only if the waters are supersaturated in calcium carbonate, so we can say that these waters must circulate in carbonatic rock masses within which saturate in calcium carbonate.

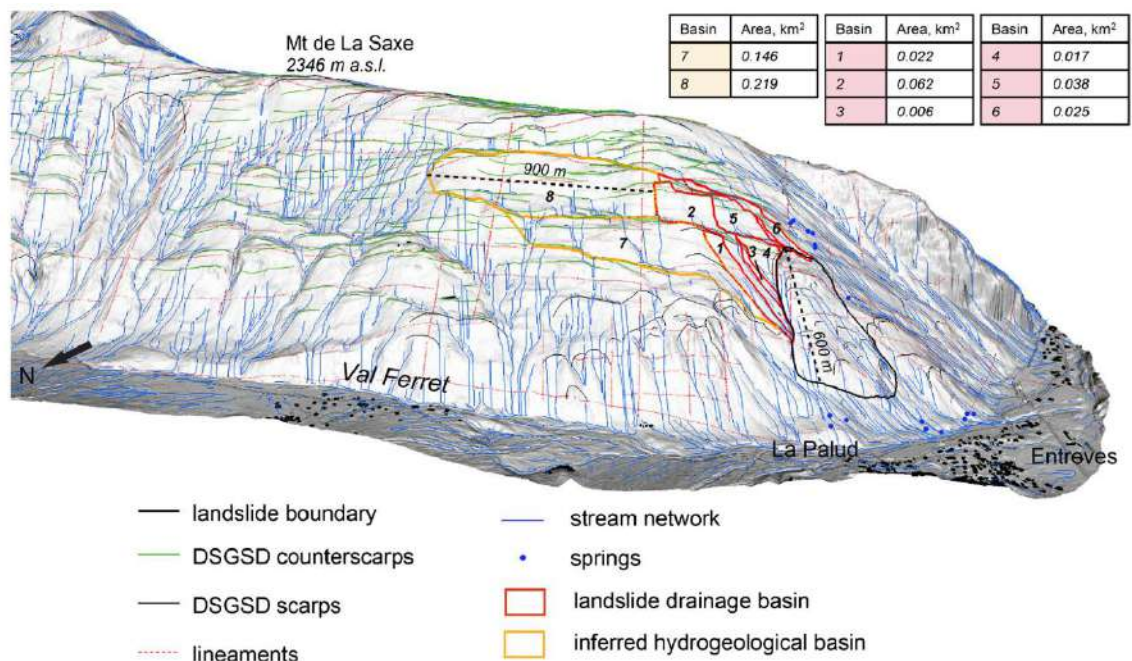


Figure 56 – Shaded 1 m × 1 m LiDAR DEM of the left-hand flank of the Ferret valley. The orientation of the morphostructures and their termination close to the rockslide crown area are visible. The superficial drainage network and the small catchments directly contributing to the rockslide at different points are shown (modify from Crosta et al., 2014)

All these sources, except for those present in S of the landslide body, are associated with shear zones and tectonic contacts or are in any case close to these. The shear zones are ubiquitously characterized by the presence of faults, carbonate rocks and mylonites and it is likely that there are gypsum bodies in the subsoil.

Crosta et al. (2013) supposes a hydrological reservoir to recharge the sources positioned NE of the landslide body. This basin has an extension of about 0.54 km<sup>2</sup> and the total rainfall would be 1470 mm with a real evapotranspiration of 370 mm. No infiltration index is provided, which could be considered cautiously equal to 0.55, which would give rise to an aquifer capable of providing an average annual flow of 9.4 l/s.

This basin is certainly underestimated because the only low source of Plan-Cereaux has an average annual flow of about 7 l/s, while all the sources of the Plan-Cereaux and Marais sector have averages estimated at least 100 l/s. Assuming a supply basin that includes the entire north-western slope of the ridge of the Mont de La Saxe, between the Plan Cereaux torrent, the Tete de Bernarde and the 1830 m altitude (minimum charge of the Plan-Cereaux springs), the contribution to the hydrogeological recharge increases considerably and is equal to about 4 km<sup>2</sup>. Using the same parameters as above, the average potential flow of the aquifer would be about 78 l/s assuming that there are no losses from the system. This flow is even lower than the estimate of the total flow of the S-shaped sources of the landslide body. The northern side of the Mont de La Saxe certainly contributes to the recharge of the aquifer, but it is not enough to feed the Plan-Cereaux and Marais sources, for which it is necessary to assume a further substantial external contribution.

The presence of two geological circuits has been supposed, whose position is located on the basis of the geological structures reconstructed on the surface, however their real position, in depth, could deviate from these traces.

The circuits identified are:

- a southern circuit set in the marbles, then passing inside calc-schists and finally coming out on the surface in correspondence of an anti-form structure in P4 driftwood underneath the schists in the Plan-Cereaux and Marais springs. In this sector, two generations of isoclinal folds have been distinguished, deformative phases D1 and D2 and it is therefore probable that the antiform D2 structure deforms a phase fold D1 with a transversal hinge to the D2 formwork.
- a northern circuit set up in discontinuous bodies of marble and then passing into calc-schists who would end with a synform structure south of Leuchey Damon where there are no conspicuous water emergencies. From this sector, towards SW, the circuit would instead use fracture and schistosity systems in shales and phyllites to feed the landslide body laterally. In the field of Leuchey-Damon there is evidence of relaxing of the rock mass that would favor the circulation of water even in non-carbonated lithotypes. Also, in this second case it is conceivable that there is a D1 phase structure in calc-schists.

## 2.5 Monitoring System

From the analysis of old aerial photos has been possible to recognize some evidences of past activity, especially since eighties onward and with an evident reactivation since 2002 (Broccolato et al., 2011; Crosta et al., 2012). Between 2002 and 2009 has been performed 15 EDM (Electronic Distance Measurement) repeated on each 8 optical targets presents along the slope using two different reference stations (Crosta et al., 2014). Since 2009, after the high level of risk has been recognized, the need was highlighted to a more deep and complete monitoring system.

Two networks have been developed and deployed integrating different types of monitoring to achieve an improved understanding of rockslide displacement, failure mechanisms, response of the rockslide to the trigger factors, in order to support emergency civil protection actions. The first one is composed by the superficial monitoring and the second one by deep geotechnical monitoring (both in point-like and spread forms), were installed and they are daily checked and regularly reviewed or updated to consider the large slope displacements which could cause damages in the instrumentations.

The Mont de La Saxe rockslide was deep investigated in order to understand the kinematic behavior, through surface mapping of the slide boundaries, geology (lithologies, discontinuities, etc.), geomorphological features (downhill- and uphill facing scarps, tension cracks, etc.), the drilling more than 20 boreholes through the basal shear surface, analyses of the historical movements and the analysis of measurements from borehole piezometers, inclinometers, 3D multi-probes and a rain gauge, all of which were installed since 2009. Surface movements on the active landslide have been measured since same year using a network of optical targets, surveyed using Leica TCA robotic total station, by GPS network and by a GB-InSAR; while since 2014, approximately 2 times per year, has been performed a terrestrial laser scan surveys (LiDAR) to map geomorphological features of the rockslide system and in to perform time-lapse analysis.

The monitoring networks are daily checked and regularly reviewed or updated to consider the large slope displacements which could cause damages in the instrumentations. Moreover, it should be recalled that the in time some instruments have been lost by the displacement of the rockslide.

The superficial monitoring system, currently is composed by:

- 5 GPS network devices for automatic continuous measurements (providing data since 1h to 24h);
- 1 permanent GB-InSAR LiSALab™ system (provided by Ellegi s.r.l.);
- 1 high-frames camera
- 1 Leica TCA robotic total station, surveying 31 optical targets (four of which relocated outside the rockslide area on stable ground).



The deep geotechnical monitoring network is collected by:

- 3 boreholes with inclinometers;
- 3 boreholes with wire extensometers;
- 8 water pressure transducers in open-pipe piezometers (below different depths, 16 to 50 m);
- 5 DMS® (Differential Monitoring System) column composed by one-meter-length and with multi-parametric probes (provided by CSG s.r.l.).

In normal direction of the landslide, on the opposite valley side has been built a small wooden house for shelter the instruments, that include GPS master reference station, High-frame camera, Leica total station and LiSARLab™ GB-InSAR system and also equipped with a server station for treatment of data and remote control of the instrumentations, with rugged high-speed data transmission connections and redundant power supply. All collected data are made available in near-real time directly into a specific website designed by Valle d'Aosta Region for EW activities.

In addition, close to the ridge of Mont de La Saxe at about 2,076 m a.s.l. a weather station is located that records the data series of rainfall, temperature and snow depth allowing an evaluation and a modelling about snow melting (Broccolato et al., 2011; Crosta et al., 2011, 2014).

The network configuration is capable of high temporal and spatial resolution monitoring of landslide movement and of the variables that influence movement, and – furthermore - the monitoring equipment was selected primarily for the temporal resolution that could be achieved, so that periods of landslide movement could be linked to the triggering factor(s).

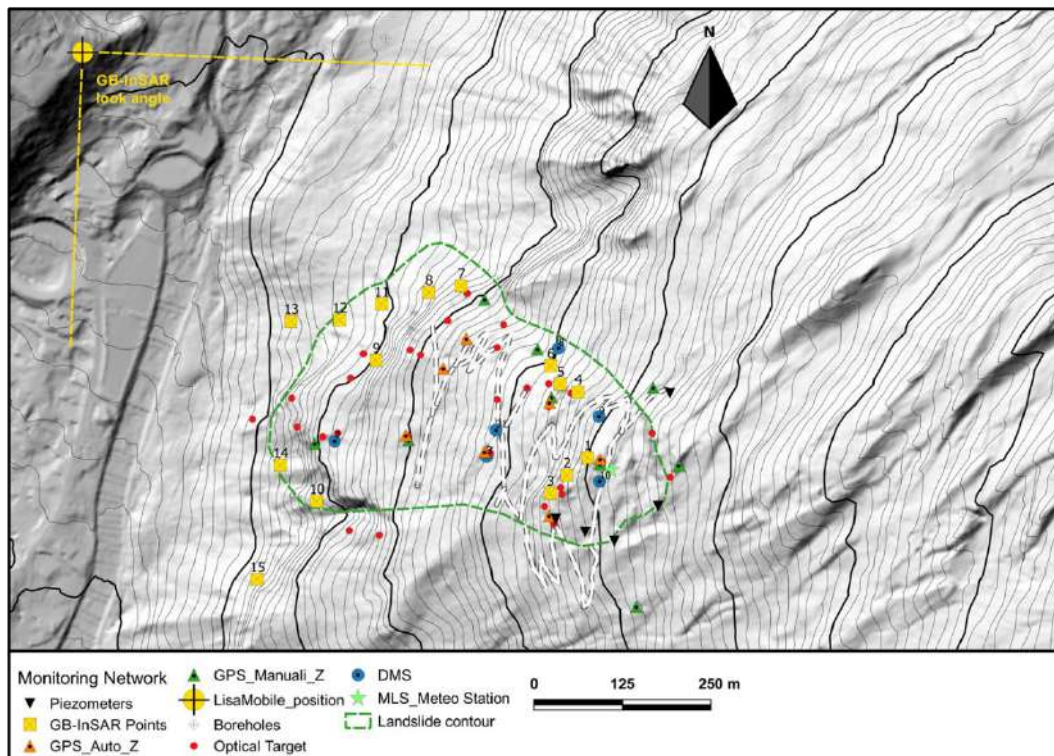


Figure 57 – distribution of the topographic and geotechnical monitoring networks. GB-InSAR points show the position of the streaming points with continuous acquisition. DMS: multi-parametric probe; inclinometer: boreholes equipped with inclinometric casing; GW level: piezometers



## 2.5.1 Ground-based network: displacement data

The results of almost ten years of monitoring (e.g. Figure 53) show a general trend of increasing displacement rate until the 2014 event. Instead, after this main event up to nowadays the trend is reverse with a general and significant decrement of displacement (Figure 59 to Figure 62). The strong conditioning by the ground-water table (hereinafter GWT) oscillation is due both rainfall and – especially – to snow-melting process (Figure 58 to Figure 62; Crosta et al., 2014).

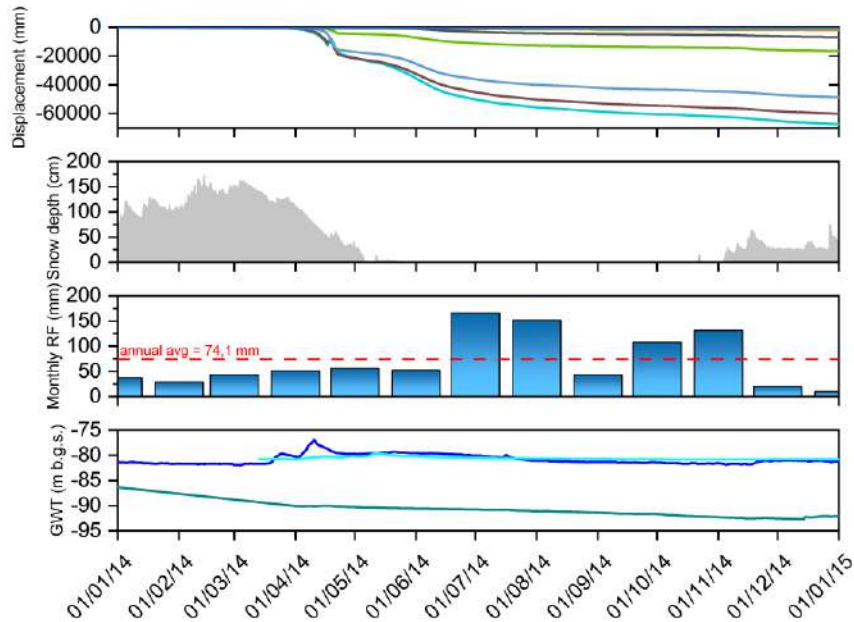


Figure 58 – Comparison between displacement of GB-InSAR POIs, snow-depth, monthly rainfall and piezometric level of DMS S3 bis (blue), piezometer A (light blue) and DMS S7 (cyano) for 2014

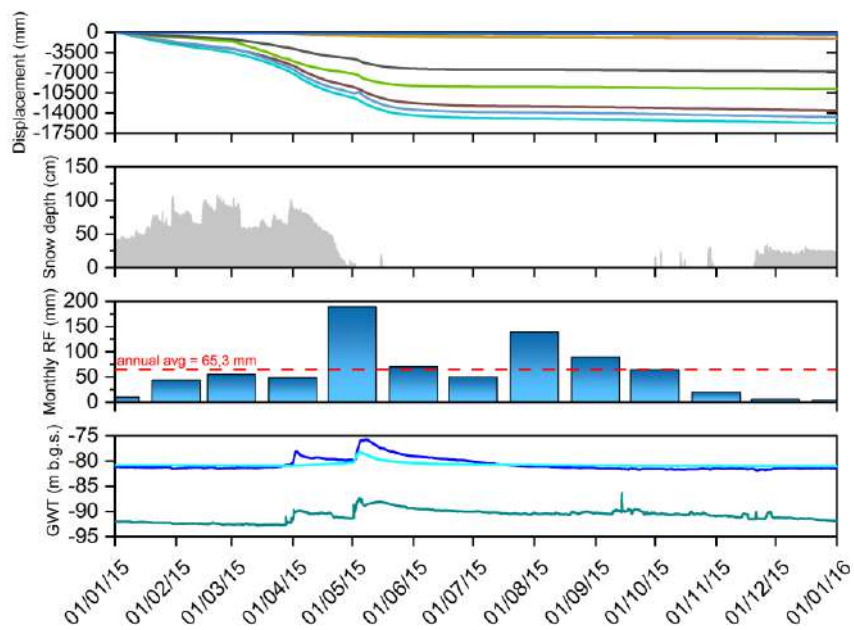


Figure 59 - Comparison between displacement of GB-InSAR POIs, snow-depth, monthly rainfall and piezometric level of DMS S3 bis (blue), piezometer A (light blue) and DMS S7 (cyano) for 2015

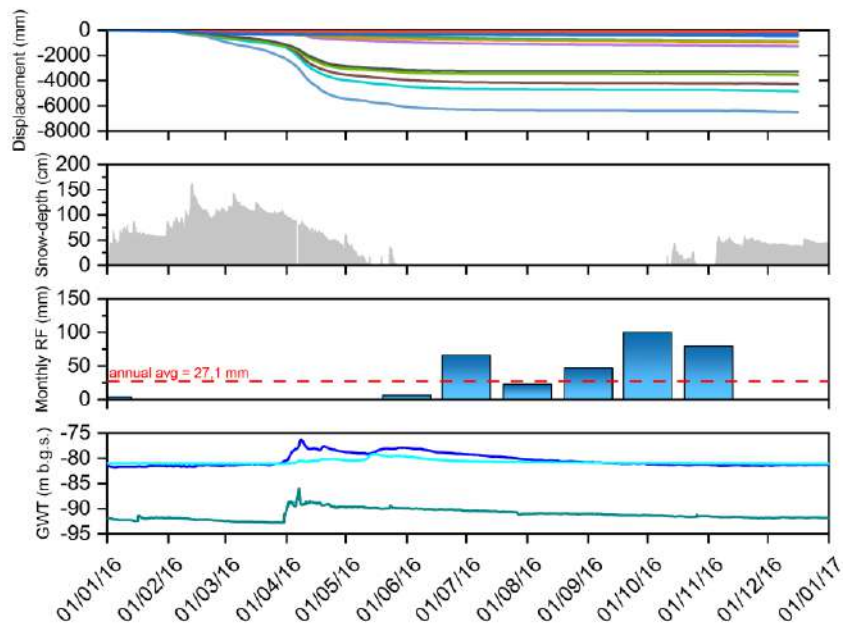


Figure 60 - Comparison between displacement of GB-InSAR POIs, snow-depth, monthly rainfall and piezometric level of DMS S3 bis (blue), piezometer A (light blue) and DMS S7 (cyano) for 2016

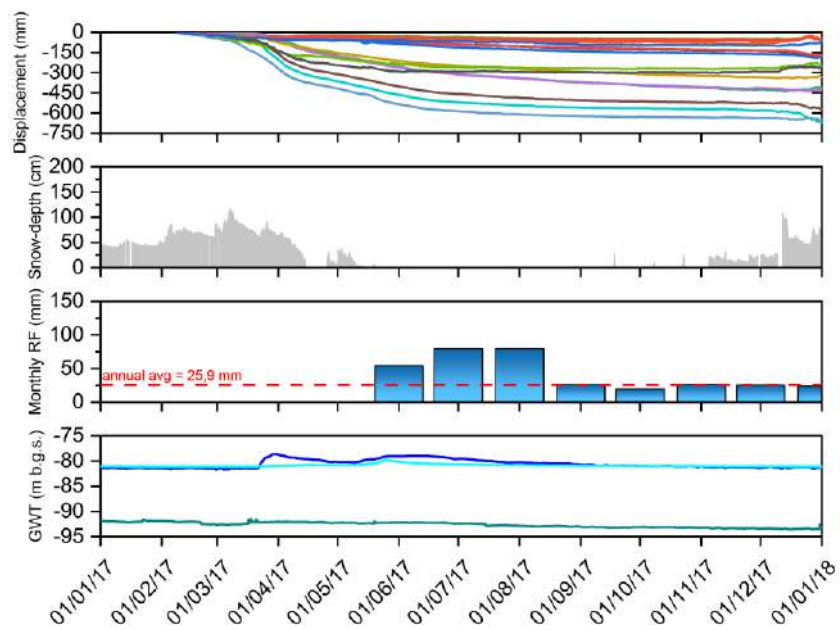


Figure 61 - Comparison between displacement of GB-InSAR POIs, snow-depth, monthly rainfall and piezometric level of DMS S3 bis (blue), piezometer A (light blue) and DMS S7 (cyano) for 2017

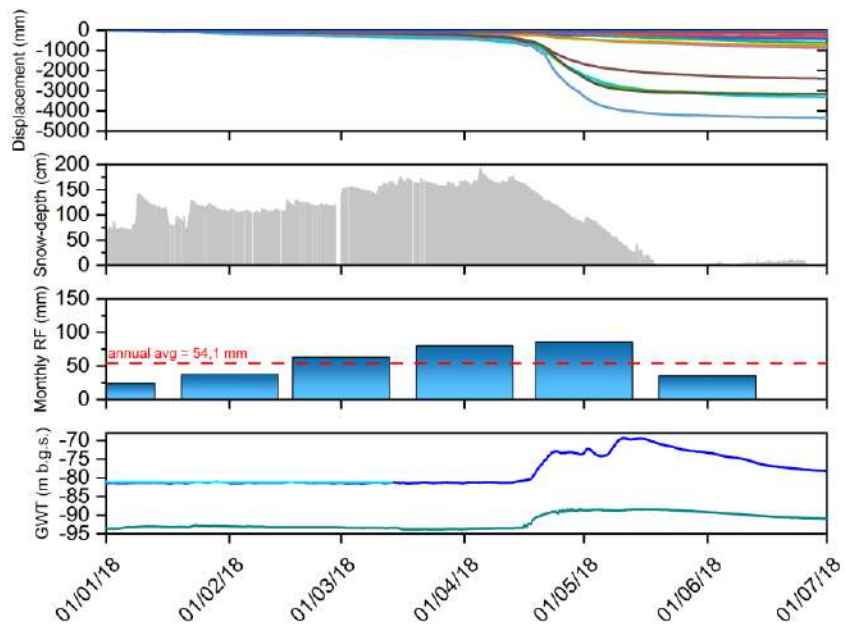


Figure 62 - Comparison between displacement of GB-InSAR POIs, snow-depth, monthly rainfall and piezometric level of DMS S3 bis (blue), piezometer A (light blue) and DMS S7 (cyano) for 2018

The displacement at depth are continuative monitored through multiparametric probe called DMS® provided by CSG s.r.l. installed along in dedicated borehole along entire slope (Figure 63). The columns are composed by 1m-length rigid segment and they are able to provide the displacements, temperature, piezometric level and ground acceleration. Since 2009 have been installed ten different columns, and actual 5 are operative (Figure 57).

Through a deep analysis of data provided by the DMS columns was possible identify the shear zones presents along the landslide mass.

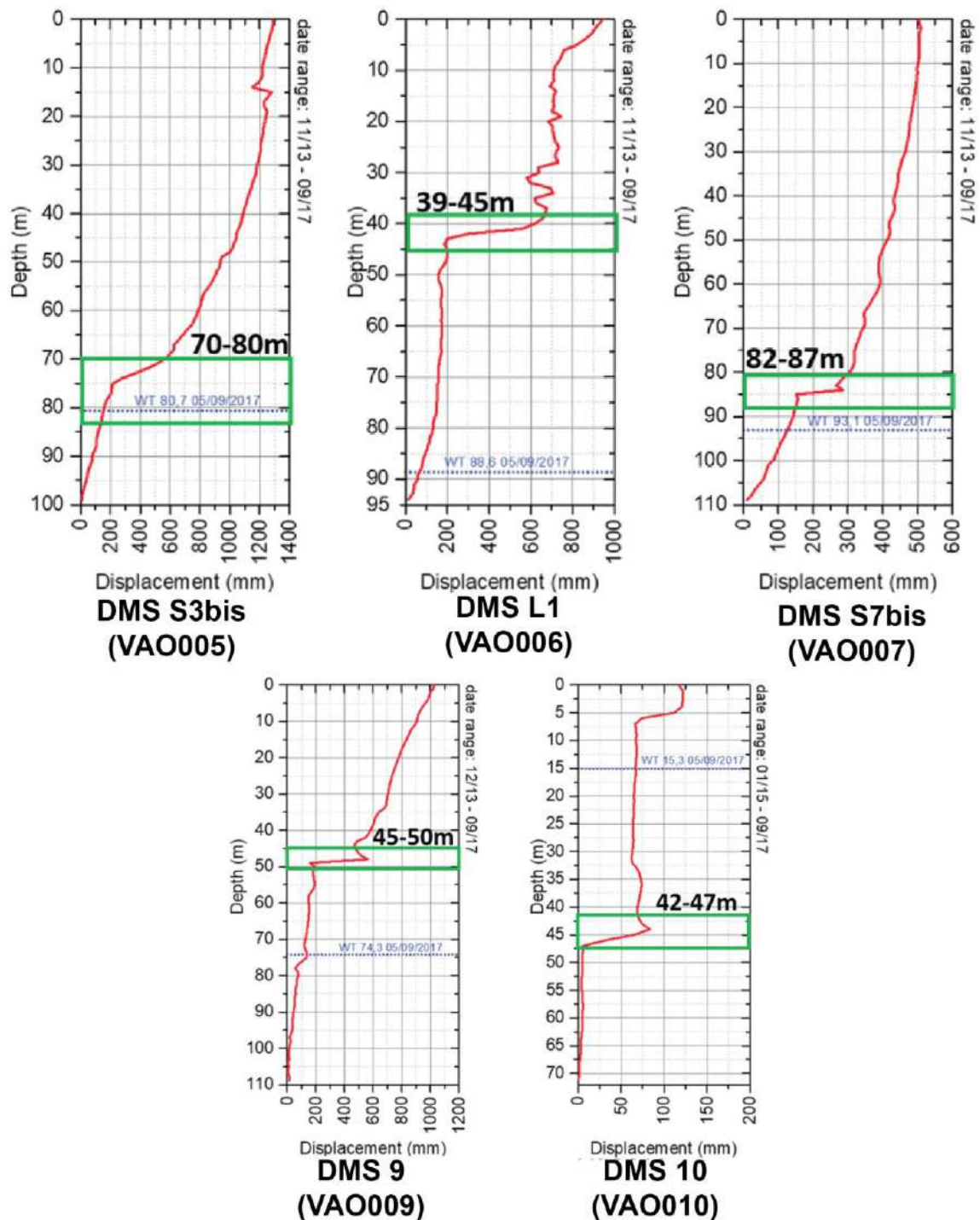


Figure 63 – the cumulative displacement for DMS® columns. VAO005: DMS S3 bis; VAO006: DMS L1; VAO007: DMS S7 bis; DMS-9: VAO009; DMS-10: VAO010

## 2.5.2 Ground-based network: piezometric data

Concerning the piezometric level and its relationship with external factors (i.e. rainfall and snow-melt), a strong link is clear (Figure 64 and Figure 65; Crosta et al., 2014). Since 2009 various piezometers were installed, because some of them considering the high displacements were broken. The maximum relative increment, considering all piezometers, is quantified in about 15 meters, but it's needed to consider that the installed piezometers are open pipe type.

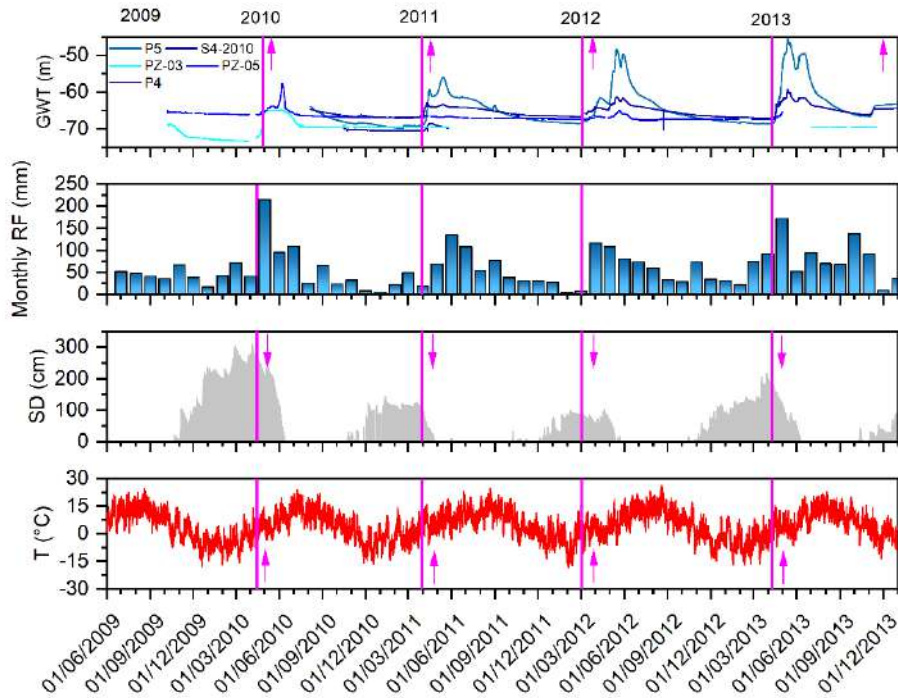


Figure 64 – comparison between ground-water table (GWT, upper graph), monthly rainfall, snow-depth and temperature since 2009 to end of 2013

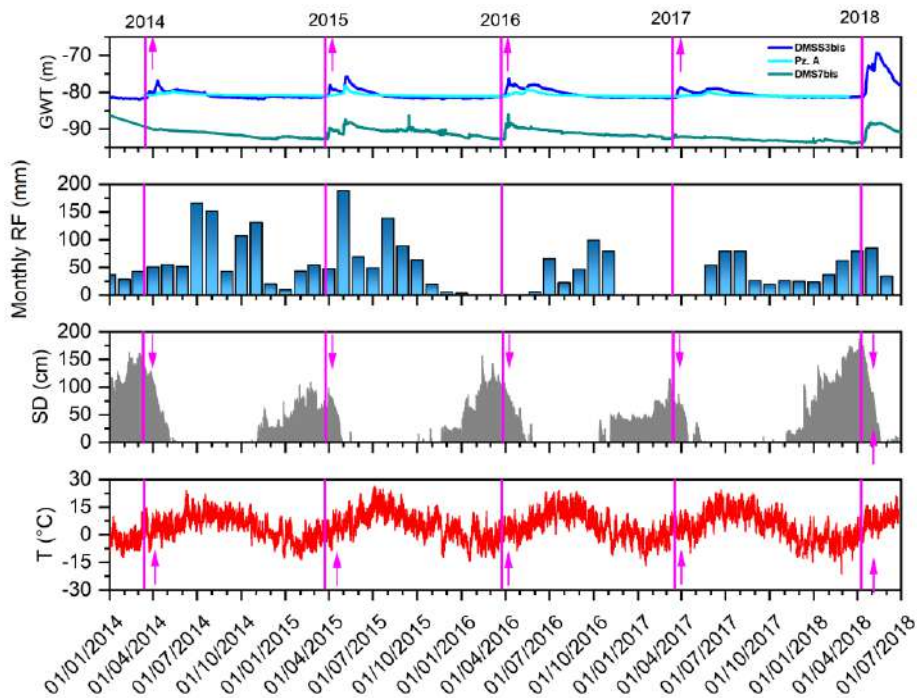


Figure 65 - comparison between ground-water table (GWT, upper graph), monthly rainfall, snow-depth and temperature since 2014 to 2018



After the 2014 event, the drainage network it was implemented (Figure 66).

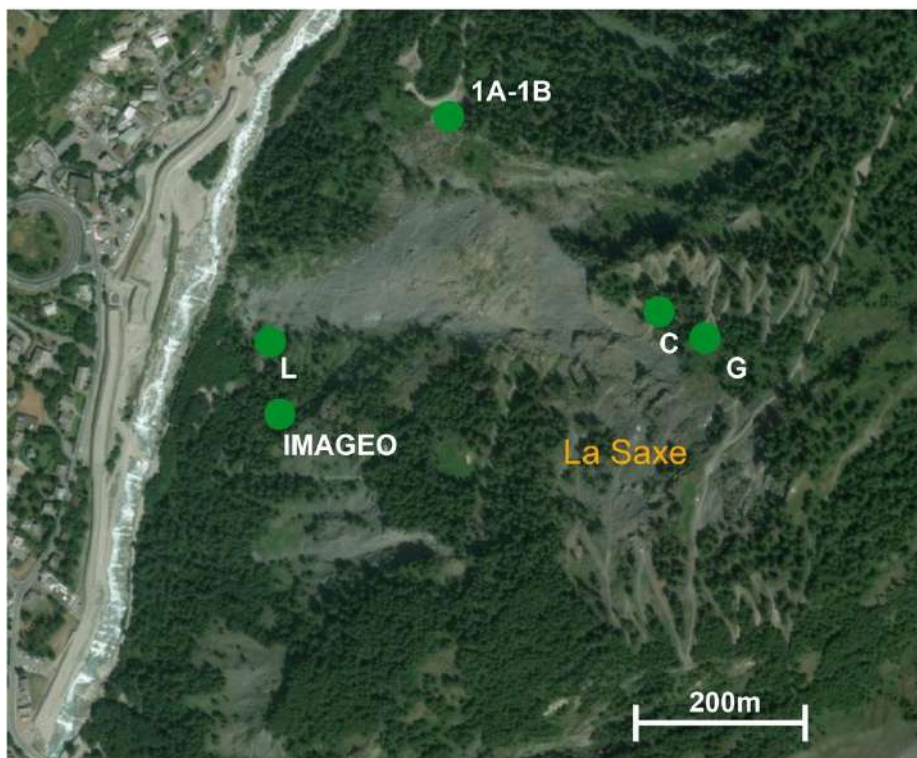


Figure 66 – drainage network on Mont de La Saxe rockslide area

The effectiveness of drainage network is clear (Figure 67), after 2014 and during the seasonal increase of GWT, the drainage network permits to discharge water flow from rockslide body to outside, and in fact decrease the general displacement (Figure 67).

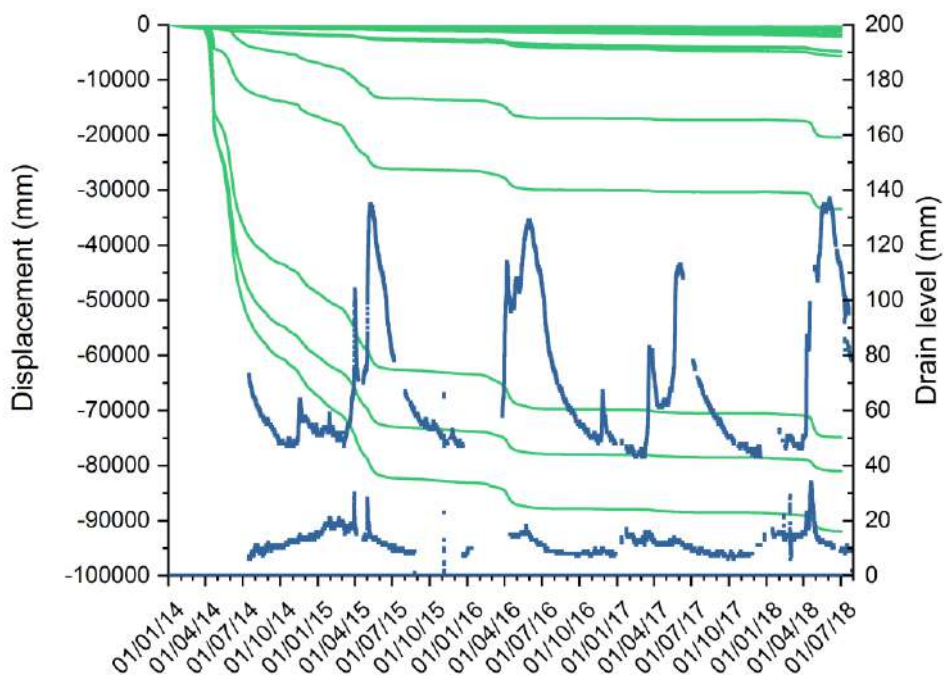


Figure 67 – GB-InSAR displacement compared with water level of two (L and C) drainage

### 2.5.2.1 GWT: Tracer tests

Since 2010, in order to understand the characteristics of circulation of the fractured mass and to support the hydrogeological model and to allow a more reasonable parameterization of the model itself, more tracing tests were carried out.

These tests provided for the introduction of a tracer (Fluorescein, Tynopal) from the piezometric pipes and directly from the surface. In the first case, the input is made directly in depth, while in the second case it was decided to insert a tracer from the surface at a trench upstream of the instability phenomenon of Plan Cereux. In this second case, the ground was eliminating the vegetation cover, forming a small tank to promote infiltration, and it was done: saturate the ground and the column of underlying material by releasing water (about 3 m<sup>3</sup>) from an anti-fire helicopter bag, and the subsequent introduction of the solution (about 2 m<sup>3</sup>) with a Fluorescein tracer. In the final phase about 2 m<sup>3</sup> of water were added to favor the piston solution.

**Test 01**

**Date** 05/06/2010  
**Injection Point** Piezometers O3  
**Fluorescein** 100 g

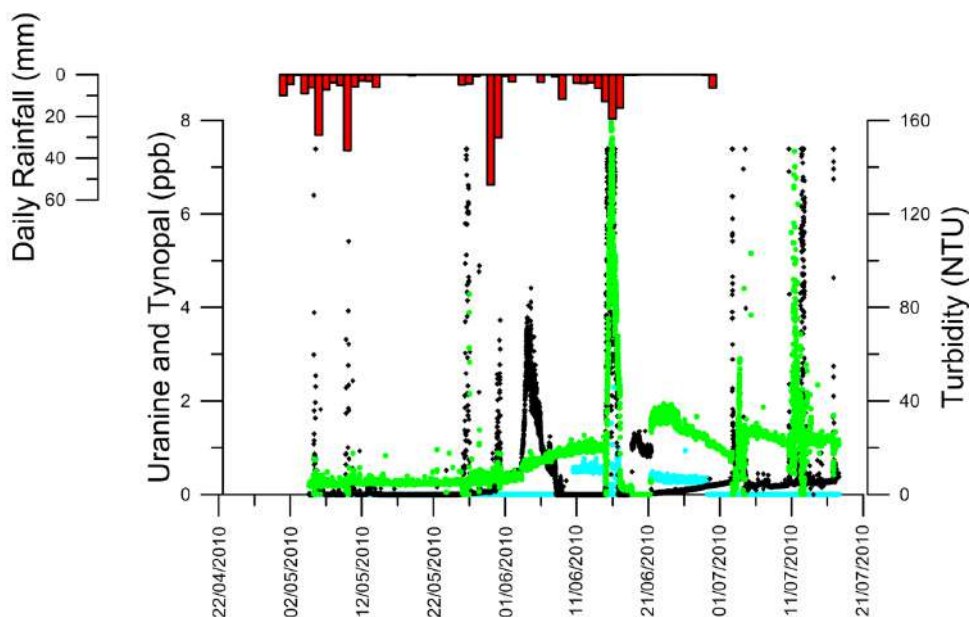
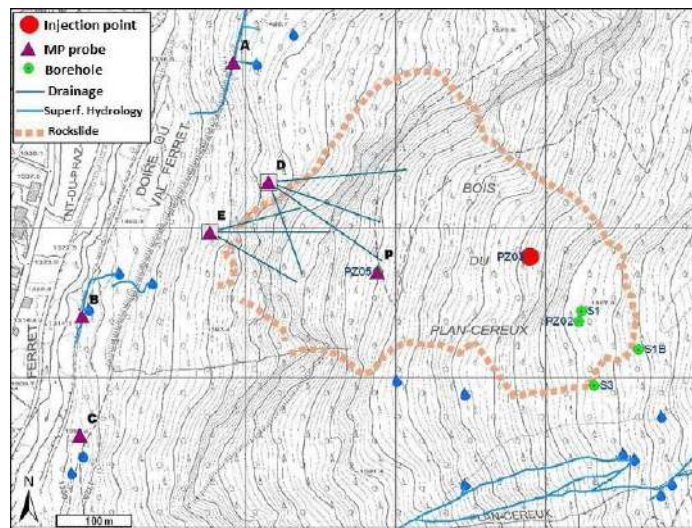


Figure 68 – results from tracer tests performed on May 2010, Uranine (green) and Tynpal (cyan) concentration, and turbidity (black)

The measured fluorescein background values oscillate around 0.2 ppb. The concentration curve shows a hint of fluorescein return starting from June 1 with peak values reaching 2 ppb observed on June 22nd. However, the fluorescence value of this return never returns to the background values and the restitution is very limited, sign of a weak degree of connection to the main fracture and circulation network, and / or of a high degree of dispersion.

Other single impulses, in which a true return curve is not recognizable, were recorded on June 15 (7.8 ppb) and 11 July (12.2 ppb) but coincide with considerable increases in turbidity due to precipitation in those days.

If the first tracer arrival recorded on June 1 was valid, and then 26 days after injection, the transit speed calculated over a linear distance of 603 m (distance between the point of entry and the monitoring point) is equal to 23.2 m / d ( $2.7 \cdot 10^{-4}$  m / s), while the peak velocity, thus considering an arrival time of 47 days, is 12.8 m / d ( $1.5 \cdot 10^{-4}$  m / s).

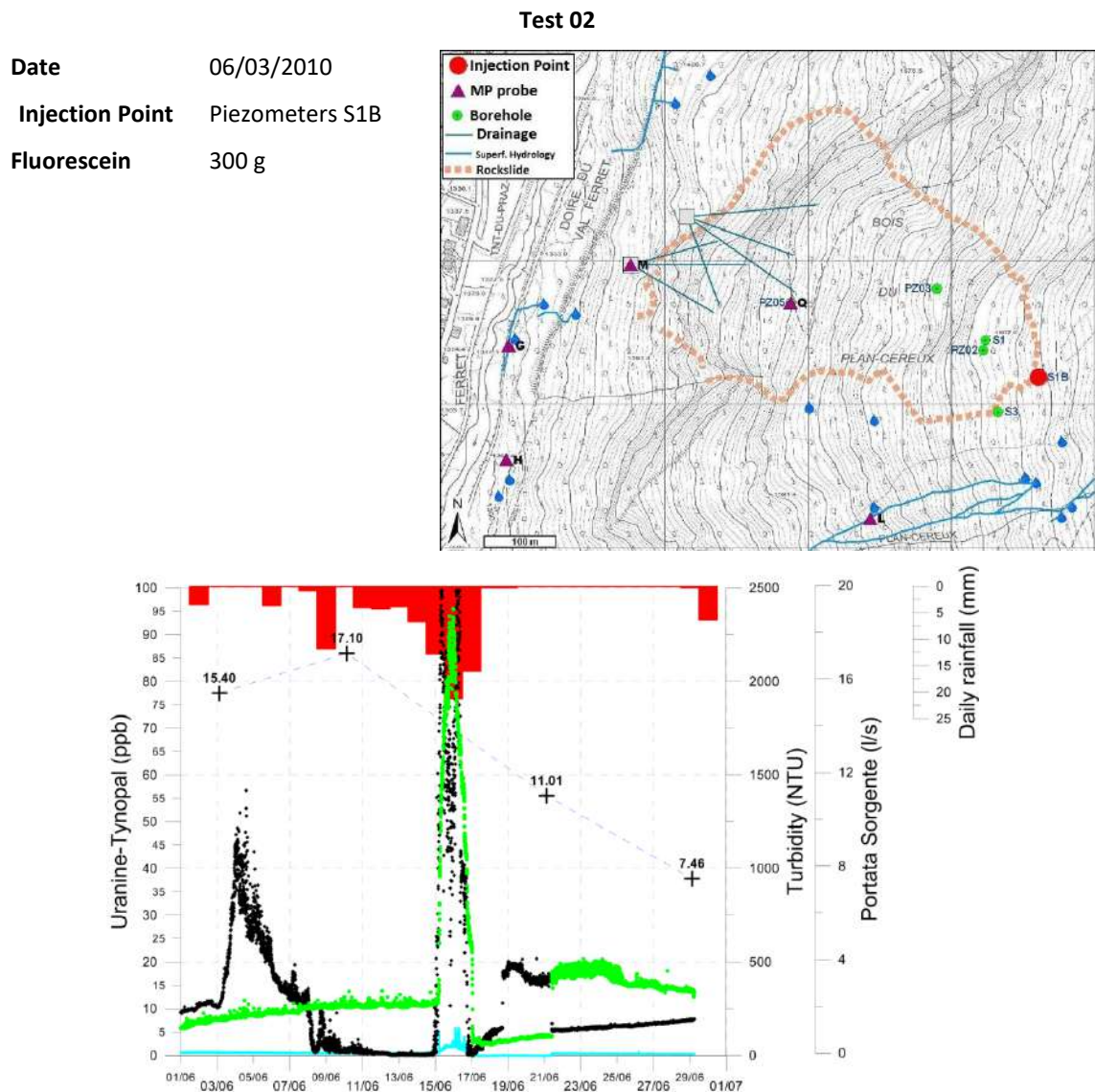


Figure 69 - results from tracer tests performed on June 2010, Uranine (green) and Tynpal (cyano) concentration, and turbidity (black)



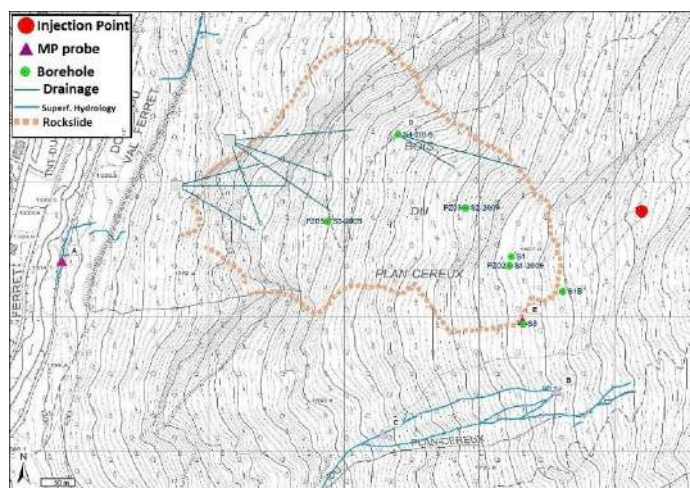
Based on direct observations, probably a most part of the tracer remained in the hole (Figure 70). The only significant event concerns the sudden increase in turbidity and the consequent fluorescein response following the rainy events of mid-June 2012.



Figure 70 – sample extracted from borehole S1B at 06/15/2011, one year later the injection

### Test 03

**Date** 06/15/2010  
**Injection Point** Trench  
**Fluorescein** 1000 g



The injection was made on the surface in correspondence of a trench connected to the deep deformations that affect the entire slope and with the prevailing ENE-WSW direction.



Figure 71 – (on left) saturation of the trench before starting the tracer test; (on right) close up on injection point

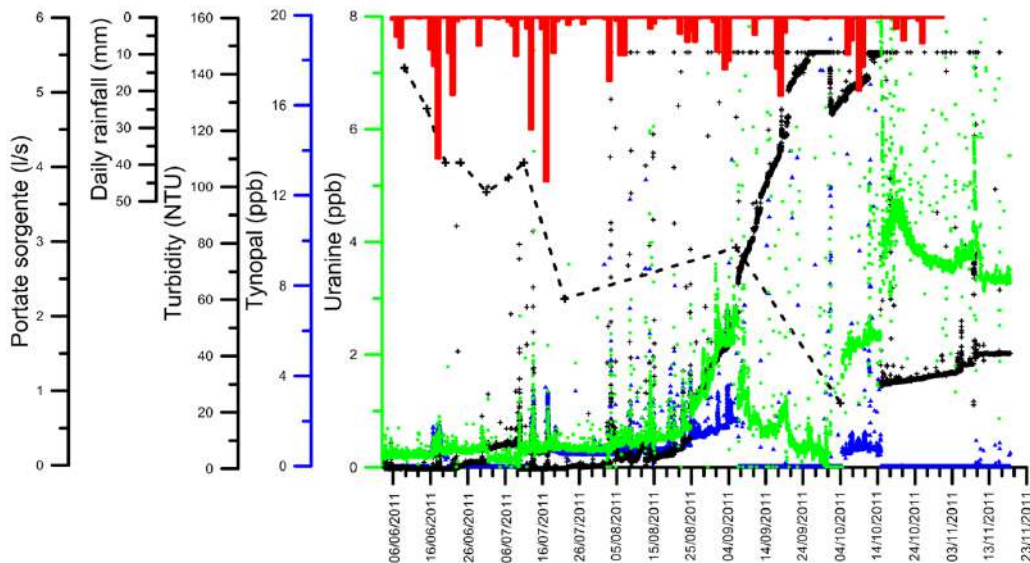


Figure 72 - results from tracer tests performed on June 2010, Uraninine (green) and Tynpal (cyano) concentration, and turbidity (black)

Fluorescein background values are around 0.2 ppb. The period June-July 2011 is characterized by intense rainfall (e.g. 18 June: 38 mm of rain, 17 July: 44 mm). Assumed the 1st arrival to 15 August, after 60 days from the entry, with a linear distance of 1046 m the maximum speed calculated is equal to about 17.4 m / d ( $1.7 \cdot 10^{-4}$  m / s). The peak concentration is recorded on September 26 (2.84 ppb). A second arrival was instead observed on October 1 with peak concentration equal to 4.75 ppb simultaneously with a net decrease in turbidity

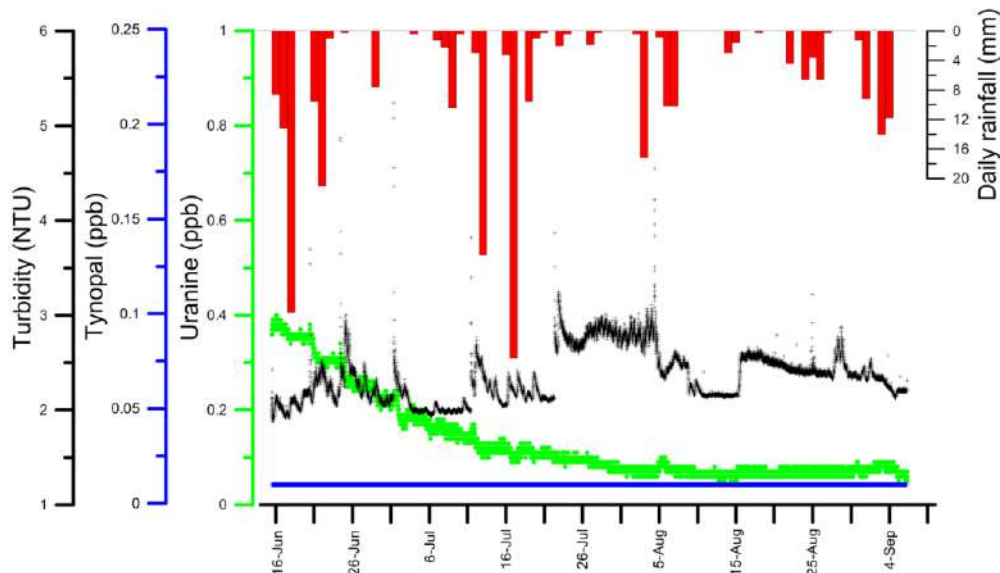
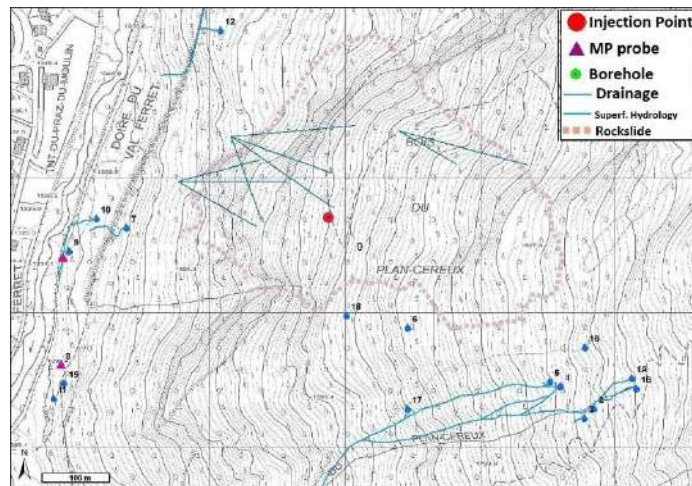


Figure 73 - results from tracer tests performed on June 2010, Uraninine (green) and Tynpal (cyano) concentration, and turbidity (black)

In S3 a dilution of fluorescein was observed, probably already present in the previous test. Using the fluorescein concentration data for the application of the single well dilution test it is possible to arrive at an estimate of the apparent horizontal flow velocity. Considering the total height of the water column from the bottom of the hole and the diameter of the piezometer, a minimum velocity of  $9.8 \cdot 10^{-4} \text{ m / d}$  is obtained. This extremely low value is considered equal to that of a cluster with a low degree of fracturing, as evidenced by the average RQD value ( $> 80\%$ ). In this condition, in fact, the rare fractures, if characterized by a small opening, can allow only an extremely limited underground flow with slow and occasional release of the tracer introduced. This observation is also supported by the presence of a tracer after a long intake period in the S1B survey (Figure 70).

#### Test 04

**Date** 03/29/2012  
**Injection Point** Borehole S5-2011  
**Fluorescein** 2000 g



The input of tracer was preceded by an injection of 300 l of water. The tracer solution was prepared with 2 kg of tynopal in 1000 l of water. The tracer input lasted 55 minutes and then a further 700 liters of water was introduced.

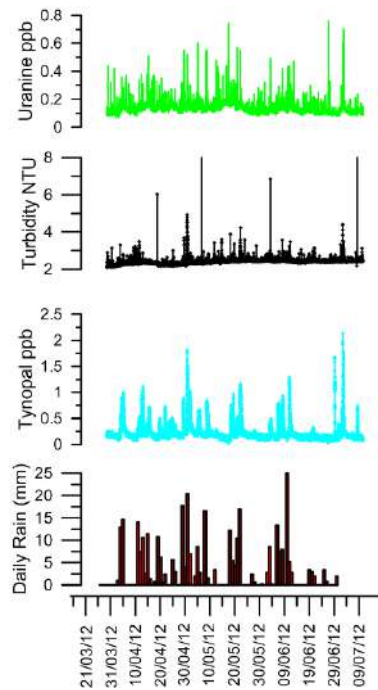


Figure 74 - results from tracer tests performed on March 2012, Uranine (green) and Tynpal (cyano) concentration, and turbidity (black)

Fluorescein has a very noisy signal, with very low concentrations <1 ppb. Turbidity is also low, with some spikes probably linked to rains. The numerous tynopal peaks show an instantaneous relationship with the rains, confirming that the water we are monitoring is superficial, with the possible effect of the organic carbon content.



### 2.5.3 2D groundwater flow model

In Crosta et al. (2014) have been presented a groundwater flow modeling that allowed to verify both the consequences and the validity of some of the surveyed characteristics, and of the assumptions made about the role played by major features (e.g., morpho-structures) and local to regional topography (Gleeson and Manning 2008). At the same time, groundwater modeling offers the means for assessing the oscillation of ground-water level which is a major input in rock slide and deep-seated gravitational slope deformation modeling (Crosta and Agliardi, 2003; Guglielmi et al., 2005; Pisani et al., 2010). To this aim, both 2D and 3D groundwater flow modeling of the slope have been performed (Crosta et al. 2011). To better outline the general behavior of the slope, the results of a 2D saturated–unsaturated flow model are presented. The model considers the presence of a highly-fractured upper rock slide mass and a slightly-fractured deep-seated gravitational instability. The two instabilities are bounded at their base by thin cataclastic shear bands. The hydraulic conductivity values have been estimated by borehole observations and measurements, infiltration testing, geophysical investigation data, and laboratory tests on samples of cataclastic breccia. Water characteristic curves have been assumed tri-linear with parameters typical of coarse (e.g., sandy–silty soils for broken weathered rock mass) up to very fine soils (e.g., cataclastic shear bands). Seismic velocities allowed us to estimate a porosity value for each of the main contour intervals. Some empirical relationships linking compressional wave velocity ( $V_p$ ) with porosity ( $n$ ) (Wyllie et al., 1956, 1958; Watkins et al., 1972; Lama and Vutukuri, 1978; Kirsch, 2006), and with degree of jointing (Sjögren et al., 1979) have been presented in the literature. Following, for example, Watkins et al. (1972) and Kirsch (2006), a progressive decrease in porosity with depth can be associated to the wave velocities presented in Figure 76 ( $V_p=1,350 \text{ m s}^{-1}$ ,  $n=0.30$ ;  $V_p=1,750 \text{ m s}^{-1}$ ,  $n=0.25$ ;  $V_p=2,450 \text{ m s}^{-1}$ ,  $n=0.19$ ;  $V_p=3,000 \text{ m s}^{-1}$ ,  $n=0.16$ ). A similar trend can be derived for RQD values or linear (1D) joint frequency (Palmstrom, 1995). The change in elastic wave velocity with RQD and 1D joint frequency allowed us to attribute fracture intensities to slope sectors delimited through seismic refraction tomography. Grain size analyses and laboratory permeability tests provided a range of hydraulic conductivity values for the breccia level ranging between  $10^{-7}$  and  $10^{-9} \text{ ms}^{-1}$ . These values are in good agreement with measurements on cataclastic breccias at the base of large deep-seated deformations (Crosta et al., 2012) and from cataclastic materials described in the literature (Fischer et al., 1998; Burgi et al., 2001; Riedmüller et al., 2001; Sausgruber and Brandner, 2003; Mansour, 2009; Mansour et al., 2011). The stage of development of the rockslide and the amount of cumulative displacements play a major role in controlling the breccia parameters. In fact, it is reasonable to suppose that for small initial displacements the breccia will represent a level more permeable than the contiguous rock mass, especially in case of quasi-translational mechanisms. On the contrary, for larger displacements the rock slide mass will progressively break, and strain localization will occur with a progressive grain size reduction by clast fragmentation and shearing. This induces a decrease in hydraulic conductivity along the basal failure zone and an increase within the fractured rock-slide mass. On the basis of all these data and from similar studies in the literature (Agliardi et al., 2001; Binet et al., 2007; Boadu, 1997; Cappa et al., 2004; Guglielmi et al., 2005; Pisani et al., 2010; Crosta et al., 2011; 2012) for large rock slides and deep-seated gravitational slope deformations, it has been decided to attribute a range of values to each of the main sectors within the Mont de La Saxe slope (Figure 75a). The finite-elements mesh

consists of 33,537 elements with an average area of about 100 m<sup>2</sup>, down to about 5 m<sup>2</sup> within the cataclastic zones (Figure 75a). Recharge has been applied at the ground surface accordingly to the total equivalent precipitation, taking into account for snow melting in spring and early summer, evapotranspiration, and concentrated infiltration at some trenches considered continuous and highly permeable as found from infiltration tests and borehole drilling (S1–12). The transient model was implemented by using daily time steps from July 1, 2009 to September 12, 2012, starting from head distribution simulated with a steady-state simulation. The net recharge rate has been calibrated starting from field surveys and the measurements mentioned above. Model results show the presence of a main groundwater table, which is located at the bottom of the rockslide. Different values of hydraulic conductivity relative to the different materials result in different groundwater geometries, with perched groundwater table above a deeper unsaturated zone, but these models were less successful in the calibration process, and a full description of the possible results is out of the scope of this paper. This groundwater table varies during the hydrologic year between 5 and 10 m, with maximum levels in late spring (Figure 75c) and minimum values in early spring, before snowmelt occurrence (Figure 75d). The hydrological dynamics in proximity of the rockslide shear zone is complex. Above the shear zone, the hydrologic response following snowmelt is extremely rapid (Figure 75b), as observed in monitored boreholes. This response seems mainly controlled by melting within the rockslide area or conveyed to the rockslide by high permeable materials (e.g., trenches). Below the shear zone, the response is significantly slower (Figure 75b), and it is associated with a deep circulation system which is also supported by the higher mineralization observed at the springs located at lower elevation. These results support the idea that the groundwater recharge close to the rockslide is mainly to be attributed to a major vertical infiltration and redirection by highly permeable structures (e.g., trenches, counterscarps).



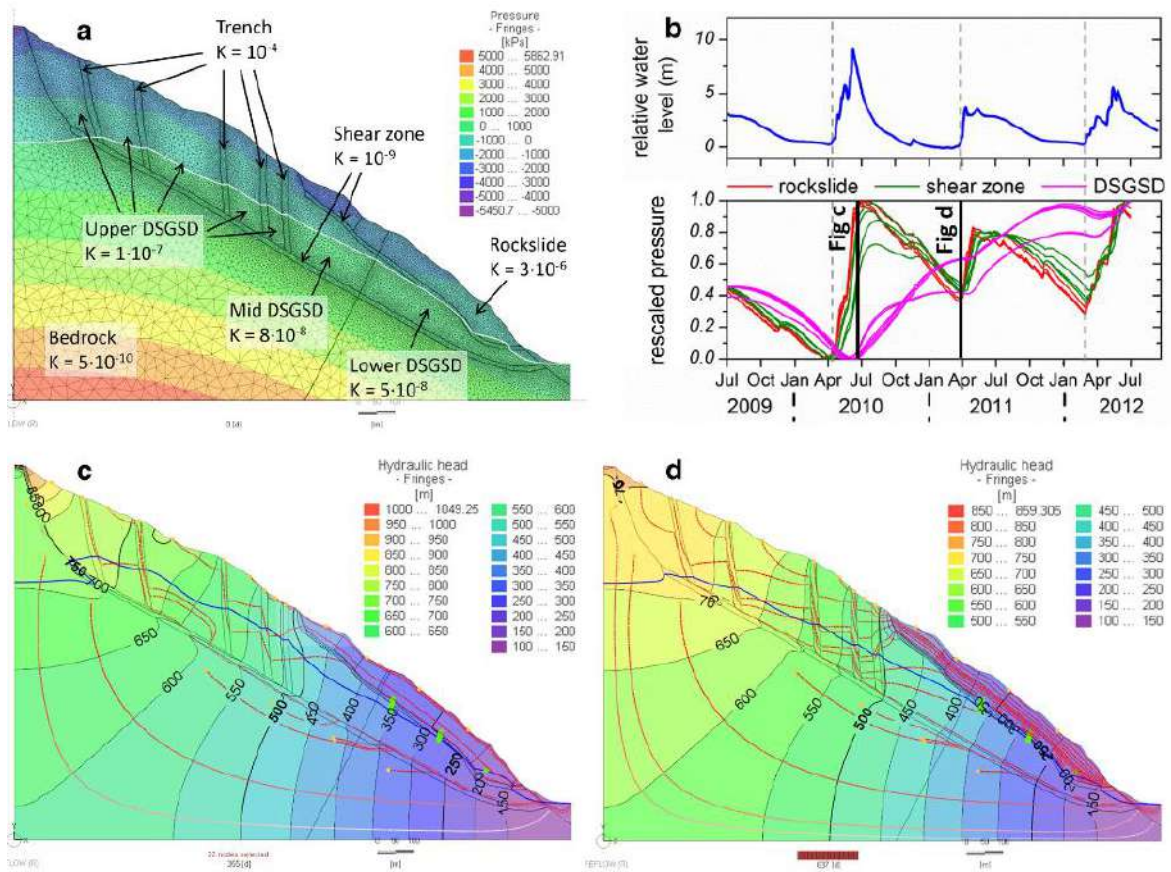


Figure 75 - 2-D transient groundwater model of the slope. a) Model setup and results of the steady-state simulation used as initial condition for the transient model; b) comparison of relative water table averaged from monitored data and pressure variations for observation points within the model; c) transient model results corresponding to maximum water table level (June 20, 2010); transient model results corresponding to minimum water table level (April 29, 2011). The reported values for the hydraulic conductivity are the calibrated values for this model, and slight changes in values can generate the formation of perched groundwater tables. Formation of a surficial and a deep groundwater flow path is shown in the model, together with the role of more permeable trench material and less permeable cataclastic shear bands (from Crosta et al., 2014)

## 2.6 Sliding surface

Most of the investigations performed since 2005 have been devoted to identifying the sliding surface of the landslide. A geophysical investigation using seismic refraction tomography method was performed. 5 seismic refraction survey lines were conducted with hundred-meter line spacing, for a total of over 3.5 km length, and using 40 Hz geophones. The results (Figure 76) show 6 different *velocity zones* divided into two main groups, called quaternary deposits and bedrock material. The first group is characterized by a low velocity ( $V_p < 2.45 \text{ km s}^{-1}$ ), that means the material is incoherent and/or highly fractured and its extension is comprised between 30 to 70 m within the landslide body. The bedrock is characterized by high velocity values ( $V_p > 3.0 \text{ km s}^{-1}$ ). At the contact between this two main groups is imposed the slip surface, with a variable thickness.

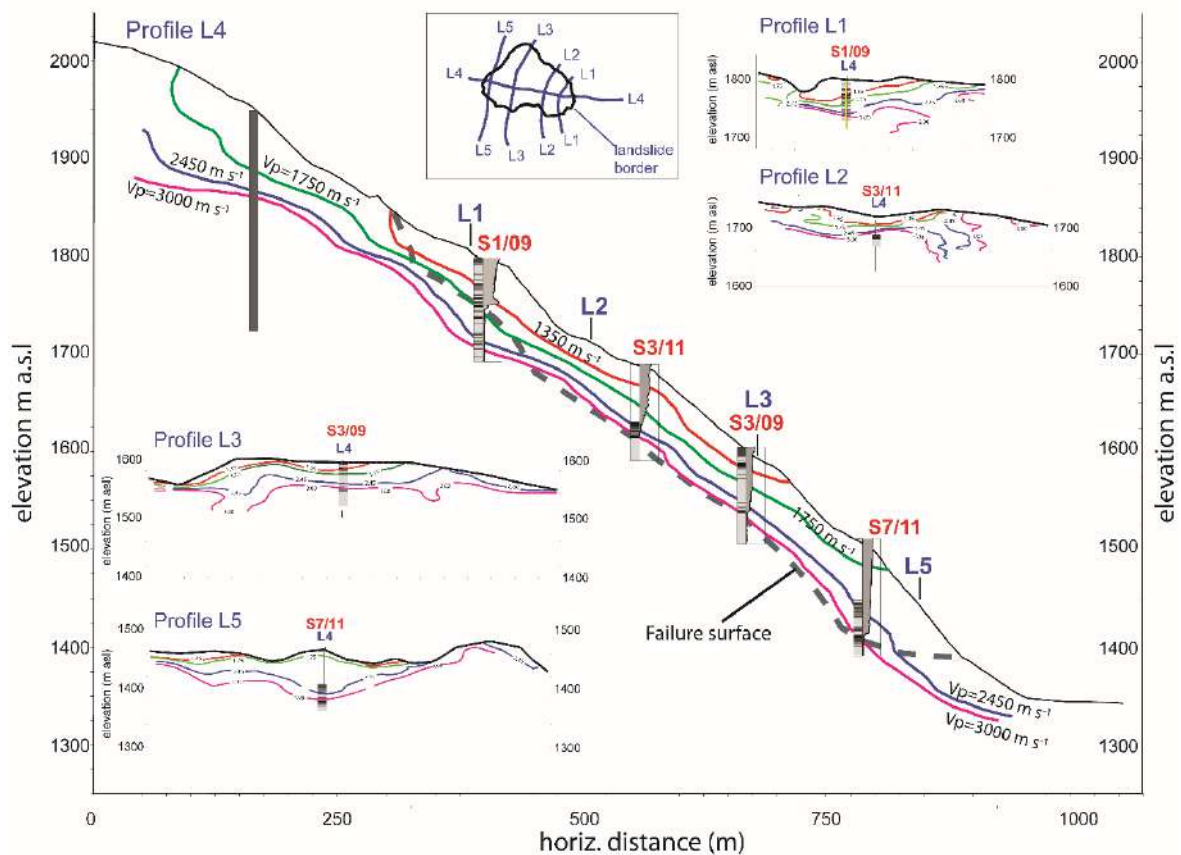


Figure 76 - seismic refraction tomography represented in terms of iso-velocity contour lines, along longitudinal and transversal investigation lines, for the lower part of the Mt de La Saxe slope. Simplified fracture intensity logs (and measured inclinometric displacements are shown (from Crosta et al., 2014)

During the coring operations it has been possible to identify a weak and weathered layer, highly fractured (soil-like rock; Figure 77). Considering the landslide geometry, this shear band is on average located between 70 and 80 m b.g.s. In the landslide mass is present more than one shear zones.

Over investigation performed during the core logging, all boreholes are instrumented.

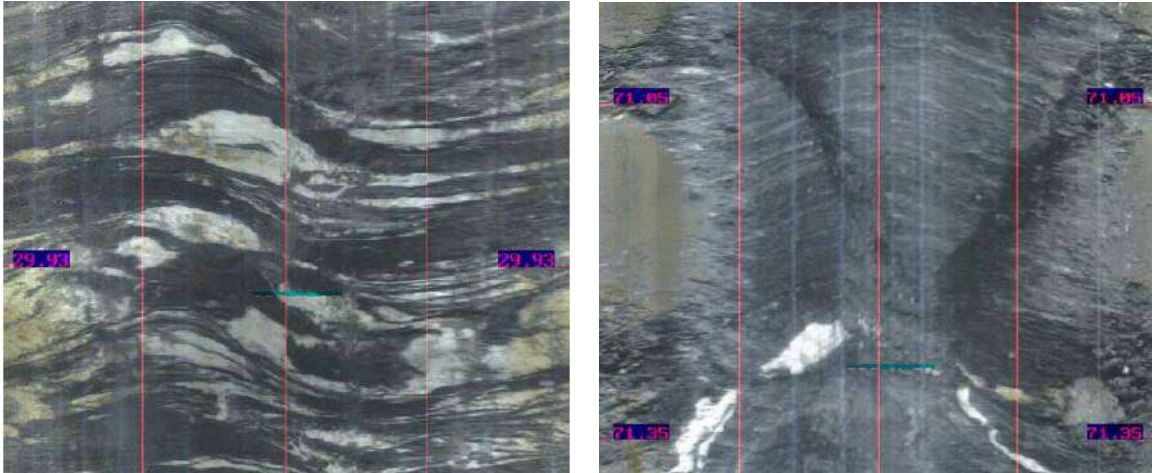


Figure 77 – schistosity (on left) and highly fractured rock (on right) from borehole tv images

Since 2009 more than 10 DMS multiparametric probes have been installed in the landslide body, in such a way to cover entire area and volume. The DMS system, provided by CSG s.r.l. is a chain of multi-parametric probe of 1 meter-long able to measure displacements in two or three directions (both horizontal and vertical at all the prefixed depths with high accuracy and precision), piezometric water levels and soil/air/water temperature (Foglino et al., 2006). Other boreholes are instrumented with inclinometers and/or piezometers.

The monitoring results confirm the presence of a metric shear zone located at 70-80 m b.g.s. (Figure 78), characterized by highly fractured rock mass and soil-like rocks.

The analysis of the displacement patterns of the shear zone in all instrumented boreholes shows that the total movement at any of the shear zones is generally composed of creep and seasonal movements. Creep is equal to the total movement during periods of zero pore pressure changes. Seasonal movements generally result from pore pressure changes due to snow-melt and – probably – rainfall, in addition to changes in the forces acting on the slide, like lateral earth pressures of the water filling the tension cracks and surface water ponding. The available piezometric and hydrologic data enabled correlating the seasonal movements only to pore pressure changes resulting from snow-melt and rainfall rather than other seasonal forces affecting the slide.



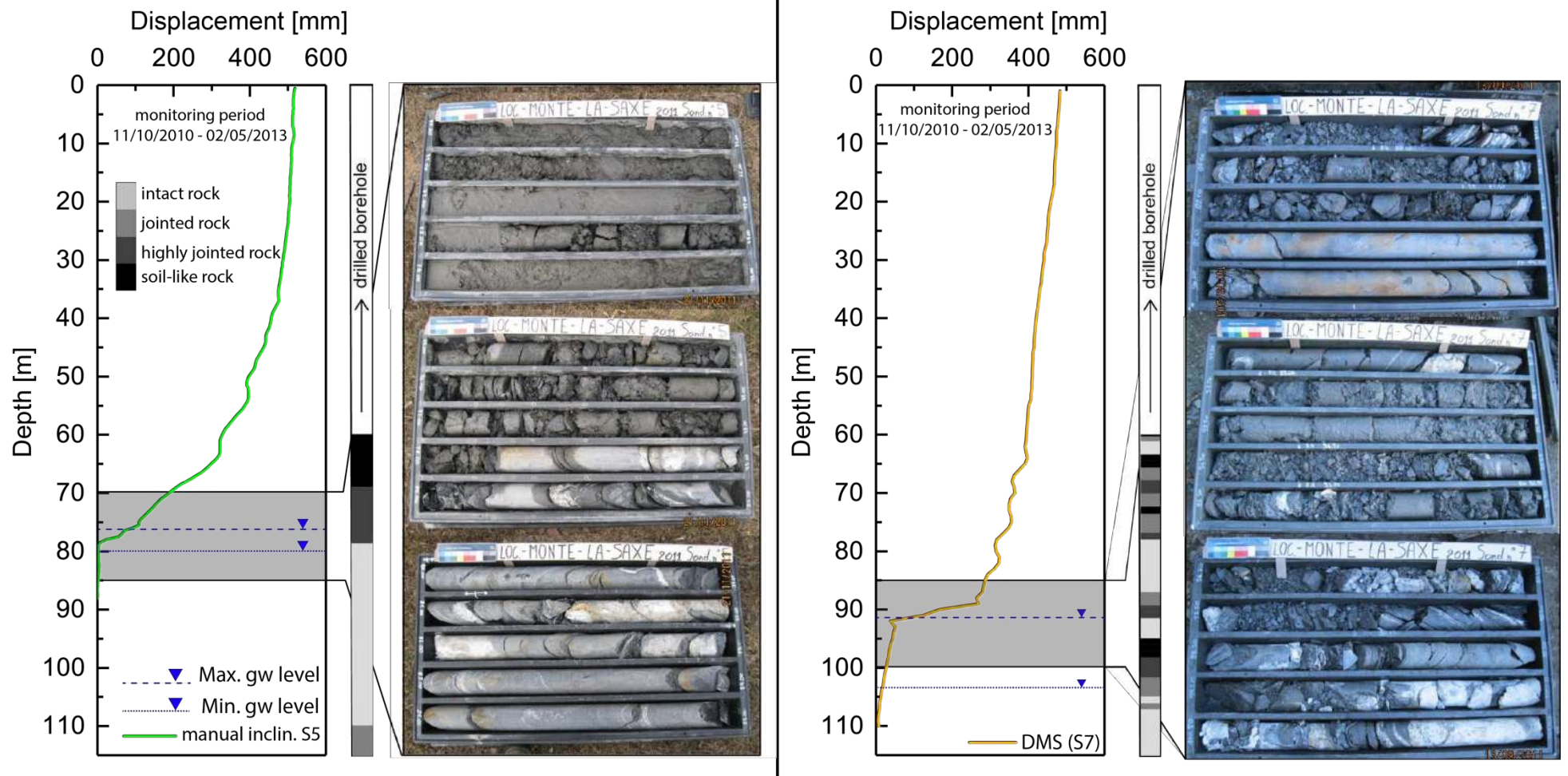


Figure 78 - Inclinometer and DMS cumulative displacement plots for different total measuring intervals (see dates above each plot) compared with simplified fracture density logs. Percussion drilling intervals, main shear zone extent, and groundwater table levels are shown

## 2.7 Chervaz Rockslide

The Chervaz rockslide is located on the southern flank of the middle Aosta Valley, about 12 km west of the village of Chatillon, between 1,100 and 1,440 m a.s.l. altitude. Natural hazard in the area is quite high due to presence of Thuy and Arlier villages located downslope Chervaz rockslide. The area is located within the Zermatt-Sass eclogitic unit of the *Piedmont Zone* including prasinites, calc-schists, serpentinites and talc-schists. And it is along faults associated to the E-W trending Aosta-Ranzola system. The instability is located at the mouth of a tributary valley, that during the Last Glacial Maximum expansion (LGM) was shaped by a lateral glacier joining the main Balteo glacier, both being part of the glacial system who carved the entire Aosta valley down to the Po Plain.

Bacenetti et al. (2014) indicate that present-day main gravitational processes within Chervaz rockslide can be described as planar rock sliding of the central sector, associated with rotational movements and toppling phenomena of the basal/distal sectors (lower east part of the area). A major sliding surface, responsible for the progressive movement of the slope, has been interpreted as associated with a thin talc-shists rock layer, outcropping at 1,440 and 1,390 m a.s.l. along the slope; it forms a NE- dipping surface with an inclination increasing from 20° (upper sector) to 35° (lower sector). The poor geomechanical properties of the highly fractured talc-shists along this inclined surface predispose progressive failure mechanisms and associated displacements. At 1,350 m a.s.l. the presence of a secondary sliding surface has been also hypothesized, characterized by a steeper inclination (45°/50°) with respect to the first one. This secondary surface could most likely join the main one at depth and could have been generated by gradual sliding towards the valley of the entire rock mass. In the eastern sector of the landslide, toppling phenomena have been detected, affecting the rock wall above the Septumian Torrent bed. In these area, gravitational phenomena are particularly active as indicated by the absence of arboreal vegetation, and the presence of deposits which completely block the channel. Moreover, in correspondence of the scarps located on both right and left flanks of the Chervaz rockslide, numerous morphological pieces of evidence testify its retrogressive behavior. Other deformation features, such as trenches and open fractures have been identified in the upper sectors; a local kinematic model was derived using also the information provided by displaced trees and other indicators. Patterns of surface deformations show an overall NW-SE trend. This agrees with the NE dipping of the major sliding surface. Two secondary slip planes with geometrically opposite immersion (SW) have been also detected in the area. Finally, in the base sector of the landslide, several areas with buckles and bulges located perpendicularly to the mean direction of the slope were identified. These landforms are characterized by scarps of m-size, dipping towards south and giving rise to counterslope features, which are typical of medium-low zones of rockslides, where the movement appears to be compressive.

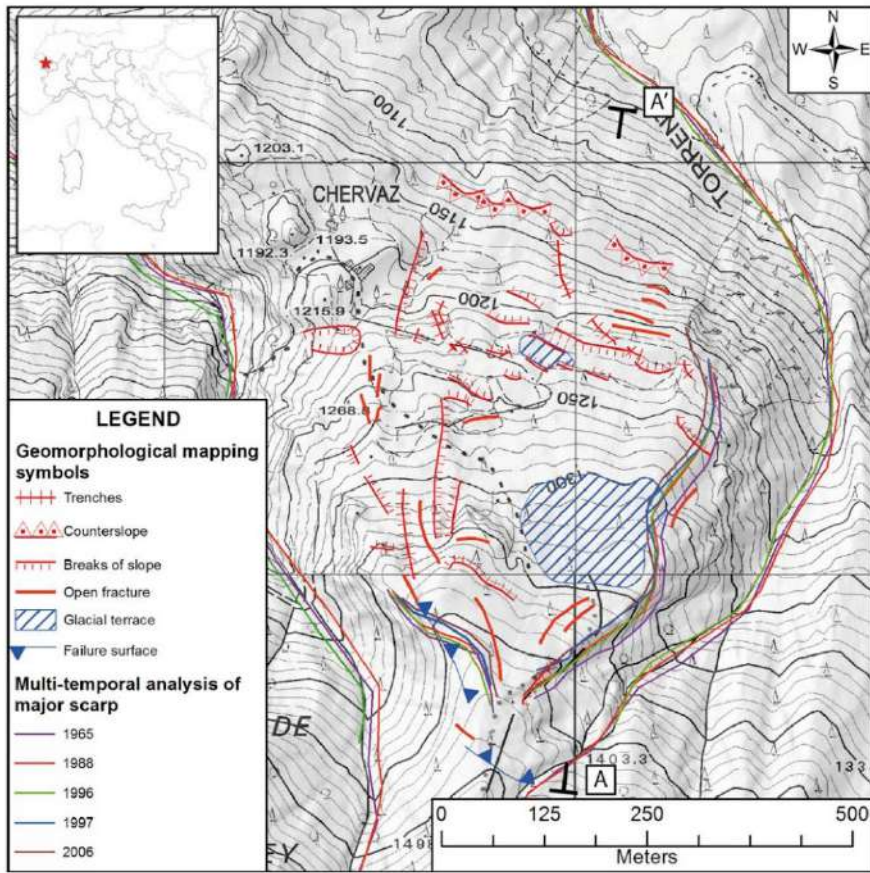


Figure 79 - Geomorphological sketch map of Chervaz DSGSD (from Bacenetti et al., 2014)



Figure 80 – Chervaz rockslide, lateral view (on left); rocky crown of the rockslide (on right)



## 2.8 Ruinon Rockslide

The Ruinon rock slide affects the right-hand flank of the Valfurva in the Upper Valtellina (Central Italian Alps; Figure 81), which is characterized by typical continental-alpine rainfall regime (i.e. rainy summer and autumn) with annual average, maximum, and minimum rainfall of 750, 1300, and 300 mm, respectively. Slope instability involves pre-Permian polydeformed phyllites of the Austroalpine Campo Nappe, as well as glacial and talus deposits (Crosta, 1999, 2000; Agliardi et al., 2001). The rockslide occurs in the lower sector of a deep-seated gravitational slope deformation (DSGSD) affecting the entire Cima di Saline slope from 1450 m a.s.l. up to 3000 m a.s.l. (Figure 81b), and is characterised by an Upper Scarp (US, 2100 m a.s.l.), mainly exposing disturbed rock masses, and a Lower Scarp (LS, 1950 m a.s.l.), involving disintegrated rock mass and a thick debris cover (Figure 81c). Swarms of ESE trending scarps, trenches and open fractures upslope of the US and the occurrence of a large, Holocene rockslide accumulation just NW of the active rockslide (Scè rockslide accumulation, Figure 81 and Figure 82) testify the structural links between the rockslide and the larger DSGSD, a long-term evolution of the rock slope instability, and a tendency to retrogression of the Ruinon rockslide up to 2200 m a.s.l. in a slope sector of highly fractured bedrock (Crosta and Agliardi, 2003). Minor, shallow slope instabilities associated to the rockslide are widespread, including fragmental rockfalls (manly affecting the US and the right flank of the rockslide) and debris slides/debris flows (affecting the LS and downslope areas).

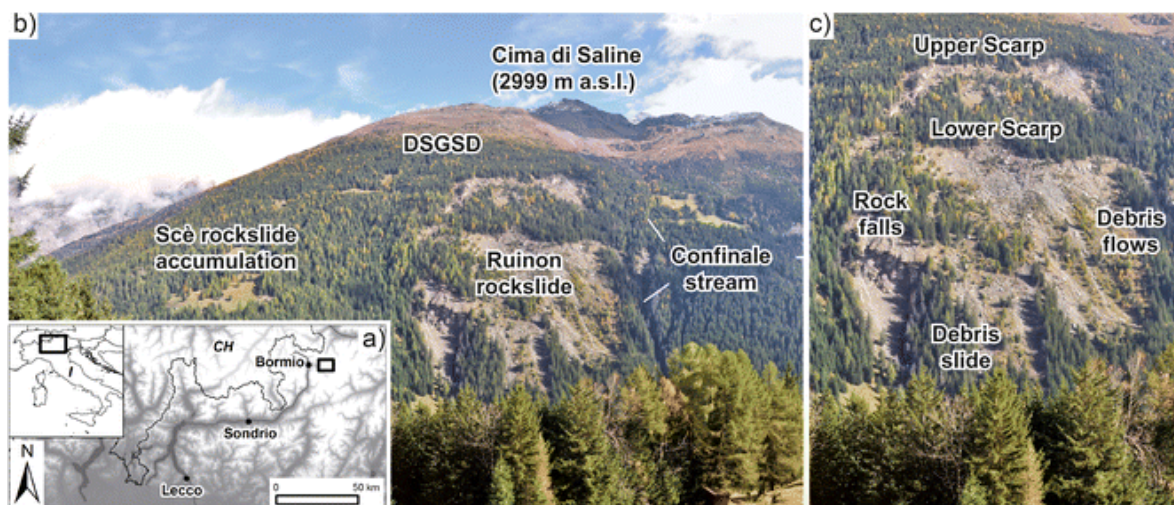


Figure 81 - The Ruinon rockslide affects the right-hand flank of the Valfurva in the Upper Valtellina (Central Italian Alps, a). The rockslide is nested into a larger deep-seated gravitational slope deformation (DSGSD), which affects the entire slope from 1450 m a.s.l. up to 3000 m a.s.l.(b). The Ruinon rockslide is characterized by two major scarps (c), namely the upper scarp (US, 2100 m a.s.l.), exposing disturbed rock masses, and the lower scarp (LS, 1950 m a.s.l.), involving disintegrated rock mass and a thick debris cover (from Crosta et al., 2017).

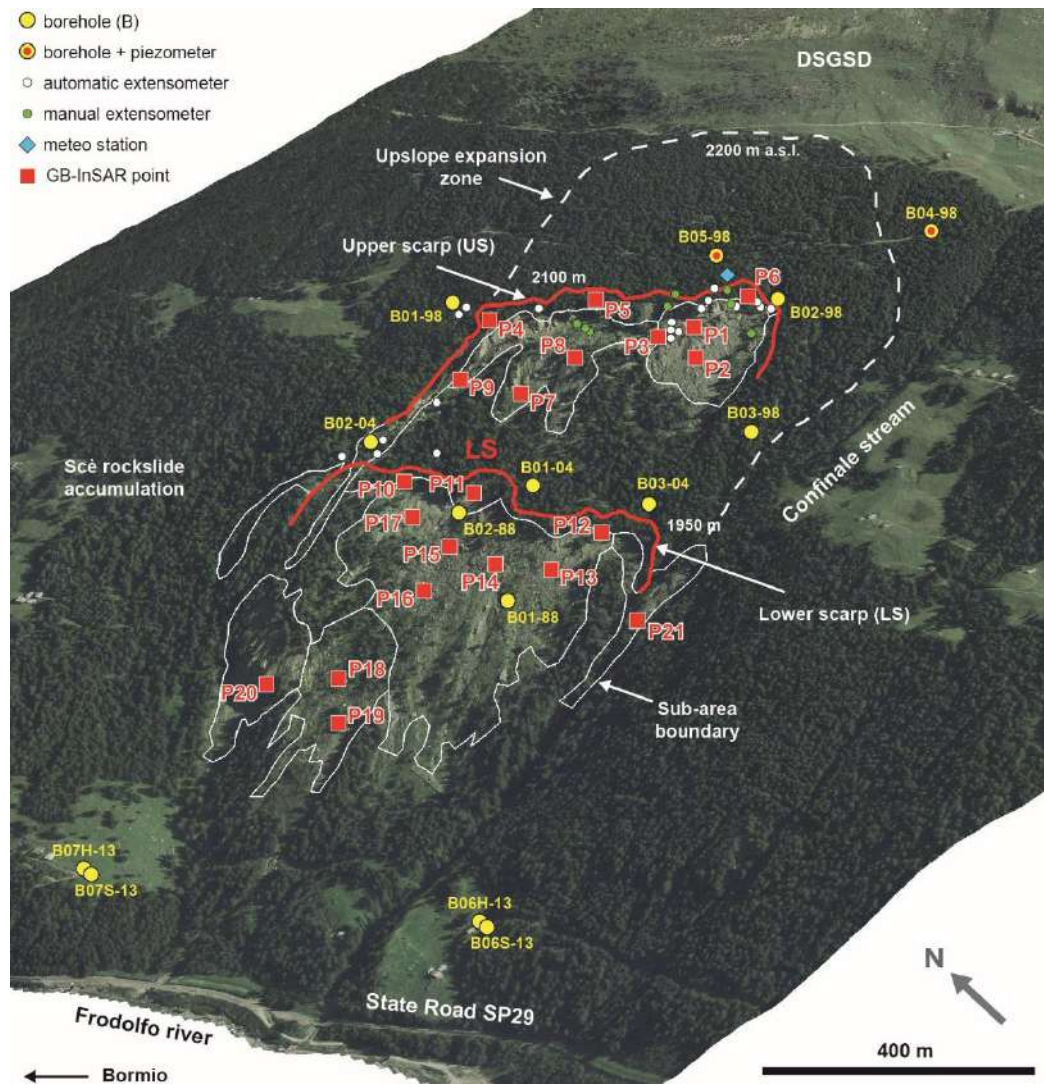


Figure 82 - 3D view of the Ruinon rockslide showing: the main morphological features and areas of possible rockslide upslope expansion (white dashed line); the location of boreholes; the layout of the ground-based monitoring network implemented since 1997; the location of GB-InSAR streaming points used for early warning (from Crosta et al., 2017).

Although first evidence dates to early 20<sup>th</sup> century, the rockslide is active since 1960, underwent instability in 1983, 1987, and entered a significant progressive stage between 1997 and 2003. This is also suggested by the evidence mapped on the aerial photo series (1954, 1976, 1982, 1997, 2000, 2003, 2007) available for the area.

The rapid evolution motivated the geotechnical site investigations carried out between 1988 and 2013. These included 14 boreholes (1988: LS area, up to 100 m long; 1998: US area, up to 120 m long; 2004: upslope of US, up to 100 m long; 2013: slope toe, up to 190 m long), several instrumented with inclinometers and standpipe piezometers. 10 boreholes provided fully-logged drill cores. Borehole information allowed constraining the complex geometry, kinematics and hydrology of the rockslide, the latter still remaining not fully resolved. The slope instability (Figure 82) consists of a compound rockslide affecting about 15 Mm<sup>3</sup> of phyllite and slope debris (including glacial and talus deposits, as well as debris produced by the degradation of the LS and US) along shear zones 30 to 70 m deep (Crosta, 1999; Agliardi et al., 2001; Crosta and Agliardi, 2003; Casagli et al., 2010). The slide toe (1700 m a.s.l.) is suspended above the valley floor (1450 m a.s.l.), in correspondence of an alignment of groundwater springs slightly changing in position with time. This daylighting of the failure surface above the valley bottom suggests a possible future evolution

into a rock avalanche in case of catastrophic failure. Morpho-structural evidence of upslope expansion suggests a total unstable volume potentially reaching up to 20 Mm<sup>3</sup>.

Rockslide is deep monitored since 1997 through a ground-based monitoring network that includes up to 25 wire extensometers, 17 GPS, optical targets and distometer baselines, plus 2 borehole inclinometers and a borehole multibase extensometers, and in recent years remote sensing techniques, as satellite (PS-InSAR® and SqueeSAR®), and as ground-based (GB-InSAR radar interferometry). Ground-based instrumentation, including a meteo station and automatic logging units, is spread over the rockslide, and clustered along the US and the LS (Figure 83). This monitoring network provides the longer and more continuous displacement time series for the rockslide (>17-year time period).

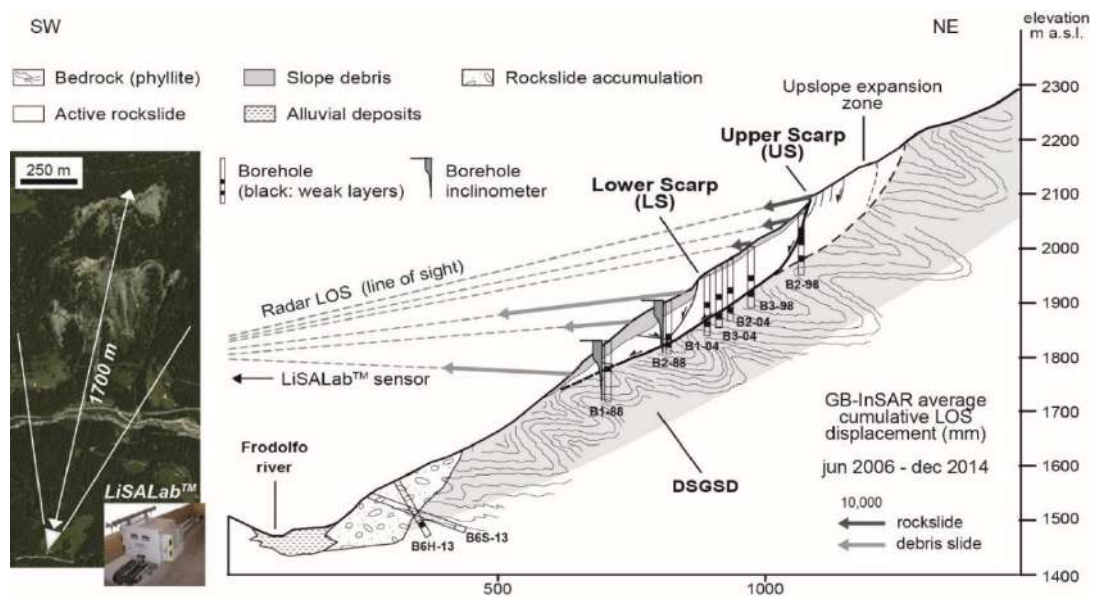


Figure 83 - Geological cross section (updated after Crosta and Agliardi, 2003) of the Ruinon rockslide, showing the main morphological features, rockslide shear surfaces, site investigations, and general distribution of the surface displacements recorded by the GB-InSAR system in the 2006-2014 period. The location and look angle of the GB-InSAR system is showed in the inset (from Crosta et al., 2017).

# EXPERIMENTAL TESTS

*Considering everything  
an experiment*

Conventional investigations of landslide mechanisms and behavior have relied heavily on conventional soil mechanics tests to evaluate the strength characteristics of the shear surface (Figure 84). These conventional tests largely include drained and undrained triaxial and direct shear tests to establish. Whilst these methods allow to assess the stability of the slope and the design of slope protection measures, their ability to allow interpretation of failure mechanisms is limited. This can often lead to inaccurate landslide models that may not be suitable to accurately assess landslide hazard potential. A major limitation of these methods is that conventional geotechnical tests initiate shear surface development by increasing deviator stress to failure at a constant displacement rate, whilst most landslide failures occur because of increasing pore pressures acting within the slope, which lead to a reduction in mean effective stress at approximately constant deviator stress or for slow progressive failure. It is also well established that the conventional geotechnical methods described above are weak at defining the true failure envelope in a slope (Zhu and Anderson, 1998, Orense et al., 2004).

A suite of detailed laboratory tests was undertaken (i) to determine the standard and advance physical and geotechnical characteristics of the materials within the shear zones of the Mont de La Saxe and Chervaz rockslides, and (ii) to simulate the conditions (e.g. pore-water pressure increase) that may occur in the landslide during failure. In the following, used experimental apparatus and the results are shown.

The physical properties were investigated through standard tests:

- ⇒ Grain-size distribution analyses
- ⇒ Consistency limits
- ⇒ Uniaxial compression tests;
- ⇒ Direct shear
- ⇒ Consolidated Drained and Undrained triaxial testing;

and:

- ⇒ 4 different types of test with DPRI #5 testing machine

which are defined as unconventional tests.

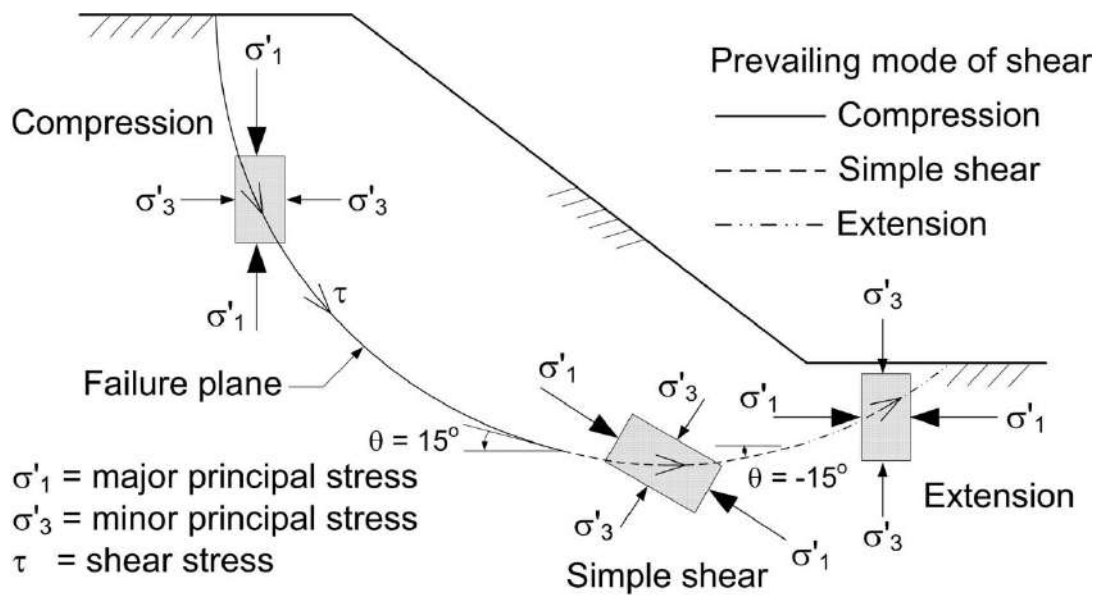


Figure 84 – Different stresses within a slope (modified after Bjerrum, 1973)



### 3.1 Shear zone sampling

Concerning Mont de La Saxe rockslide, twenty deep (70 m to 300 m) vertical and inclined boreholes have been drilled (between 2005 and 2015) at the site both within and outside landslide body. Drill cores showed a series of shear zones and fragile fracture zones (Crosta et al., 2014; Figure 85). The more superficial ones were characterized by abundant voids and intense rock oxidization, whereas the deeper present evidence of brittle deformation without flow folding structures typical of ductile syn-metamorphic deformation. The Rock Quality Designation (RQD) profiles show the presence of a thick (60-100 m) intensely fractured layer passing to a more compact bedrock. Brecciated levels were not frequent but intensely fractured material was found with a thickness ranging between few centimeters and some meters. Some samples have been collected at shear zones from centimeters to meters thick characterized by loose granular material (from silt to clay up to 90% with sand and gravel up to 22%) and intact rock. Polished and slicken-sided surfaces in dark black layers with graphitic appearance have been found. Being difficult to collect enough material to perform all the analyses on the same sample (e.g. for the LHV DPRI#5 ring shear test at least 2 kg of material  $\leq 2$  mm are requested for every test). Different samples have been used (see Table 2 for list of experimental tests) considering that they have the same mineralogical composition and belong to the same shear zone (Crosta et al. 2014).

The Chervaz samples (Figure 86) have been sampled from two different borehole cores, where two different shear zones were identified. The first more superficial one, located at about 23 m b.g.s., was characterized by highly fractured rock with sand filling. The considered basal shear zone was located at about 92 m b.g.s. and characterized by green schists reduced to powder (Figure 86). Unfortunately, was not possible to collect the amount of material (2 kg) necessary for perform both the ring shear test, and direct shear tests. Therefore, the priority was assigned to direct shear tests.

Furthermore, to characterize the rock before deformation (i.e. fine crushing), belonging to the same lithology of main shear zone, some intact material collected at about 104 m b.g.s. has been crushed.

Table 2 – List of tests performed on collected samples from Mont de La Saxe (LS) and Charvaz (CH) rockslides: FC: Force Control test, SSC: Shear Speed Control test and PWP: Pore-water Pressure test (USCS Soil Classification  $W_L$ : liquid limit,  $W_P$ : plastic limit; Direct Shear; Uniaxial; Triaxial: drained and undrained; Ring Shear test) and summarized parameters obtained by each test.

Sample #	Atterberg limits			Direct Shear		Uniaxial	Triaxial		Ring Shear LHV	
	USC S.C.	WL [%]	WP [%]	$\Phi_{peak}$ [°]	$\Phi_{res}$ [°]	$\sigma_c$ mean [MPa]	$\Phi_{res}$ [°]	$\Phi_{res}$ [°]	Type	$\Phi_{res}$ [°]
LS-01	-	-	-	-	-	-	-	-	FC	37.4
LS-02	-	-	-	-	-	-	-	-	SSC	-
LS-03	CL	27.8	16.8	22.1	18.4	-	-	32.5	-	-
LS-04	-	-	-	-	-	-	-	-	PWP	35.7
LS-05	CL	28.9	16.1	27.5	24.6	-	-	-	-	-
LS-06	-	-	-	-	-	-	34.1	-	-	-
LS-07	CL	26.2	11.1	-	-	-	-	-	-	-
LS-08	CL	22.4	9.1	-	-	-	-	-	-	-
LS-09	CL	21.0	11.1	-	-	-	-	-	-	-
LS-10	-	-	-	-	-	41.36	-	-	-	-
LS-11	-	-	-	-	-	-	-	-	FC	45.0
CH-1	-	-	-	24.8	19.6	-	-	-	-	-
CH-2	-	-	-	-	-	-	-	-	FC	40.3
CH-3	-	-	-	-	-	51.45	-	-	-	-



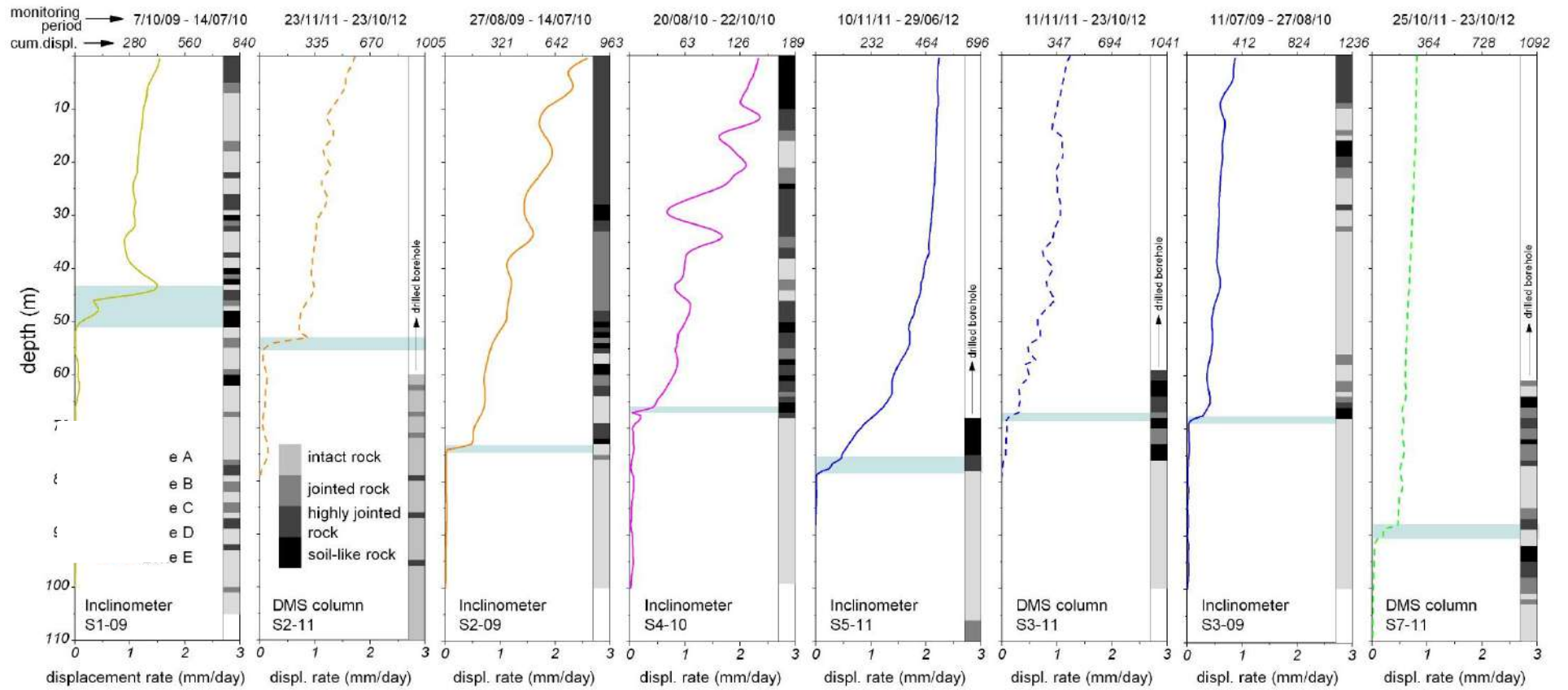


Figure 85 – Inclinator and DMS cumulative displacement plots and average displacement rate at different rockslide sectors for different total measuring intervals (see dates above each plot) compared with simplified fracture density logs. Percussion drilling intervals, main shear zone extent, and groundwater table levels are shown (modify after Crosta et al., 2014)



## **3.2 Mechanical Characterization**

### **3.2.1 Conventional geotechnical tests**

A detailed suite of standard soil classification tests was undertaken to establish the physical properties of the landslide materials at the basal shear zone. A certain number of samples was considered for each material sample collected from the two different case studies to assess physical variability in the samples collected at the site, and for grouping samples for their further testing which comprised particle-size analysis and consistency (Atterberg) limits for each core and box sample. Other mechanical properties were evaluated during uniaxial, triaxial and direct shear tests.

#### **3.2.1.1 Grain-size distribution and Consistency limits analyses**

Grain size analyses and the Atterberg limit tests followed the Standard ASTM procedures (ASTM D4318-17e1, 2017; ASTM D6913/D6913M-17, 2017). The finer fraction below 1000  $\mu\text{m}$  has been analyzed by means of a laser diffraction granulometry (Mastersizer 2000, Malvern Instruments Ltd.) with dispersion unit, configured for particle sizes in the 0.02 to 2000  $\mu\text{m}$  range.

#### **3.2.1.2 Standard uniaxial compression test**

The uniaxial compression tests follow the ASTM D7012. Different specimen dimensions were adopted, and 6 different tests were completed. One sample was from Mont de La Saxe rockslide and one from Chervaz rockslide. The schistosity of Mont de La Saxe samples, was aligned along the axial stress direction (Figure 90). Whereas Chervaz samples do not show a marked schistosity (Figure 91).

#### **3.2.1.3 Direct Shear tests**

The 60 mm square samples were prepared and sheared in wet and drained conditions, respectively. The state of compaction of the sample was monitored by measuring sample height up to the required initial density was achieved. Each sample was tested at three different normal loads (200 – 400 - 600 kPa) and for six shear cycles using shear rates of 8  $\mu\text{m}/\text{min}$  for a first shearing, followed by four cycles at 40  $\mu\text{m}/\text{min}$  and by a final cycle at 20  $\mu\text{m}/\text{min}$  (ASTM D3080).

#### **3.2.1.4 Standard triaxial test**

Drained and undrained triaxial tests (CU and CD) have been performed following the ASTM standards (D4767-11 and D7181-11) at confining pressures of 800 kPa, 1400 kPa and 2000 kPa and a strain rate  $6.6 \cdot 10^{-5} \text{ s}^{-1}$  which was sufficiently high to avoid creep phenomena that have been investigated in the LHV ring shear tests.

### **3.2.2 Unconventional tests: Ring Shear Apparatus (RSA)**

The ring shear apparatus has been widely used to measure the residual shear strength of soils (Bishop et al., 1971; Sassa et al., 2003; Wang and Sassa, 2004; Wang et al., 2010). In this work we used the DPRI-5 (Disaster Prevention Research Institute) ring shear apparatus (Sassa, 1997; Sassa et al., 2003) because it allows to investigate the residual shear strength along the sliding surface from Low to High Shear Velocities (LHV). The apparatus is composed by: (i) a shear box (inner diameter: 120 mm, outer diameter: 180 mm, shear area: 141  $\text{cm}^2$ ) divided in two superposed parts separated by a rubber edge, (ii) a loading platen to apply the normal stress ( $\sigma_n$ ) and (iii) a torque-controlled servo-

motor (automatically controlled by a servo-amplifier) to apply the shear stress ( $\tau$ ). Due to the imposed kinematic condition, the shear surface is constrained to develop at the plane dividing the shear box.

The gap between the upper and bottom parts of the shear box controls the rubber-edge friction and it is set by imposing a no water leakage condition. In our tests this condition was reached for a gap value of 0.439 mm. During the tests, the shear resistance acting on the shear surface is monitored by two load cells considering the rubber-edge friction (usually around 15-20 kPa). A small rubber-edge friction is preferable, and during our tests was maintained at about 17-18 kPa. Furthermore, the pore pressure, vertical displacement and shear displacements were measured. Pore water pressure transducers are connected to a gutter extending along the entire circumference of the inner wall of the outer ring in the upper box half. The gutter extends about 2 mm above the imposed shearing plane assuring durability against shearing and sensitivity to pore water pressure changes. The shear speed can range between 0.001 and over 200 cm/s and the maximum normal stress is about 1000 kPa for long-time tests.

The sample preparation was constituted by in three phases: (i) deposition, (ii) saturation and (iii) consolidation. The dry deposition method (Ishihara, 1993) was used with fraction finer than 2 mm). To create a normally consolidated state the layers were not tamped. The samples were successively saturated with the help of carbon dioxide ( $\text{CO}_2$ ) and de-aired water. This process took about half a day according to the nature of the samples. The degree of saturation was checked by using the BD parameter (Sassa, 1988) who extends the B-value usually employed in TXD and TXU (Skempton and Bishop, 1954) to the ring shear apparatus.

To achieve the characterization of the residual shear behavior and to check the effect of different controlling variables, three types of test were performed:

1. **Force Control test (FC)**, investigates the material creep behavior during the shear zone evolution in time. After the consolidation phase, the normal stress was kept constant with the same value used during the consolidation (i.e. 600 kPa) while the tangential stress follows an history characterized by a set of steps of 50 and 100 KPa increments from the first step considering the rubber friction which requires an additional increment of about 17-18 kPa. The first test conducted on Mont de La Saxe sample consisted of 9 steps till the failure stage, which occurred at a 459 kPa tangential stress, followed by a stage with imposed tangential velocity to evaluate the post-failure behavior. The same test was performed using 100 KPa increments with 5 different steps with a rubber friction of 18 KPa, and the gap value equal to 0.285 mm. For the Chervaz sample, the failure occurred at 509 kPa for Chervaz sample. Concerning Mont de La Saxe sample, the failure occurred at 600.9 kPa.

During both tests the transition from a step and to the subsequent one, the tangential stress is incremented at constant velocity of 0.084 kPa/s. The transition is completed only when the steady-state condition was reached for that loading step. The tangential and normal displacements were measured during the experiment.

2. **Shear Speed Control test (SSC)**, in which the normal stress was kept constant at 600 kPa while the tangential velocity was imposed and varied according to a prefixed history (from 0.004 to 0.008 mm/s with an incremental variation of 0.001 mm/s) under drained conditions. During the test, the tangential force was monitored because the target of this type of test consists in evaluating the material degradation process occurring at constant velocity due to the increasing permanent strain.

3. **Pore Water Pressure Control test (PWPC)**, where the pore pressure was progressively increased, under undrained condition, while the tangential stress and the total normal stress were kept constant and equal to 300 kPa and 600 kPa, respectively. The key feature consists of increasing pore-water pressure within a soil sample at constant total normal stress and constant shear stress. This testing procedure replicates the most realistic field conditions for most of the rainfall and groundwater induced landslides.

4. **Aging Test (AT)**, gives a deep insight into the material strength increment after a rest period. The test simulates in-situ condition when periods of movement are cyclically followed by rest periods. To achieve this goal, a sudden increment of shearing until failure and a following period of rest were repeated for 5 or 6 times. From the experimental data, it is possible to derive the material strength for every cycle of activation and rest. This kind of tests were performed just after the FC tests completion to simulate the in-situ conditions. At rest periods lasted about 24 hours.

Table 3 - List of the type of control, the variable and time test duration for the tests performed in the LHV DPRI#5 ring shear apparatus.

Test Type	Controlled variable	Variable increment	Imposed variable [kPa]	Test duration [s]
FC	Tangential stress increment; tangential velocity	50 kPa and 100 kPa; 0.084 kPa/s	$\sigma_n = 600$ ; $u = 0.0$	$1.4 \cdot 10^6 - \approx 13 \cdot 10^5$
SSC	Tangential velocity	0.001 cm/s steps from 0.004 to 0.008 cm/s	$\sigma_n = 600$ ; $u = 0.0$	$6.0 \cdot 10^4$
PWPC	Pore water pressure	0.005 kPa/s	$\sigma_n = 600$ ; $\tau = 300$	$2.0 \cdot 10^4$
AT	Tangential velocity	0.001 cm/s	$\sigma_n = 600$ ; $u = 0.0$	$3.5 \cdot 10^5 - 5 \cdot 10^5$

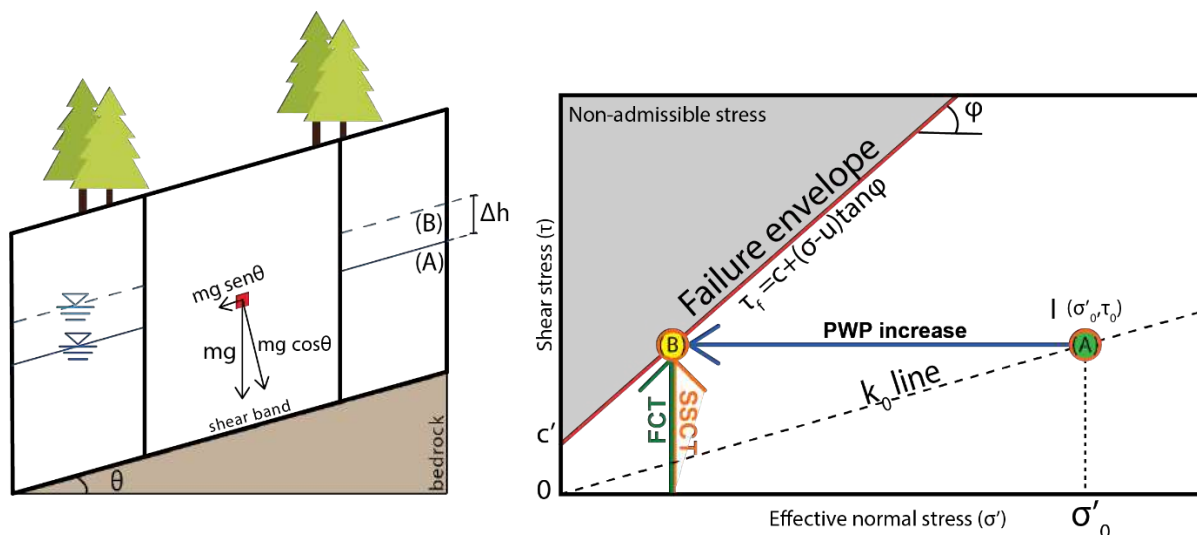


Figure 87 - illustration of in-situ stress conditions in a slope (on left) and stress paths with Mohr-Coulomb Failure envelope during the tests performed on Ring Shear Apparatus (on right). The orange and green arrows represent the stress path during the FC and SSC tests until reach the failure (point B). While, the point A represents the in-situ tensional state of specimen before the PWPC test, and the blue horizontal arrow represents the stress path for PWP increment until the failure (point B).



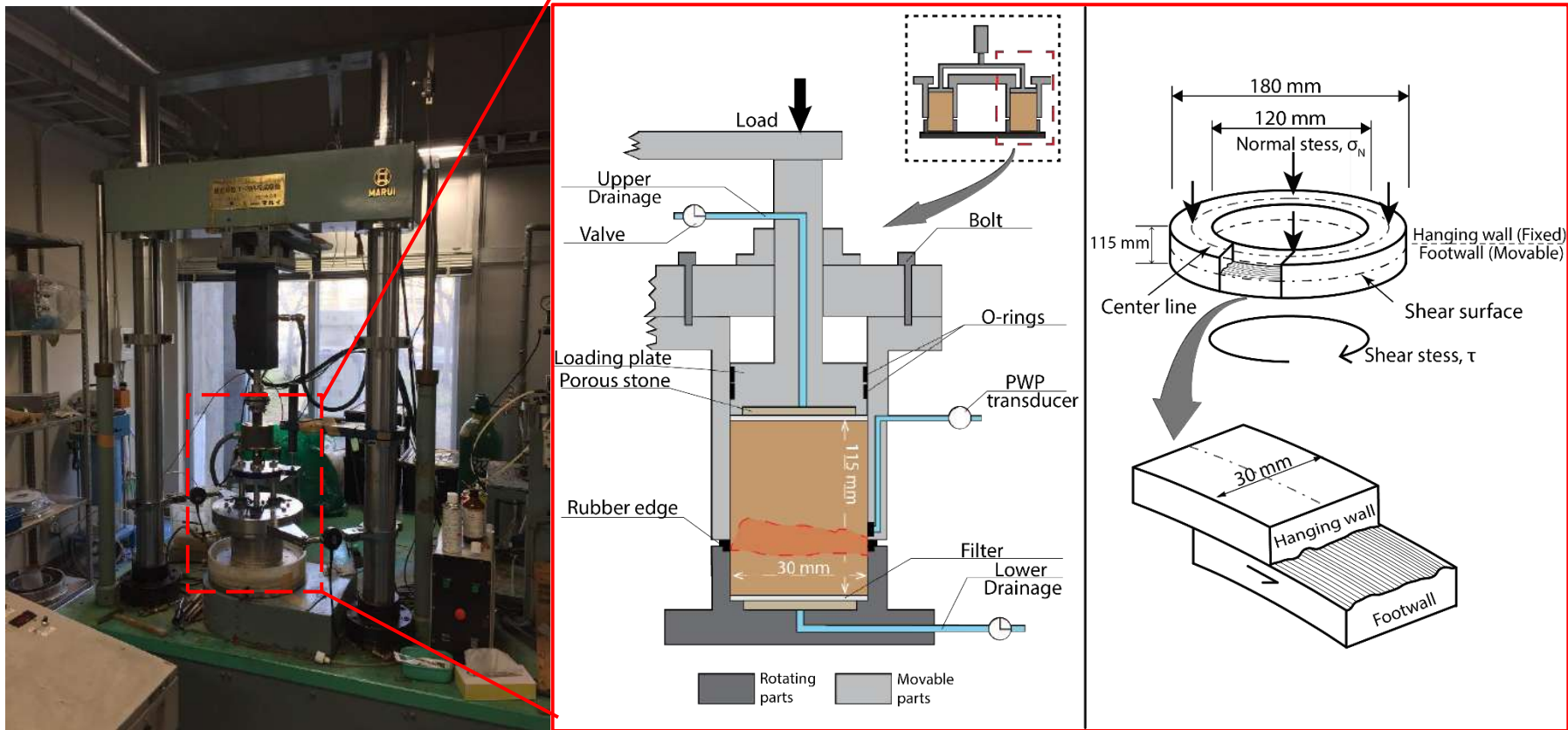


Figure 88 – Photo of the testing machine, schematic section of DPRI-5 ring shear apparatus and sample representation with geometrical size values (modified after Sassa, 1997).



### 3.3 Results

#### 3.3.1 Grain Size Distribution and Consistency limits

Five specimens for the Mont de La Saxe rockslide, from different boreholes and different depths were used to evaluate the grain-size distribution and the Atterberg limits (Figure 85). Fine portion ( $\leq 2$  mm) of all the samples are classified as CL soils suggesting a relative homogeneity of the lithology and comminution of the material in the shear zones. Regarding Chervaz rockslide it has not been possible to evaluate the consistency limits.

The Mont de la Saxe samples contain up to 90% in weight of fines (clay and silt) and up to 22% of sand (Figure 89).

The area between the pre- and post-shear grain-size curves was computed for each different interval of diameters as a measure of grain-size reduction (GSR) (Figure 89). The results refer only to the material from the shear bands. In the FC test, no significant GSR was observed in comparison to the other tests. For SSC test, a remarkable grain size reduction was observed for large diameters due to the comminution while for small diameters it tended to reduce. Indeed, the SSC sample was subjected to a complete sharing cycle for each stage while in the Force Control test the apparatus was stopped after an initial shear failure.

On the contrary, the PWPC test reveals an increment of particles with large diameters. This phenomenon could be explained by the fine particle migration from the shear band to the surrounding zones by water seepage and suffusion due to the increment of pore pressure.

The samples contain up to 90% in weight of fines (clay and silt), and up to 22% for sand. After shearing, the particle size of the material located in the shear band, was reduced up to 1 % (Figure 89).

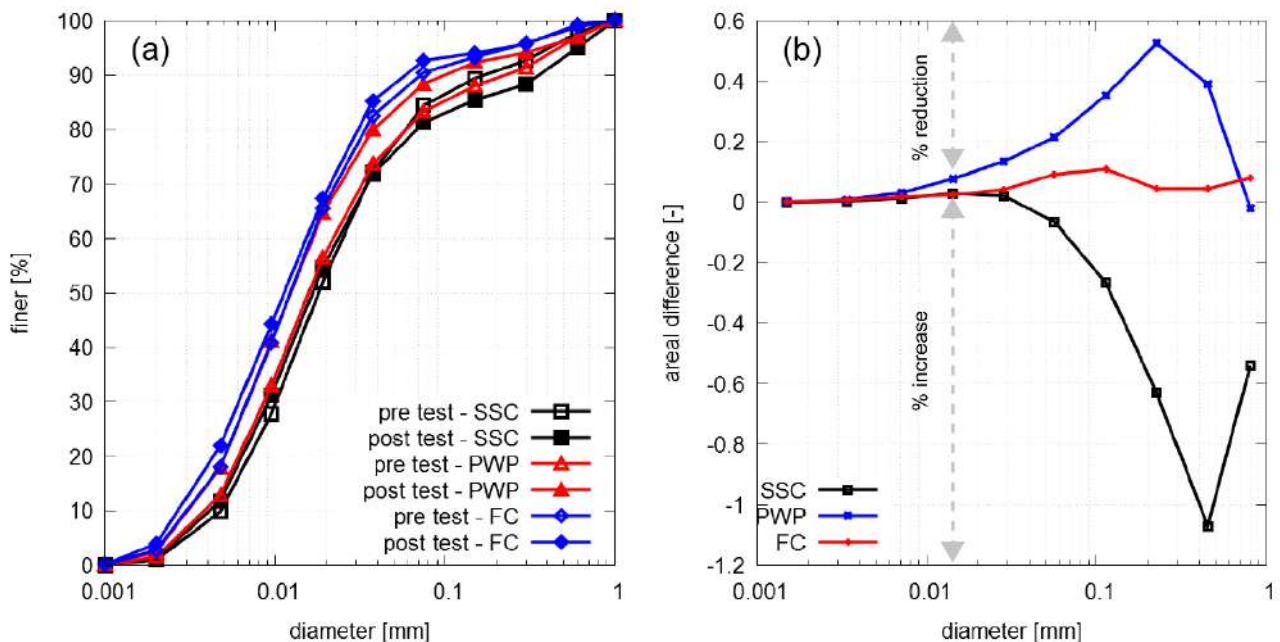


Figure 89 - Pre-shearing and post-shearing grain size curves for: FC test, SSC test and PWPC test. Continuous line before shearing Dashed line after shearing; (b) difference in terms of area between the pre- and post-shear test grain-size curves.

### 3.3.2 Uniaxial compression tests

The uniaxial tests, performed on three samples coming from the Mont de La Saxe (Figure 90) and the Chervaz (Figure 91) landslides, reached a maximum stress value of 44.50 and 58.57 MPa. The related Young module is quantified in 7948,53 and 7000 MPa. The initial values of 22 MPa represent the pre-load of testing machine.

Samples after failure reveals two different modes of rupture: the specimens from Mont de La Saxe, are characterized by schistosity planes where the cracks propagate: so that multi failure planes are observed. In contrast, the Chervaz samples do not present marked weak planes and consequently their failure mechanisms are typically characterized by a well-defined shear plane.

Furthermore, the stresses at failure are more homogenous for samples of the Mont de La Saxe (with a range of 5.0 MPa) rather than the Chervaz (with a range of 14 MPa).

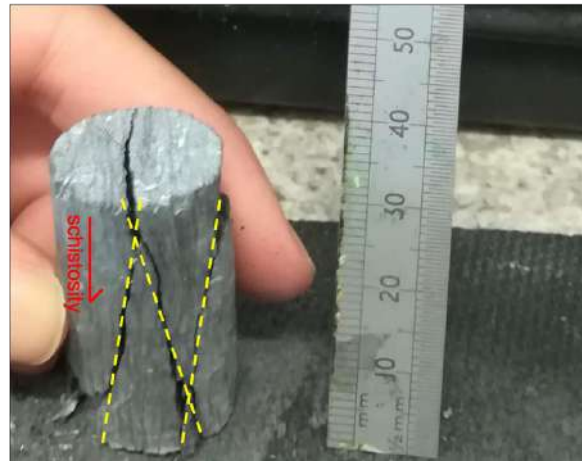
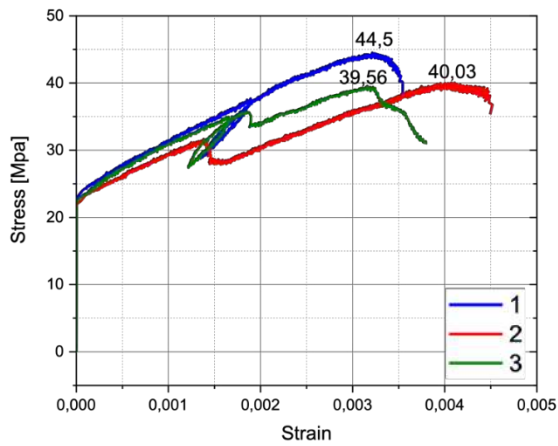


Figure 90 – Mont de La Saxe uniaxial compression test results (on left); sample after failure (on right) with failure planes and schistosity

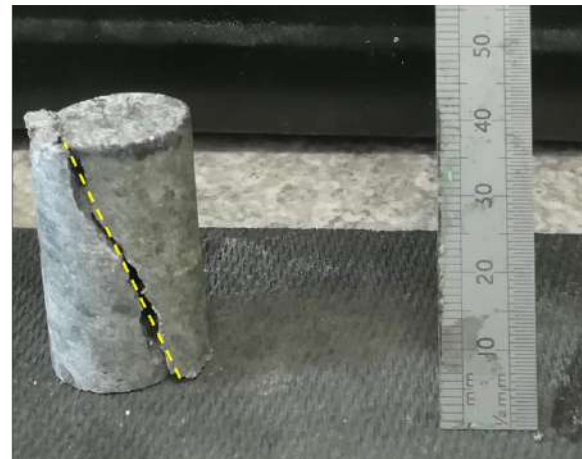
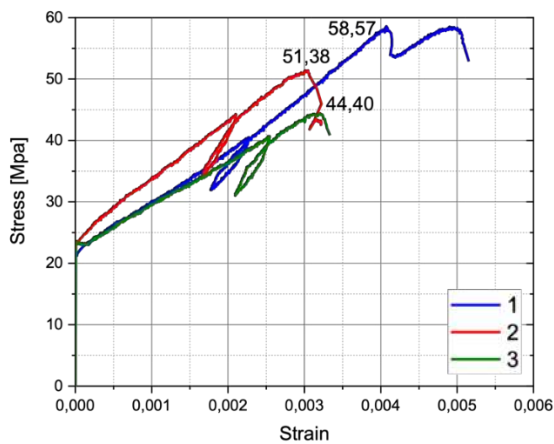


Figure 91 – Chervaz uniaxial compression test results (on left); sample after failure (on right) with failure planes

### 3.3.3 Standard triaxial and direct shear tests

Drained triaxial tests (Figure 92), performed at 800 kPa, 1400 kPa and 2000 kPa under a constant strain rate of  $6.6 \cdot 10^{-5} \text{ s}^{-1}$ , show an expected monotonic increment in the deviatoric stress up to peak (2090 kPa, 3672 kPa and 5333 kPa) for every confining pressure. The stress paths (Figure 92b) show an envelope with friction angle of  $34.1^\circ$ . A volume reduction is observed for all samples (Figure 92a).

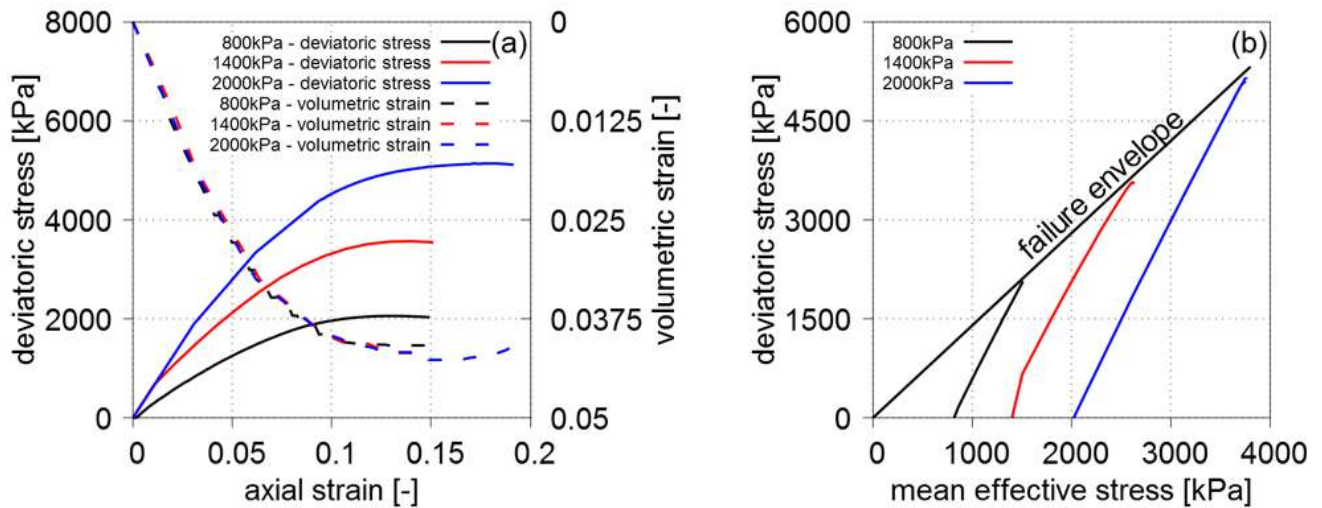


Figure 92 - Drained Triaxial tests results at 800 kPa, 1400 kPa and 2000 kPa of confining pressure: (a) axial strain versus deviatoric stress and volumetric strain as a function of axial strain; (b) stress-path with Mohr-Coulomb failure envelope

The undrained triaxial tests (Figure 93) shows trends quite similar to the drained results and a friction angle is  $32.5^\circ$ , slightly smaller than in drained tests. In both drained and undrained tests there is no clear evidence of viscous behavior (creep).

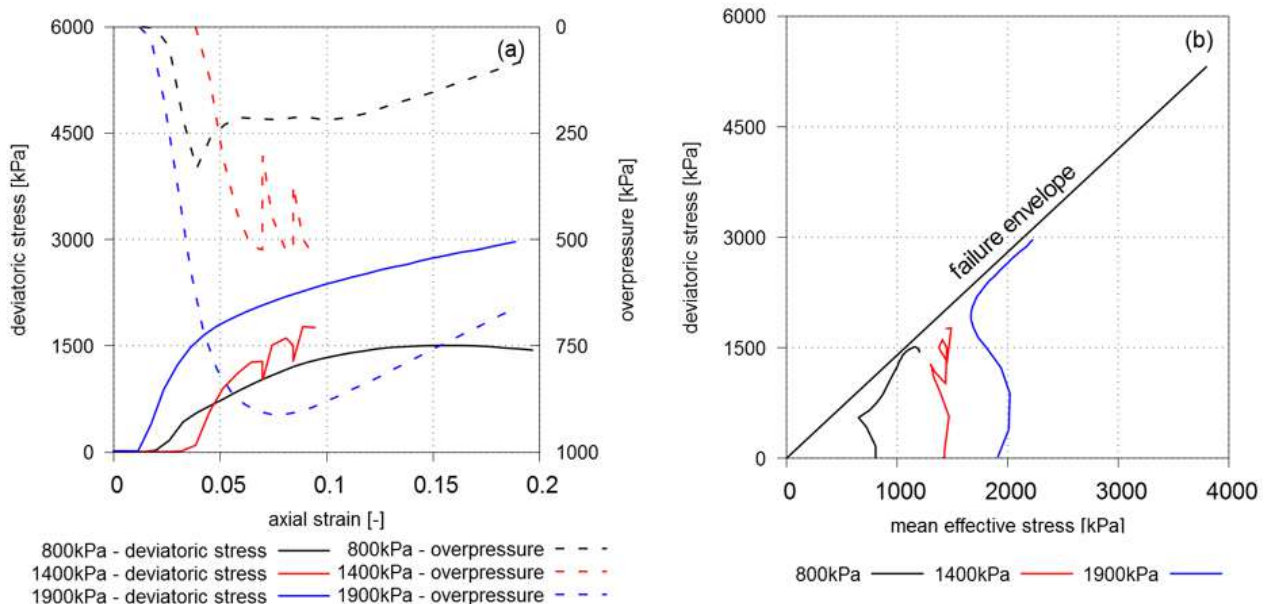


Figure 93 - Undrained Triaxial tests results at 800 kPa, 1400 kPa and 1900 kPa confining pressures: (a) axial strain versus deviatoric stress and volumetric strain as a function of axial strain; (b) stress-path with Mohr-Coulomb failure envelope obtained considering the drained triaxial tests.

Results of direct shear tests on two different samples show a peak friction angle between 22.1° and 27.5°, and residual values between 18.4° and 24.6° with zero cohesion for Mont de La Saxe samples (Figure 94).

Concerning the Chervaz rockslide, the results of direct shear tests shows a peak friction angle of 24.8° and a residual value of 19.6° with zero cohesion.

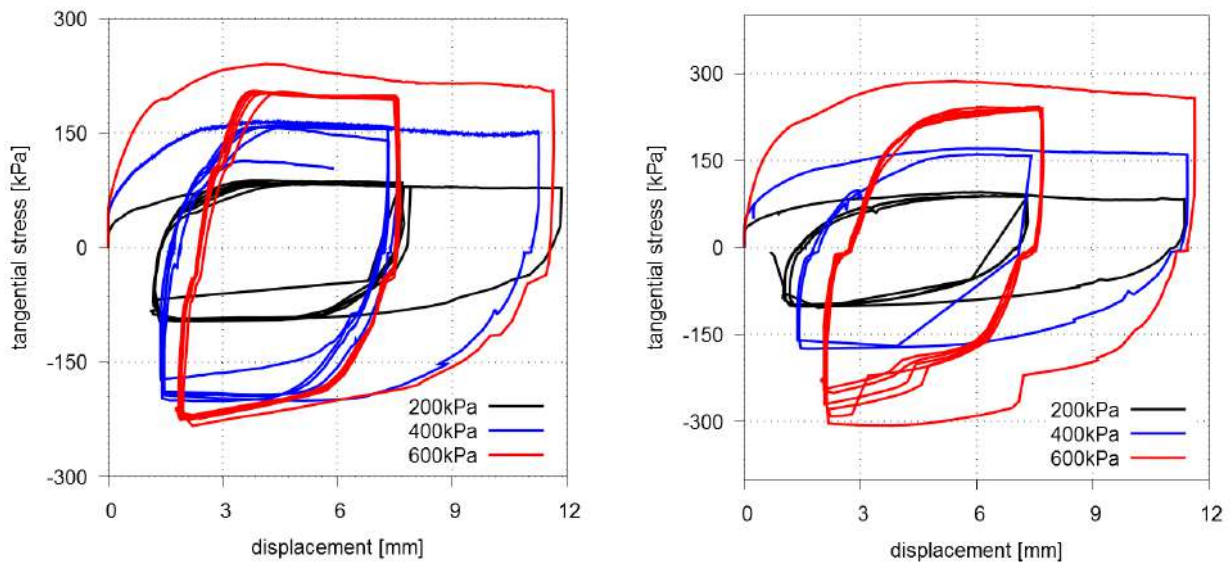


Figure 94 - Results of Direct Shear tests of samples S5-2011 (76.6 – 77 m) from Mont de La Saxe rockslide (on left) and samples from Chervaz rockslide (on right), with three different loads: 200, 400 and 600 kPa.

### 3.3.4 Force Control test

Because of the imposed kinematics, slickensides and striae on the shear plane point to the sense of motion (Figure 95a). In the samples, the shear zone is located slightly below the imposed shear plane and its thickness slightly reduces moving from the outer to the inner boundary (Figure 95b). This effect might be induced by the external boundary conditions or by the position of the drainage system or the different shear displacement. After failure, the tangential stress varies because it is not imposed. The increments for both displacement components (Figure 95b) follow the steps in tangential stress with a strong increment at the transition between subsequent steps and a slight increment during the constant stress phase. During each stage, where the tangential stress is constant, shear velocity is around  $4.0 \cdot 10^{-3}$  m/s and it is due to creep. Therefore, the tangential and normal displacements are characterized by two stages: an instantaneous increment and a creep phase.

In order to evaluate the effect of the incremental step, another force control test has been carried out by imposing 100 kPa increments. The mechanical response, expressed in terms of tangential and normal displacements (Figure 95), is similar to the previous test suggesting that the incremental stress step does not affect the general behavior.

Furthermore, despite of the increment of the tangential force (or equivalently the tangential stress) is constant during each test stage, the incremental tangential displacement observed before the steady state increases progressively, the last displacement increment being five and seven times of the initial displacement increment for first (50 kPa) and second (100 kPa) tests, respectively.



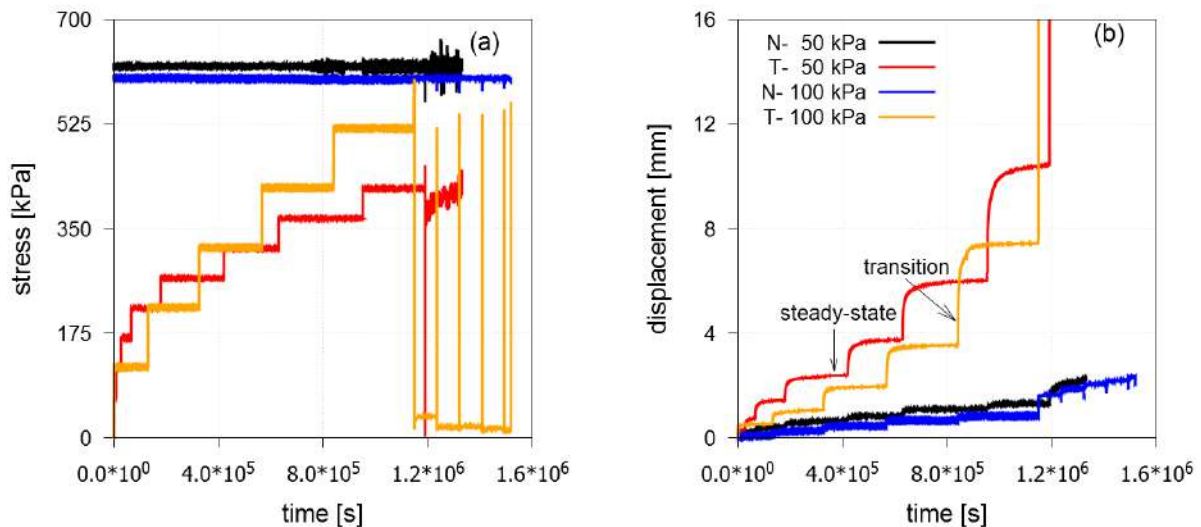


Figure 95 – FC and Aging tests results for 50 kPa and 100 kPa steps in tangential stress for Mont de La Saxe samples: (a) normal (N) and tangential (T) effective stress versus time; (b) normal and tangential displacement versus time.

The test with 100 kPa steps has been performed also with the Chervaz rockslide sample. The obtained results show a general trend similar to the same test performed with Mont de La Saxe sample, from qualitative point of view. The displacement measured during the transition phases, comparing first and last steps, is greater six times the initial value.

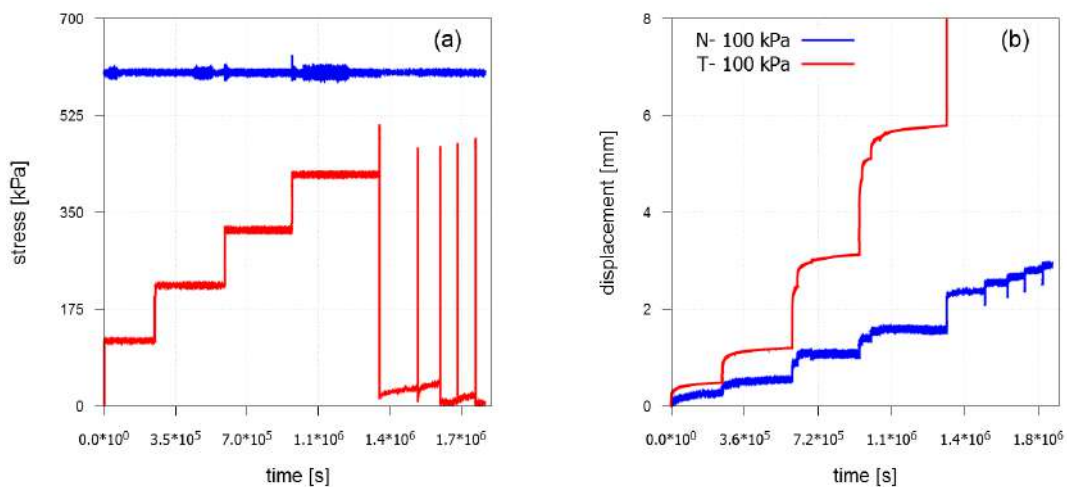


Figure 96 - FC and Aging tests results for 100 kPa steps in tangential stress for Chervaz samples: (a) normal (N) and tangential (T) effective stress versus time; (b) normal and tangential displacement versus time.

### 3.3.5 Shear Speed test

This test was performed under constant normal stress, in drained condition at a normal stress of 600 kPa (Figure 97a). The tangential velocity was imposed (Figure 97b) equal to 0.003 cm/s from 0 s to 22,375 s (first stage), 0.008 cm/s from 22,376 s to 31,115 s (second stage) and 0.004 cm/s from 31,116 s to 46,815 s (third stage) and finally, 0.006 cm/s from 46,816 s to 53,111 s (fourth stage). The tangential stress showed (Figure 97a) an increase and a sudden peak, then its value slightly increased with some oscillations confirming the previously mentioned hardening behavior. The normal displacement (Figure 97b; red curve) increased continuously despite the tangential velocity (Figure 97b; black curve) increased or decreased.

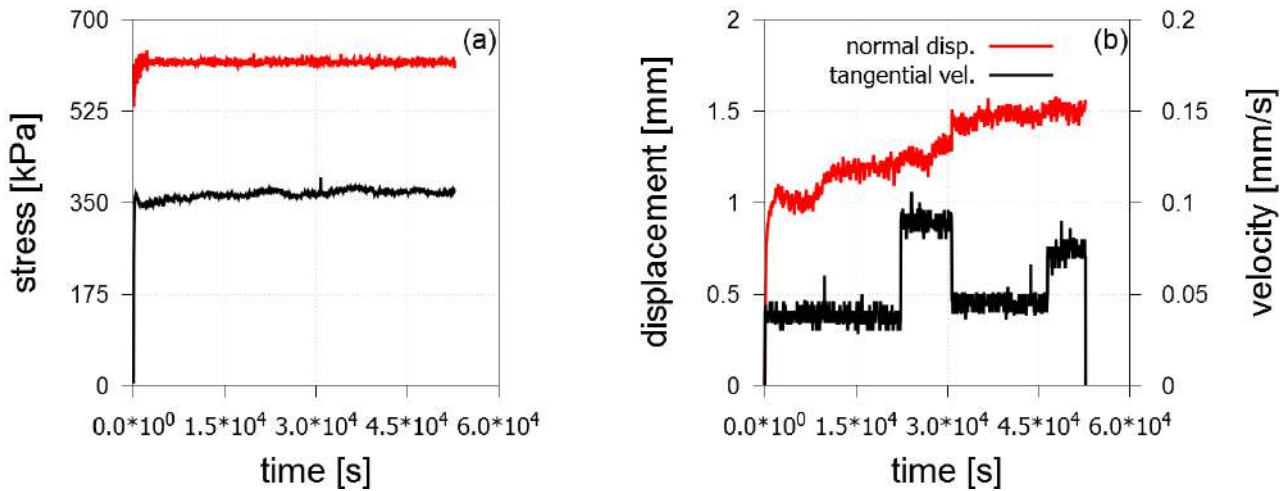


Figure 97 - SSC test results: (a) normal and tangential effective stress versus time; (b) the normal displacement and tangential velocity versus time.

### 3.3.6 Pore-Water Pressure Control test

In this test the sample was saturated ( $B_D > 0.98$ ) and then consolidated up to a normal stress of 600 kPa (Figure 98a). Then the tangential stress was increased to 350 kPa and kept constant while the PWP was gradually increased at a rate of  $\Delta u = 0.005$  kPa/s under undrained conditions (Figure 98a). The normal displacement during the test (Figure 98b) was lower than in other tests because of the imposed boundary condition (i.e. undrained) making the variation of normal displacement negligible. On the contrary, the tangential displacement (Figure 98b) had an initial sudden increment due to the tangential stress increment and a subsequent gradual increase with the PWP. This demonstrates the sensitivity of the velocity along the shear zone to the pore-water pressure oscillations. In the final stage of the test, the velocity increased abruptly up to failure. The tangential stress which was constant during the test, suddenly decreased during the failure stage (Figure 98a). This means that at failure there is loss of controllability of the test corresponding in nature to the landslide collapse (i.e. the equilibrium conditions are not satisfied anymore). The normal effective stress (Figure 98a) reduced during the test due to the increment of the PWP until failure when a sudden increment was recorded (Figure 99).



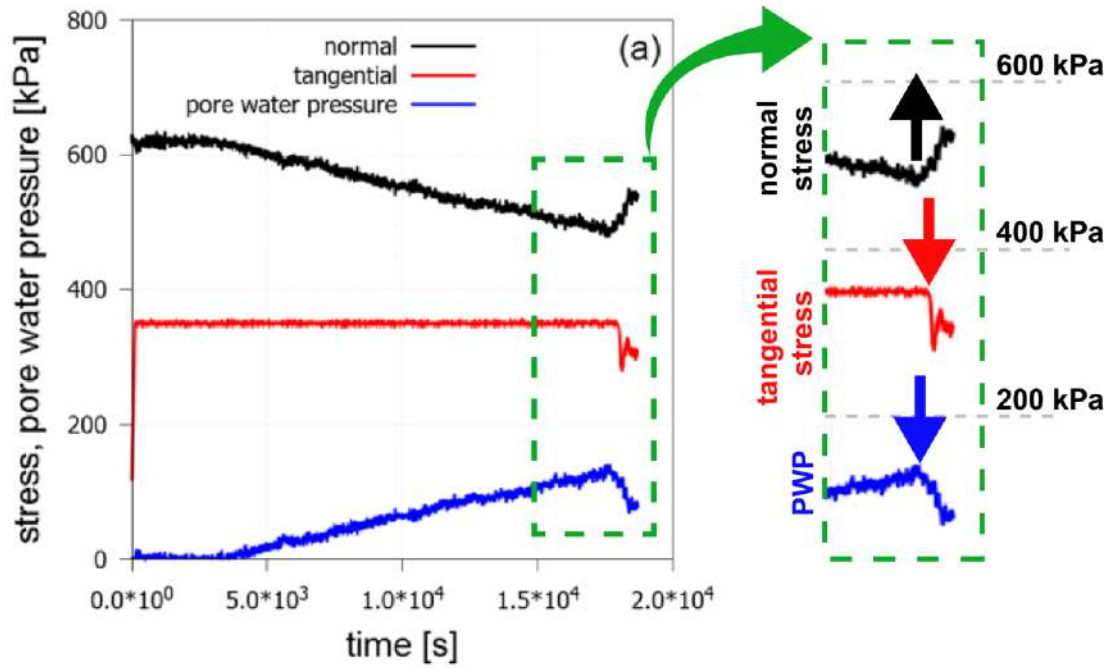


Figure 98 - PWPC test results: normal and tangential effective stress and pore water pressure versus time and zoomed window

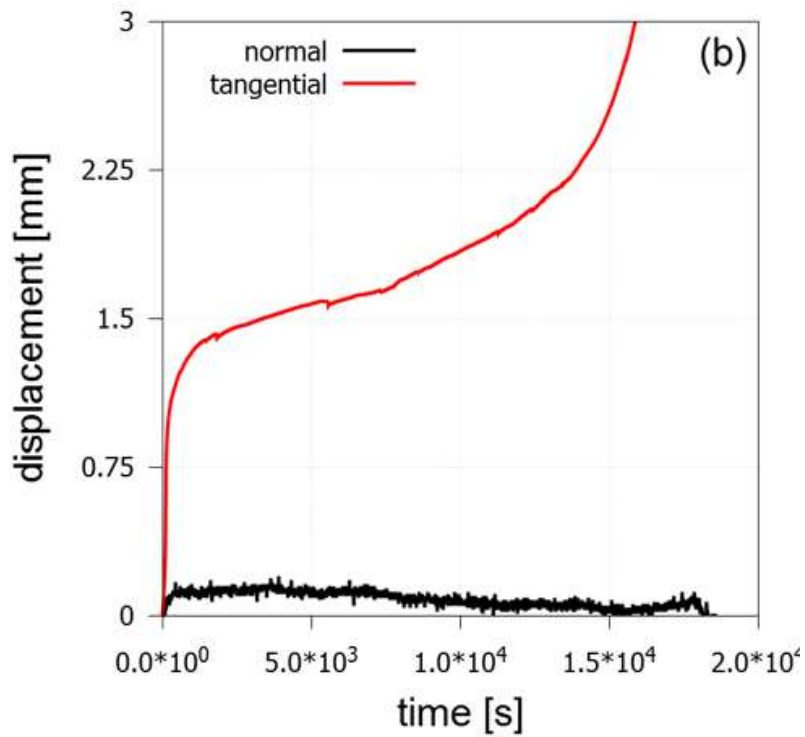


Figure 99 - PWPC test results: (b) normal and tangential displacements versus time.

### 3.3.7 Aging test

The results obtained for the Mont de La Saxe and the Chervaz rockslide are quite similar. Concerning Mont de La Saxe, after the failure FC test happened at 600 kPa of tangential stress, the first stage of aging test showed a significant decrement of about 9% in friction angle values. In the followed step, the general trend show hardening with a maximum increment of friction angle quantified in about 5.6% at the last stage of this test.

Table 4 – data from Aging test for Mont de La Saxe rockslide sample.  $\tau$ : shear stress;  $\phi_p$ : peak friction angle;  $\sigma$ : normal stress

Mont de La Saxe				
$\tau$	$\sigma$	$\tau/\sigma$	$\phi_p$	Note
600.9	600	1.00	45.0	end of FC test
519.95	600	0.87	40.9	Stage I
542.86	600	0.90	42.1	Stage II
541.57	600	0.90	42.2	Stage III
550.30	600	0.92	42.5	Stage IV
563.14	600	0.94	43.2	Stage V

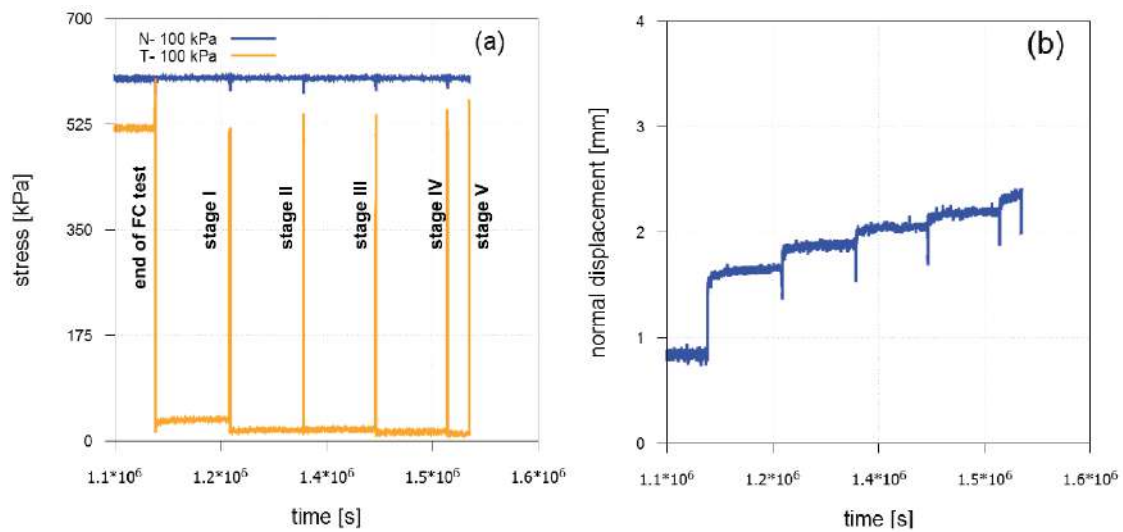


Figure 100 – Results of Aging test for Mont de La Saxe sample, after the first failure at about 600 kPa, the general trend is to hardening behavior with an increasing of shear resistance. (a) normal (N) and tangential (T) effective stress versus time; (b) normal displacement versus time for aging test

## Mont de La Saxe

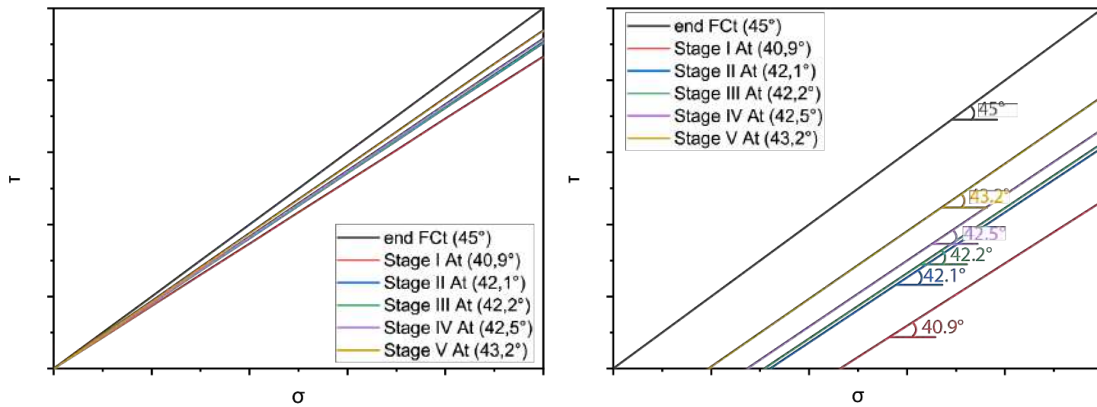


Figure 101 - The response of material for each failure cycle on the peak shear resistance (Mont de La Saxe sample)

Considering data from Chervaz sample, the friction angle at first stage of aging test had a decrement of about 5.3% if compared with the peak friction angle obtained during FC test. In the successive steps, the general trend showed a slightly hardening behavior if compared with the Mont de La Saxe data, with a maximum increment of friction angle quantified in about 2.7%.

Table 5 - data from Aging test for Chervaz rockslide sample.  $\tau$ : shear stress;  $\phi_p$ : peak friction angle;  $\sigma$ : normal stress

Chervaz				
$\tau$	$\sigma$	$\tau/\sigma$	$\phi_p$	Note
509.29	600	0.85	40.3	end of FC test
467.7	600	0.78	37.9	Stage I
469.97	600	0.78	38.1	Stage II
475.12	600	0.79	38.4	Stage III
484.94	600	0.81	38.9	Stage IV

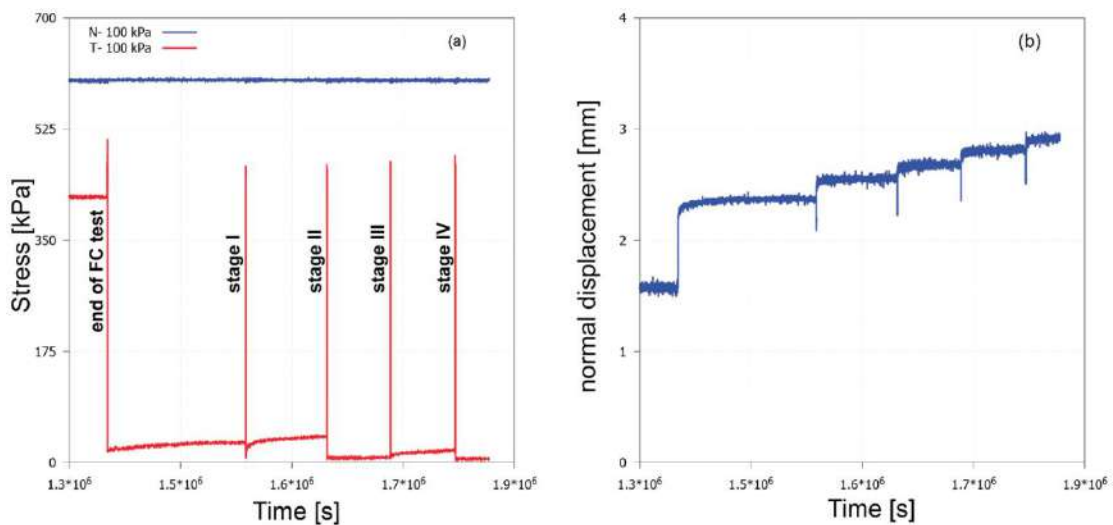


Figure 102 - Results of Aging test for Chervaz sample, after the first failure at about 600 kPa, the general trend is to hardening behavior with an increasing of shear resistance. (a) normal (N) and tangential (T) effective stress versus time; (b) normal and displacement versus time for aging test.

# Chervaz

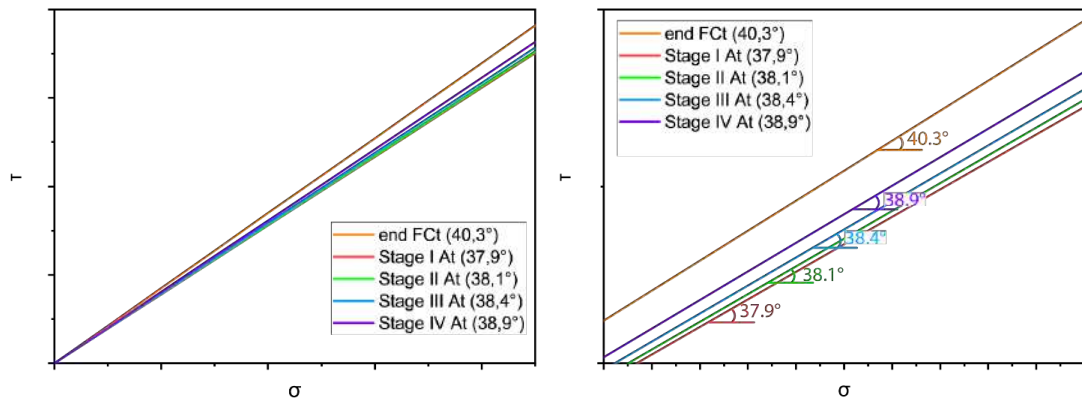


Figure 103 - The response of material for each failure cycle on the peak shear resistance (Chervaz sample)

### 3.4 Discussion

As highlighted by the uniaxial compression test on intact material, the presence of preferential failure plane (due to the original material schistosity) can influence the failure mechanism and thus the formation of slip surface. Generally, anisotropic and foliated rocks such as slates, schists and phyllites, whose behavior is dominated by closely spaced planes of weakness, cleavage or schistosity, present difficulties in the determination of the uniaxial compressive strengths. The uniaxial compressive strength (UCS) depending upon the direction of loading (Salcedo, 1983). Evidence of this behavior suggests that the rock mass properties are dependent upon the strength parallel to schistosity rather than that normal to it (Autio et al., 2000). In our tests, the Mont de La Saxe sample (Figure 90) shown a marked schistosity (probably due to phyllosilicates) while Chervaz was not affected by significantly weakness planes (Figure 91). The UCS for Mont de La Saxe samples was lower than Chervaz samples, considering that mineral composition, grain size, grade of metamorphism and tectonic history all play a role in determining the characteristics of the rock mass (Hoek & Brown, 1997).

The standard triaxial test results confirm that shear band material reached the completely degraded state with no further strength reduction. This is confirmed by the SEM analyses (see section 4.2.2) which show a preferred alignment of the platy minerals. This alignment generates micro-shear zones surrounded by graphite patches which contribute to the friction reduction. The observed compacting behavior could be explained by reduction of the inter-particle spacing due to platy minerals alignment.

Different authors (e.g. Angeli et al., 1996, Corominas et al., 2005; Ranalli et al., 2010; Di Maio et al., 2013; Schulz et al., 2018) investigated landslide movements revealing that observed displacements cannot be interpreted and simulated considering only equilibrium but material viscosity is required.

The new types of test carried out with the DPRI#5 apparatus have been designed to quantify the material creep characteristics and the material behavior with time after failure. The results point out that displacement rate at steady-state does not depend on the accumulated damage. This is an innovative result when compared with previous works and experiments with the same type of apparatus. Differently from previous works (Sassa et al., 2003; Sassa et al., 2004, Wang et al., 2007; Wang et al., 2010), where the shear rate ranged from less of  $1 \text{ cm}\cdot\text{min}^{-1}$  to more than  $200 \text{ cm}\cdot\text{s}^{-1}$ , in our tests velocity was the minimum allowed by the apparatus ( $0.001 \text{ cm}\cdot\text{s}^{-1}$ ). This choice was formulated to simulate the slow movement observed during initial evolution of a rockslides. In order to simulate the effect of pore-water pressure increase on slope stability, the Pore-water Pressure Control test (PWPC) was performed by increasing the pore-water pressure in undrained condition at constant tangential and normal stresses. Since rockslides initially occur at slow shearing, a grinding process changes the grain size distribution and the movement aligns the generated grains in the sliding direction. This probably causes a decrease in hydraulic conductivity, the sealing of landslide portions included between shear zones, and it facilitates undrained conditions. Eventually, as suggested by Skempton (1985), if during motion there is a sudden increment of the shear strain the particles may lose their orientation causing an increment of shear strength. This demonstrates the sensitivity of the velocity along the shear zone to the pore-water pressure seasonal oscillations observed in nature (Angeli et al., 1996; Crosta et al., 2014).

Under an imposed shear stress step (FC test) the viscous behavior is evident in the time-dependent response. Indeed, the FC test confirms a sort of standard trend in the normal and tangential displacements.

Indeed, in the damaged material, at the same force increment, the velocity is higher. During the tests the velocity is suddenly affected by the change in the tangential stress and this effect reduces with time until the velocity reaches an asymptotic value (Figure 95 and Figure 96). Our results confirm that this asymptotic value does not depend significantly on the tangential stress level until failure occurs. This behavior is not considered by the mathematical models generally employed to describe the delayed effects which are observed in situ (Angeli et al, 1996; Gasparetto et al., 1996; Fernández-Merodo et al., 2014). Hence, these mathematical models are not able to capture all the displacements because they are limited to the second creep stage. According to SEM observations, the transition and the steady-state phases during FC tests could be interpreted in the following way: just after the tangential stress application the material starts to align platy particles and after a large cumulative displacement the creep behavior characterizes the response, and consequently the steady state is observed. For each tangential stress value, not all particles are aligned and consequently for each successive step the reorientation of misaligned particles occurs. The comparison between the grain-size curves before and after the test (Figure 89) reveals that the grain size reduction was pronounced in SSC test rather than FC test. Indeed, in the force control test the failure condition is reached only in the last step that appears as a vertical line (Figure 95 and Figure 96).

Consequently, the creep phenomenon before the failure controls the displacement in the shear zone but the grain crushing influences the shear band evolution.

Under the hypothesis that the material behaves as a Newtonian fluid (e.g. Hunt, 1994; Coussot, 1995; Straub, 1997; Iverson, 1997; Poisel and Preh, 2008), the dynamic viscosity is computed from the FC test results both for the transition phase and steady state condition (Table 6, Figure 104).

Table 6 - Equivalent dynamic viscosity computed from FC test results. LS: Mont de La Saxe rockslide; CH: Chervaz rockslide.

Case study - Incremental $\tau$ step[kPa] - state	$\mu_{min}$ [kPa · s]	$\mu_{max}$ [kPa · s]	$\mu_{mean}$ [kPa · s]
LS – 50 – transition	$5.33 \cdot 10^6$	$8.94 \cdot 10^6$	$6.40 \cdot 10^6$
LS – 50 – steady	$3.94 \cdot 10^7$	$3.46 \cdot 10^8$	$2.01 \cdot 10^8$
LS – 100 – transition	$5.12 \cdot 10^7$	$7.33 \cdot 10^7$	$6.39 \cdot 10^7$
LS – 100 – steady	$2.78 \cdot 10^9$	$9.35 \cdot 10^9$	$5.89 \cdot 10^9$
CH – 100 – transition	$6.19 \cdot 10^6$	$1.80 \cdot 10^7$	$1.11 \cdot 10^7$
CH – 100 – steady	$3.55 \cdot 10^8$	$8.48 \cdot 10^8$	$5.83 \cdot 10^8$



The computed dynamic viscosities demonstrate that increasing the tangential stress step size, the material increases its viscosity (e.g. rate and state) of at least one order of magnitude (Table 6).

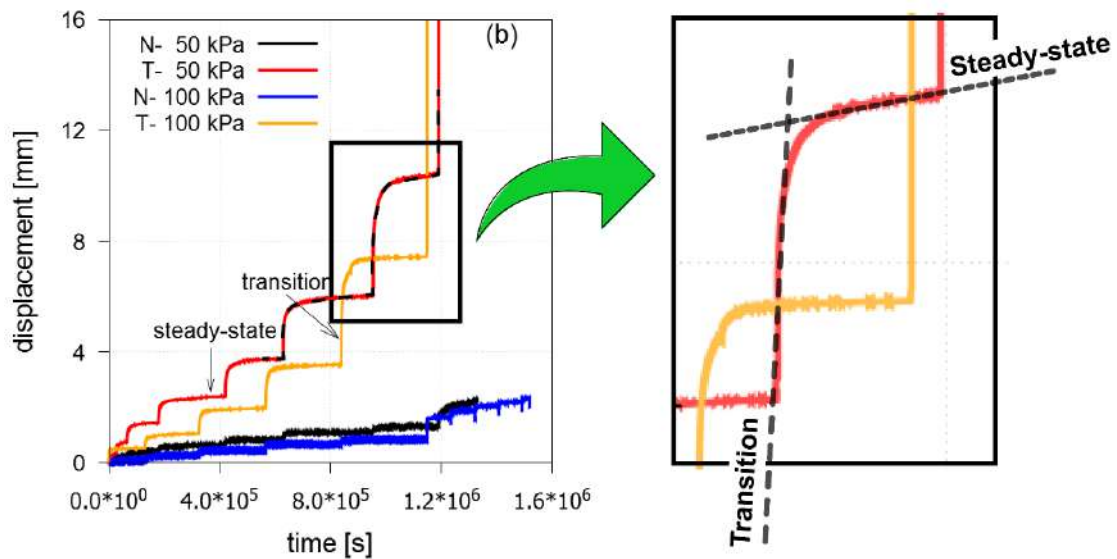


Figure 104 – analyses of viscosity for each transition and steady-state phases. An example to Mont de La Saxe data from FC tests.

Based on this series of experiments, a hypothetical mechanism of the shear-zone development process can be proposed (Figure 105) from mechanical point of view. At the beginning the shear zone itself consists of a mixture of coarse grains and fine particles which are randomly distributed. The first phase, after the increment of tangential stress (or velocity), was a transition stage (Figure 105a), that represents the transitional-structure development process, i.e., a randomly oriented structure becomes oriented parallel along the shear zone (including the results of grain crushing). In this phase was observed a grain-size reduction (GSR). At the steady-state stage (Figure 105b), the shear zone was separated into two parts by a segregation process. The first part is the core in which parallel orientation of the grains occurred. This part consists mainly of coarse grains with limited fine particles. Finally, when the material fails (post-failure stage), its strength starts to decrease (sometimes rapidly) to prevent the increment of stress that acts along the potential failure plane. Due to the shear-zone development process after failure, pore-water pressure is generated and the mobility (acceleration) of the failed mass subsequently increases. In this situation, the shear zone develops in an asymmetrical and uneven form (Figure 105c).

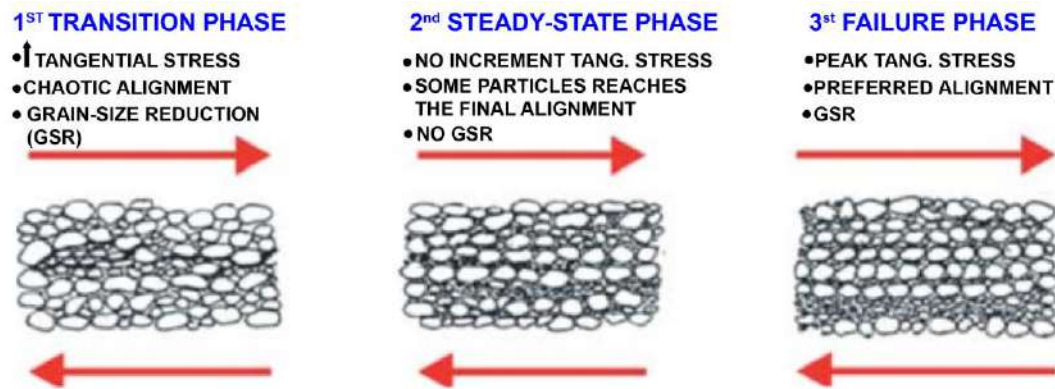


Figure 105 – Conceptual model of shear-zone structure processes by means ring shear test. Three different phases are shown: transition phase (increasing of tangential stress or velocity), steady-state phase (maintaining of tangential stress) and failure phase (reaching the peak value of shear strength). GSR: Grain-Size Reduction

Another important issue is the role of dilatancy in controlling the reduction of the pore water pressure and the effective stress path during SSC and PWP tests. Conversely, the test at imposed shear displacement rate (SSC test) shows the effects of sample compaction because the normal displacement increases (i.e. the sample height reduces), and no tangential stress reduction is recorded. This confirms that the residual shear strength is attained in the shear zone during failure for all the imposed velocities. The residual shear strength seems unaffected by the tangential velocity, within the tested range (0.003 – 0.008 cm/s), and consequently can be considered a material property. Consequently, when a rockslide reaches the failure condition it slides under constant tangential stress and consequently its motion is due to the unbalanced forces.

Finally, the tests conducted after the first failure of FC test, Aging tests, used to understand the response of the material post-failure after an at rest period, evidences a sort of hardening behavior (i.e. rate and state), with a relevant increase of friction angle up to about 6%.

Changes in the residual shear strength of the shear zone material could be caused by changes in displacement (shear) rate. Rate induced changes in shear strength could therefore be an important control on landslide movement.

Skempton (1985) using the results from ring-shear tests on clays carried out by Petley (1966) and Lupini (1981), found that when sheared at slow rates the average change in strength is less than 2.5% per order of magnitude variation in shear rate, and that variations in strength within the usual range of slow laboratory tests are negligible. From ring-shear tests on clays sheared at higher rates, an increase in strength becomes pronounced at specific rates (i.e. exceeding 100 mm/minute), when a qualitative change in behavior occurs. Lupini et al. (1981) and Skempton (1985) suggested that this behavior was probably associated with the disturbance of the originally ordered structure. Some disturbance appears plausible, as when sheared at high rates ( $\approx 300$  mm/minute) followed by over impressed lower rates of shear a peak in strength is observed, with resistance falling to the residual only after considerable further displacement (Skempton, 1985). However, Nieuwenhuis (1991) and Angeli et al. (2004), suggested that once residual strength has been achieved and shearing has stopped, consolidation of the shear band may lead to strength regain, attenuating the likelihood of reactivation (van Asch et al., 2007). This can be linked to the Mont de La Saxe monitoring data, where after a strong displacement pattern up to several meters per day (since 2012 to 2014) and

culminated with a possible failure, the displacement rate considerably decreased, according to an increment of shear resistance.

In summary, the shear zone materials have been characterized through conventional and unconventional tests, showing a non-linear and complex behavior characterized by a sort hardening during the creep phases

## FABRIC CHARACTERIZATION

As demonstrated by various authors (Zulauf et al., 1990; Craw, 2002; Nakamura et al., 2015; Straühal et al. 2017) there is no marked difference in structure, mineralogical composition or mechanical properties and behavior between the brittle tectonic fault zones and the shear zones of rockslides (Straühal et al., 2017) located in low-strength metamorphic rock (schists, phyllites, paragneiss series). In a more general consideration, structural geology techniques have increasingly become important in the study of rock-slope failures (Agliardi et al., 2001; Savage and Morin, 2002; Blikra et al., 2002; Crosta and Agliardi, 2003; Braathen et al., 2004; Crosta et al., 2004; Johnson and Cotton, 2005; Ambrosi and Crosta, 2006; Crosta et al., 2006; Zangerl et al. 2010; Straühal et al., 2017). In particular, the study of breccia zones at the base of potential hazardous rock-slope failures have been assessed in terms of their particle characteristics (Chigira, 1992; Bürgi, 1999; Shuzui, 2001). However, the shear strength of natural materials in relation to rockslide potential has hereunto solely addressed clays in soil landslides (Wan and Kwong, 2002; Stark et al., 2005). Understanding the frictional and mechanical properties of the non-cohesive fault- confined breccias is critical to the stability assessment of the overlying rock mass in potential rock-slope failures.

The mechanical behavior of geologic materials deforming in the brittle regime has been the subject of considerable interest for over a hundred years, owing to its role both in interpreting deformed rocks and in understanding seismic phenomena (e.g., Gilbert, 1884; Cloos, 1928; Riedel, 1929; Morgenstern and Tchalenko, 1967; Sibson, 1977; Byerlee, 1978; Crawford et al., 2008; Collettini et al., 2009, 2011; Haines et al., 2013).

The kinematics of deep-seated rockslides, usually characterized by slow to extremely slow rates of movement, is influenced by deformation along one or several discrete shear zones (e.g. Noverraz 1996; Bonzanigo 1999; Bonzanigo et al. 2007; Zangerl et al. 2010; Straühal et al., 2017). In contrast, to the deformation within these shear zones, the deformation that occurs within the rockslide mass is often small (e.g. Noverraz 1996; Tentschert 1998; Bressani et al. 2008; Zangerl et al. 2010; Straühal et al. 2017; Fossen & Cavalcante, 2017). These shear zones, up to several meters in total thickness, often comprise centimeter- to meter-thick fine-grained zones characterized by a silty-clayey soil (i.e. fault gouge) (e.g. Barla 2010; Barla et al. 2010) also called soil-like rock. In addition to other influencing parameters (including pore pressure distribution, in situ stress, internal deformation), the slope stability and temporal deformation behavior of rockslides are consequently dominated by shear zone properties rather than by overall rock mass properties. Particularly for rockslides situated in mica-rich metamorphic rocks (e.g. schists, phyllites, gneisses), failure typically does not occur suddenly (e.g. Crosta and Agliardi 2002; Helmstetter et al. 2004; Bruckl and Parotidis 2005; Bruckl et al. 2006; Bonzanigo et al. 2007; Zangerl et al. 2007, 2010; Straühal et al. 2017); but deformation occurs at very slow to slow velocities.

Several theoretical models have been proposed that relate evolution of shear zone thickness to strain and displacement accumulation (Means, 1984, 1995; Hull, 1988; Vitale and Mazzoli, 2008; Fossen, 2016). Four idealized models (Fossen and Cavalcante, 2017) producing different displacement profiles across the zone (Figure 106) can be considered. It is emphasized that each one is idealized and should only serve as reference models. Type 1 thickens over time as strain propagates into the walls, leaving an inactive central part behind. In the type 2, where strain increasingly localizes to the central part of the shear zone and a characteristic shear-strain distribution develops and

evolves into a peak-type profile. Types 1 and 2 can be explained by strain hardening and weakening, respectively. Type 3 has constant active thickness (also attributable to weakening or confinement to a weak preexisting layer), while Type 4 grows thicker while the whole shear zone remains active, and develops a bell-type profile that, unlike Type 2, does not grow into a peak-type profile.

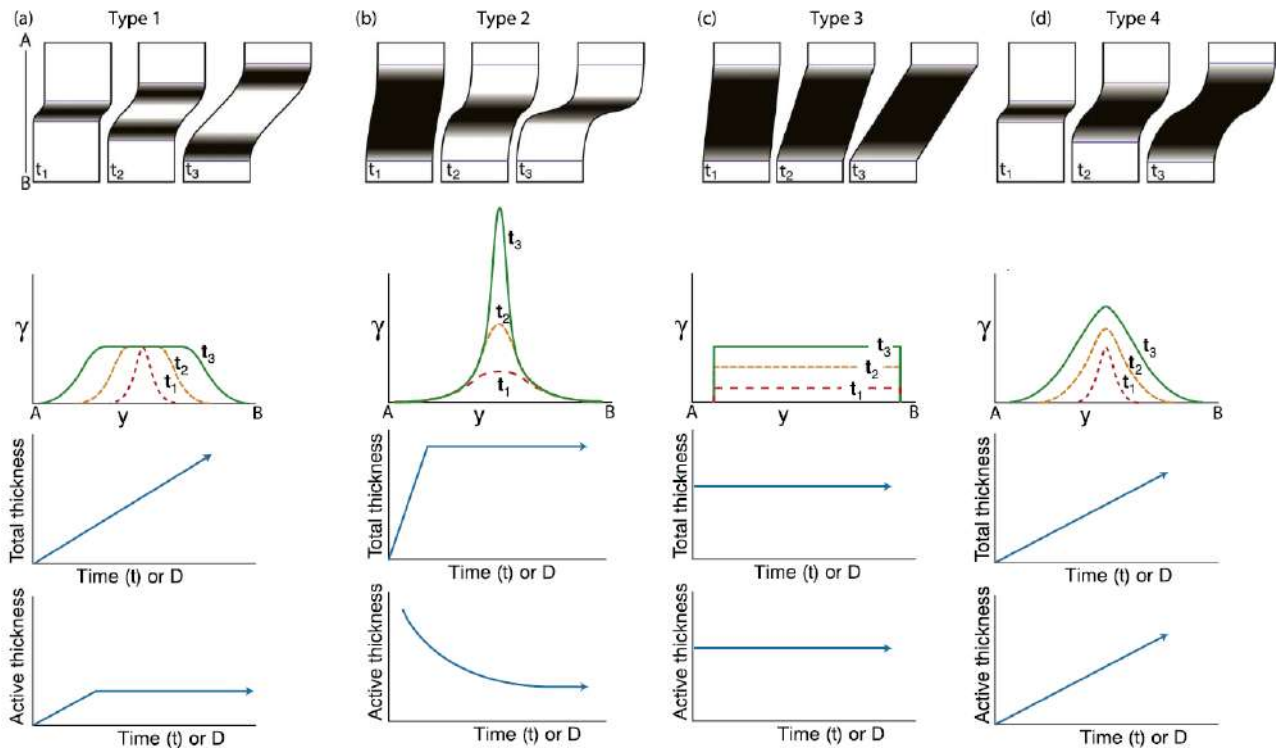


Figure 106 - Four different types of shear zones based on thickness and activity through time, where the black-gray fields represent active portions of the shear zone. a) Type 1, where the zone widens and leaves the central part inactive. b) Type 2 where strain localizes to the central part of the zone. c) Type 3, which maintains its thickness and is everywhere active at any given time. d) Type 4, where the zone widens and is everywhere active. Shear strain profiles, thickness-evolution, and thickness of active part of shear zone through time are shown for each case. (from Fossen & Cavalcante, 2017)

Given that shear zones are the product of the rockslide evolution, information and data about the geological structure, mineralogy and mechanical properties of a rockslide shear zone can help in understanding the stability evolution of a rockslide.

As illustrated by Kenney (1967) and Tsiambaos (1991) as well as Tiwari and Marui (2005), for example, mineralogical composition has a major influence on the residual shear strength. Their studies demonstrate that soil with high amounts of clay minerals (especially swelling clay minerals, such as montmorillonite) is characterized by low residual friction angles. The occurrence of clay minerals in shear zones of rockslides is common (e.g. Bonzanigo 1999; Bonzanigo et al. 2007) and is caused by the chemical weathering of crushed and fragmented host rock. Concerning also landslide shear zone, phyllosilicates (biotite, muscovite and chlorite) are present in high proportions (Straühal et al., 2017).

Straühal et al. (2017) demonstrated that the deformation of the rockslides in foliated metamorphic rocks occurs within decimeter to meter-thick shear zones (up to more than 10 m) and not along distinct, single shearing planes. Suggesting that many characteristics observed in the field that would influence the friction angle, such as the fabric, the inclined slickenside surfaces and the local variations in mineral content, could not be assessed by laboratory tests.

The mineralogical composition (i.e. no strength-sensitive clay minerals for almost all samples), the residual shearing behavior—with no noticeable change even after very large displacements in the shear apparatus—and the grain size distribution suggest no further strength reduction, at least at the laboratory scale.

Another key point shown by Fossen & Cavalcante (2017) is represented by developing of shear zones, usually preferentially along preexisting fabrics, layers, veins and dikes in ways that depend on their rheological contrasts and orientations relative to the stress field. Typically, strain is localized within weak layers or structures, but can also be localized along lithologic boundaries.

A characterization was performed on shear zone samples from Mont de La Saxe and Chervaz rockslides, including a mechanical behavior characterization (see section 3.2).



## **4.1 Mineralogical, textural and structural characterizations**

A mineralogical characterization has been performed to identify, and try to quantify, the mineralogical phases in the shear zone materials. Additionally, a textural and structural analysis has been performed through Micro Computed Tomography (micro-CT) on samples on which ring shearing tests was previously presented.

### **4.1.1 XRD and XRF analyses**

X-Ray Power Diffraction (XRPD) characterization have been performed using a PANalytical X'Pert3 (2theta range: 380, step size: 0.0167) on powder using a ceramic X-ray 3 kW generator and the quantitative analysis via the GSAS software (Larson and Von Dreele, 1994). Mineral quantification was completed by a simplified procedure based on the standard Rietveld's method based on empirical correction factors improved for phyllosilicates (Schulze, 1994).

XRF analyses were carried out using a PANalytical Epsilon 3 with a silver anode and a window of 50  $\mu\text{m}$ . The samples were prepared via a multi-stage approach which includes sieving for separating the fraction below 2 mm and grinding in an onyx mill. For the XRF analysis, powder tablets by pressing the rock dust with an acrylic polymer resin were prepared. In this technic, the resin is dissolved in acetone which vaporizes leaving a grain-coated coagulate of grains behind. Under pressure, it flows and binds the grains together resulting in a solid tablet to be inserted in the XRF spectrometer.

### **4.1.2 SEM analysis**

The internal structure of the samples was studied by means a Tescan VEGA TS 5136XM SEM coupled with EDS (Energy Dispersive Spectroscopy) micro-probe Genesis 4000 XMS Imaging for chemical analysis and with Dual BSD detector and W emitter operating at an accelerating voltage of 20 kV. The EDS detector is equipped with an ultra-thin window allowing detection of mineral elements and carbon.

A Zeiss Gemini 500 Field-Emission SEM equipped with EDS for elemental mapping was used. The benefits of mapping are the visual assessment of the spatial distribution of the elements in the sample (e.g. phyllosilicates preferred alignment), and the RGB color overlays to assess regions of interest.

The samples before testing were analyzed in the form of dried dust mounted (with Tescan VEGA SEM) on a metal stub with adhesive, coated with 40-60 nm graphite and in the form of polished section after araldite fixing process (with Zeiss Gemini 500). The samples after direct shear and ring shear tests were directly embedded in araldite resin, made conductive by graphitization process and then observed at the microscope. This process is highly time-consuming and, in this case, about 3 months were required for preparation of the polished sections (Figure 107).



*Figure 107 – epoxic resin embedding process (left-hand side); finale result on polished sections (right-hand side)*

#### **4.1.3 Micro-CT analysis**

A High-resolution X-ray computed tomography (CT) was performed using a BIR (Varian Medical Systems) Actis 130/150 system (5  $\mu\text{m}$  theoretical resolution). Radiation, emitted by an X-ray fixed generator, passes through the sample and it is reduced as a function of its density and atomic number. X-rays are collected on a fixed detector and converted into light radiations which are detected in raw data by a digital camera and sent to a computer for the image processing phase. The here presented images (Figure 122 and Figure 123) have a  $24 \times 24 \times 27 \mu\text{m}$  voxel size.

## 4.2 Results

### 4.2.1 XRD and XRF analyses

According to XRD and XRF analyses, samples present a variety of trace elements as: V, Cr, Ni, Cu, Zn, Rb, Sr, Zr, Nb; Sn, Ba and abundance of Quartz and Calcite. Quartz X-ray reflection spectra commonly overlaps the graphite  $d(002)$  reflection (Aladekomo and Bragg, 1990), and consequently it was not possible to recognize the presence of graphite. Other minerals in the samples are: Muscovite, Clino-chlore, Vermiculite, Ankerite and Chabazite which are typical of low and medium metamorphic and altered rocks by hydrothermal processes, and usually are characterized by a presence of Ca, Al, Mg and Fe (Kristmannsdóttir, 1979). This mineralogical association is confirmed by the XRF and permanganometry results, that shows a high content of these elements associated with water. This is typical for the meta-sedimentary sequence (usually calc-schist and mica-schist) in the area (Perello et al., 1999). Consequently, the phyllosilicates in the analyzed samples (e.g. biotite, muscovite and chlorite) are original minerals of the metamorphic bedrock and did not form due to weathering. Given that swelling clay minerals are missing or are only rarely present, chemical alteration is not considered a dominant process in forming strength-sensitive minerals in the shear zones.

*Table 7 – three different typical results from XRD analyses for samples from Mont de La Saxe rockslide. Qtz: quartz; Cal: Calcite; Musc: muscovite; Clino-chl: Chlre; Verm: vermiculite; Chab: chabazite and Ank: ankerite. Symbol +: relative content of minerals with greater content indicated by greater number of symbols.*

Sample	Qtz	Cal	Musc	Clino-chl	Chab	Ank
LS#1	+++	+++	++	++	+	-
LS#2	+++	+++	++	++	-	-
LS#3	+++	+++	++	++	-	+

*Table 8 – three different typical results from XRD analyses for samples from Chervaz rockslide. Qtz: quartz; Cal: Calcite; Clino-chl: clino-Clore; Verm: Vermiculite; Chab: chabazite, Ank: ankerite, Trem: tremolite and Ant: Antigorite.*

Sample	Qtz	Cal	Clino-chl	Verm	Chab	Trem
CH#1	+++	-	-	-	+	-
CH#2	+++	-	++	-	-	+
CH#3	-	-	++	+	+	-

Table 9 – XRF analyses results as % oxides for Mont de La Saxe (LS) and Chervaz (CH) rockslides

% Ox.	LS#4	LS#5	LS#6	LS#7	LS#8	LS#9	LS#10	CH#4	CH#5	CH#6
Na <sub>2</sub> O	0.48	0.41	0.46	0.39	0.40	0.37	0.54	0.00	0.26	0.67
MgO	2.39	2.54	2.38	3.04	3.21	2.09	1.27	21.57	19.30	15.70
Al <sub>2</sub> O <sub>3</sub>	19.06	19.22	19.12	24.87	23.04	16.62	23.41	15.50	15.38	15.00
SiO <sub>2</sub>	45.41	46.35	43.90	42.37	39.69	43.50	52.47	34.26	36.34	40.68
SO <sub>3</sub>	0.01	0.06	0.08	0.06	0.32	0.01	0.05	0.00	0.00	0.00
K <sub>2</sub> O	3.00	2.99	3.01	4.75	4.09	2.61	3.45	0.04	0.17	1.45
CaO	9.69	8.83	10.12	5.99	8.77	13.88	3.75	5.02	5.35	6.27
TiO <sub>2</sub>	0.77	0.79	0.78	1.27	1.16	0.71	1.10	0.70	0.90	1.13
MnO	0.14	0.11	0.16	0.06	0.07	0.04	0.08	0.27	0.23	0.20
Fe <sub>2</sub> O <sub>3</sub>	6.37	6.84	6.62	6.48	6.35	4.81	6.48	13.97	13.95	12.33
H <sub>2</sub> O	11.73	10.16	11.54	9.61	12.25	13.54	7.19	8.15	7.62	6.25
<b>SUM</b>	<b>99.05</b>	<b>98.30</b>	<b>98.18</b>	<b>98.88</b>	<b>99.36</b>	<b>98.19</b>	<b>99.79</b>	<b>99.47</b>	<b>99.50</b>	<b>99.68</b>

#### 4.2.2 SEM analysis

SEM investigations performed on loose granular samples before the tests (Figure 109), and on polished sections after shearing (e.g. Figure 110), and considered representative of the entire sample, show presence of graphite usually as plates concerning the Mont de La Saxe samples.

Considering that the SEM analyses were performed on loose material also before the tests, the presence of graphite, phyllosilicates and quartz is confirmed (Figure 109).

Quartz was well crystallized and accessory minerals such as pyrite, titanite, apatite, epidote and hematite were also found. These samples represented only the central portion of the shear zone and domains of aligned phyllosilicates, forming shear-induced foliation, were observed.

After shearing the phyllosilicates are distinctly oriented in the shear direction (Figure 110, Figure 113, Figure 116 and Figure 121) and are easily identified because of their platy morphology with (001) planes as both sheet and cleavage planes (Wenk et al., 2010). The elemental map for Carbon (graphite and/or carbonates) and Silica-Aluminum-Magnesium (phyllosilicate minerals) shows the phyllosilicates distinctly oriented in the shear direction and graphite at spots presence at boundaries of this alignment (e.g. Figure 114). The other elements are: potassium (K), sodium (Na), oxygen (O), calcium (Ca), iron (Fe), titanium (Ti), aluminum (Al), silica (Si), sulfur (S), chlorine (Cl), carbon (C) and phosphorus (P) representing the main mineral elements association in the metamorphic rocks.

Some SEM images taken into the shear zone show a complex fabric (Figure 110 and Figure 117), coarse fragments mainly in the 'hinge' zone with parallel platy particles on the limbs. This result – probably – is due to the metamorphic deformation, and these structures can be assimilated to the S-C structures (Lister and Snoke, 1984) of mylonitic shear zones. The maximum value of the strain is located at the boundaries of this mineral phases (i.e. quartz, phyllosilicates and calcite) (Figure 110).

Also, small coarse fragments located outside the boundaries of this complex shape result aligned toward shear direction (Figure 110).

Preferred alignment of phyllosilicates is widely recognized in most of the analyzed samples (e.g. Figure 113 and Figure 116), with graphite distributed along the shear zone (e.g. Figure 114 and Figure 117).

Concerning the Chervaz rockslide samples, it has been possible to analyze only the sample before the tests, that showing a mixed structure with packed arrangement and small particles mainly concentrated in the center of agglomerates and not a preferred alignment of the particles.

Microstructural studies of the tested rocks show that the sliding surfaces of the foliated solid wafers are located along the pre-existing very-fine-grained foliation made of tremolite and phyllosilicates (Figure 119).

An analysis of particles alignment was performed through the ImageJ software (Rueden et al., 2017) (Figure 133).

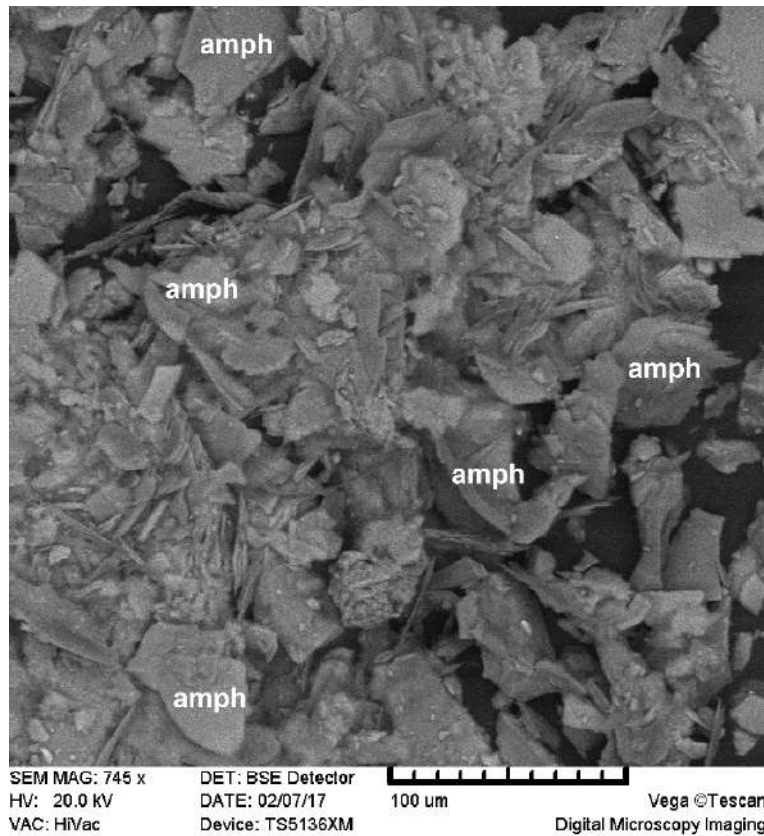


Figure 108 - SEM image acquired before the ring shear tests on loose sample for Chervaz sample. Amph: amphibole.

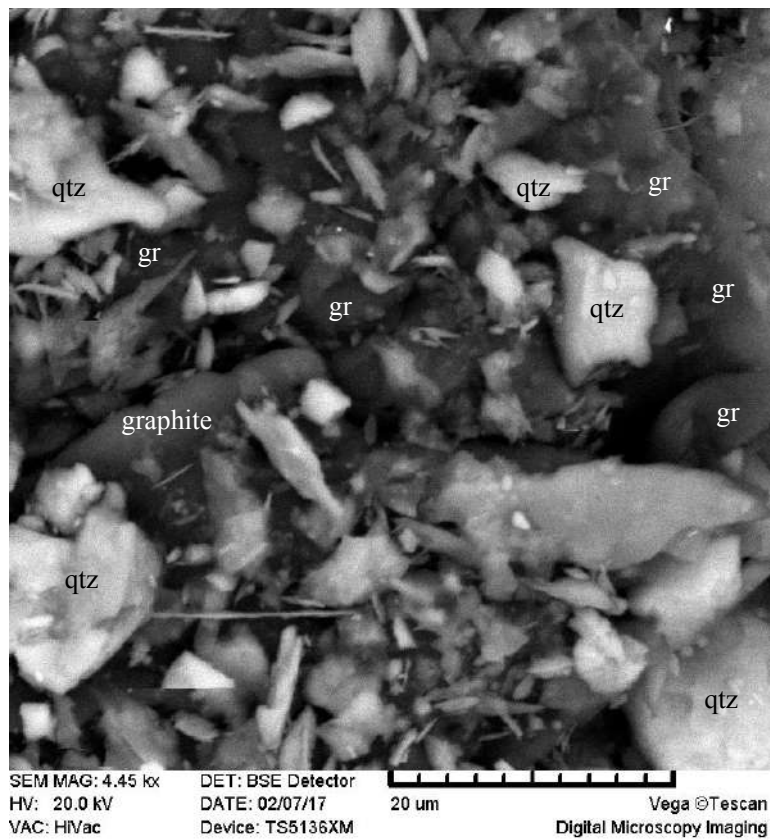


Figure 109 - SEM image acquired before the ring shear tests on loose sample for Mont de La Saxe rockslide. The spot presence of graphite (gr) and quartz (qtz) is confirmed.



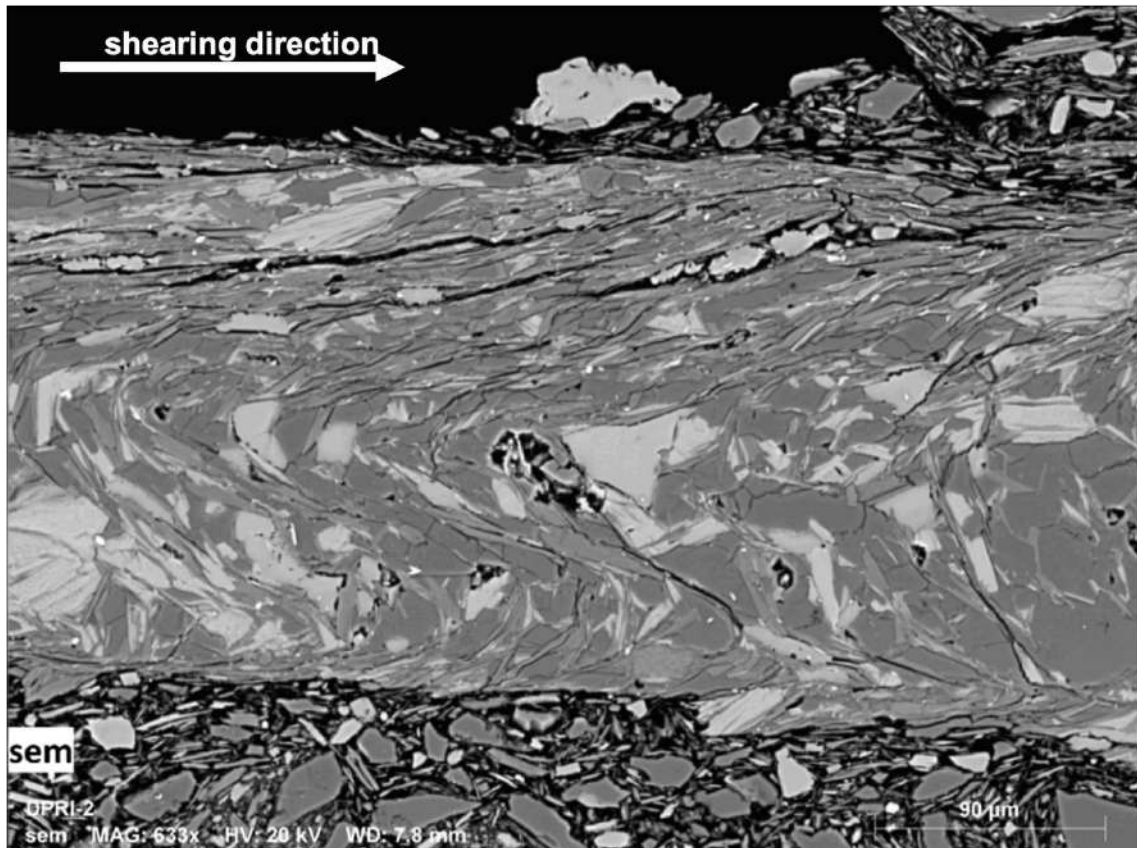


Figure 110 – complex mineralogic fabric at SEM into the shear zone. This sample is taken after ring shear test

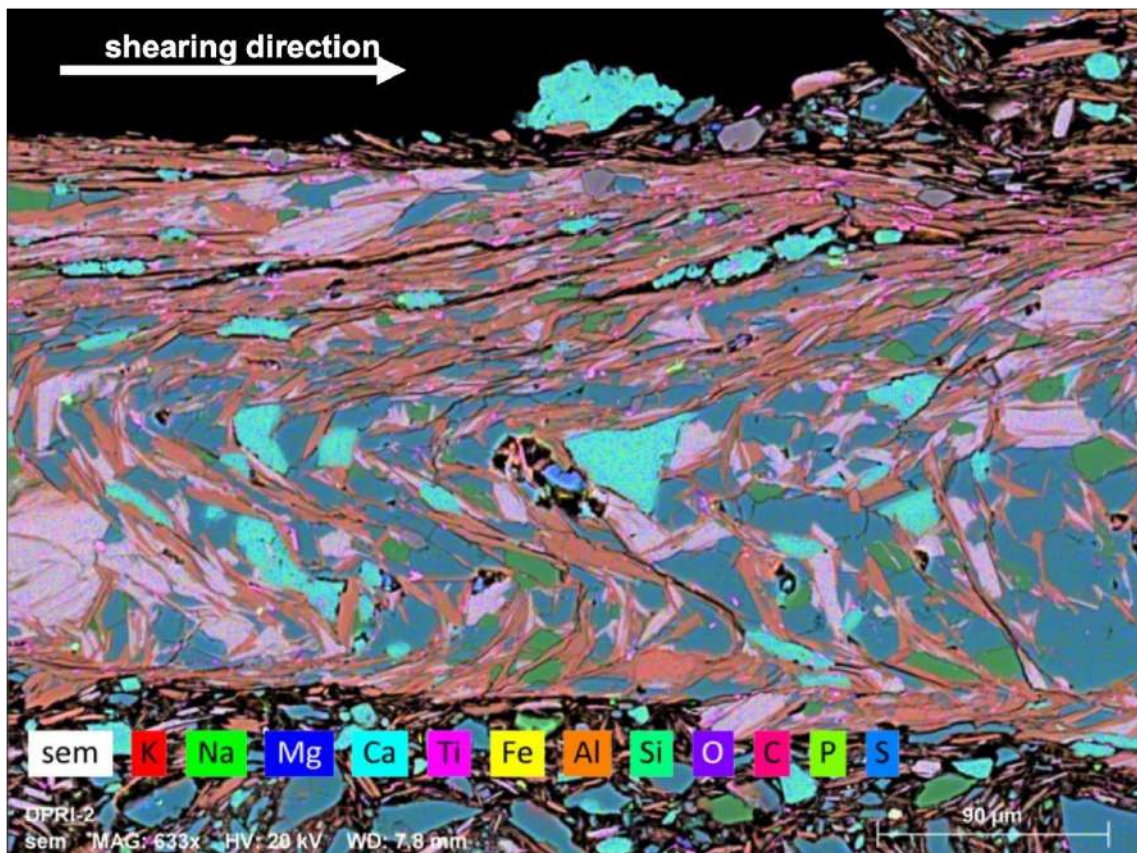


Figure 111 - complex mineralogic fabric at SEM into the shear zone with elemental map for K, Na, Mg, Ca, Ti, Fe, Al, Si, O, C, P and S. This sample is taken after ring shear test.



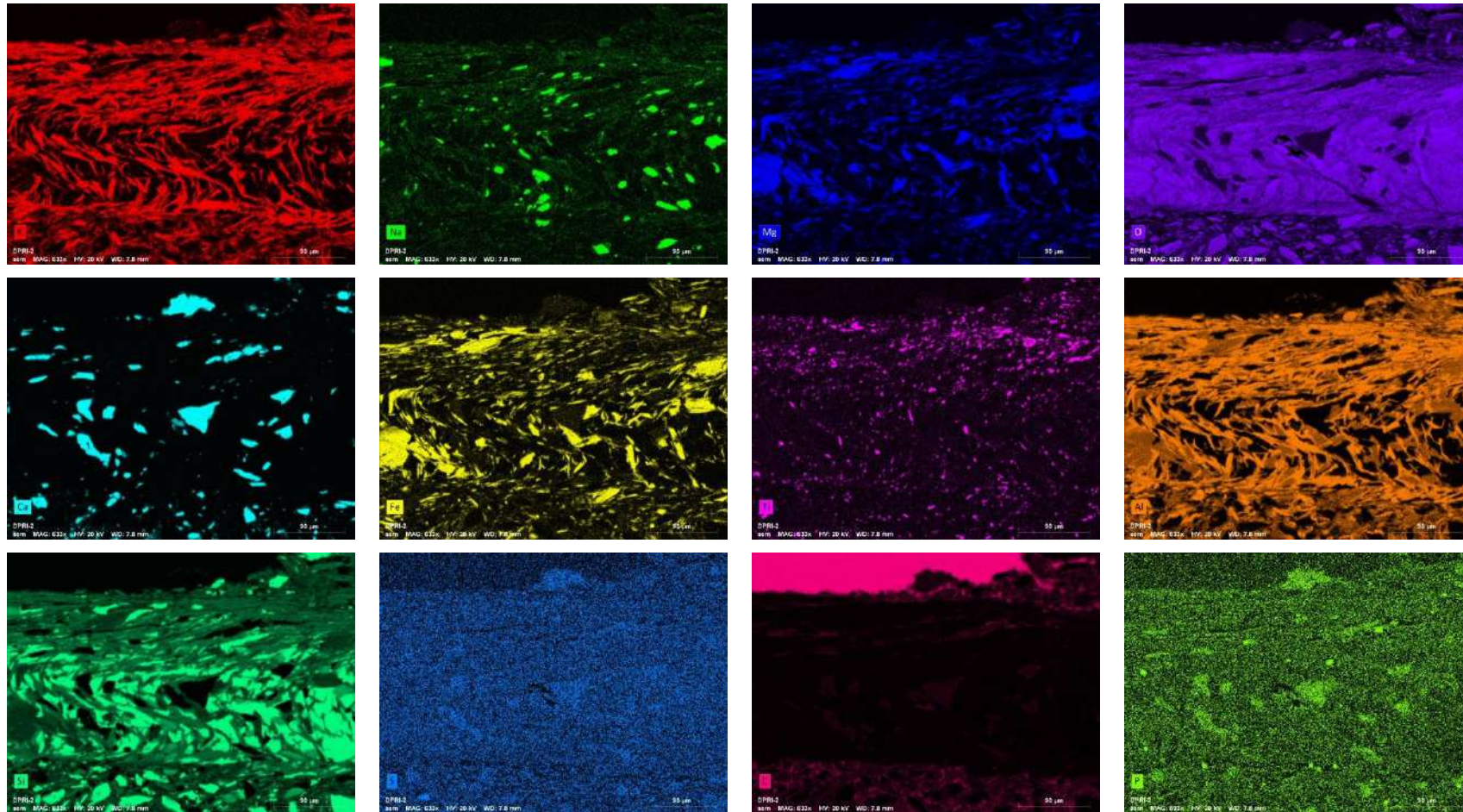


Figure 112 – Single elemental maps for Mont de La Saxe sample. Potassium (K), sodium (Na), oxygen (O), calcium (Ca), iron (Fe), titanium (Ti), aluminum (Al), silica (Si), sulfur (S), carbon (C) and phosphorus (P). The analyzed sample derives from ring shear test.



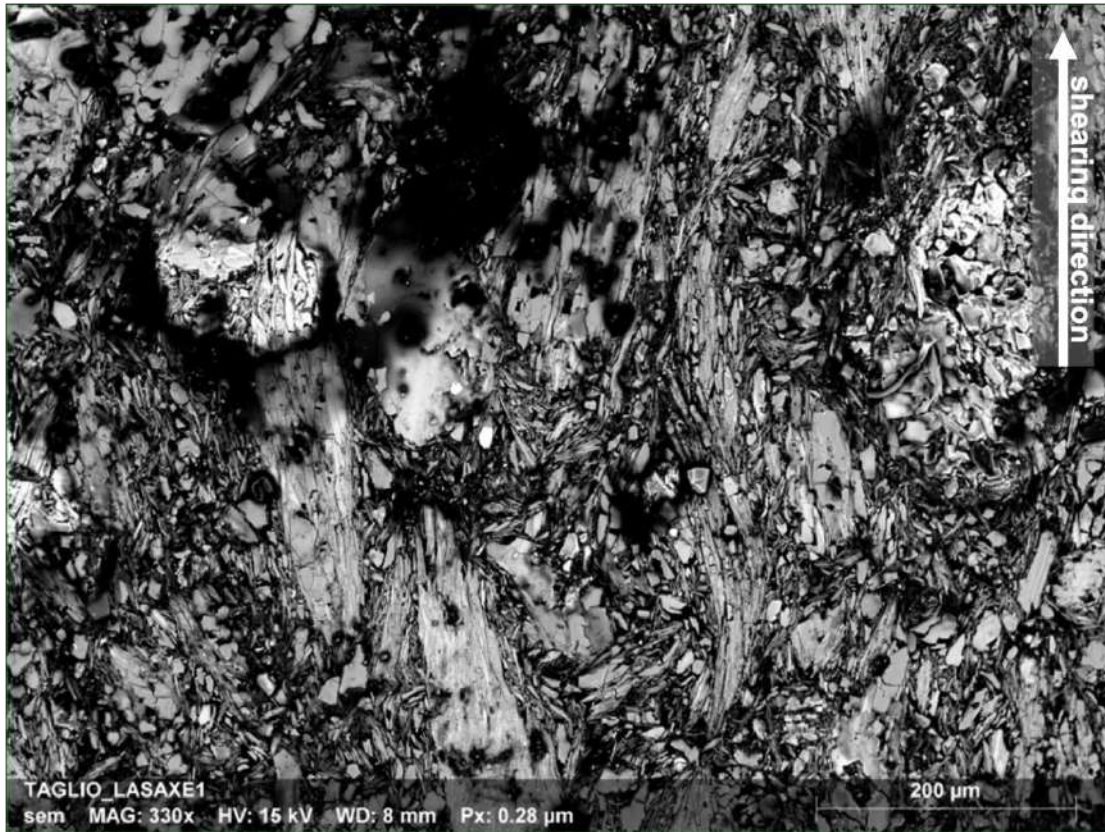


Figure 113 – SEM of DPRI test sample, with a preferred alignment of phyllosilicates and a presence of graphite (gr; black spots)

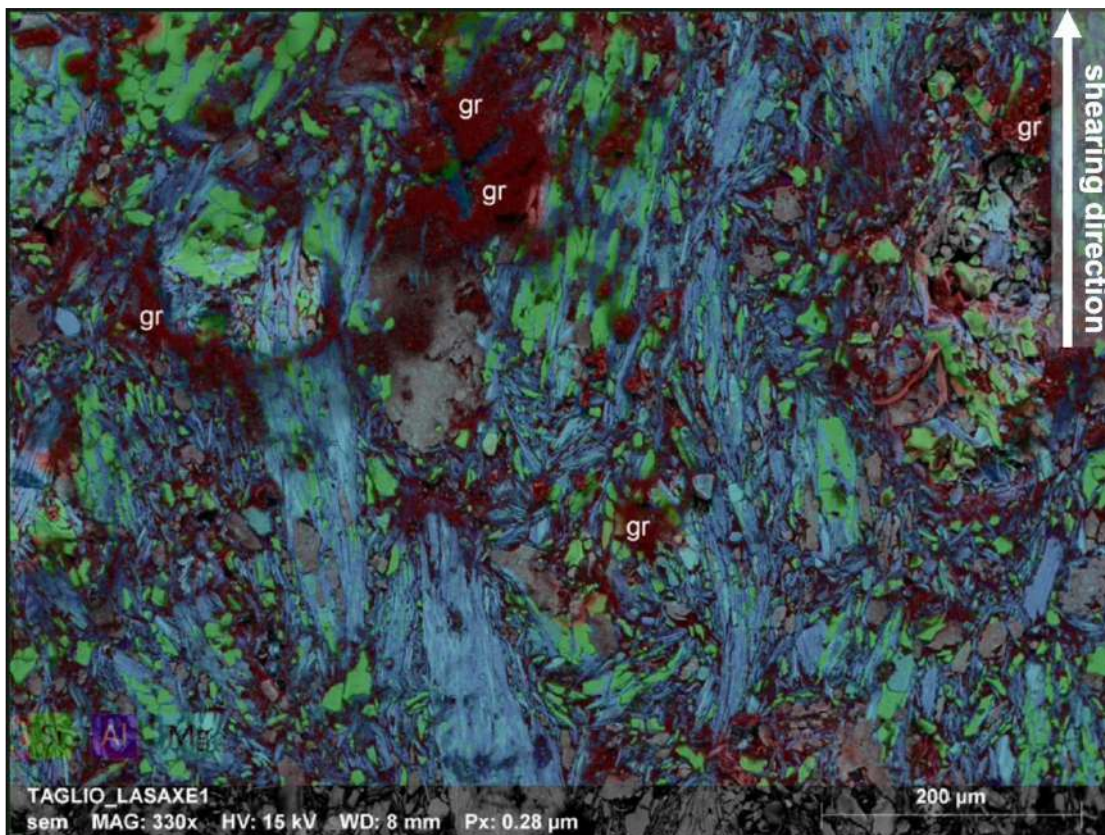


Figure 114 - SEM of DPRI test sample with elemental map for Silica Aluminum and Magnesium. A preferred alignment of phyllosilicates (blue and green spots) and a presence of graphite (black spots) is shown.



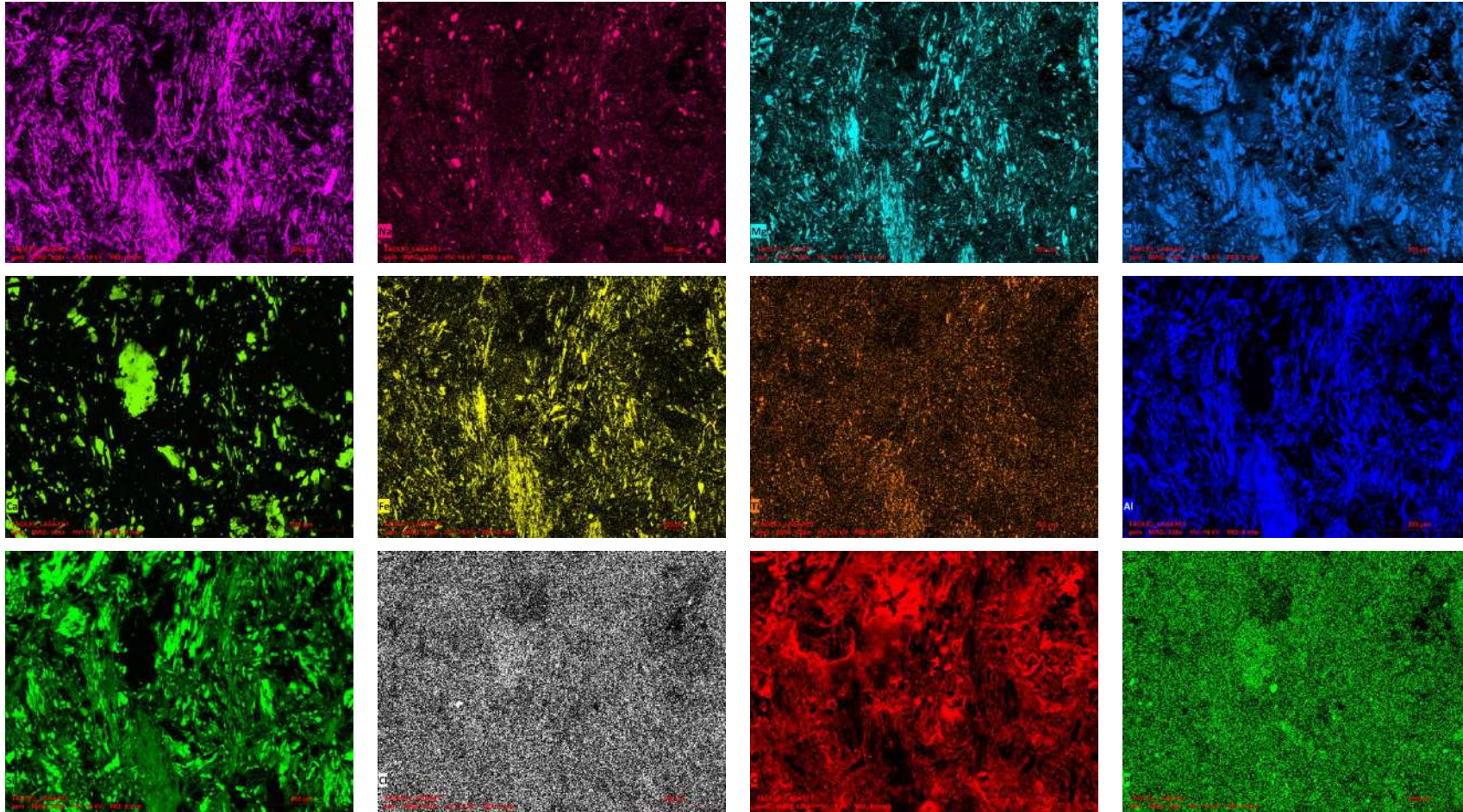


Figure 115 - Single elemental maps for Mont de La Saxe sample. Potassium (K), sodium (Na), oxygen (O), calcium (Ca), iron (Fe), titanium (Ti), aluminum (Al), silica (Si), sulfur (S), carbon (C) and phosphorus (P). The analyzed sample derives from direct shear test.





Figure 116 - SEM of DPRI test sample, with a preferred alignment of phyllosilicates and a presence of graphite (gr; black spots)

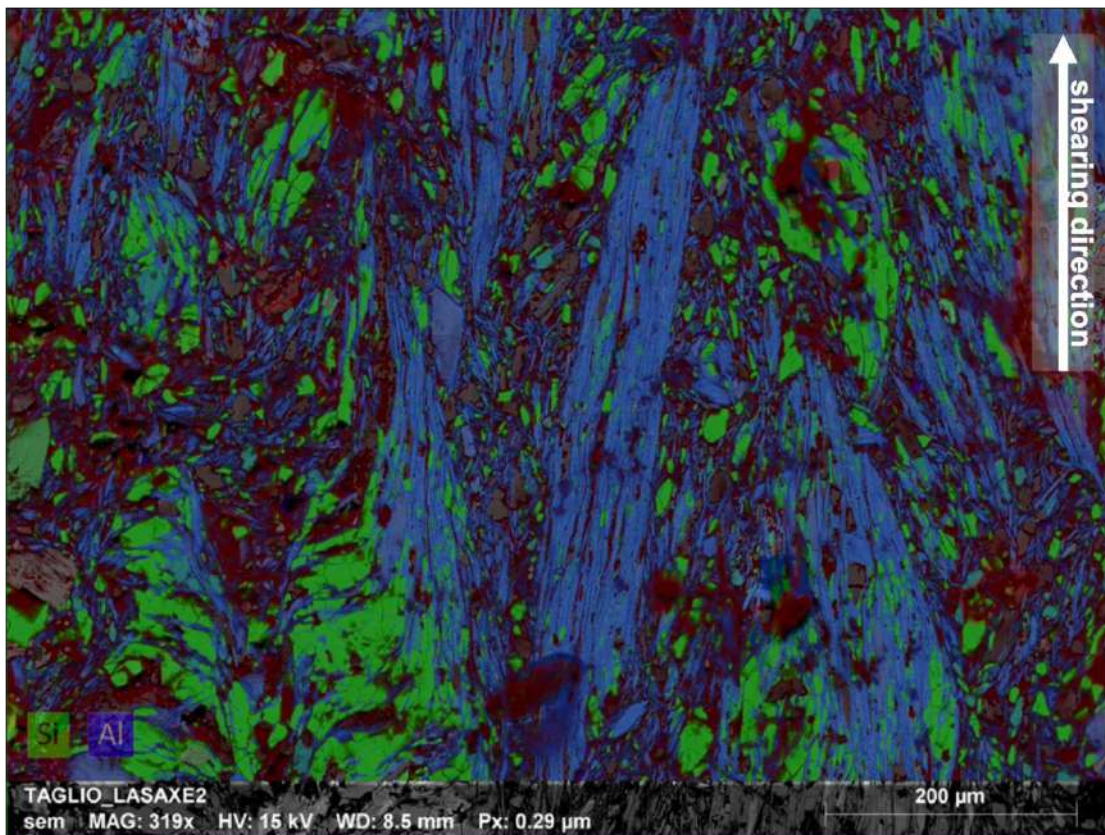


Figure 117 – SEM of DPRI test sample with elemental map for Silica Aluminum and Magnesium. A preferred alignment of phyllosilicates (blue and green spots) and a presence of graphite (black spots) is showed.



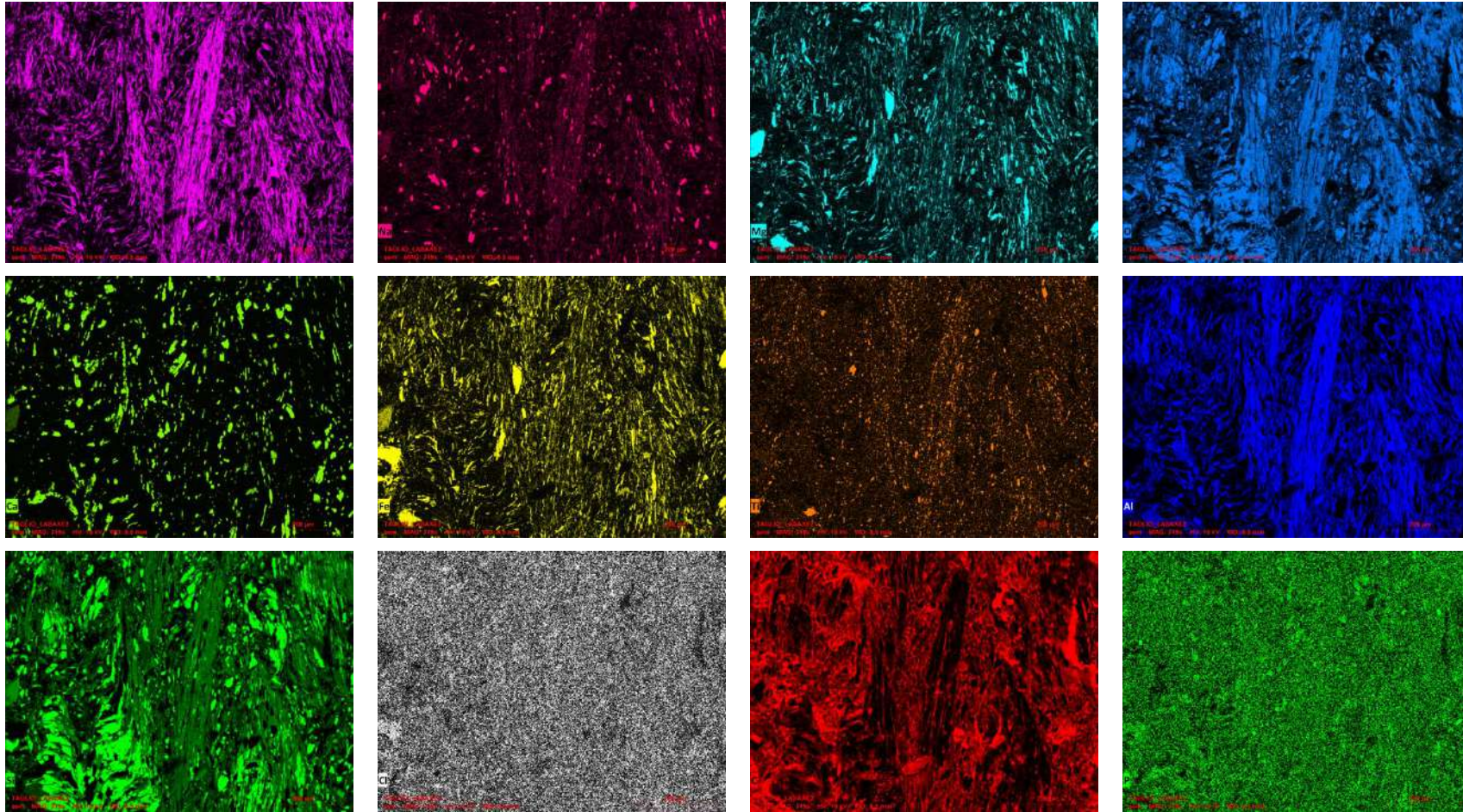


Figure 118 - Single elemental maps for Mont de La Saxe sample. Potassium (K), sodium (Na), oxygen (O), calcium (Ca), iron (Fe), titanium (Ti), aluminum (Al), silica (Si), sulfur (S), carbon (C) and phosphorus (P). The analyzed sample derives from direct shear test.



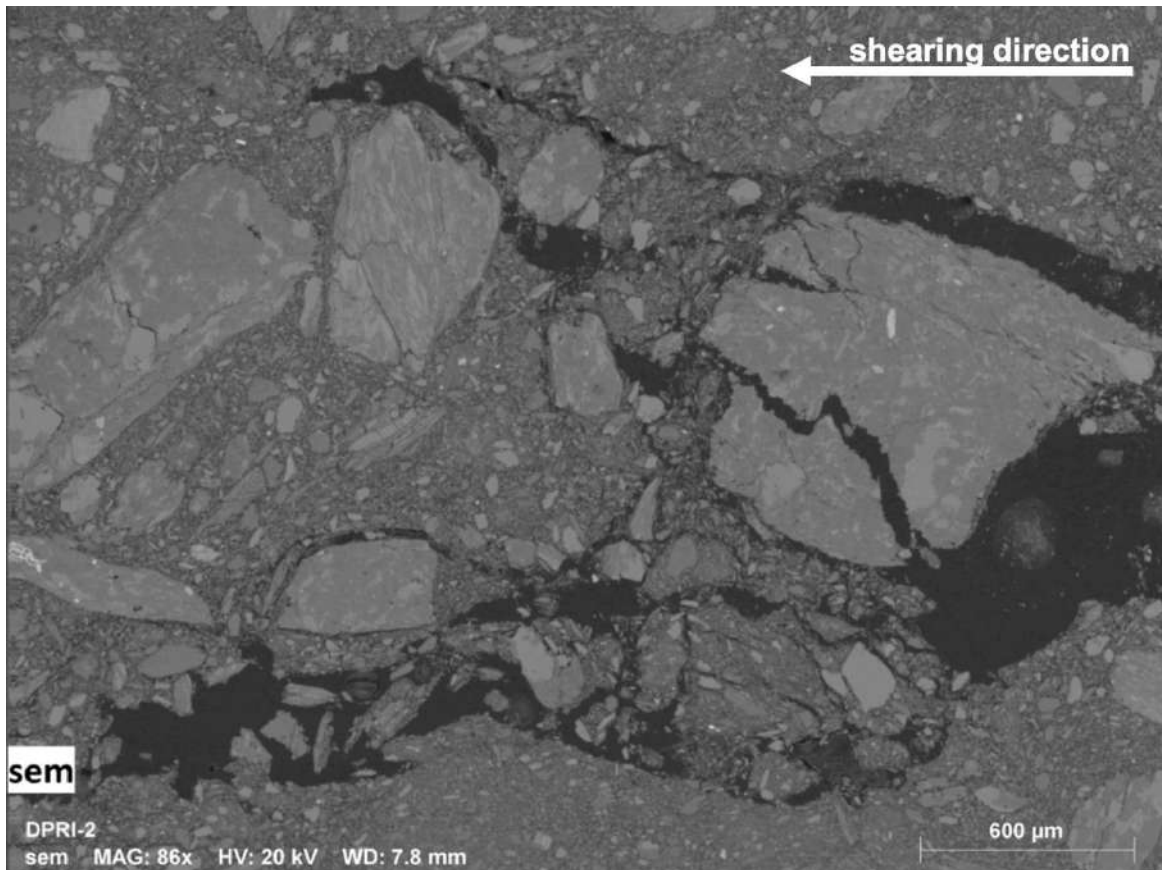


Figure 119 – SEM image of DPRI test sample, with particle crushing and presence of graphite (gr; black spots) due to graphitization process for SEM analyses

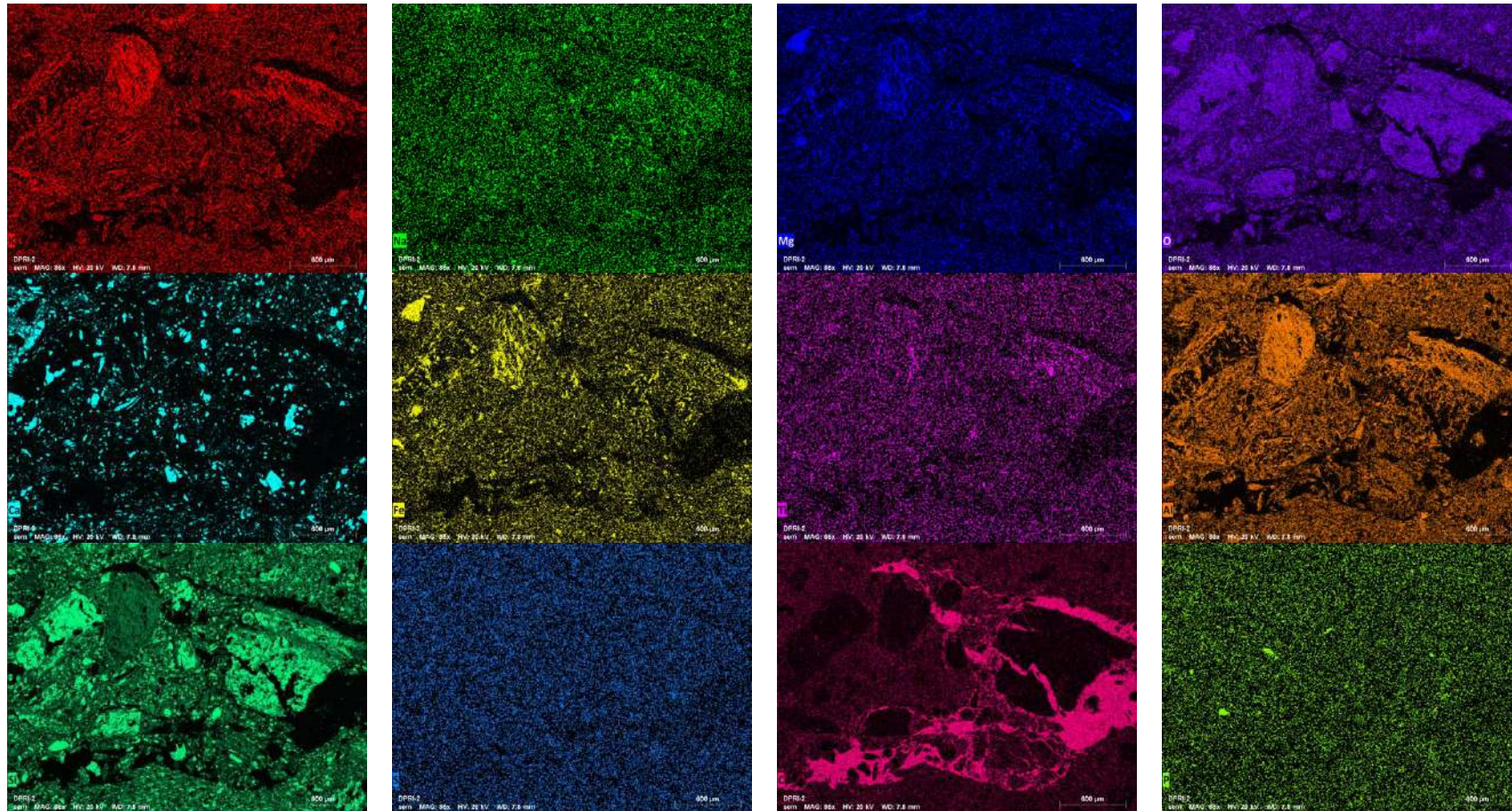


Figure 120 - Single elemental maps for Mont de La Saxe sample. Potassium (K), sodium (Na), oxygen (O), calcium (Ca), iron (Fe), titanium (Ti), aluminum (Al), silica (Si), sulfur (S), carbon (C) and phosphorus (P). The analyzed sample derives from direct shear test.

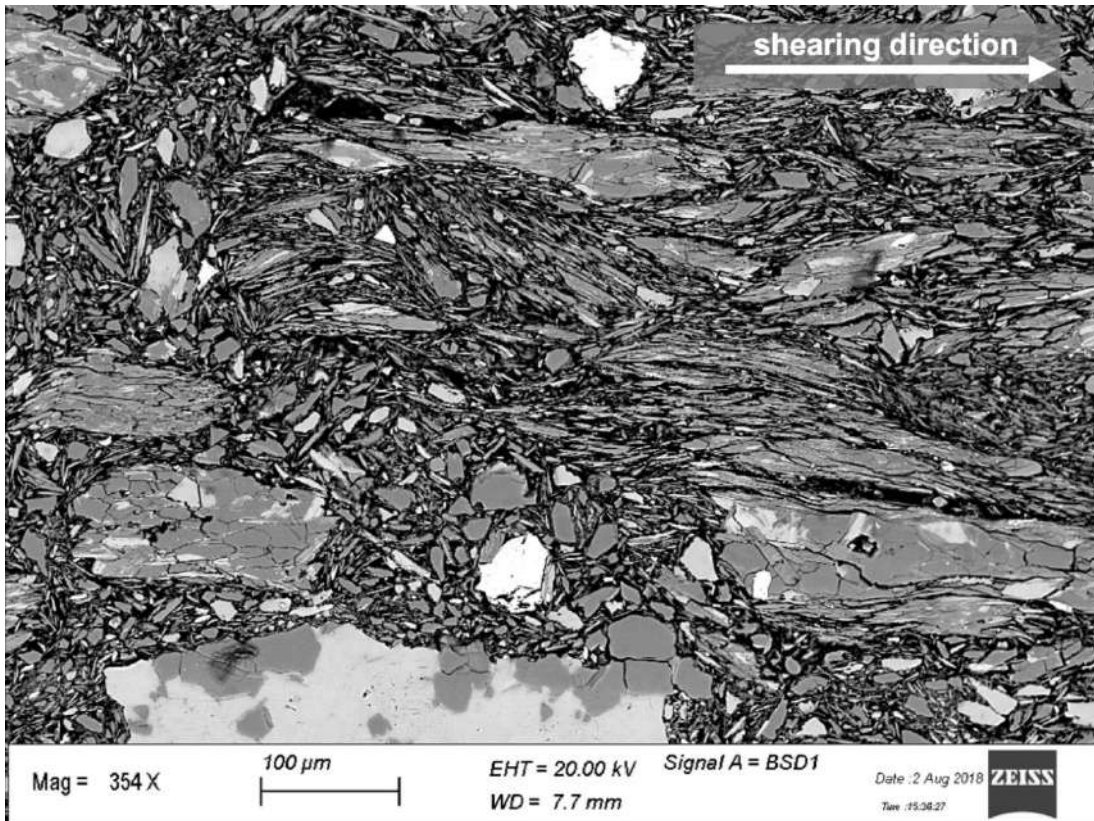


Figure 121 - SEM of DPRI test sample on fisheye backscattered view, with a preferred alignment of phyllosilicates, a particle crushing and a presence of graphite (black spots).



### 4.2.3 Micro-CT analysis

All the samples show a localized shear band 10 to 15 mm thick, characterized by a reduction of grain size. Larger grains of strongly reflecting minerals are mainly represented by oxides and sulfides. These grains are less abundant in the central part of the shear zones and become more frequent at the upper and lower limits of the shear zone. This can suggest hard grain (e.g. oxides and sulfides) ejection by mechanical action (e.g. Figure 124). Grain-size reduction has been observed in all analyzed samples even if in different proportion (Figure 124).

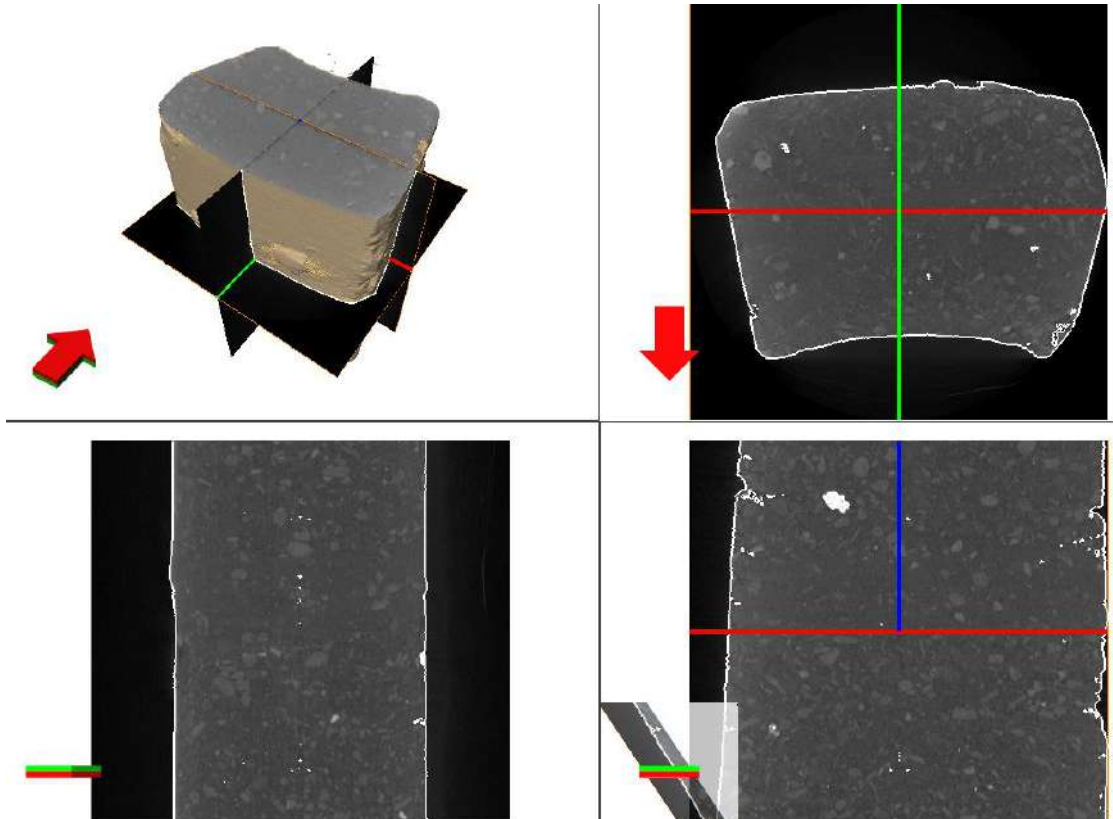


Figure 122 – example of slices and 3d reconstruction of the sample through micro-ct analyses. Bright minerals in the images are oxides and sulfides. a comminution in the central part of the sample is visible.

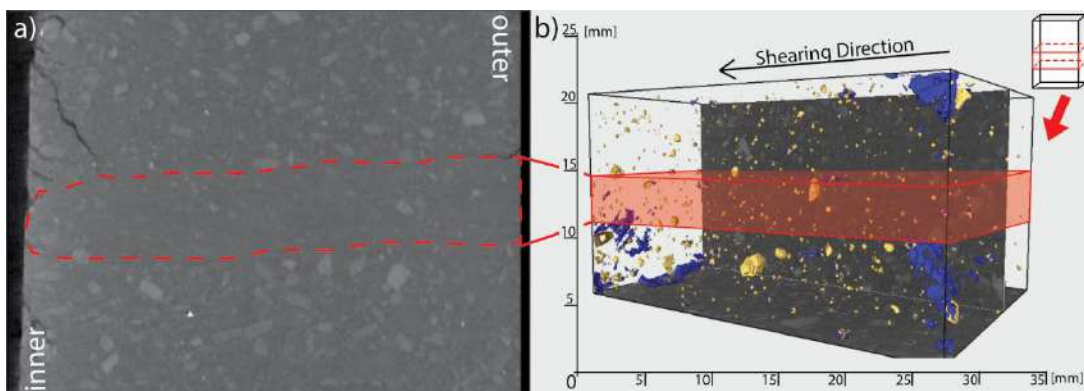


Figure 123 - Micro-CT analysis performed on a sample derived from Ring Shear tests of Mont de La Saxe rockslide. A) Slice with evidenced the grain size reduction zone (red box). b) The blue color gradient show the distribution and persistence of empty fractures, while the golden color represents the oxides minerals distribution.

An analysis on presence of oxides and sulfides through the sample was performed on samples from shearing tests (FC, SSC and PWPC). To avoid the boundary effects due to irregular shape of the samples, only the inner portion with rectangular-section of the samples has been considered.

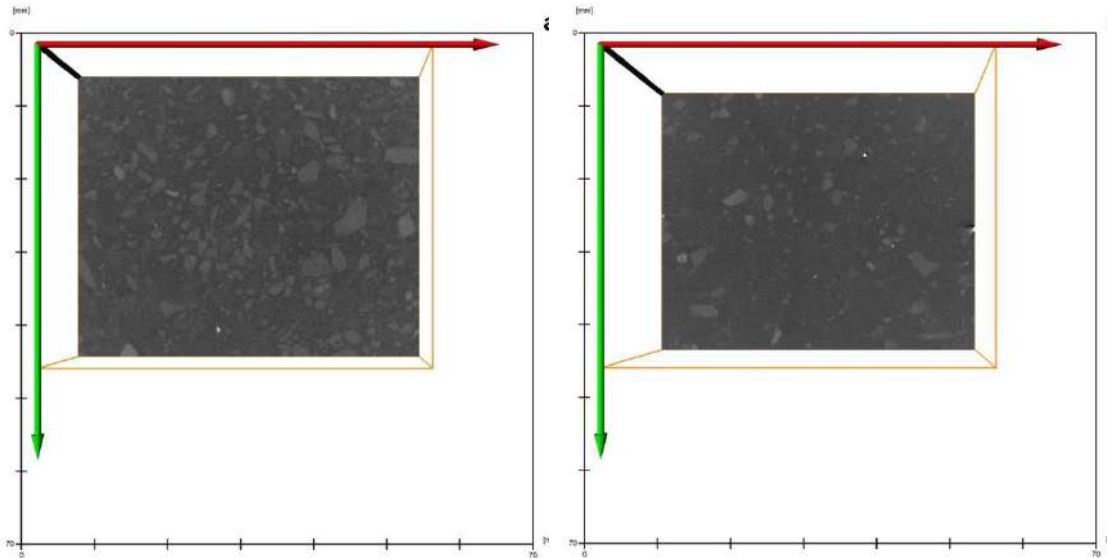


Figure 124 – example of differences between slice from outside (a) and inside the shear zone (b). Mont de La Saxe (67.4-67.7m) sample.

The results (Table 10) showed that the shear zones presents a less hard mineral grains (e.g. oxides and/or sulfides) in comparison with the outer parts (Figure 125, Figure 127 and Figure 129). This suggests mechanical ejection of hard particles from shear zone. The enrichment in the lower part was – probably -due to samples preparation inside the shear box by means of dry deposition.

Table 10 – percentage distribution of oxides and sulfides inside the samples from DPRI tests

SAMPLE	LOWER PART	SHEAR ZONE	UPPER PART
	Oxides and Sulfides [%]		
SSC test (67.4-67.7m)	47	5	48
FC test (73.4-73.7m)	69	10	21
PWP test (77.0 – 77.4m)	56	8	36



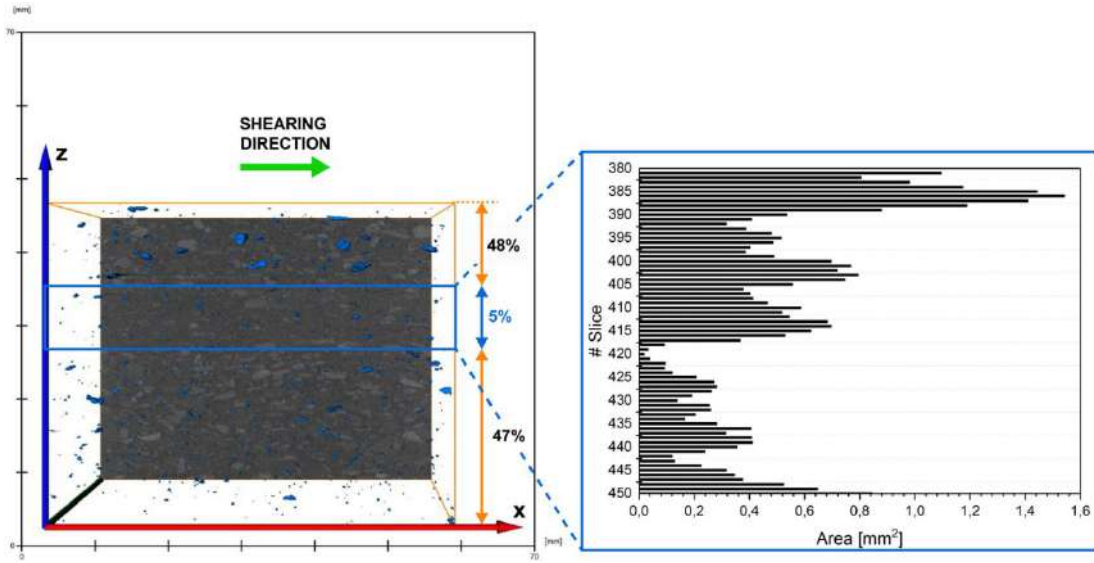


Figure 125 – distribution for different parts of the sample of hard minerals from SSC sample test (67.4-67.7m) and close up to the shear zone with single distribution for slice

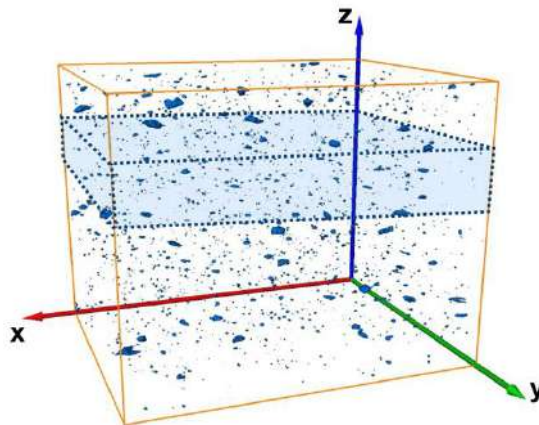


Figure 126 - 3D distribution of the hard minerals with indicated (colored part) the shear zone

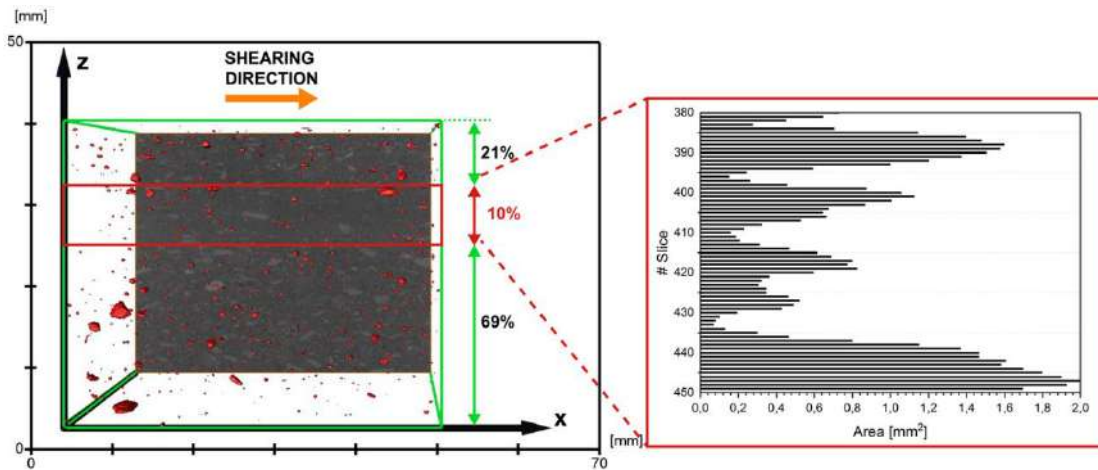


Figure 127 – distribution for different parts of the sample of hard minerals from FC sample test (73.4-73.7m) and close up to the shear zone with single distribution for slice

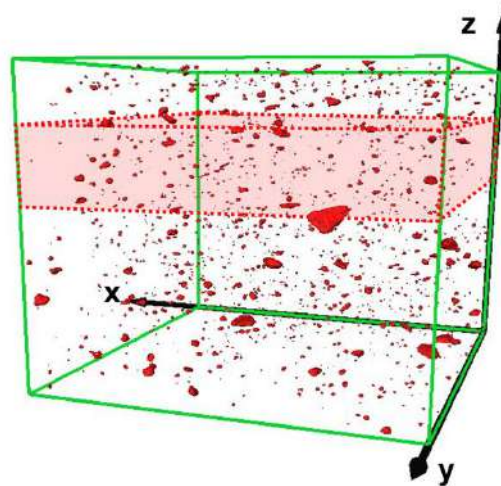


Figure 128 - 3D distribution of the hard minerals with indicated (colored part) the shear zone

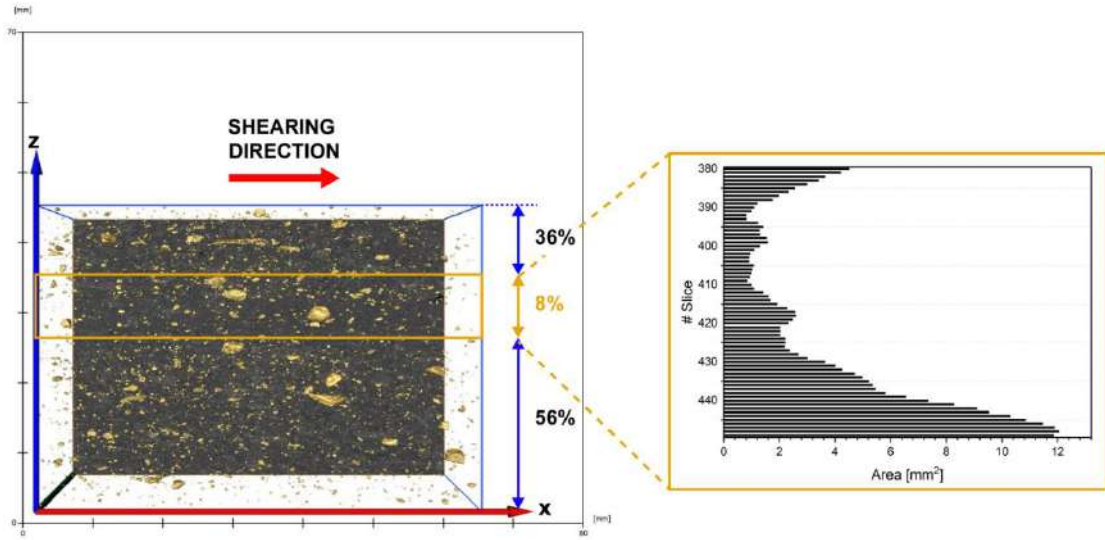


Figure 129 – distribution for different parts of the sample of hard minerals from PWPC sample test (77.0-77.4m) and close up to the shear zone with single distribution for slice

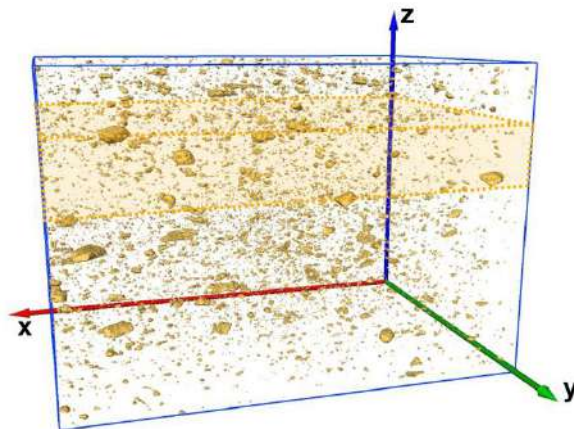


Figure 130 - 3D distribution of the hard minerals with indicated (colored part) the shear zone

### 4.3 Discussion

Most of samples used in the experimental campaign come directly from shear zones where the physical degradation process already occurred, and the material was affected by a grain-size reduction. In the shear zone the material is not uniform and even a hand sample observation reveals zones highly fractured and other reduced down to powder. Therefore, it is possible to highlight a gradual transition from the shear zone material to intact rock. The intact rock mineralogic composition, characterized by the presence of carbonates, phyllosilicates, quartz (single or in veins), graphite and sulfides (Perello et al., 1999) is essentially the same detected on shear zone samples and close to that observed by other authors (Tiwari and Marui, 2005, Yamasaki and Chigira, 2011, and Straühal et al., 2017) for similar lithologies. The SEM analyses provide evidence about texture before and after the mechanical tests. This is important to understand how the shear band movement influence the presence, distribution and the preferred orientation of minerals. The SEM analyses conducted before and after the shearing tests, evidenced also the presence of graphite and phyllosilicates in all the samples. Graphite is a well-known solid lubricant, and the phyllosilicates – usually – show a preferred alignment. Their presence can lead to decreasing friction coefficient values and the macroscopic sliding in a slip zone is most likely dominated by sliding of sheet silicate particles (e.g. Colletini et al., 2009; Schäbitz et al., 2018). These mechanisms involved in the formation of landslide basal shear zones are similar to those occurring in faults (Oohashi et al., 2011, 2012; Straühal et al., 2017).

Two main microstructures have been recognized, defined cracked and gouge (Figure 131). Typical features of a cracked microstructure are angular fragments and a relatively low area fraction of matrix, whereas in gouge, the grains are more rounded, and the area fraction of matrix is higher. In both cases, the term matrix denotes those grains of the shear zone, which are smaller than a given threshold size or smaller than the resolution at the given magnification. This terminology is purely geometrical and has no implications for the mechanical properties such as cohesion.

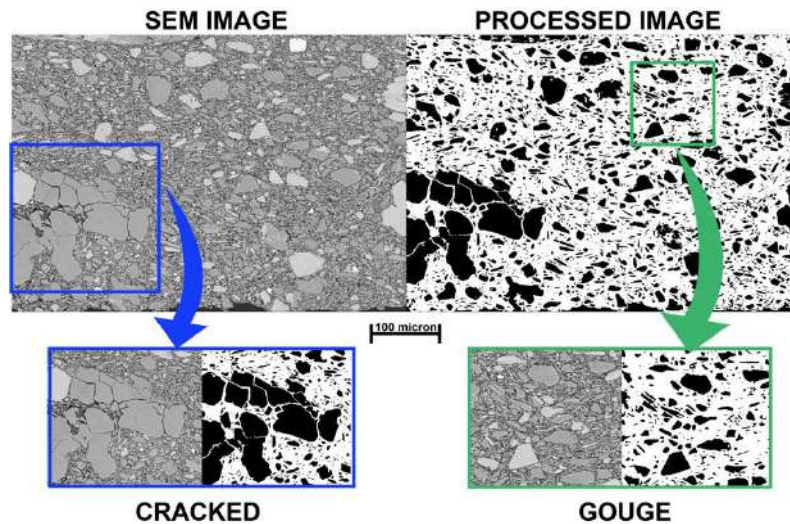


Figure 131 – Microstructures attained during progressive shearing. Scale 100  $\mu\text{m}$ . Frames outlining distinct microstructures types, with an enlarged view. Note that both microstructures consist of quartz grains.

Complex fabric was recognized through SEM investigation, that structure is assimilable to the SC-fabric on phyllites (fine-grained mylonitic) shear zone (Figure 132), also known as kinematic indicator for the shear direction.

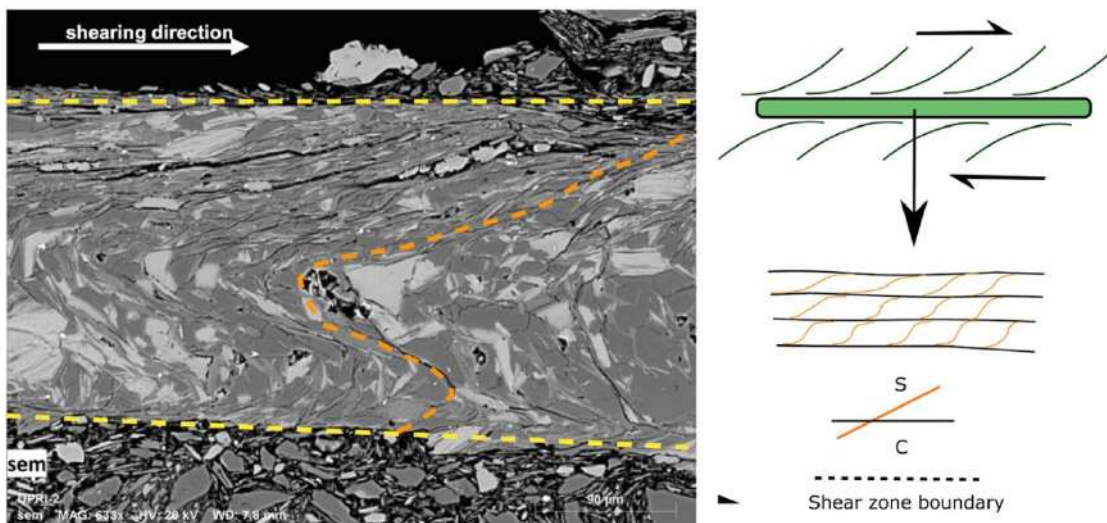


Figure 132 – similar microstructures between sample from DPRI tests and SC-fabric in mylonitic shear zone (modify after Passchier & Simpson, 1986).

Image analyses were performed to characterize particles into the samples (Figure 133) by extracting parameters (e.g. area of particles, Feret's diameter, i.e. the longest distance between any two points along the selection boundary, also known as maximum caliper); Feret's Angle, 0 - 180°, i.e. the angle between the Feret's diameter and a line parallel to the x-axis of the image; Aspect Ratio, i.e. major axis/minor axis and roundness, i.e. inverse of Aspect Ratio).



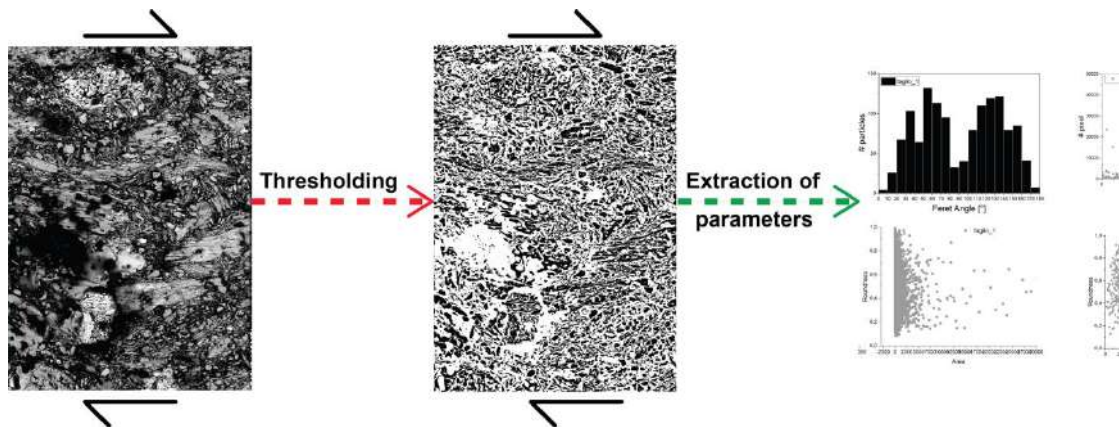


Figure 133 – workflow for data extraction from SEM images through image thresholding

First phenomenon observed through these analyses is the preferred alignment of the particles (e.g. Figure 113). In contrast to data presented by Straühal et al. (2017) a significant and preferred alignment of phyllosilicates after shearing was always observed, and – according with them – domains with a subparallel alignment of phyllosilicates forming shear-induced foliation structures were observed. As shown in Figure 134 the preferred alignment of the particles is made clear by observing the Feret's Angle distribution. For chaotic samples (e.g. Figure 119; Figure 134c) the alignment is not present and the angle distribution is quite casual with all classes well represented with the exception for values around  $90^\circ$  (i.e. sub-vertical in the images). Instead the samples with a marked preferred alignment (e.g. Figure 113 and Figure 116) showed a different distribution, the samples with the shearing direction sub-vertical (e.g. Figure 113) the classes angles distribution is largest toward sub-vertical, i.e. over  $70^\circ$  and below  $140^\circ$  (Figure 134b), while for samples with a shearing direction nearly to horizontal (Figure 134a) the most represented classes are low angle (i.e.  $<45^\circ$  and  $>130^\circ$ ). As shown in Figure 140 most of the particles have a low roundness (i.e. with Aspect Ratio  $>1$ ) and – according to shear direction – are aligned toward shear direction.

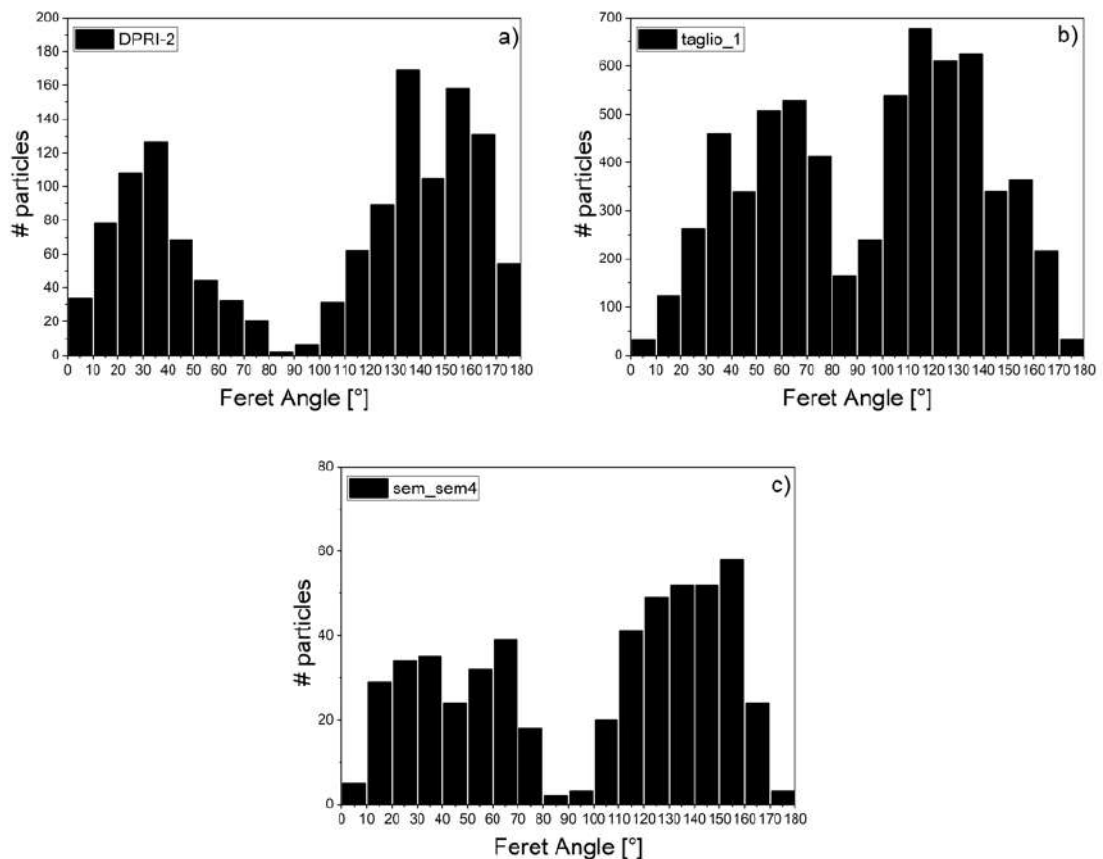
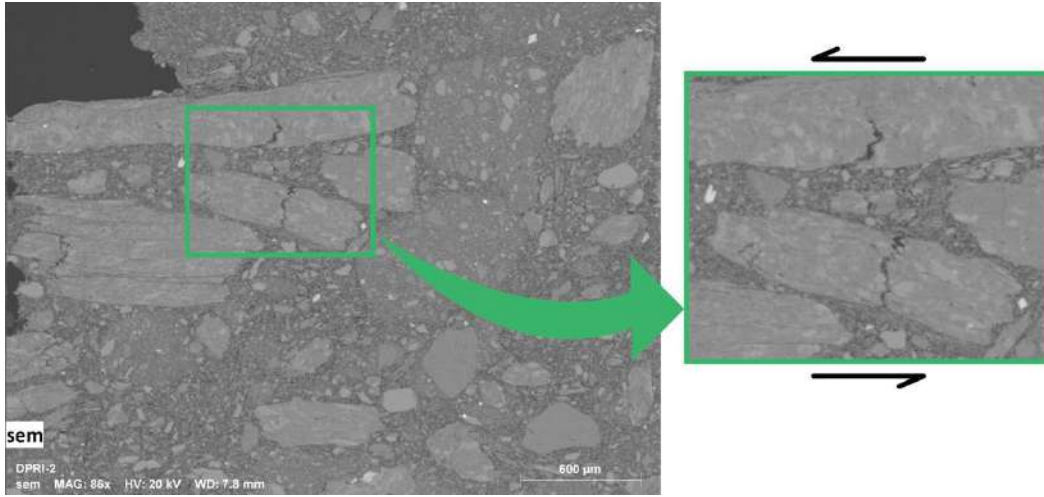
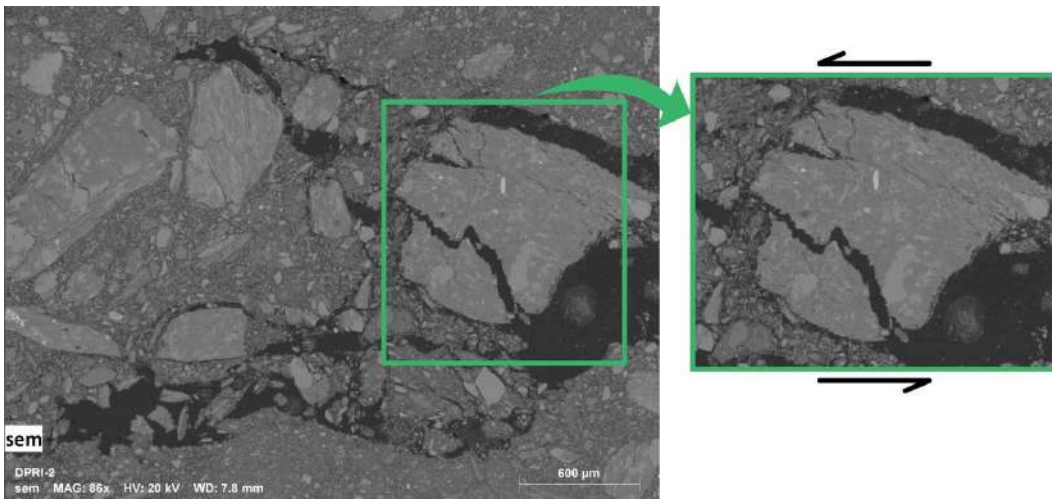


Figure 134 – Feret's angle derived by thresholding process; three different organization of particles are presented, the first one (on left) is with shearing direction parallel to x-axis (0-180°); instead, in centre is the distribution of angles for sample with shearing direction parallel to y-axis; finally, the third graph (on right) is for chaotic sample, characterized by not a real alignment for particles.

Another phenomenon occurring during shearing is the grain size reduction (GSR) by grain crushing, the re-orientation of grains and the larger grains ejection from the shear zone by shearing, which generate an extremely fine-grained gouge described (Wang and Sassa, 2000; Fedà, 2002; Luzzani, 2002; Okada et al., 2004, Agung et al., 2004; Wang et al., 2010; among others) both in faults and in landslides (Schäbitz et al., 2018). In our tests the GSR is computed in about 1 % (see section 3.3.1). At SEM scale it is possible recognize the inception of the process (Figure 135 and Figure 136). Considering that the computed roundness is low, meaning that most of the particles have an Aspect Ratio > 1 and that have not accommodated large displacements. Furthermore, the roundness of the particles compared with the area of the particles (Figure 137) showed a tendency to small values of roundness for small particles meaning a generalized trend toward alignment in the shear direction.



*Figure 135 – example of incipient grain crushing in a SEM image*



*Figure 136 – example of completed grain crushing in a SEM image*

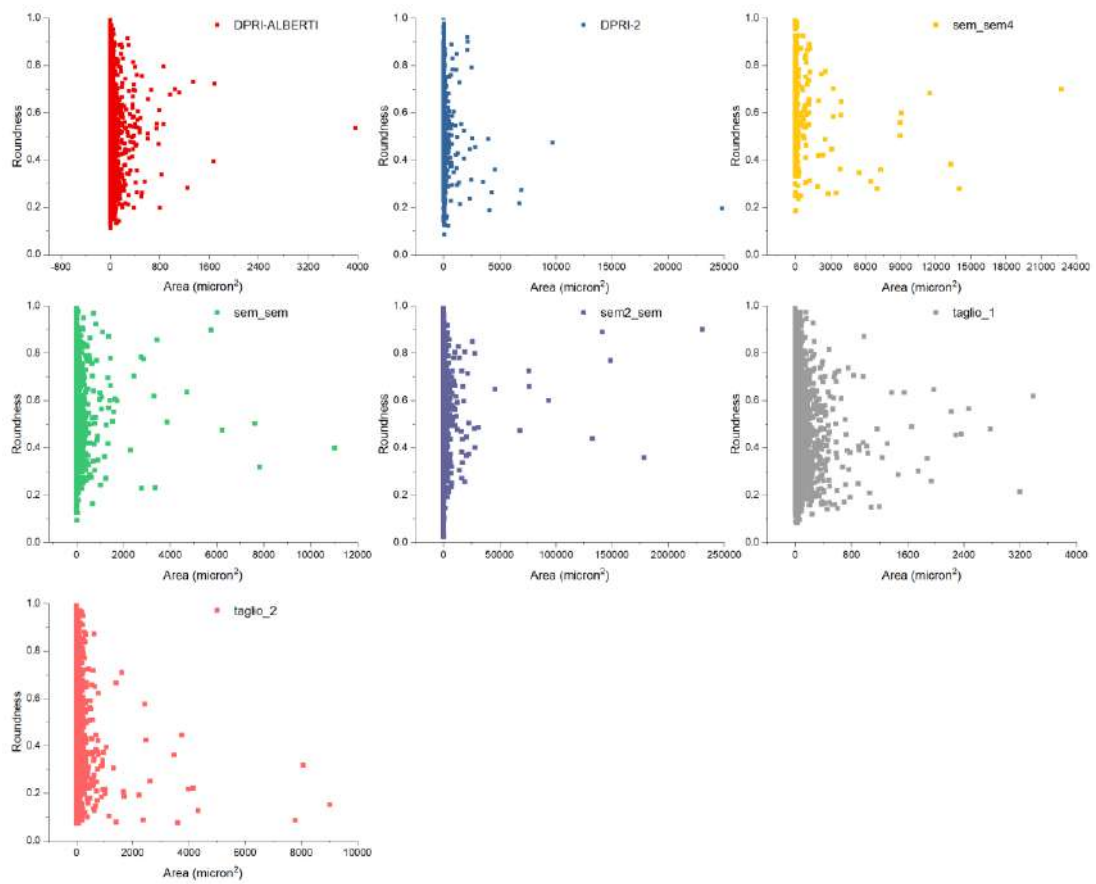


Figure 137 – distribution of roundness plotted with dimension (area in square  $\mu\text{m}$ ) of particles. In most of samples the roundness is low ( $< 0,6$ ) and the particles shown small dimension

A strong GSR was observed through the Micro-CT analyses for the three different samples of experimental tests. As demonstrated by grain-size analyses, the FC test (Figure 138a) and PWPC test (Figure 138b), due to small shearing accumulated during the tests, not shown a significant GSR, while the sample from SSC (Figure 139), that accumulated a lot of shearing, show a substantial GSR.

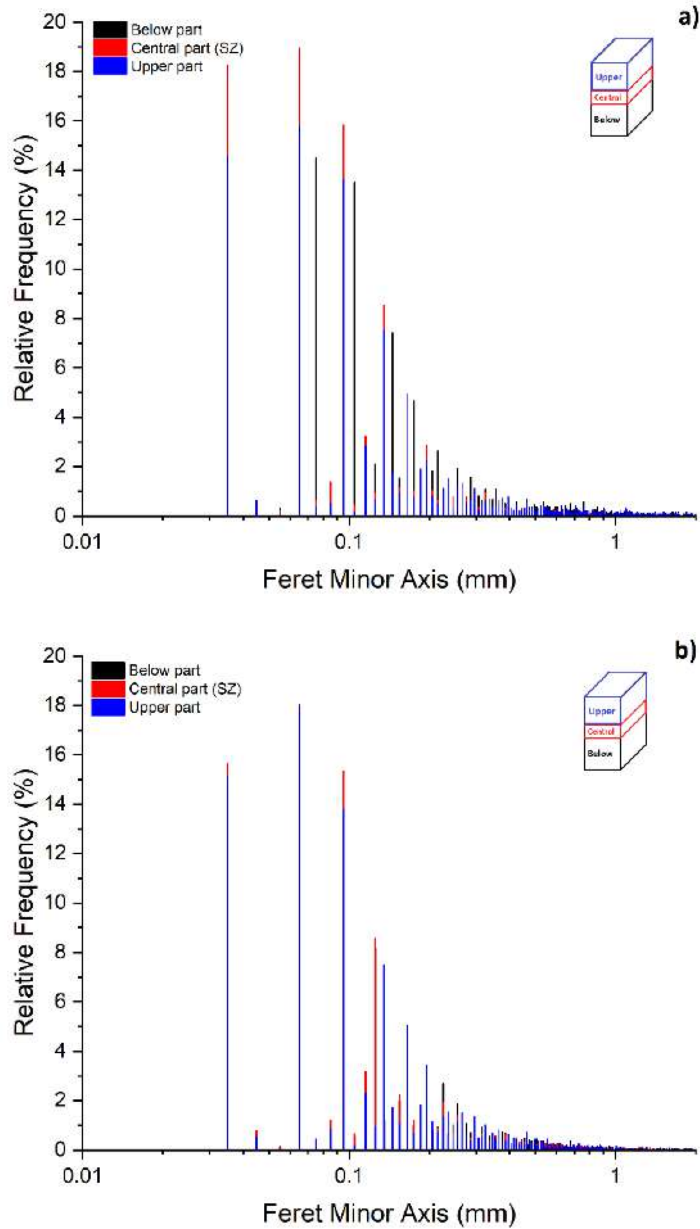


Figure 138 – grain size distribution for samples of FC test (a) and PWPC test (b).



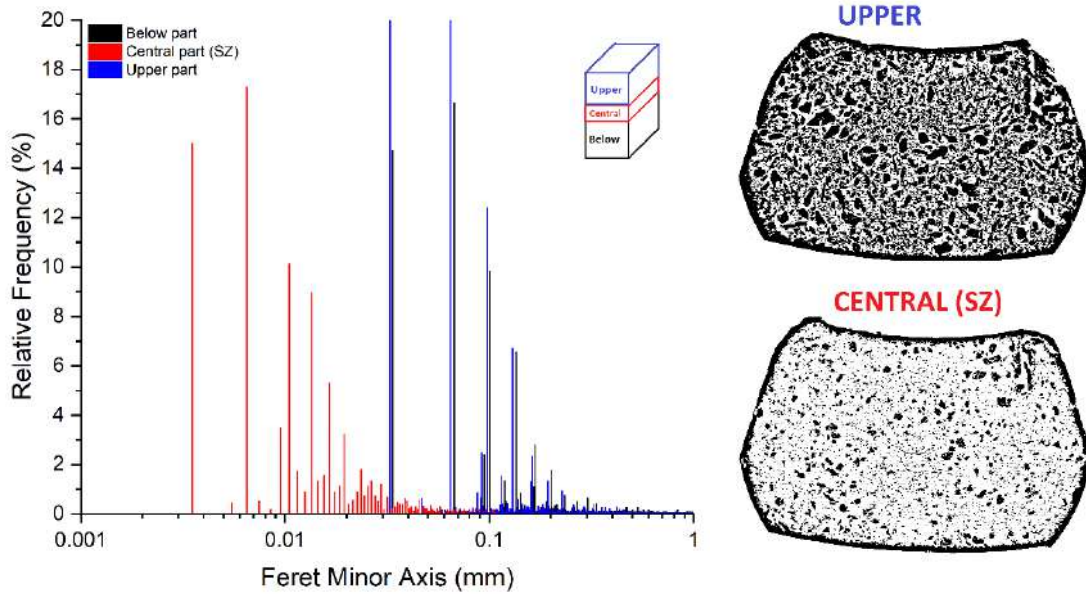


Figure 139 – grain size distribution for sample SSC test

Considering the GSR and shape of the fragments, these can be used to distinguish mature gouges (i.e., gouges which have accommodated large displacements) from fresh gouges or newly fragmented rocks. Increasing roundness is a sign of increasing wear, i.e., increasing deformation or displacement (Cladouhos, 1999; Storti et al., 2003).

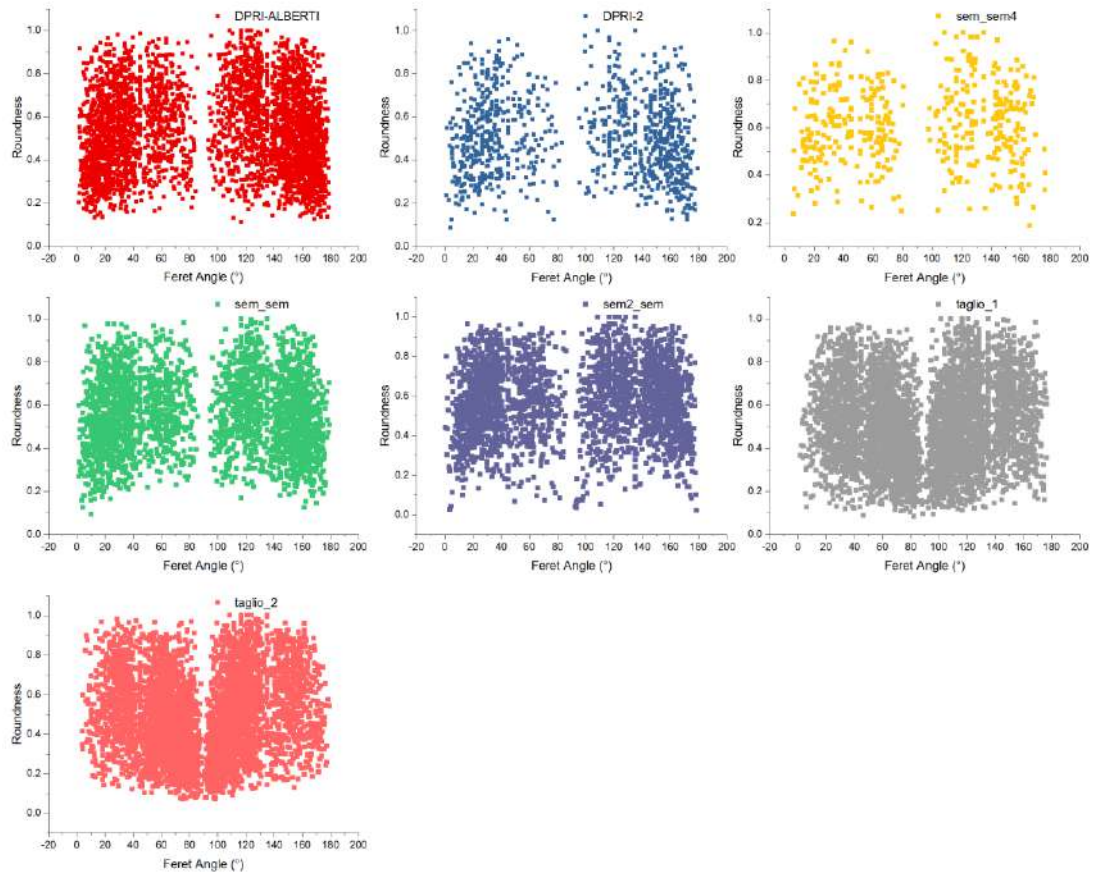


Figure 140 - distribution of roundness plotted with Feret's angle of particles. In most of samples the roundness is low ( $< 0,6$ ) and the particles showed – usually - a preferred alignment in the shearing direction

Although many studies demonstrated that the origin of graphite in faults is due to the graphitization process (mechanical or chemical processes) during the seismogenic motion (Oohashi et al., 2011, 2012), in our case the presence of the graphite could be explained by the host rocks composition and in some cases by hydrothermal precipitation of C H O rich fluid (Antoine et al., 1975; Guermani and Pennacchioni, 1998; Leloup et al., 2005).

In our samples, where the graphite content (approximately 10%; Figure 141) could be sufficient to explain the decrease in friction (e.g. Chigira et al., 2011; Oohashi et al., 2013), the shear strength reduction could be considered an effect of the presence of other phyllosilicates (e.g. Chlorite and micas) quantified by XRF analyses in at least 20%.

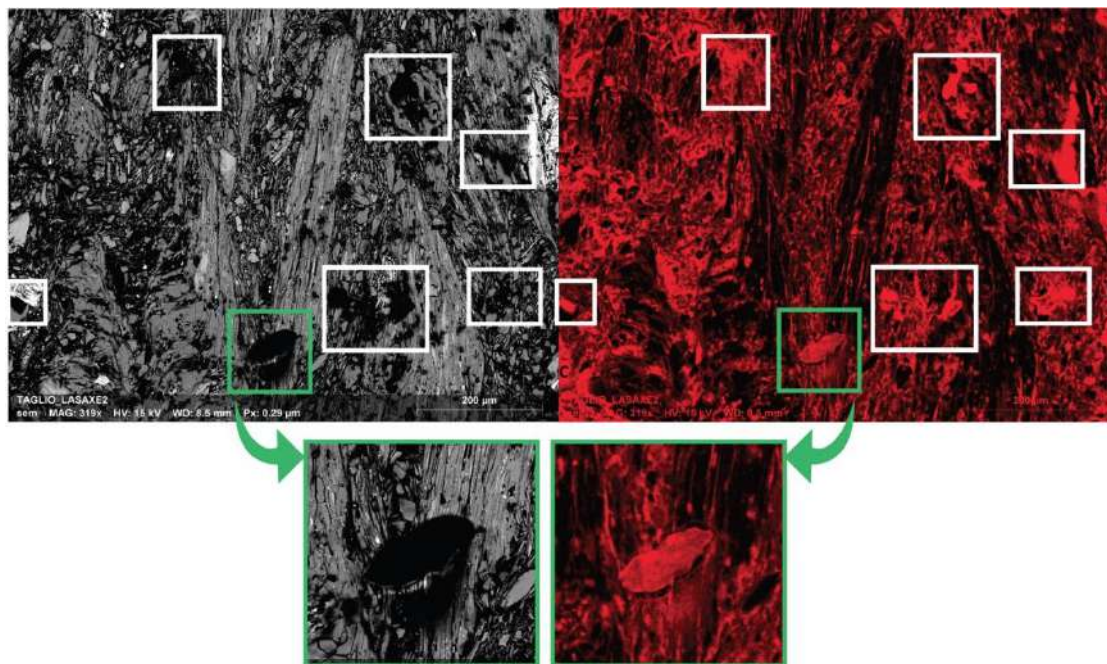


Figure 141 – example of presence of graphite in the samples with SEM images and elemental map for Carbon (C). Frames outlining a plate of this mineral.

Finally, a possible process that involves the shear band during the tests (Figure 142) includes three different phases (Fossen et al., 2016). In the first phase (Stage 1), samples present disorganized particles (*chaotic band*) inside the shear zone; starting the shearing, progressively the tested material starts to align the phyllosilicates and the grain crushing occurs (*phyllosilicates band*, Stage 2); finally, close to failure and when the process of comminution is completed, appears a well localized *cataclastic band* in the central part of the sample (Stage 3).

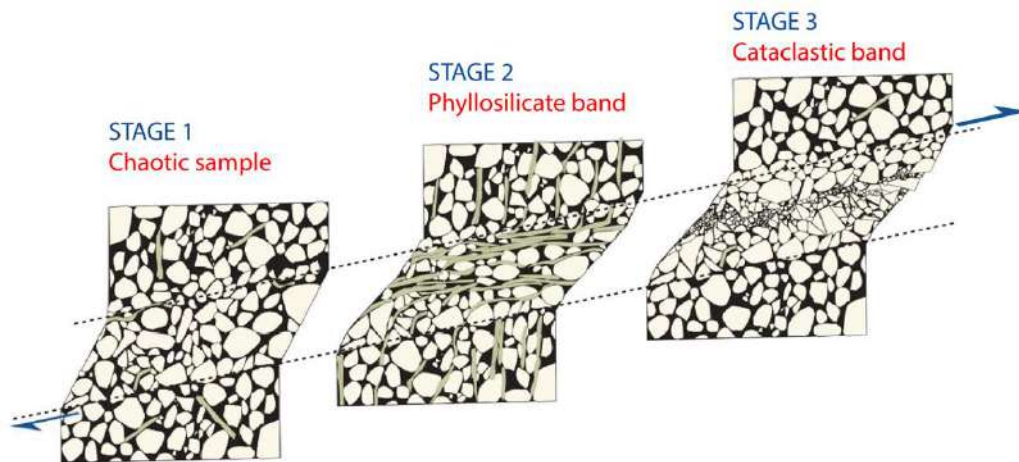


Figure 142 – possible evolution of the shear zone through time increasing the shearing (modify after Fossen, 2016)

## 1D BLOCK VISCO-PLASTIC MODELING

*Essentially all the models are wrong, but some are useful.*

Numerical modeling has been applied by several authors, with the aim to comprehend and verify landslide mechanisms, kinematics, and dynamics (Eberhardt et al. 2004; Hungr & McDougall 2009). Accurate investigations, the geological investigations of the area, the definition of the boundary conditions and the characterization of the shear zone material are fundamental to obtain a successful description of the acting phenomena. Numerical simulations aided the scientific understanding of the analyzed phenomena, forecast their future evolution and the design of effective countermeasures. In any mathematical model, only the essential information required to achieve the goals for which the model is used, are taken into account since every model is a simplification of the reality. Critical analysis, regarding the factors that mostly influence the slope behavior, should be done before and after the modelling phases. Several authors (Jing & Hudson 2002; Carter et al. 2000; Stead et al. 2001; Stead et al. 2006) described and discussed the applications of numerical methods for slope stability analysis. In Stead et al. (2006) an overview of the conventional and advanced methods is presented. The methodologies developed for slope stability analysis are subdivided into three main categories: from traditional preliminary kinematics and limit equilibrium techniques to the continuum and discontinuum numerical modelling, to the most advanced hybrid methods. Stead et al. (2006) stressed that the choice of the performed stability analysis methodology should be related with the complexity of the investigated mechanism. If the simple methodology can be considered too much simplified compared to the advanced numerical codes, they in contrast provide essential information easily to be managed in comparison with the great amount of data given by more sophisticated techniques.

In order to model complex sliding masses subject to continuous slow movements, especially for phenomena where the displacement is related to water table fluctuations, it is quite convenient to:

- i) analyze and model the time-dependent shear zone mechanical behavior of the materials;
- ii) assume the water table fluctuation as main driving factor to reproduce acceleration;
- iii) maintaining



a high level of simplicity such to allow implementation within EWS (Early Warning System) for risk management.

The evolution of Mont de La Saxe rockslide motion can be interpreted as the superposition of two mechanisms: (i) a sort of “creep”-driven movement that is always present even under dry-winter conditions, when the water table is either below or close to the failure surface, and (ii) a superimposed (seasonal) acceleration-slowness trend directly related to the snow-melt (late spring–early summer) and to the consequent water table fluctuations, which disappears when the water inputs are reduced (late summer and winter conditions).

For the analysis of time-dependent material behavior, such as the creep in geo-materials (Desai and Zhang, 1987; Cristescu, 1994; Samtani et al., 1996; Cristescu and Cazacu, 2000), several visco-plastic material models have been proposed. Some authors (Butterfield, 2000; Gottardi et al., 2001; Corominas et al., 2005) adopted a typical viscous fluid type approach (e.g. Bingham model) or analytical laws (Ranalli et al., 2010). Another formulation is the visco-plastic model based on the Perzyna’s approach (Perzyna, 1963, 1966; Olszak and Perzyna, 1969). According to this, the viscous-plastic strain rate is governed by the stress values through a definition of a viscous-plastic nucleus. The main feature and advantage of the Perzyna’s approach is the capability to extend the models originally developed under the elasto-plasticity framework to viscous-models. The characteristics of the Perzyna’s model as well as the numerical discretization have been addressed by various authors (Simo, 1989; Sluys, 1992; Wang, 1997; Simo and Hughes, 1998; Heeres et al., 2001).

In this thesis, we present an improved version of the 1D pseudo-dynamic visco-plastic numerical model proposed by Frigerio (2010) and lately extended by Secondi et al. (2011, 2013), Crosta et al. (2014), Frigerio et al. (2014) and Castellanza et al. (2015) and its validation through a comparison between in situ monitoring data and model results based on selected case study to refine the landslide evolution scenarios.

In Secondi et al. (2013), 1D pseudo-dynamic visco-plastic model, based on Perzyna's approach, was developed, and it was applied to the Bindo- Cortenova translational landslide (Italian Prealps, Lombardy, Italy). The viscous nucleus has been assumed to be bi-linear: in one case, irreversible deformations develop uniquely. The model has been calibrated and subsequently validated on a long temporal series of monitoring data and it seems quite reliable in simulating the in-situ data. The model was applied also to Vallcebre case study (Spain; Corominas et al. 2005) (Figure 143).

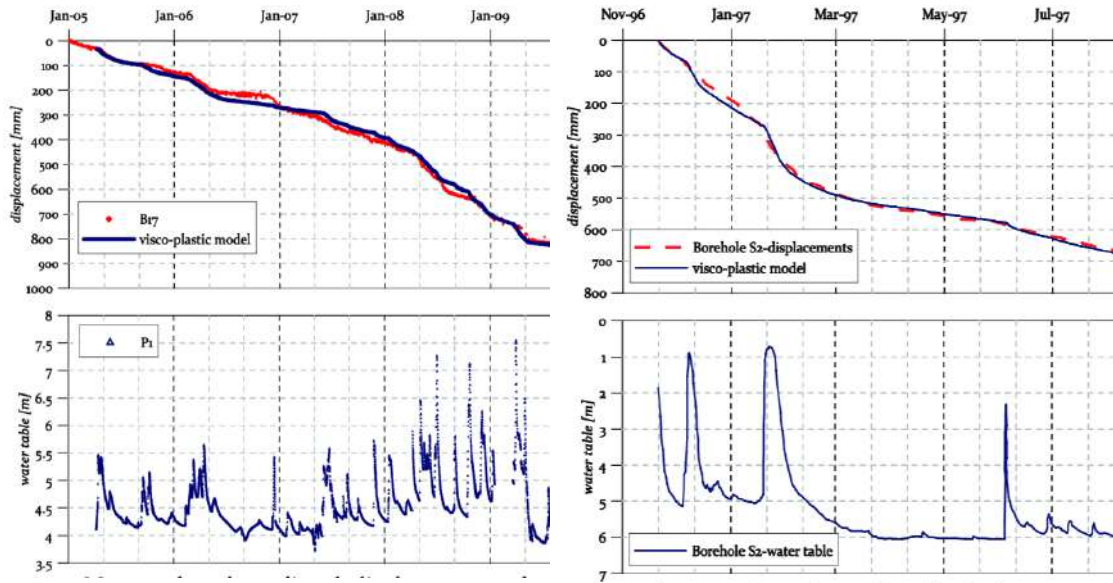


Figure 143 - Measured and predicted displacements obtained by using the previously discussed approach for Bindo-Cortenova case study (on left) and Vallcebre case study (on right) (from Secondi et al., 2013)

Subsequently, Crosta et al. (2014), improved the original version and have applied it to Mont de La Saxe case study. The model was calibrated through the analysis of the piezometric and snowmelt data allowing the forecast of the expected displacements, showing a good performance at predicting rockslide displacements during acceleration and deceleration phases controlled by groundwater level oscillations. Also, in this work, the viscous nucleus is assumed bi-linear. Then, the model has been calibrated and subsequently validated on a long-time series of monitoring data for Mont de La Saxe rockslide (period 2010-2012), and it seems reliable for simulating the in-situ data. A 3D simplified approach is suggested by subdividing the landslide mass into distinct interacting blocks by three different discretization (Figure 147).

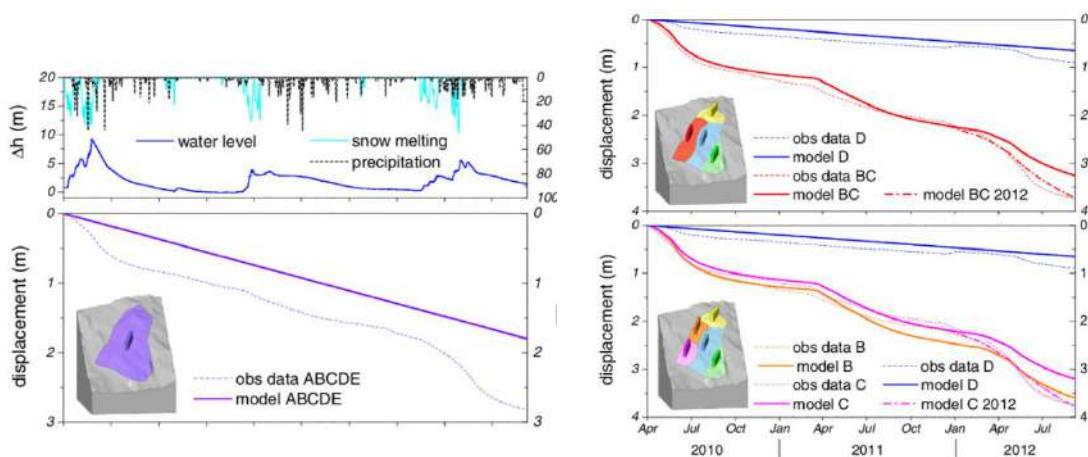


Figure 144 - Plots comparing the results of the visco-plastic model to the measured cumulative displacements for different discretization schemes (1 to 3) of the rockslide mass and of the piezometric surface. Color codes refer to the different subareas. Model 2012 shows the results of a best-fitting model for the 2012 displacements only (from Crosta et al., 2014)

In Castellanza et al. (2015) it was presented a similar 1D rigid visco-plastic model, modified for what concerns the expression of the viscous nucleus by the friction strain-rate weakening. The viscous nucleus was replaced with an exponential law characterized by parameter  $\alpha$ , governing the shape of the viscous nucleus (Figure 145).

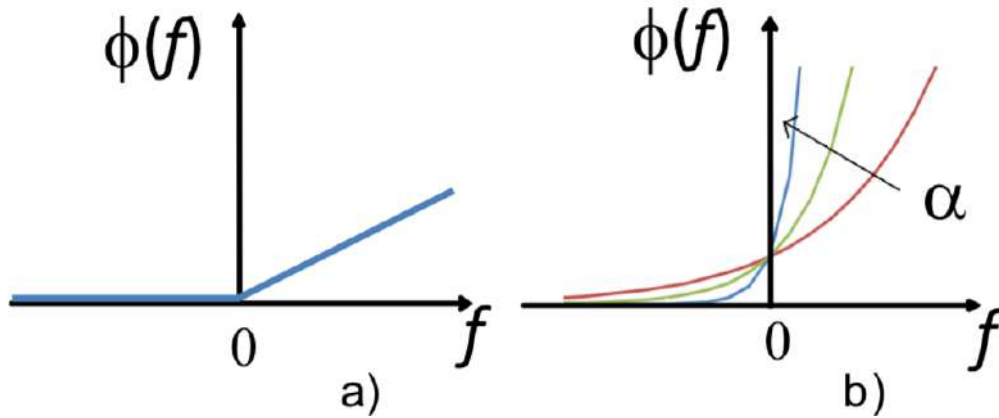


Figure 145 - a) bilinear viscous nucleus; b) exponential viscous nucleus (from Castellanza et al., 2015)

## 5.1 Multi Interacting Blocks Slope Analyses (MIBSA model)

MIBSA (Multi Interacting Blocks Slope Analysis) model overcomes the traditional methods based on the limit equilibrium analysis thanks to its capability of reproducing slope displacements after the failure occurrence. In this model the Newmark's approach (1965) and the Perzyna's theory (1963) have been coupled (Frigerio 2010; Secondi et al. 2011, 2013, Frigerio et al., 2014) to model rockslide behavior. According to Newmark's approach, each volume in which the rockslide is subdivided is interpreted as a rigid block, where the active forces considered are (i) the weight, (ii) the inertial forces, and (iii) the seepage force deriving from the water table level which is a function of time,  $\Delta h_w(t)$ . All the non-linearities are lumped both (i) at the interface between the rigid block and the bedrock and (ii) at the interface between each volume and those surrounding it. The mechanical response of these interfaces, that is usually assumed to be rigid-visco-plastic, has been tested using a power law viscous nucleus. Similar approaches have been introduced in the recent past by Karampatakis and Hatzigogos (1999), and also Puzrin and Schmid (2012).

### 5.1.1 Single block motion

The proposed model is based on these hypotheses:

- The block is rigid, and it is in contact in perfect adherence with underlying layer;
- The block movement is due to the shear zone deformation whose constitutive model is viscous-plastic and based on Perzyna's approach;
- The block motion is water and gravity driven so that the motion evolution is governed by the ground water table variations.

Considering the forces acting on the block:

- Seepage force  $\rightarrow \mathbf{J}$ ;
- Self-weight of the block  $\rightarrow \mathbf{W}$ ;
- Soil reaction  $\mathbf{R}$  between the shear band and block;

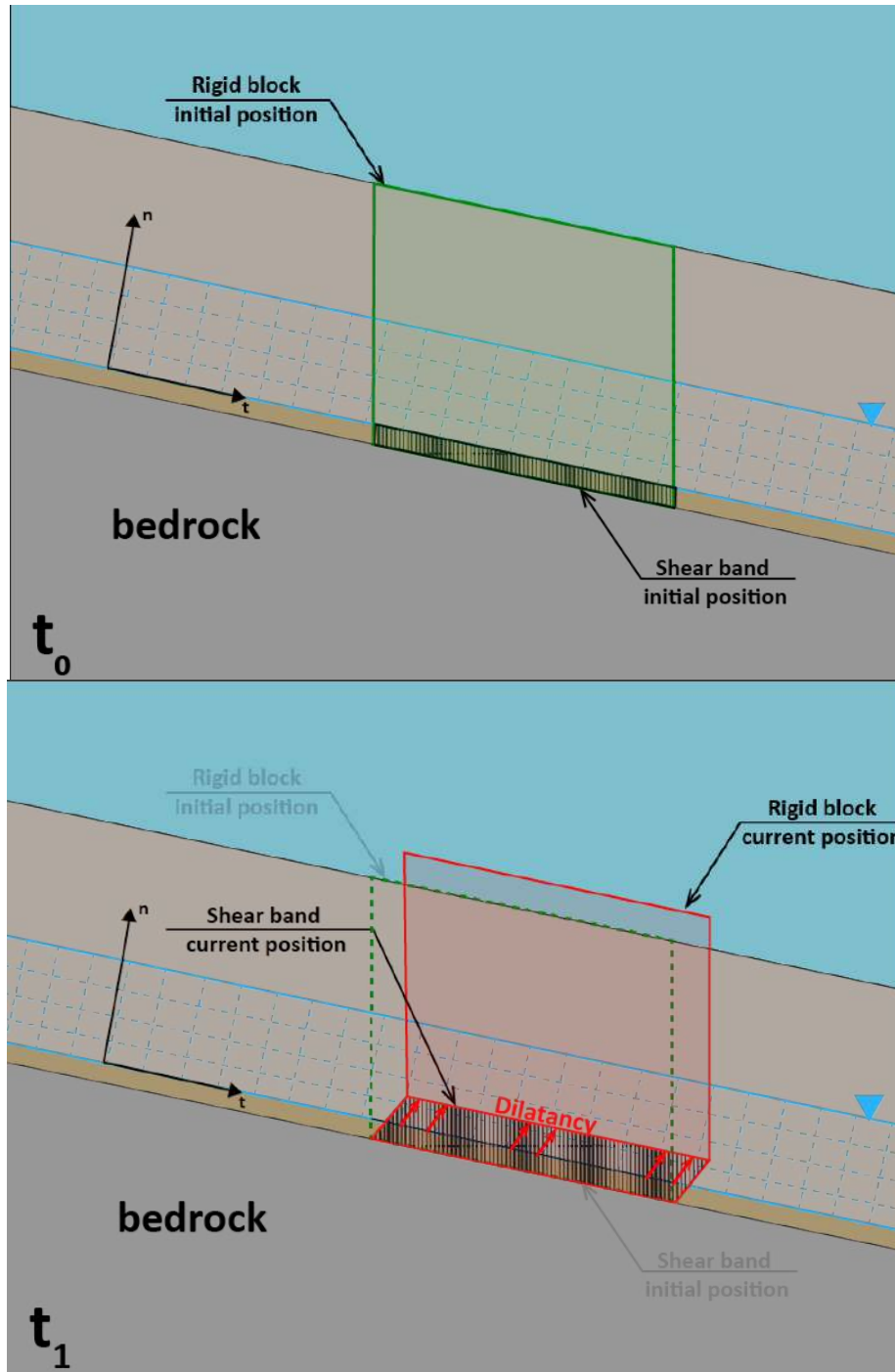


Figure 146 – 1D model at initial time ( $t_0$ ) and after starting ( $t_1$ )

According to linear momentum balance equation:

$$\mathbf{R} + \mathbf{W} + \mathbf{J} = m\ddot{\mathbf{u}} \quad (\text{eq. 5.})$$

where  $\ddot{\mathbf{u}}$  is the block acceleration and  $m$  is the block mass. The dot above the variables stands for the time derivatives).



Assuming the uniformity of the normal and tangential stress at bottom of the block, the soil reaction can be expressed as:

$$\mathbf{R} = (\sigma' + u_w)BL\hat{\mathbf{n}} - \tau BL\hat{\mathbf{t}} \quad (\text{eq. 6.})$$

where  $B$  is the out of plane size, while  $L$  is the block length along the slope direction,  $\tau$  and  $\sigma$  are the tangential and normal stresses components, respectively, and  $u_w$  is the pore-water pressure at the block bottom.

Furthermore, weight forces and seepage forces can be written as:

$$\mathbf{W} = -(mg \cos \alpha)\hat{\mathbf{n}} + (mg \sin \alpha)\hat{\mathbf{t}} \quad (\text{eq. 7.})$$

where  $\alpha$  is the slope angle measured with respect to the horizontal plane. Finally, the displacement, velocity and acceleration can be written as:

$$\mathbf{u} = u_n\hat{\mathbf{n}} + u_t\hat{\mathbf{t}} \quad (\text{eq. 8.})$$

$$\dot{\mathbf{u}} = \dot{u}_n\hat{\mathbf{n}} + \dot{u}_t\hat{\mathbf{t}} \quad (\text{eq. 9.})$$

$$\ddot{\mathbf{u}} = \ddot{u}_n\hat{\mathbf{n}} + \ddot{u}_t\hat{\mathbf{t}} \quad (\text{eq. 10.})$$

Substituting the force and displacement decomposition into the motion equation, and projection along the normal and tangential directions the following ordinary differential equation system is obtained:

$$\begin{cases} (\sigma' + u_w)BL - mg \cos \alpha = m \ddot{u}_n \\ -\tau BL + mg \sin \alpha + J = m \ddot{u}_t \end{cases} \quad (\text{eq. 11.})$$

The block mass  $m$ , the seepage force component  $J$  and the pore-water pressure  $u_w$  depend on the water table height by means of the following expressions:

$$m = [\rho_{dry}(H - H_w) + \rho_{sat}H_w] LB \cos \alpha \quad (\text{eq. 12.})$$

$$J = BLH_w \sin \alpha \cos \alpha \quad (\text{eq. 13.})$$

$$u_w = \gamma_w H_w \cos^2 \alpha \quad (\text{eq. 14.})$$

where  $\rho_{dry}$  and  $\rho_{sat}$  are the dry and saturated density. This system is not sufficient to solve the problem because the unknowns are more than the equations, so that the shear band model equations are required.

### 5.1.2 The shear band model

From the experimental point of view, the mechanical behavior of the shear band can be described by means of a viscous plastic model because it takes into account the measured delayed effect in the strain field development. Furthermore, for the sake of simplicity, we assume that the strain field is uniform and characterized by normal  $\epsilon^{vp}$  and tangential  $\gamma^{vp}$  components. According to this, the corresponding displacement field is given by:

$$u_n^{vp} = -\epsilon^{vp}\Delta s \quad (\text{eq. 15.})$$

$$u_t^{vp} = \gamma^{vp}\Delta s \quad (\text{eq. 16.})$$

where  $\Delta s$  is the shear band thickness assumed to be constant in time and in space,  $u_n^{vp}$  and  $u_t^{vp}$  are the normal and tangential components of the viscous plastic displacements. The sign minus in the above equation is introduced to take into account the geotechnical convention, in which the  $\epsilon^{vp}$  is positive in compaction.

In this work, the viscous plastic model is based on the Perzyna's approach, where the viscous plastic strain increment is evaluated by means of the following flow rule:

$$\begin{bmatrix} \epsilon^{vp} \\ \gamma^{vp} \end{bmatrix} = \tilde{\gamma}\phi(f^{vp})\frac{\partial g^{vp}}{\partial \sigma} \quad (\text{eq. 17.})$$

where  $\tilde{\gamma}$  is a parameter called fluidity,  $\phi$  is the viscous nucleus,  $f^{vp}$  is the viscous loading function,  $g^{vp}$  is the viscous plastic potential, and finally, the stress vector  $\sigma$  is defined as:

$$\sigma = \begin{bmatrix} \sigma' \\ \tau \end{bmatrix} \quad (\text{eq.18.})$$

The yield function is classical Mohr-Coulomb criterion rewritten in dimensionless form as:

$$f^{vp}(\sigma) = \frac{\tau - \tau_{res}}{\sigma'} \quad (\text{eq.19.})$$

Where  $\tau_{res}$  is the tangential strength, a function depending on the cohesion  $c$  and the current value of the friction angle  $\phi$  as:

$$\tau_{res} = c + \sigma' \tan \phi \quad (\text{eq.20.})$$

The viscous nucleus is defined as:

$$\phi(f^{vp}) = \langle f^{vp} \rangle \quad (\text{eq.21.})$$

where  $\langle \cdot \rangle$  stands for the McCauley brackets defined as:

$$\langle x \rangle = \begin{cases} x & \text{if } x \geq 0 \\ 0 & \text{if } x < 0 \end{cases} \quad (\text{eq.22.})$$

This choice of the viscous nucleus implies that if the stress point lies in or lies on the yield surface no viscous plastic strain is developed.

Finally, the plastic potential is defined as:

$$\frac{\partial g^{vp}}{\partial \sigma} = sgn(\tau) \begin{bmatrix} d \\ 1 \end{bmatrix} \quad (\text{eq.23.})$$

where  $sgn$  is the sign function,  $d$  is dilatancy factor obtained by the following dilatancy-stress ratio relationship:

$$d = m - \frac{\tau}{\sigma'} \quad (\text{eq.24.})$$

where  $m$  is a model parameter which represents the stress ratio when the dilatancy is null. As it was mentioned early, the friction angle is not constant because it changes during the viscous plastic strain development due to the hardening process.

This is governed by the following hardening rule:

$$\dot{\phi} = -c_{\phi}(\phi - \phi_f)\dot{\gamma}^{vp} \quad (\text{eq.25.})$$

where  $\phi_f$  is the friction angle at failure and  $c_{\phi}$  is a material parameter controlling the friction angle rate for a fixed value of the shear strain rate. It is worth noting that since the  $\dot{\gamma}^{vp}$  has the same sign during the landslide motion, the friction tends progressively to  $\phi_f$  even if its initial value is greater or less than  $\phi_f$ .

### 5.1.3 Compatibility condition and the final system

The compatibility condition imposes the perfect adherence between the shear band and the block, therefore:

$$u_n^{vp} = u_n \quad (\text{eq.26.})$$

$$u_t^{vp} = u_t \quad (\text{eq.27.})$$

According to this, the system of equations is:

$$\left\{ \begin{array}{l} m\ddot{u}_n - (\sigma' + u_w)BL + mg \cos\alpha = 0 \\ m\ddot{u}_t + \tau BL - mg \sin\alpha - J = 0 \\ \dot{u}_n - \tilde{\gamma}\phi(f^{vp}) \frac{\partial g^{vp}}{\partial \sigma'} (-\Delta s) = 0 \\ \dot{u}_t - \tilde{\gamma}\phi(f^{vp}) \frac{\partial g^{vp}}{\partial \tau} (\Delta s) = 0 \\ \dot{\phi} + c_\phi \frac{\phi - \phi_f}{\Delta s} \dot{u}_t = 0 \end{array} \right. \quad (\text{eq.28.})$$

which is a partial differential equation.

### 5.1.4 Calibration and improvements

Comparing the models in the literature with the new here proposed model, the main improvements are:

- the possibility to set the parameters for shear zone model obtained through the mechanical characterization performed by the experimental campaigns conducted with ring shear apparatus at DPRI laboratories;
- $c_\phi$ , evolution of mobilized friction angle by means of the hardening rule
- the possibility to compute normal displacements due to the introduction of a dilatancy variable.

The model has been applied and validated by artificial data using two different discretization. The first discretization (#1 in Figure 147), considering a single block for entire slope and a successive with three different blocks not taking into account their interactions because not yet implemented in this version of the model (e.g. A, B and C blocks in Figure 146).

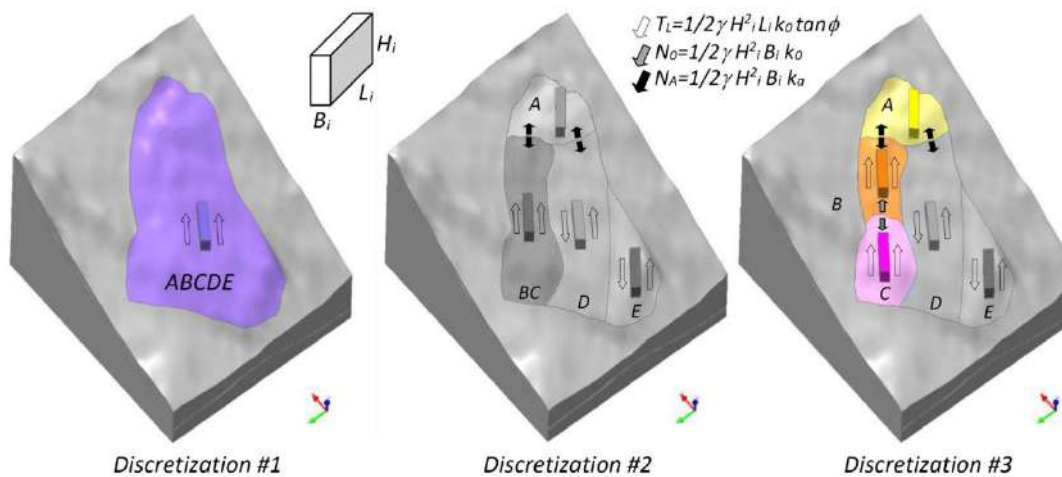


Figure 147 – different discretization schemes adopted in the model: #1 single equivalent rockslide block; #2, #3 multiple equivalent rockslide blocks (from Crosta et al., 2014)

Regarding the geometric (Table 11) and mechanical (Table 12) parameters of each discretization were used those proposed by Crosta et al. (2014) as reference values.

Table 11 - Geometric parameters for each rockslide sector relative to each of the two discretization schemes

Discretization	Zone	Slope Inclination $\alpha$ [°]	Depth failure surface [m]	Transversal length [m]	Longitudinal length [m]	Shear band thickness $\Delta s$ [m]
#1	ABCDE	33.5	62.4	280.0	620.4	1
#2	A	39.0	60.8	180.0	169.2	1
	B	37.2	78.0	107.5	198.9	1
	C	29.0	70.3	122.0	226.6	1

Table 12 - Values for the mechanical parameters adopted in the 1D visco plastic model to compute displacements for each one of the discretization schemes

Discretization	Zone	$c'$ [kPa]	$\phi'$ [°]	$\gamma$ [1/s]	$c_\phi$
#1	ABCDE	0.0	30.65	4.00 E-06	
#2	A	0.0	30.65	4.00 E-06	
	B	0.0	29.04	4.00 E-06	
	C	0.0	26.69	4.00 E-06	



Before the comparison of numerical and in-situ results, parametric analyses have been performed to highlight the role played by the fundamental parameters. To distinguish between the effects of parameters to the hydrologic input, three different artificial configurations have been used. Evaluate the long-term effects the length of artificial inputs was equal to complete seasonal cycle ( $\approx 1$  year). The first one with constant value, and the others characterized by triangular shape or – closer to real case – a rapid increasing followed by exponential decreasing (Figure 148a). Finally, a real GWT oscillation of Mont de La Saxe has been used (Figure 148b) derived by three different piezometers using the instrument closest to the relative block.

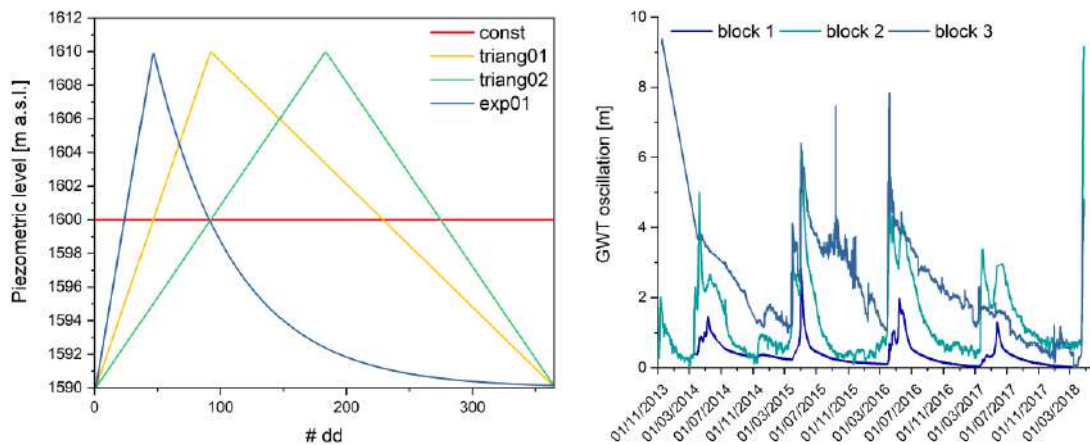


Figure 148 – GWT oscillation considered (on left) during the parametric analysis and on application to case study (on right)

In the parametric analyses, the following four selected parameters have been investigated:

- $c_\phi \rightarrow$  hardening variable parameter related to rate of friction angle degradation [-]
- $\Delta s \rightarrow$  shear band thickness, geometric parameter [m]
- $\tilde{\gamma} \rightarrow$  viscous fluidity, viscous parameter [ $s^{-1}$ ]
- $\phi \rightarrow$  initial value of friction angle, mechanical parameter [°]

In Table 13 the list of parameter values is shown together with the corresponding labels. This list is independent of the hydrological inputs and the base label refers to the standard set of variables that it used as reference (Crosta et al., 2014).

*Table 13 - parameter values for sensitive analysis. Base is considered the values from Crosta et al. (2014), gt: fluidity viscosity; ds: thickness of shear zone; fi: friction angle and cf: hardening parameter related to rate of friction angle degradation*

Parameters							
$\tilde{\gamma}$ [1/s]	<b>base</b>	<b>gt_01</b>	<b>gt_02</b>	<b>gt_03</b>	<b>gt_04</b>	<b>gt_05</b>	<b>gt_06</b>
	4,00E-08	4,00E-09	2,00E-08	8,00E-08	4,00E-07	4,00E-06	4,00E-05
$\Delta s$ [m]	<b>base</b>	<b>ds_01</b>	<b>ds_02</b>	<b>ds_03</b>	<b>ds_04</b>	<b>ds_05</b>	<b>ds_06</b>
	1,00E+00	1,00E-02	2,50E-01	5,00E-01	2,00E+00	4,00E+00	1,00E+01
$\phi$ [°]	<b>base</b>	<b>fi_01</b>	<b>fi_02</b>	<b>fi_03</b>	<b>fi_04</b>	<b>fi_05</b>	<b>fi_06</b>
	3,57E+01	3,74E+01	3,39E+01	3,92E+01	4,71E+01	3,21E+01	2,85E+01
$c_{\phi}$ []	<b>base</b>	<b>cf_01</b>	<b>cf_02</b>	<b>cf_03</b>	<b>cf_04</b>	<b>cf_05</b>	<b>cf_06</b>
	0,00E+00	1,00E-02	1,00E-01	2,00E-01	5,00E-01	1,00E+00	2,00E+00

### 5.1.5 Results and discussion

The first parameter evaluated was  $c_\phi$ , a dimensionless hardening variable parameter related to rate of friction angle degradation. It has been tested with the previously presented ground-water oscillations (Figure 148). In the previous versions of the model, this parameter was not implemented, and the degradation of friction angle was not taken into account.

The  $c_\phi$  parameter, varies up to 1 order of magnitude (cf05 and cf06; Table 13). The results show a linear trend for constant ground-water table with a small difference in the results, while the triangular and exponential oscillations (Figure 148) show a sensibility to the variations of the piezometric level with a curvilinear trend.

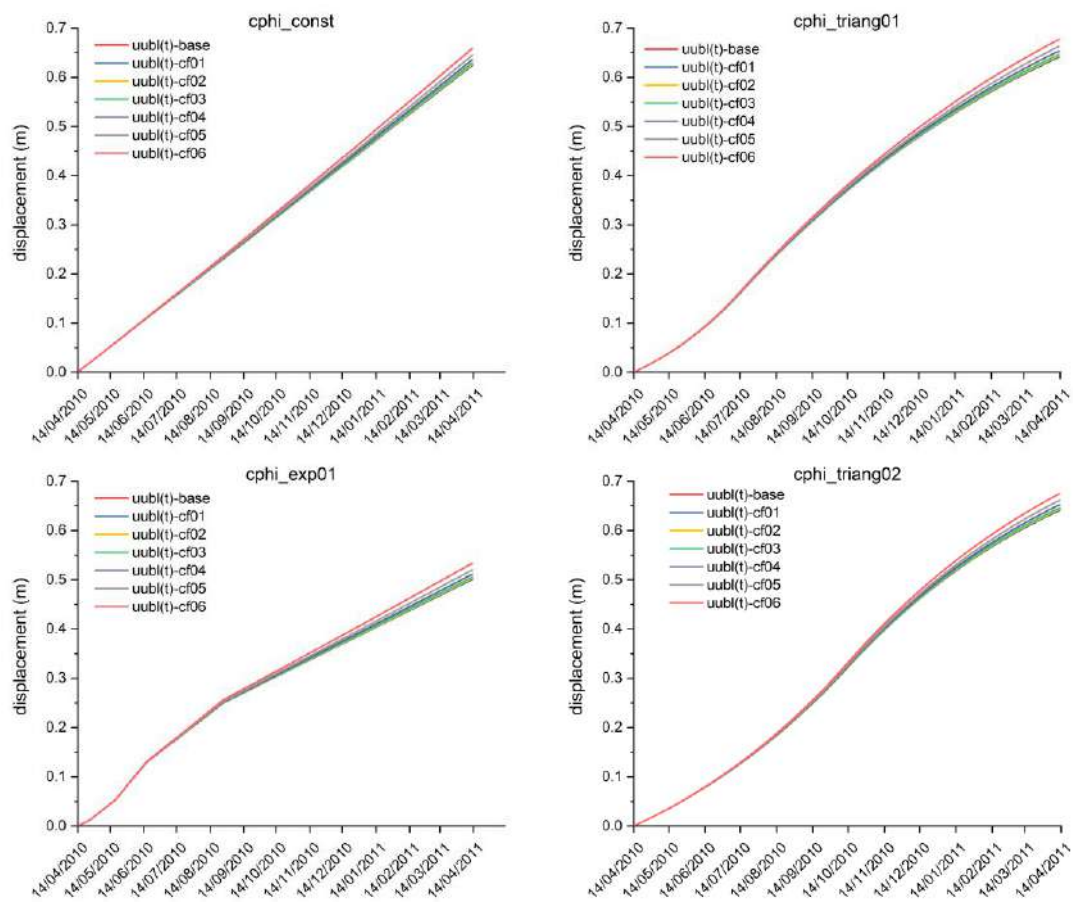


Figure 149 – parametric analyses for  $c_\phi$  and 4 different ground-water oscillations. In clockwise direction: constant GWT, triangular 01, triangular 02 and exponential oscillations (Figure 148)

In order to appreciate the importance of this parameter the final values of tangential displacements obtained in the previous simulations are reported in Figure 150, where the results are grouped according to the hydrological input. The results show that increasing  $c_\phi$  the final value of displacement increases independently of the input, this is due to fact that increasing  $c_\phi$  the reduction of friction angles is more marked and consequently the material strength reduces, and this implies great values of displacement. The shape of the correlation is dependent on the chosen hardening rule since in this work, a saturation law has been suggested, the graph shows a sort of asymptotic values.

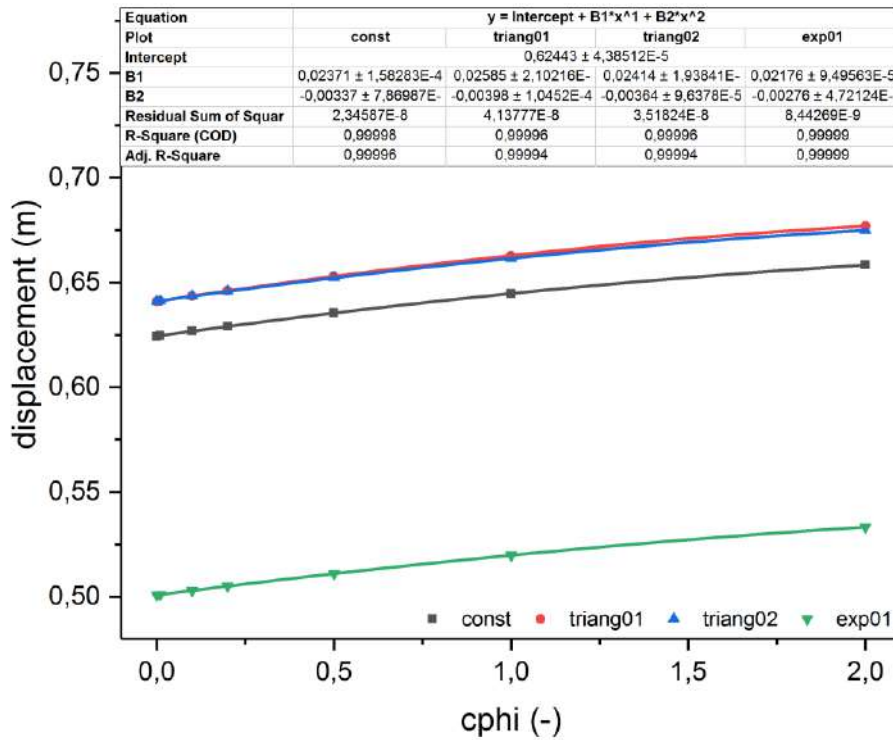


Figure 150 – relationship between  $c_\phi$  vs maximum displacement

The second parameter evaluated was a geometric parameter, the thickness of shear band (Ds) expressed in [m]. In the previous versions of the model this parameter was adopted of 1m for all considered blocks, but as demonstrated in this work the thickness of the shear zone is not constant along the entire slope affected by the rockslide, for this reason was tested with different values.

In the sensitivity analysis this parameter has been varied over 3 orders of magnitude (from ds01 and ds06; Table 13). The results shown a linear trend for constant ground-water table with a significant difference in the final results and also for triangular and exponential oscillations (Figure 148) show a sensibility to the variations of the piezometric level with a curvilinear trend.

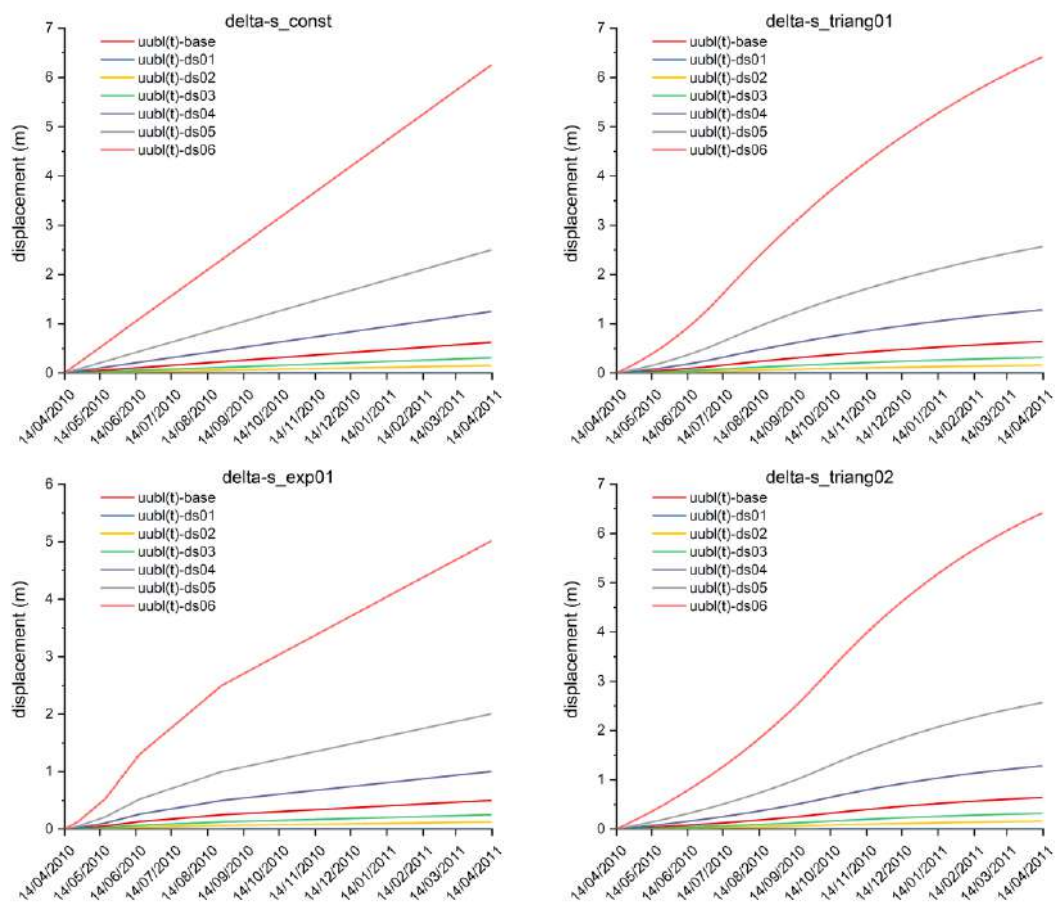


Figure 151 - parametric analyses for  $\Delta s$  and 4 different ground-water oscillations. In clockwise direction: constant GWT, triangular 01, triangular 02 and exponential oscillations (Figure 148)



In these simulations the tangential stress and normal effective stress are the same, since they are controlled only by block size, involved material and the GWT, the normal and tangential strain are the same according to flow rule (eq. 17.). This implies that the normal and tangential displacements are directly proportional to the shear band thickness according to the compatibility equations (eq. 15. and eq. 16.). Therefore, the correlation follows a straight line, suggesting the direct proportionality (Figure 152).

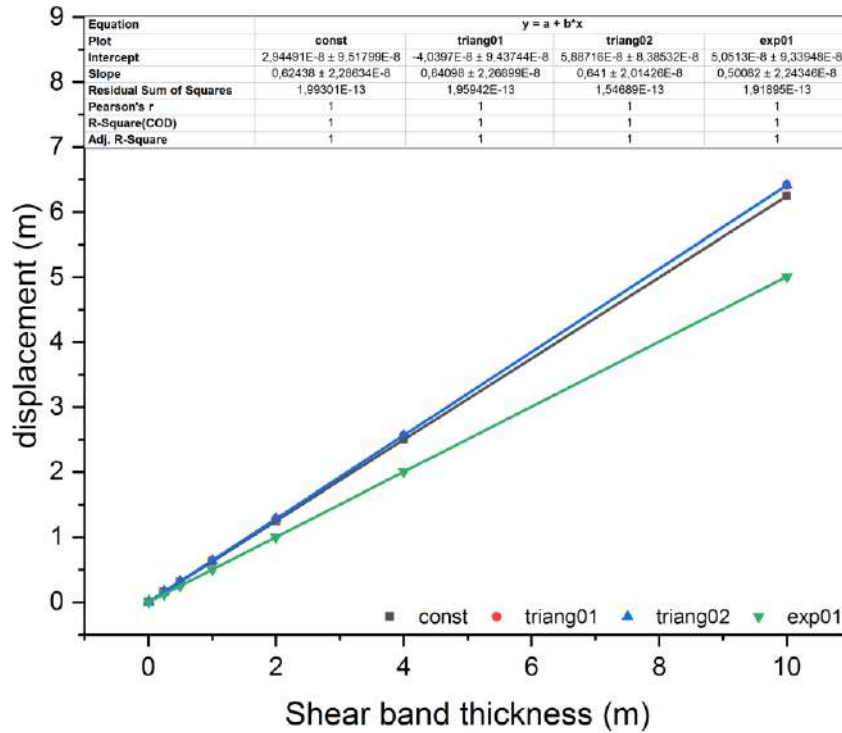


Figure 152 – relationship between shear band thickness vs maximum displacement

The third parameter evaluated was a viscous parameter  $\tilde{\gamma}$ , i.e. the viscous fluidity expressed in  $[s^{-1}]$ . In the previous versions of the model, this parameter has been kept constant at  $4 \cdot 10^{-8} s^{-1}$ . By increasing this value, the fluidity  $\tilde{\gamma}$  increases.

In the sensitivity analysis, this parameter has been varied up to 4-orders of magnitude (from gt01 and gt06; Table 13). The results show a linear trend for constant ground-water table with a significant difference in the results and also for triangular and exponential oscillations show a sensitivity to the variations of the piezometric level with a curvilinear trend.

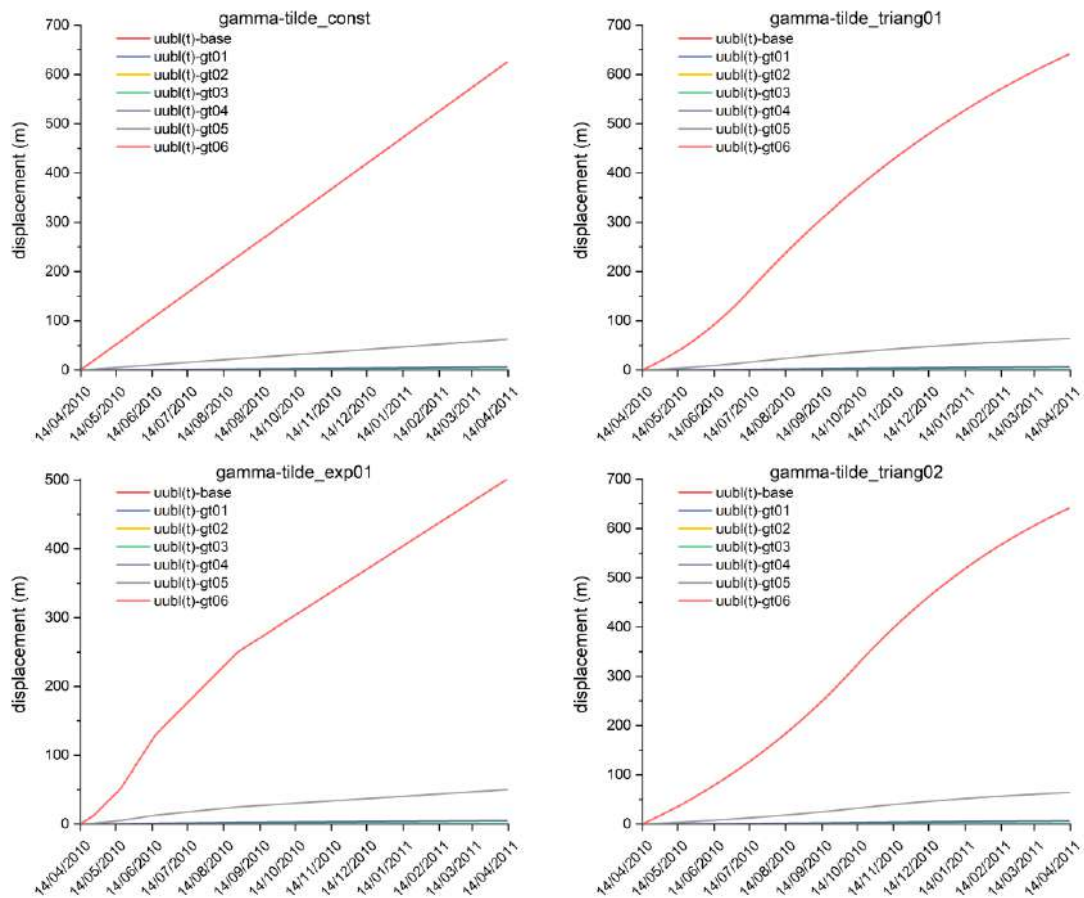


Figure 153 - parametric analyses for  $\tilde{\gamma}$  and 4 different ground-water oscillations. In clockwise direction: constant GWT, triangular 01, triangular 02 and exponential oscillations (Figure 148)

Considering the eq. 17., the relationship between variation of  $\tilde{\gamma}$  and displacement, increasing the fluidity (higher values of  $\tilde{\gamma}$ ), the displacement increases linearly (Figure 154) with a direct proportion.

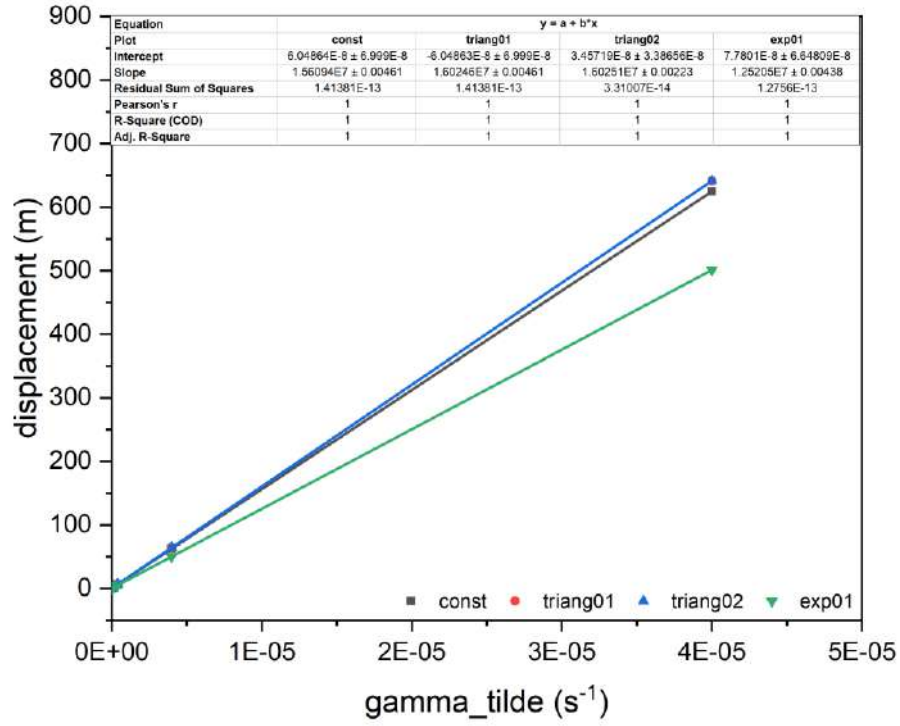


Figure 154 – relationship between  $\tilde{\gamma}$  vs maximum displacement

Finally, the last parameter evaluated has been the friction angle ( $\phi$ ) expressed in  $[\circ]$ . In the previous versions of the model this parameter was initially settled at  $30.65^\circ$ , and there was no degradation law for this parameter, which has been kept constant for the entire simulation.

The  $\Delta s$  parameter, varies until 4 orders of magnitude (ds01 and ds06). The results show a linear trend for constant ground-water table with a small difference in the results, while for the triangular and exponential oscillations (Figure 148) it shows a sensitivity to the variations of the piezometric level with a curvilinear trend.

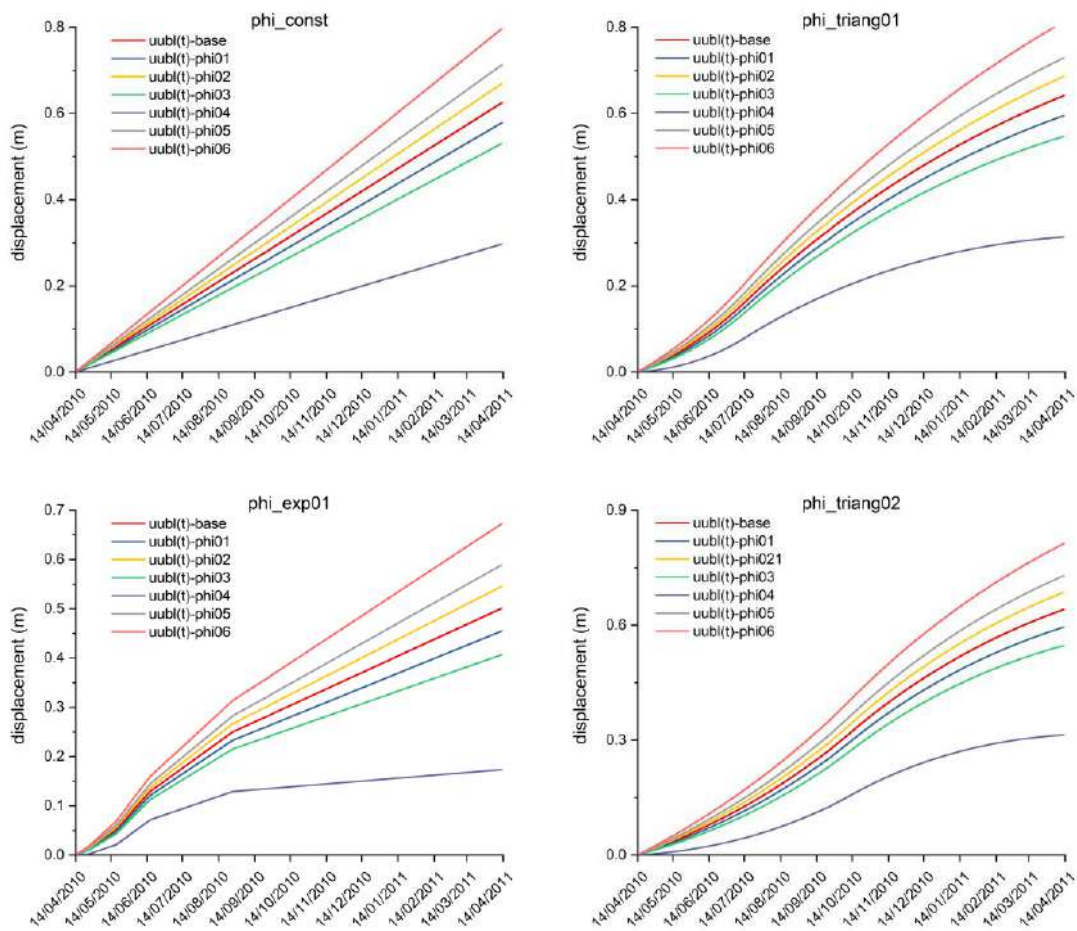


Figure 155 - parametric analyses for  $\phi$  and 4 different ground-water oscillations. In clockwise direction: constant GWT, triangular 01, triangular 02 and exponential oscillations (Figure 148)

Increasing the friction angle with a non-linear relation (eq.25.) leads to an increasing shear strength. Obviously, increasing the shear resistance the strain values reduce and - consequently - also the displacement.

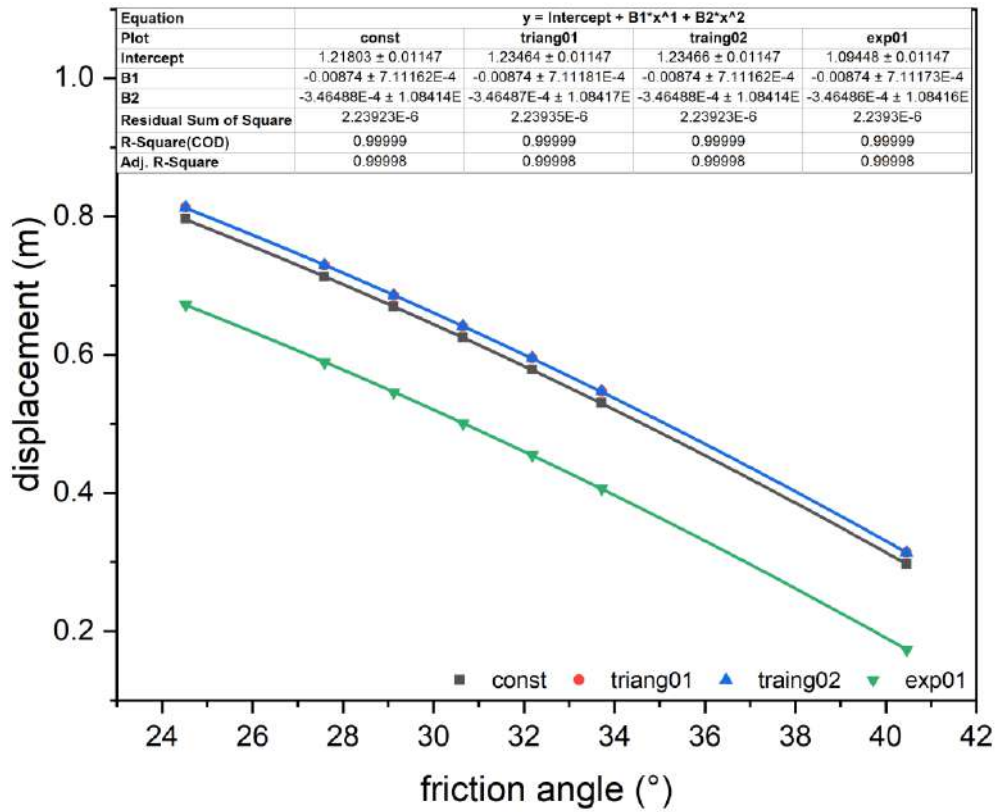


Figure 156 – relationship between friction angle vs maximum displacement



Finally, the proposed model has been applied to the case study of Mont de La Saxe. The blocks considered (i.e. #1, #2 and #3), discretized a part of the entire slope characterized by three different kinematic behaviors. The parameterization of three different blocks (Table 14) is conditioned by the involved material and consequently their kinematic behavior sectors of these. Block 1 includes the landslide head, block 2 is related with the main landslide body and – finally – block 3 is close to the landslide toe and it is characterized by debris material.

*Table 14 -Values for the mechanical parameters adopted in the 1D visco plastic model to compute displacements for each block*

Block	Ds	c' [kPa]	$\phi$ [°]	$\gamma$ [s <sup>-1</sup> ]	$c_{\phi}$
1	1.0	0.0	38.90	4.00 E-06	0
2	1.0	0.0	37.10	4.00 E-06	0
3	1.0	0.0	29.04	4.00 E-07	0

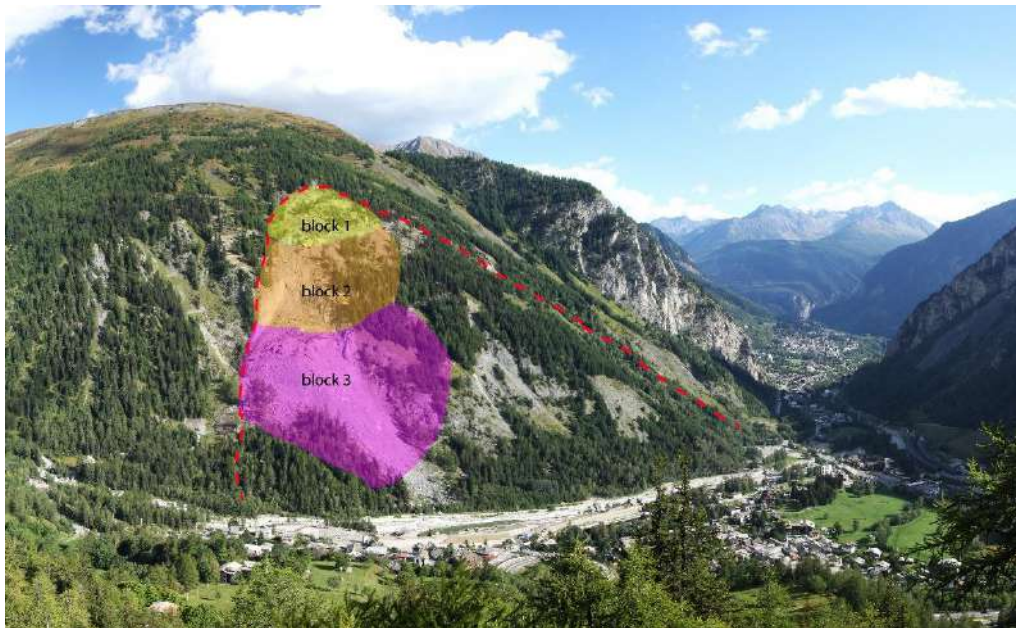


*Figure 157 – discretization of the rockslide into the different sector and blocks; in red dashed line the boundaries of the Mont de La Saxe rockslide*

The numerical simulation and the monitoring data are strongly conditioned by the GWT oscillation, considering that – as aforementioned – the behavior of rockslide is characterized by *creep*-driven movement (dry-conditions, when the water table is either below or close to the failure surface), and by seasonal acceleration trend related to water table increasing (due to snow-melt). Consequently, a strong increase of GWT leads to a significant increment of displacement rates, while during the steady-state or decreasing of GWT the displacement rate is conditioned by the viscous behavior (creep), as observed in monitoring data, experimental tests and numerical models.

The different displacements of three blocks is due to the part of landslide considered, block 1 and 2 shows a good fit between monitoring data (GB-InSAR POIs; green dotted lines) and numerical model (Figure 158 and Figure 159; red lines). In contrast, the block 3, as mentioned above, characterized by debris material, is not assimilated to a rigid block as shown by monitoring data, where close GB-InSAR POIs are characterized by great ranges of variability.

Best fitting is obtained with the parameters settled in Table 14.

Considering the results of the simulation for block 1 (Figure 158), it is clear how the model well reproduces the real displacements during 2014, 2015 and 2016, with a good response to the real ground-water oscillations. Instead, during 2017 the model seems to not fit closely the real displacement behavior, anticipating the displacements acceleration following the GWT oscillations. This is probably due to the countermeasures implemented to regime the GWT, i.e. installation of drainages networks.

Block 2 (Figure 159) show a good trend compared with real displacements, even if it underestimates the single acceleration phases, while the amount of the total displacement at the end of the simulation is close to the real one. This can be due to a larger influence of the creep phenomena in the simulation, with respect to the effects of the groundwater oscillations.

Block 3 is not showing a good fit between real displacements and numerical model. It is possible to note that, in this area, displacement of GB-InSAR POIs belonging to the same sector and located close to one another, show a high variety of values (from 10 to 70 m in about 5 years). This sector is characterized by debris material, not assimilable to a rigid block and so not perfectly included in the hypotheses of the model. It is representing one of the limitations of this approach.

As aforesaid the kinematic behavior of the landslide is different for different sectors, a deepest sensitivity analysis could allow to refine the fitting of these curves.

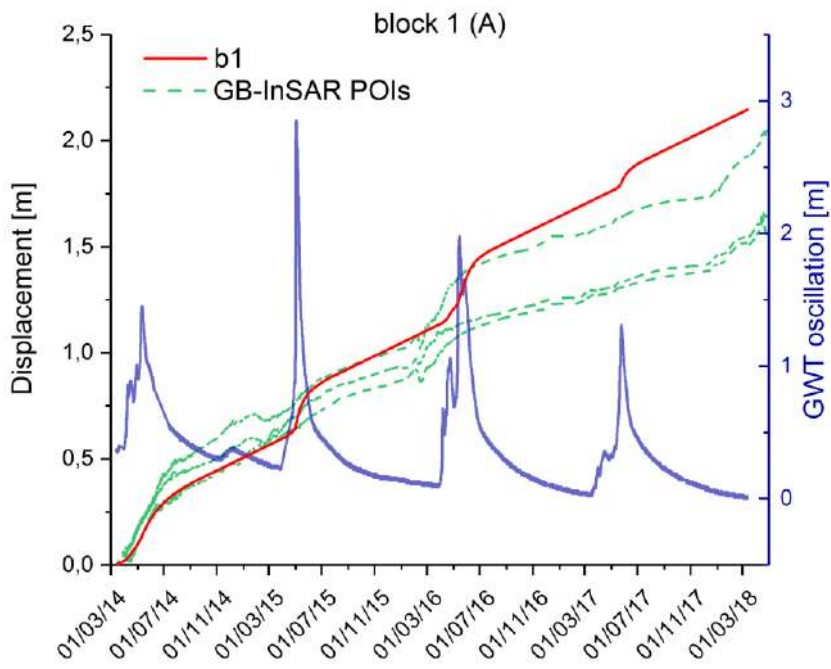


Figure 158 – results of model (red line) for block 1 (b1) compared with monitoring data (GB-InSAR POIs) and GWT oscillation

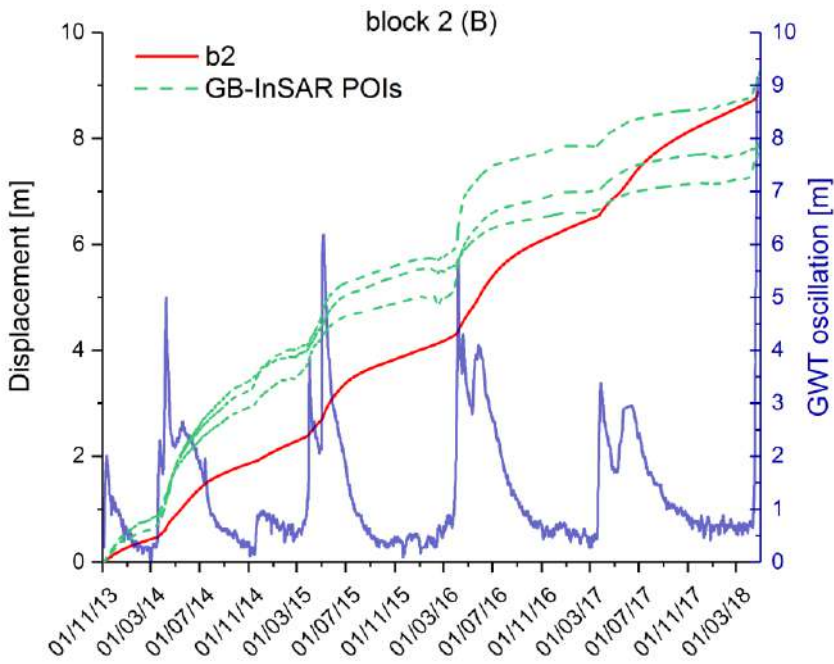


Figure 159 - results of model (red line) for block 2 (b2) compared with monitoring data (GB-InSAR POIs) and GWT oscillation

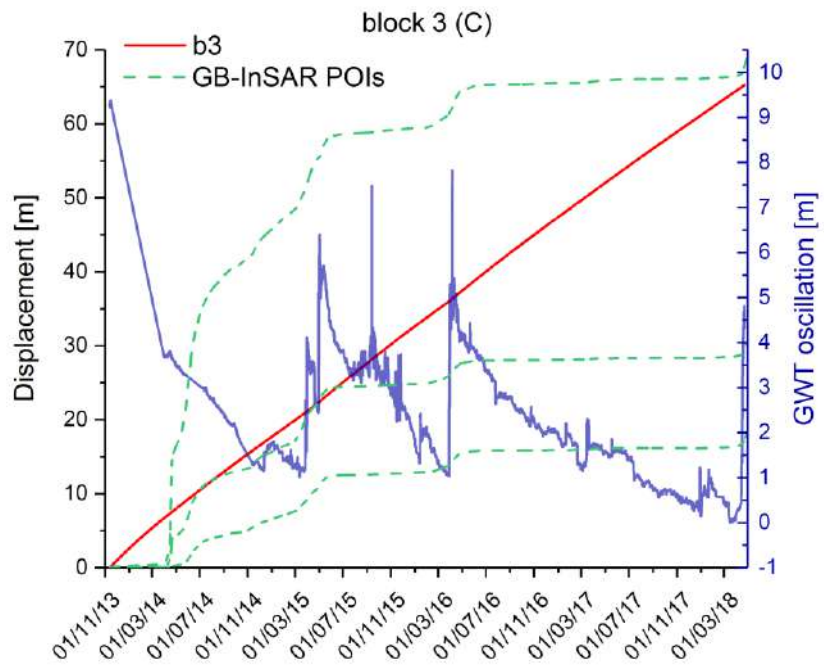


Figure 160 - results of model (red line) for block 3 (b3) compared with monitoring data (GB-InSAR POIs) and GWT oscillation

Concerning the actual limitations of the proposed model, we list:

- GWT is used as punctual inside the single block, but should be considered as a surface, that means an interpolation method will be implemented for piezometric data and it extended to all considered blocks
- In this version it is not considered the interaction between blocks that can strongly affect the displacements. This requires an interaction law between blocks
- In all versions of the model the blocks are considered rigid, which is not true for sectors of the slide characterized by debris material or intensively fractured rock mass
- Most rockslides are characterized by several shear zones, and the kinematic behavior can lead to different evolution inside the same sector with a further differentiation

## 5.2 Conclusions

Considering the results, we can derive the following remarks:

- It is evident that discretization #1 (single block) is very useful (i) to evaluate the viscosity-driven movements, (ii) to assess the viscous parameter,  $\tilde{\gamma}$ , and (iii) to constrain the strength parameters representative of the average rockslide behavior.
- Discretization #3 (three different blocks) for zones of landslide head, main body and debris sector, reveals the capability of the model to describe the displacement oscillation due to groundwater table changes. This suggests the necessity of considering a subdivision into different zones. In fact, by properly considering the input parameters for each zone, the different behavior of the debris sectors with respect to other zones is quite well captured, considering also the different value for the viscous parameter. The discrepancy in the last year between data and predictions suggests the occurrence of a degradation process that seems to be suitably described by a slight reduction in the friction angle.
- Significant improvements concerning the interaction law between blocks and to create a GWT surface can lead to a more detailed model maintaining the simplified approach



## STATISTICAL ANALYSES OF MONITORING DATA

*There are three types of lies:  
lies, damn lies, and statistics.*

Forecasting the failure of landslides is a hard task, because of the large number of interplaying factors, barely taken into account by models. Complex geometric and temporal evolution, non-linearity displacement trends and the superposition of seasonal effects (Bhandari, 1988) are just some of these factors. The successful implementation of EWSs lies in the capability to identify and measure in real time but significant indicators, i.e. precursors, which precede a landslide failure (Antolini and Barla, 2016). In order to define the emergency state, the most used approach consists in the definition of alert thresholds, that are usually obtained by the identification of lower-bound lines related to the rainfall conditions that resulted in landslides acceleration. Frequently, the thresholds are drawn visually, i.e. without any rigorous mathematical, statistical, or physical approach (Guzzetti et al., 2007). The thresholds can be calculated both at regional or local scale, and they fit - reasonably well - in the area where they were developed but cannot be easily exported to neighboring areas (Crosta, 1989).

The latest developments and improvements in monitoring instrumentation have increased the potential to obtain highly reliable measurements of different parameters, which can be successively used to identify the precursors of a slope failure (Teza et al., 2007; Monserrat and Crosetto, 2008; Abellán et al., 2009, Barla et al., 2010; Casagli et al., 2010, Antolini, 2014), and – consequently – more accurate alert thresholds. The increase of availability of synthetic aperture radar data, derived by several international satellite missions (e.g. COSMO-SkyMed, ERS-1 and ERS-2) and – especially – by ground-based systems (e.g. Tarchi et al., 2003; Casagli et al., 2010, Del Ventisette et al., 2012, Di Traglia et al., 2014, Frodella et al., 2016), allowed to collect near-real time data and make them available for prompt analysis. Multi-parametric probes (equipped with biaxial inclinometers, piezometers, accelerometers, digital compasses; e.g. DMS columns) can be also used to obtain a near-real time data (Lovisolò & Della Giusta, 2005; Foglino et al., 2006).

In the present work, monitoring data from GB-InSAR and DMS columns systems have been analyzed to test the use of normal probability plots (NPP) for the displacement-rate analysis. Data from selected points of interest (POI), belonging to different landslide sectors and recorded during almost ten years of monitoring, have been examined. The analyses have been performed using data averaged with different time intervals to study the effects of noise on the threshold values.

These analyses allow us to define: (i) values with a specific probability value expressed in terms of percentiles; (ii) values for which a specific change in behavior is observed which could be associated to a specific type of triggering event (e.g. rainfall intensity, duration; snowmelt). These values could be used to support the choice of threshold values for the management of Early Warning System, by considering also the minimization of false alarms.

This statistical approach can be compared with results from methods like the Fukuzono-Voight (Fukuzono, 1985; Voight, 1988 and Voight, 1989) approach. Integration of the different data could allow to obtain more accurate threshold (Crosta and Agliardi, 2002). The Fukuzono-Voight inverse velocity method has been shown to be suitable to set alarm thresholds based on displacement measurements. Anyway, when a complex instability is analyzed, multiple factors contribute to rock slope failure and the different movement patterns (e.g. creep and seasonal) are superimposed the applicability of the same can be difficult (Hungri et al. 2005).

The presented approach could represent an innovative strategy to define velocity thresholds of Early Warning system and to analyze quantitative data derived from remote sensing and ground-based monitoring systems, by linking them to both spatial and temporal changes. Furthermore, the development of a simplified methodology to calculate the thresholds values becomes of particular importance during the emergency phases, considering the necessity to analyze the monitoring data in a near-real time and to provide fast responses.

## 6.1 Normal Probability Plots (NPP)

The normal probability plot (Chambers et al., 1983) is a graphical technique for assessing whether or not a data set is approximately normally distributed (i.e. a bell curve). The data are plotted against a theoretical normal distribution in such a way that the points should form an approximate straight line. Departures from this straight line indicate departures from normality. The NPP is a special case of the probability plot.

If the points in the probability plot all fall along a straight line, you can assume that the data follows that probability distribution. Types of patterns that coincide with departures from the straightness of this line, usually are (Figure 1):

- **Outliers:** Outliers are values that do not follow the pattern of body of the data. They show up as extreme points at either end of a probability plot. Since large outliers will severely distort most statistical analyses, it is important to investigate them closely. If they are errors or one-time occurrences, they should be removed from the analysis. Once outliers have been removed, the probability plot should be redrawn without them;

- **Long tails:** Occasionally, a few points on both ends will stray from the line. These points appear to follow a pattern, just not the pattern of the rest of the data. Usually, the points at the top of the line will shoot up, while the points at the bottom of the line will fall below the line. This is caused by a data distribution with longer tails than would be expected under the theoretical distribution (e.g., normal) being considered;

- **Asymmetry:** If the probability has a convex or concave curve to it (rather than a straight line), the data are skewed to one side of the mean or the other;

**Plateaus and Gaps:** Clustering in the data shows up on the probability plot as gaps and plateaus (horizontal runs of points). This may be caused by the granularity of the data, i.e. the level of detail.

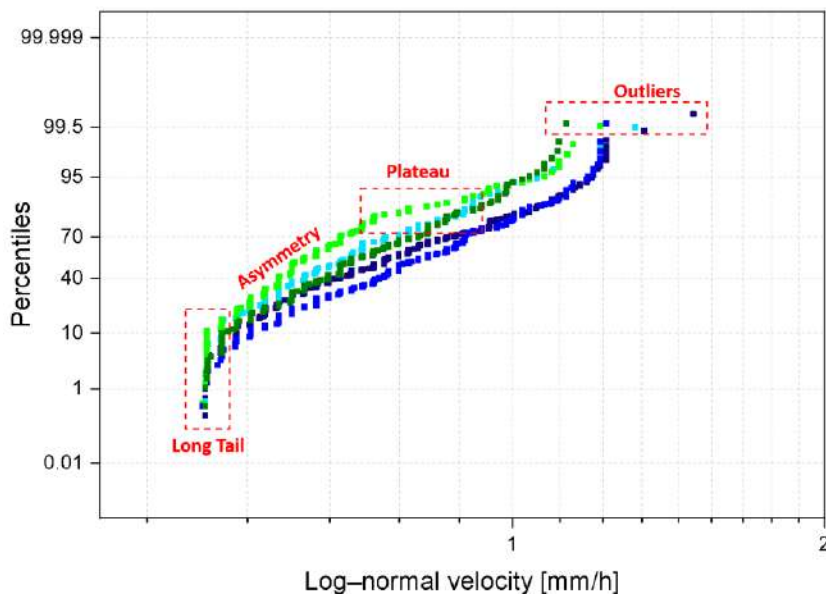


Figure 161 – example of NPP from GB-InSAR data

### 6.1.1 Results and discussion

Concerning Mont de La Saxe rockslide, data from GB-InSAR and from DMS columns were analyzed (Figure 162).

### 6.1.2 GB-InSAR data

The displacement data derived from the GB-InSAR for the 15 streaming points (POIs) were analyzed to assess their distribution. Then, a correlation between piezometric level and GB-InSAR POIs through NPP have been performed (e.g. Figure 175). The key issue is to find out if the overcome of a threshold in the displacement data can be directly correlated to the overcome of a threshold in the piezometric data.

Finding this correlation could make possible to define the early warning thresholds, with an approach that should be more suitable, than or could integrate the Fukuzono-Voight method (e.g. Saito, 1965; Fukuzono, 1985; Voight 1985, 1989) even if this method cannot allow to take into account for possible changes in material and processes behavior.

GB-InSAR data was analyzed since monitoring starting date (i.e. June 2009), while the DMS columns data was analyzed since the calibration of the sensors (usually one month after the installation).

GB-InSAR POIs are located in different areas of the rockslide, some of them represents the displacement observed in areas covered by debris material (e.g. P7, P8, P11 and P12) while others are linked to rocky sectors (e.g. P1, P2, P3, P4, P5 and P9). Due to this, the analysis of displacements derived from different POIs can provide information related to different landslide mechanisms (e.g. linked to more superficial instabilities in the areas covered by debris material or more representative of the displacements related to the rockslide shear surface in the rocky outcrops).

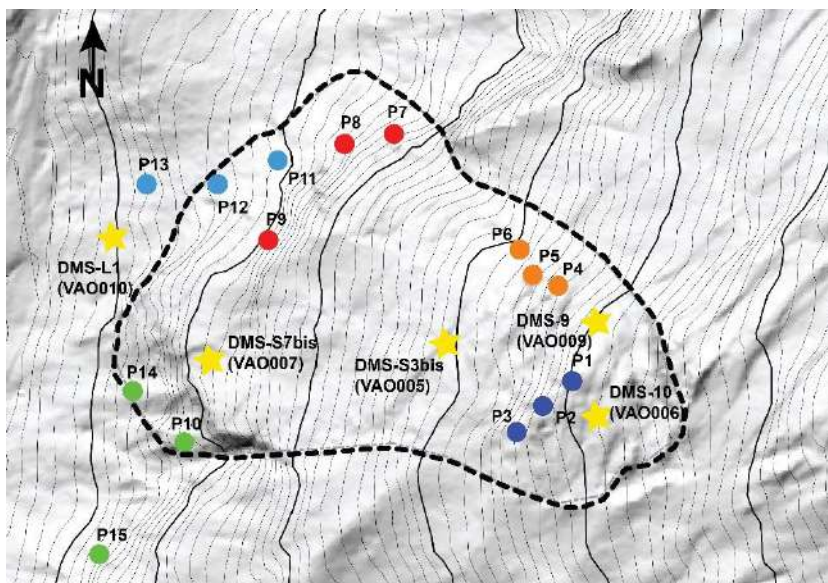


Figure 162 – GB-InSAR POIs (rounded colored points) and DMS® columns (star points) along the slope of Mont de La Saxe

The results (from Figure 163 to Figure 167) concerning the GB-InSAR points of interest showed an increment of displacement rate from 2011 to 2014, and a decrement trend since 2014.

As expected, the POIs with higher displacement rate are located in the rockslide sectors characterized by debris material (e.g. P7, P8, P11, P12), showing a characteristic trend confirmed also after 2014. Concerning the POIs for the head and the central sectors (e.g. P1, P2, P3, P4, P5, P9) the displacement rate is least of one order of magnitude lower than POIs that are located in the debris material.

The actual early warning thresholds comprise 2 levels of alert, 1 (pre-alert) and 2 (alert) defined by 1 and 2 mm velocity thresholds, respectively obtained by Fukuzono-Voight approach on an earlier dataset. Analyzing the data, it is clear that from 2014 to 2016 these values were too low, because for 70% of the days in 2014 ( $\approx$ more than 255 days) the displacement rate was over on average above 2,7 mm/h with peaks of more than 25 mm/h (e.g. P7).

Nowadays with a significant change in behavior of the landslide, these thresholds look more appropriate.

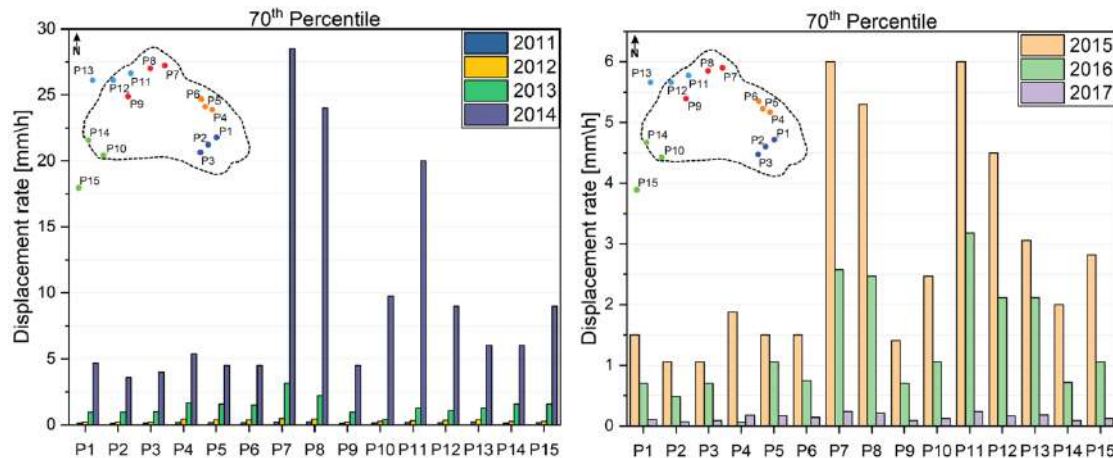


Figure 163 – 70<sup>th</sup> percentile for displacement rate of GB-InSAR POIs since 2011 to 2018

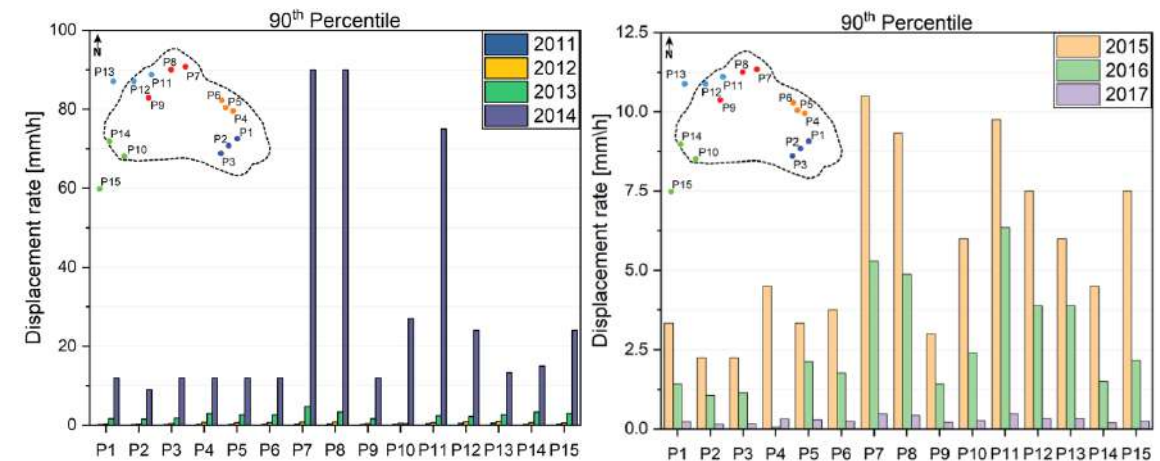


Figure 164 - 90th percentile for displacement rate of GB-InSAR POIs since 2011 to 2018



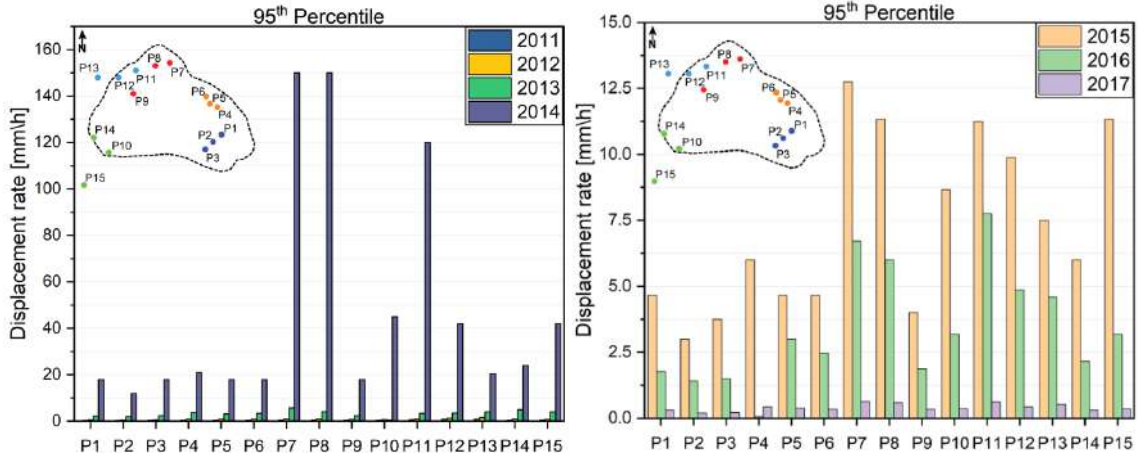


Figure 165 - 95th percentile for displacement rate of GB-InSAR POIs since 2011 to 2018

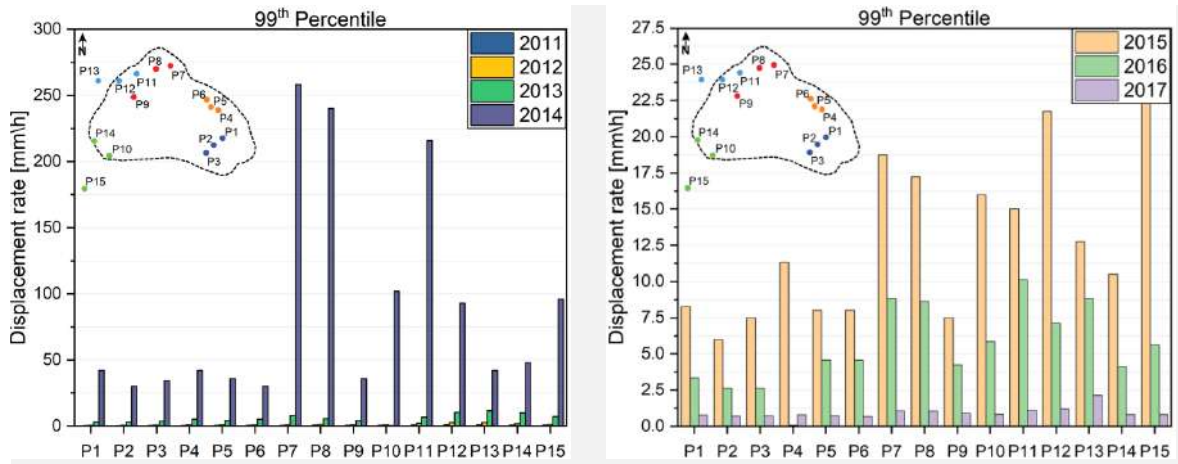


Figure 166 - 99th percentile for displacement rate of GB-InSAR POIs since 2011 to 2018

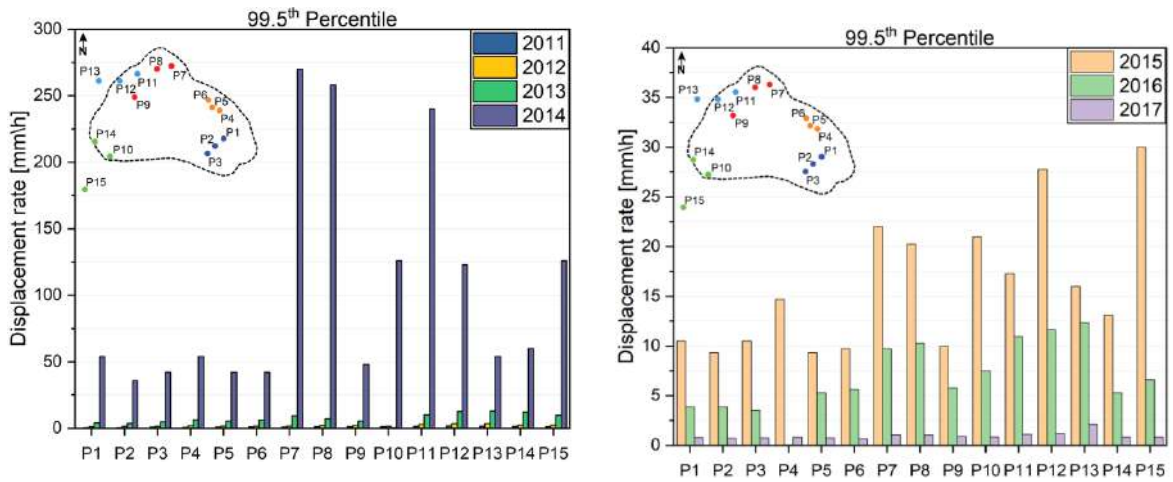


Figure 167 - 99.5th percentile for displacement rate of GB-InSAR POIs since 2011 to 2018

### 6.1.3 DMS® columns data

The displacement data derived from the DMS® columns (Figure 162) for the 5 columns and especially for the modules located in main shear zone (Figure 85).

The results about the DMS columns showed the same behavior for all the considered columns, with very similar values of significant percentiles. This could mean that the rockslide at depth is assimilable to a rigid block that slide over a shear zone. This concept will be a key point during the numerical modeling. The columns are installed in different sectors of the landslide and is worth to note the main shear zone is located at different depths. Analyzing the single column, a common behavior is observed, up to 90% (90<sup>th</sup> percentile) of all the displacements are located in a close range, while analyzing the 95<sup>th</sup> percentile this range results to be more variable. Whilst, the module (1 meter-length) where the maximum displacement is localized shows higher values (more than the double, e.g. module 27 for DMS L1, module 62 for DMS 9 or module 55 for DMS 10) with respect to those of the 70<sup>th</sup> percentile. Most of the modules of each columns show a similar behavior, while the displacement rate for different columns is variable. The modules involved in the maximum displacement shows a large variability between outliers (i.e. 99<sup>th</sup> and 99.5<sup>th</sup> percentiles), this could represent the occurrence of an instability event.

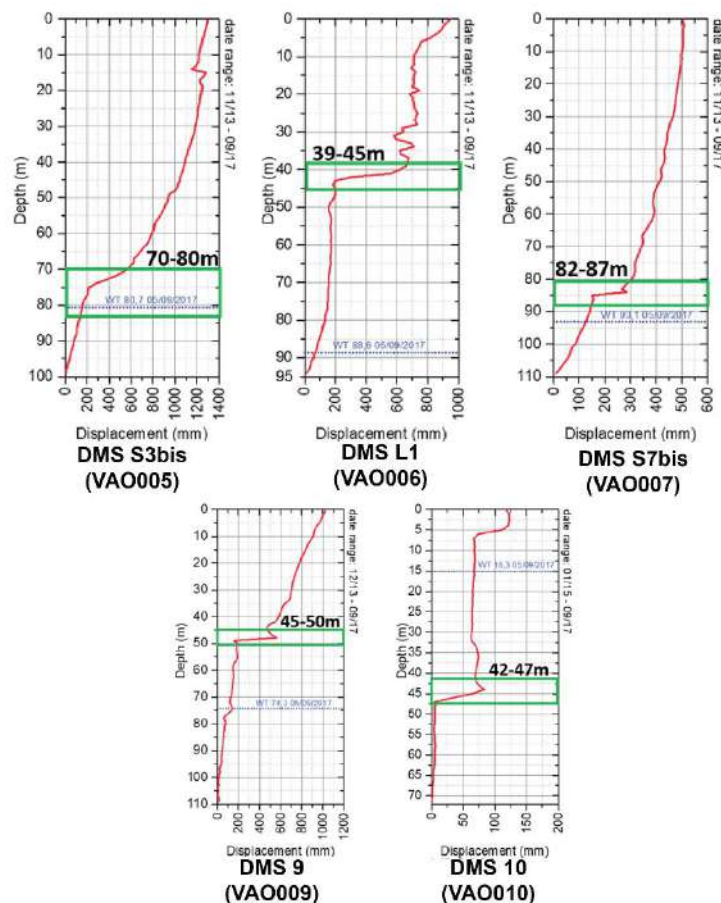


Figure 168 - cumulative displacement for DMS columns. In the green box, the module used in the analyses, that correspond to main shear zone where is located most of displacement, is indicated

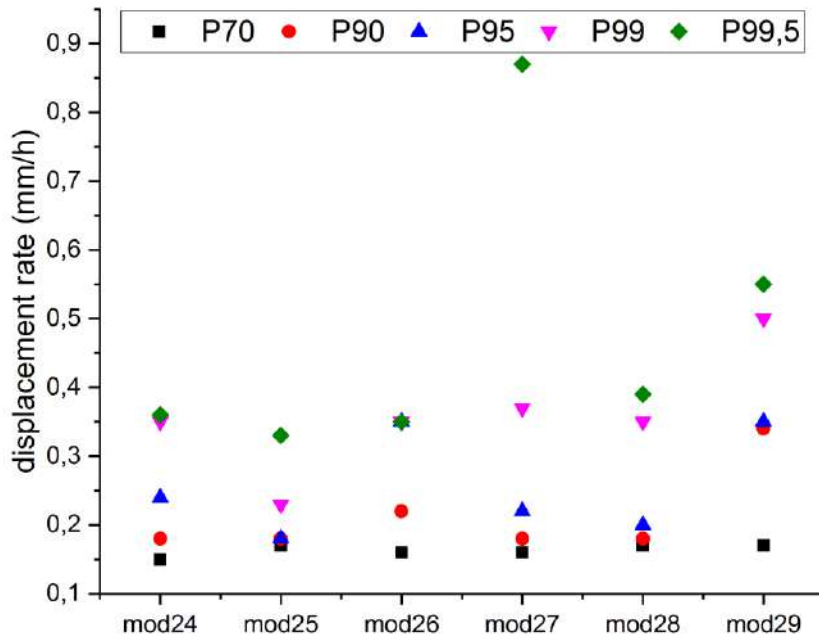


Figure 169 - percentiles (70<sup>th</sup>, 90<sup>th</sup>, 95<sup>th</sup>, 99<sup>th</sup> and 99.5<sup>th</sup>) of DMS L1 for modules (1 meter-length segment of column) from 24 to 29 (at depth from 39 to 45 m)

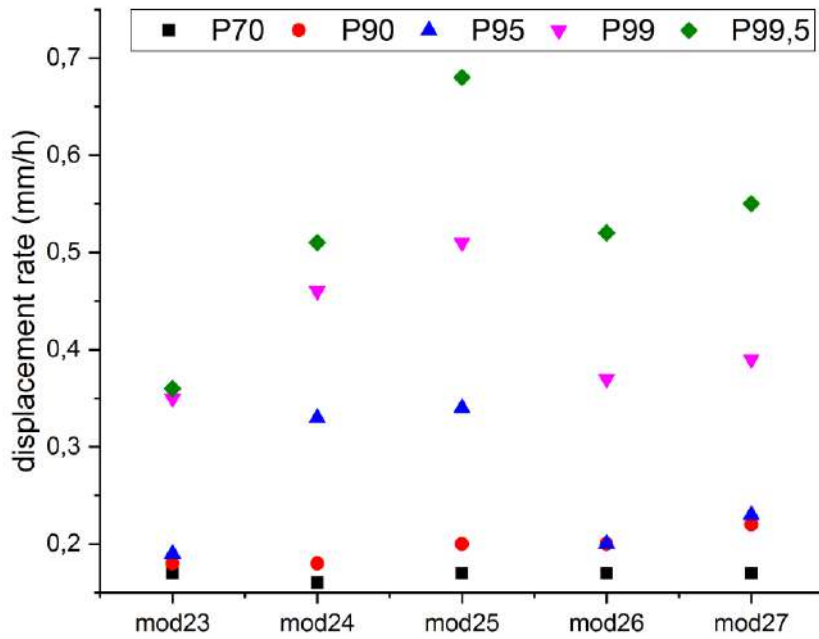


Figure 170 – percentiles (70<sup>th</sup>, 90<sup>th</sup>, 95<sup>th</sup>, 99<sup>th</sup> and 99.5<sup>th</sup>) of DMS9 from modules (1 meter-length segment of column 60 to 64 (at depth from 45 to 50 m)

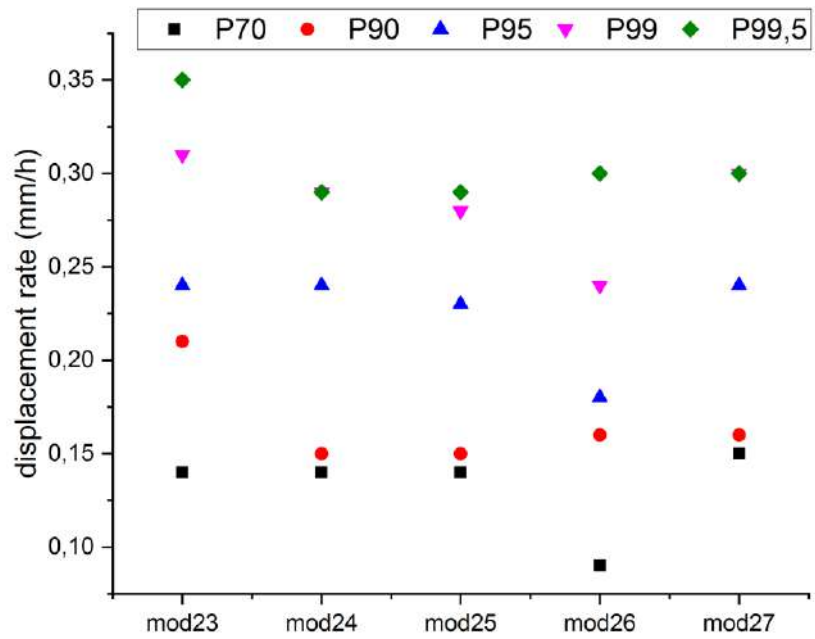


Figure 171 – percentiles (70<sup>th</sup>, 90<sup>th</sup>, 95<sup>th</sup>, 99<sup>th</sup> and 99.5<sup>th</sup>) of DMS 7bis from modules (1 meter-length segment of column) 23 to 27 (at depth from 82 to 87 m)

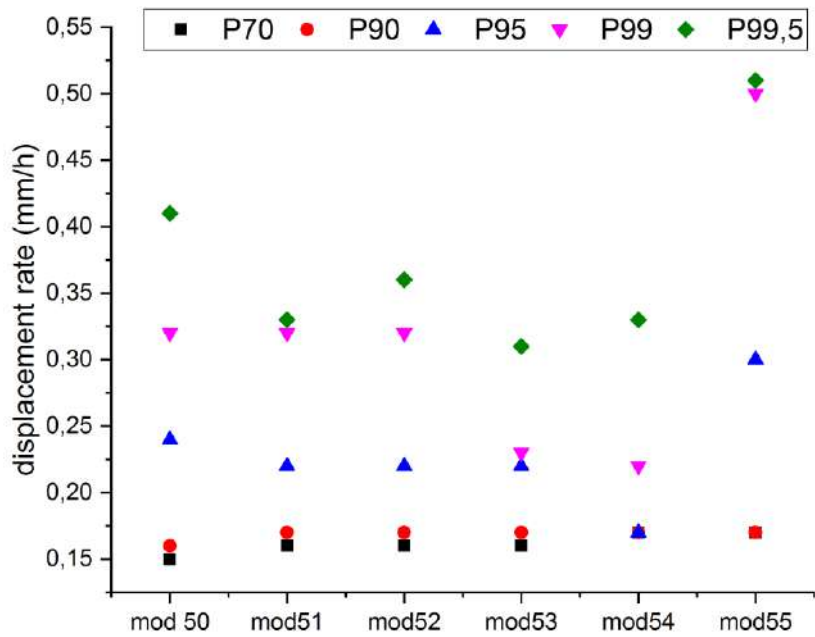


Figure 172 – percentiles (70<sup>th</sup>, 90<sup>th</sup>, 95<sup>th</sup>, 99<sup>th</sup> and 99.5<sup>th</sup>) of DMS10 from modules (1 meter-length segment of column) 50 to 55 (at depth from 42 to 47 m)

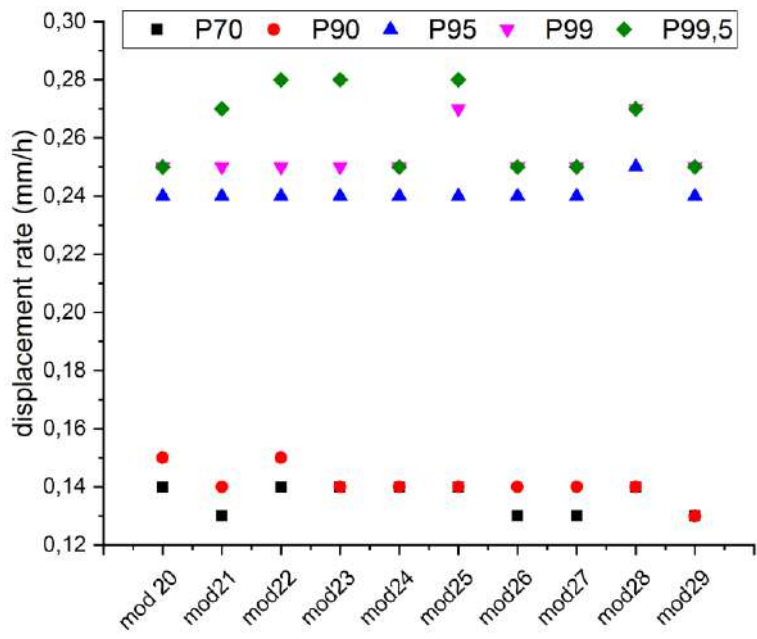


Figure 173 – percentiles (70<sup>th</sup>, 90<sup>th</sup>, 95<sup>th</sup>, 99<sup>th</sup> and 99.5<sup>th</sup>) of DMS 3bis from modules (1 meter-length segment of column) 20 to 29 (at depth from 70 to 80 m)



### 6.1.4 Piezometric data

To investigate a possible correlation between piezometric level and GB-InSAR POIs, a NPP analysis was conducted investigating the selected significant percentiles 70th, 90th, 95th, 99th and 99.5th for piezometer DMS S3 bis, which was chosen for its position, as representative of the entire landslide body, and for points of interest from GB-InSAR monitoring from the end of 2013 to 2018. The basic idea is trying to understand if the increase of landslide velocity and the increase of GWT are correlated and - eventually - which is the relation between them.

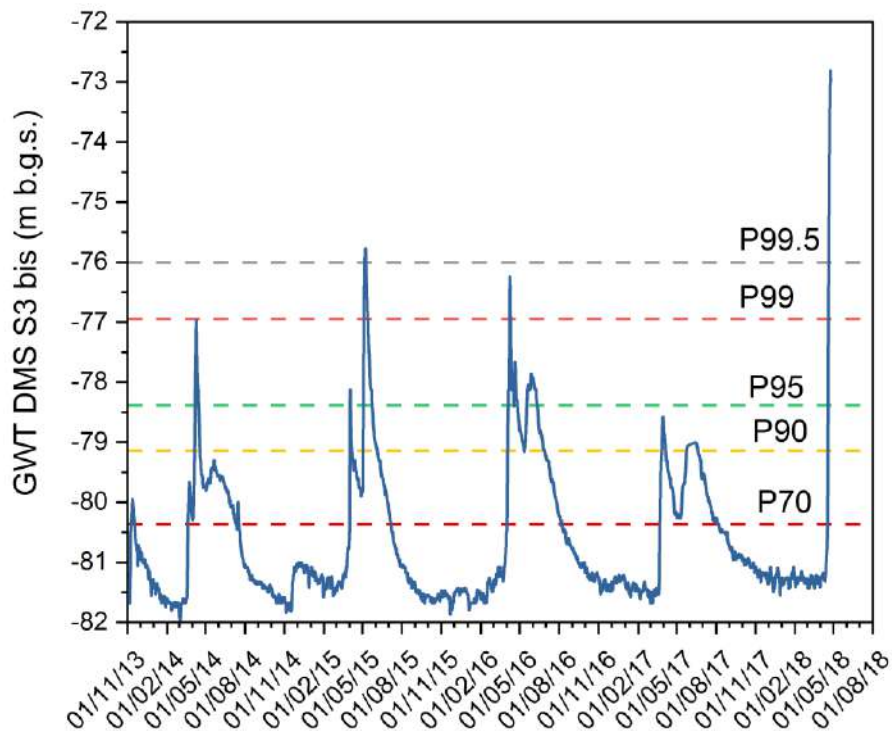


Figure 174 – GWT oscillation for piezometer DMS S3 bis and distribution of significant percentiles of piezometric level

The analyses of the data showed an interesting relationship when the GWT overcome the significant percentiles and they answer to the question: what happen when the GWT overpass the ‘base level’, i.e. piezometric level not exceeded for the most part of the year (e.g. 70<sup>th</sup> percentile)?

Considering the GWT long-term monitoring, the 70<sup>th</sup> percentile corresponds to more than 3 years, which means that in the last four years, for about three year the piezometric level was equal to the ‘base level’. In the other one the GWT presented suddenly increment and decrements of GWT, traduced in acceleration or decelerations of displacement rate.

Results regarding the POIs P1, P7 and P13, located in different sectors of the landslide are presented (Figure 175, Figure 176 and Figure 177).

All the analyzed POIs show a good fit between 70<sup>th</sup> percentiles of the GWT and the displacement rate, the same can be observed also for 90<sup>th</sup> and 95<sup>th</sup> percentiles. Instead, 99<sup>th</sup> and 99.5<sup>th</sup> percentiles are not showing a good fit, an explanation can be found considering that, most probably, when the landslide displacements start to increase, their relationship with the GWT become less important.

Usually the slow-moving landslides are characterized by basic creep behavior ('basic level') continuous through time and seasonal acceleration due to GWT oscillation due to snow-melt or rainfall. Comparing data from these analyses, the direct relationship between GWT oscillations and displacements acceleration is clear and it is possible to observe how the increment of GWT controls the displacement rate.

Furthermore, these results suggested a change in displacement behavior through time. The 2014 was characterized by the highest displacement rate ever recorded. It is worth to note how, during 2015, a year also characterized by large displacements, no one among the POIs overcame the 99<sup>th</sup> and 99.5<sup>th</sup> percentiles. Moreover, during the last three years (2016, 2017 and 2018) even if the GWT reached high levels, comparable to the ones recorded on 2014, they did not generate larger displacement rate.

In 2017 a smaller displacement was observed, together with a lower piezometric surface. This is particularly evident when observing the graphs related to the 95<sup>th</sup> percentile for POIs P1 and P13.

As anticipated, these correlations are not taking into account several aspects of the landslide mechanism, anyway, due to their simplicity and straightforward application, they can be fundamental to help in the alert threshold definition and landslide behavior forecasting.

The basic concepts derived from these analyses and the presence of a clear correlation between GWT oscillations and displacements were also used to implement the numerical modelling strategy (), i.e. to simulate displacement accelerations due to the interaction between the landslide shear zone and the groundwater level superimposed to a basal creep displacement behavior.

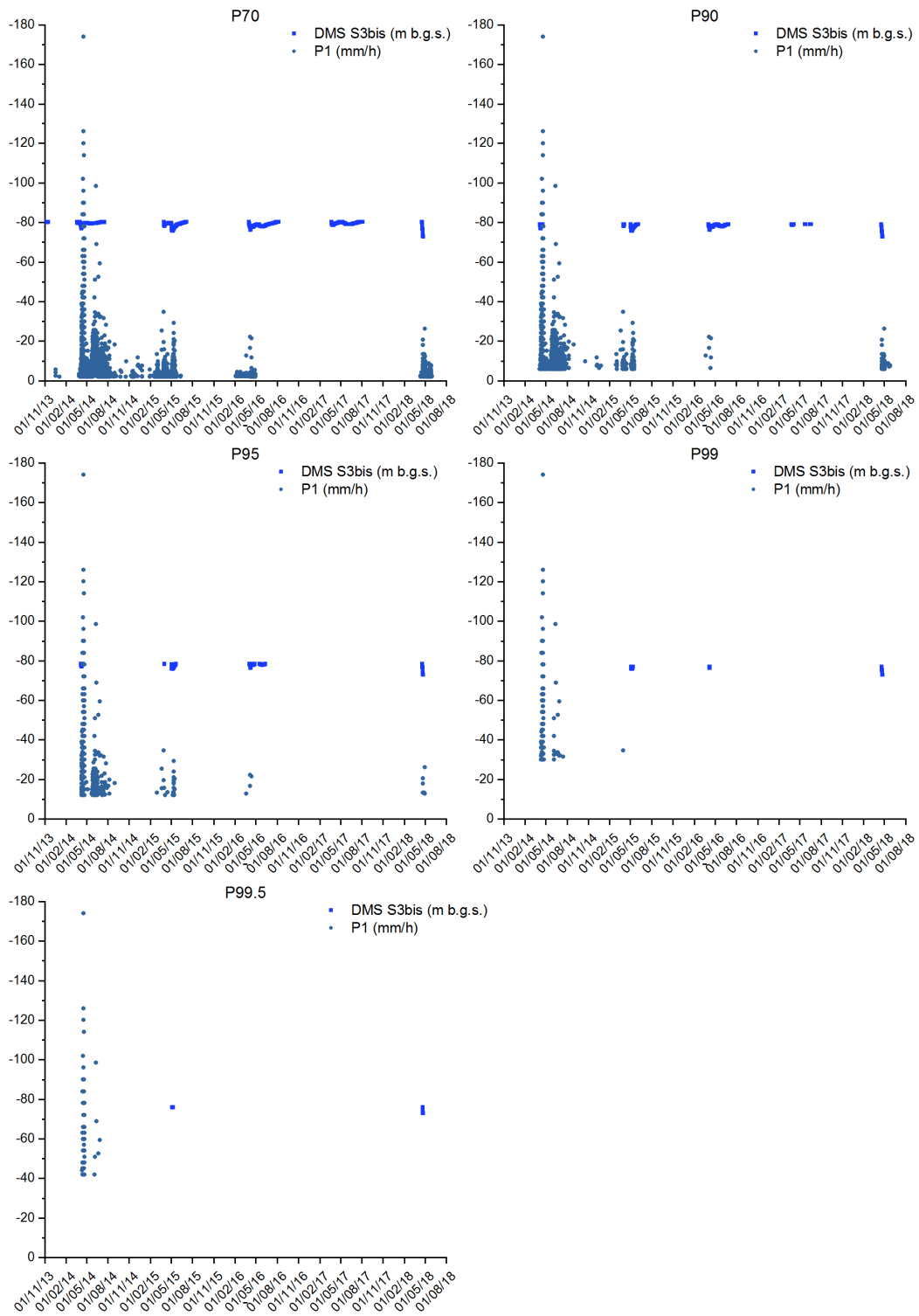


Figure 175 – compared analysis for piezometric data (DMS S3bis) and GB-InSAR POI (P1) for significant percentiles (70<sup>th</sup>, 90<sup>th</sup>, 95<sup>th</sup>, 99<sup>th</sup> and 99.5<sup>th</sup>)

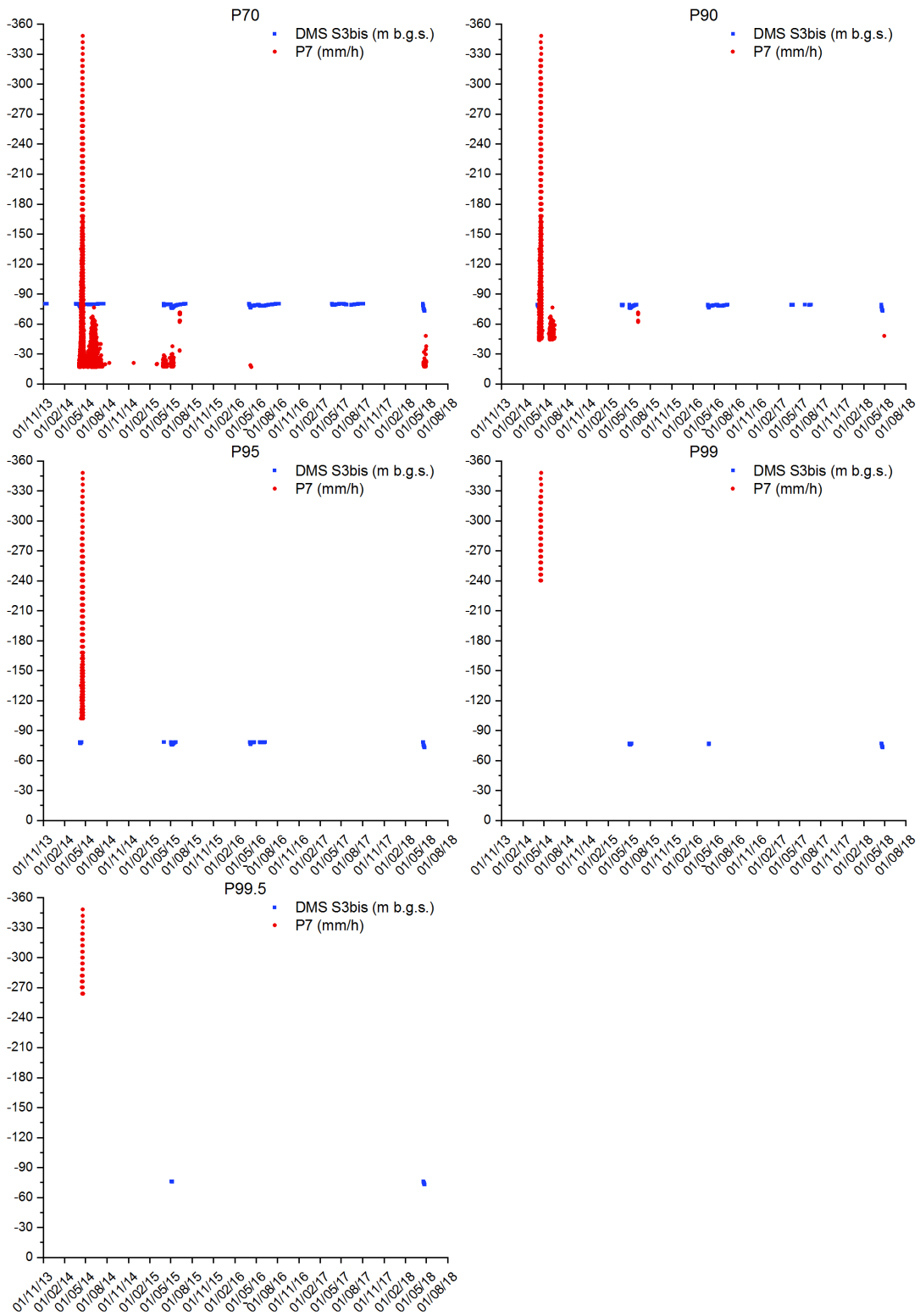


Figure 176 - compared analysis for piezometric data (DMS S3bis) and GB-InSAR POI (P7) for significant percentiles (70<sup>th</sup>, 90<sup>th</sup>, 95<sup>th</sup>, 99<sup>th</sup> and 99.5<sup>th</sup>)

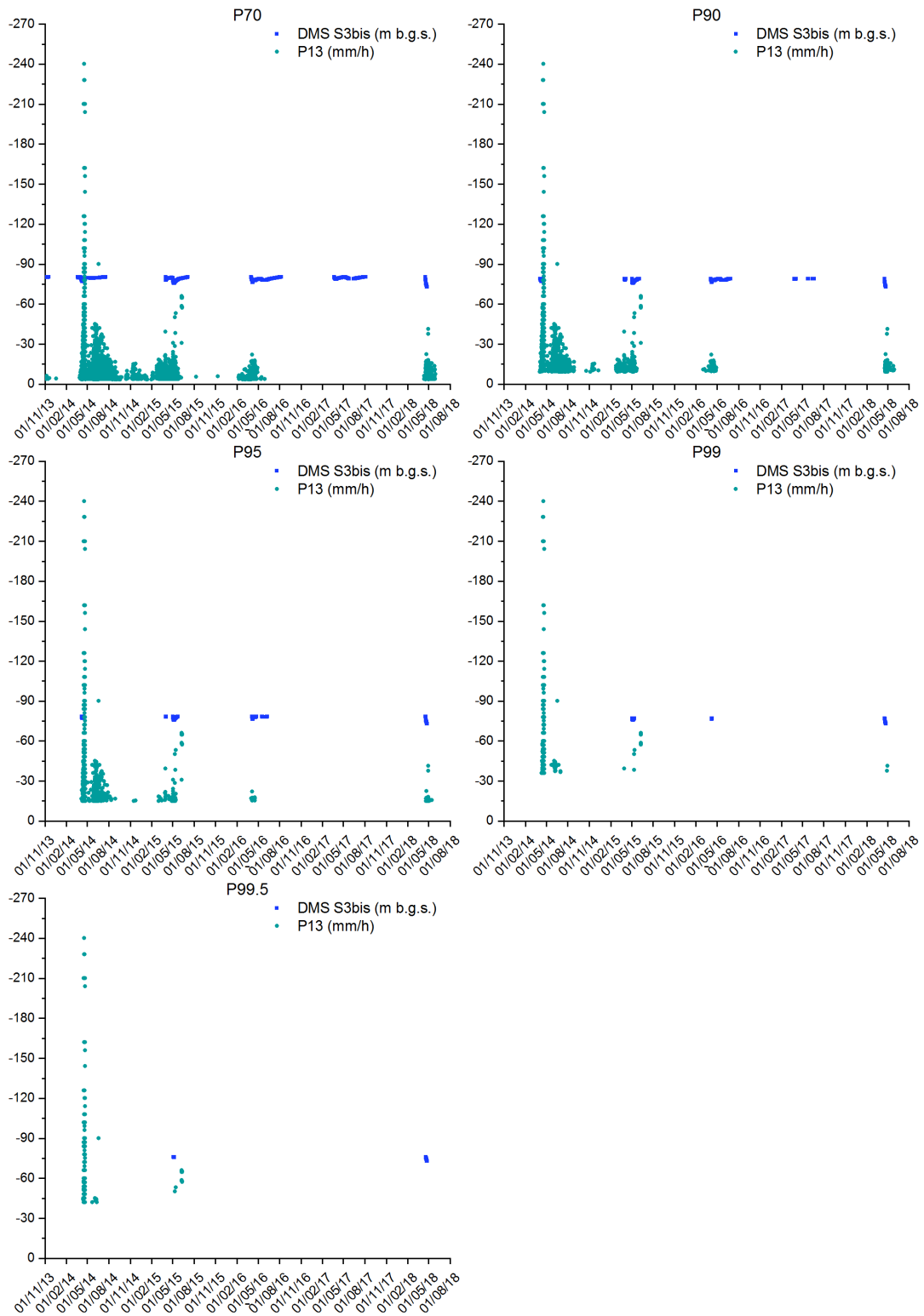


Figure 177 - compared analysis for piezometric data (DMS S3bis) and GB-InSAR POI (P13) for significant percentiles (70<sup>th</sup>, 90<sup>th</sup>, 95<sup>th</sup>, 99<sup>th</sup> and 99.5<sup>th</sup>)

# THE RUINON ROCKSLIDE

*... the whole Valtellina not only looks beautiful and smiling,  
but also noble and fertile like no other region*

The Ruinon rockslide is an active phenomenon for which Early Warning (hereinafter EW) strategies for managing have been developed and tested. The existing EW thresholds developed by using Fukuzono-Voight approach have been updated and an innovative statistical methodology adopted to support definition for less evident time series.

## **7.1 Monitoring system**

Rockslide displacement measurements have been carried out since 1997 by a ground-based network (up to 25 wire extensometers and backup distometer baselines, 17 GPS, optical targets, 2 borehole inclinometers, 1 borehole multi-base extensometer) and in recent years by radar interferometry (i.e. satellite-based PS-InSAR™ and SqueeSAR™ and ground-based GB-InSAR™). The monitoring network covers the rockslide area and is denser around the upper scarp (US) and the lower scarp (LS). Inclinometer tubes were rapidly damaged allowing only few measurements, the monitoring network provided the longer and more continuous time series of surface displacements for a rockslide (>18 years) and also for GB-InSAR (>12 years).

### **7.1.1 Ground-based geotechnical network**

Data provided by the ground-based monitoring network allowed identifying rockslide sectors with different styles of activity and response to external triggers. Crosta and Agliardi (2003) identified three different patterns of displacement, namely *brittle*, with stick-slip movement of limited rock volumes; *chaotic*, observed in areas of debris/disrupted rock and lacking a well-defined temporal trend, and *seasonal creep* non-linear acceleration phases during wet seasons and resting periods during winter and early spring. Seasonal reactivations, associated to rainfall and snowmelt,



were superimposed over a generally progressive (i.e. accelerating) trend from 1997 to 2002, whereas a stage of long-term stabilization took place between 2003 and 2007. From 2008, the rockslide started accelerating again over the long-term, suggesting that progressive behavior occur at different timescales due to a complex interaction between rock failure mechanisms and the superposition of precipitation and ground-water recharge events.

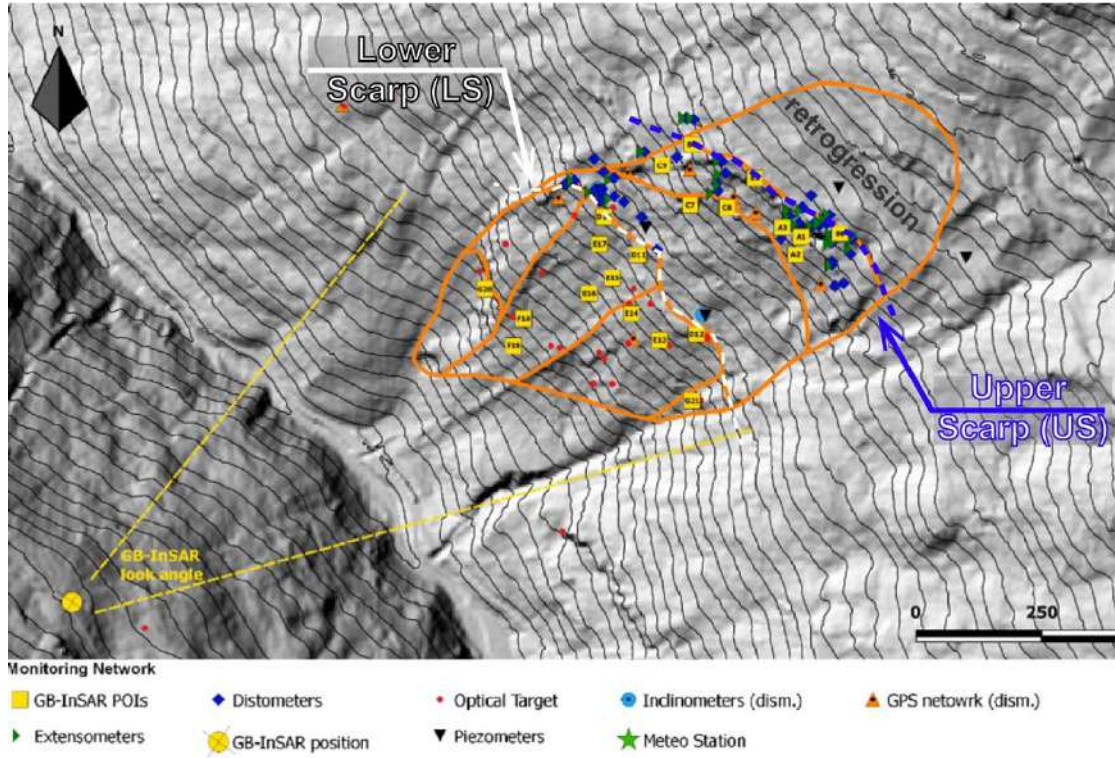


Figure 178 – monitoring network on the Ruinon rockslide

### 7.1.2 Ground-based radar interferometry

To monitor the rockslide displacement field, a LiSALab™ GB-InSAR system was installed in June 2006 (Casagli et al. 2010) and has been providing continuous operation. The active sensor is located on the opposite valley slope at 1775 m a.s.l., at a distance from the rockslide ranging between 1000 m (rockslide toe) and 1800 m (US) along the line- of-sight. The system, initially installed as part of a research experiment (Tarchi et al. 2003; Antonello et al. 2004; Casagli et al. 2010), was incorporated in the near real-time monitoring network operated for civil protection purposes. In the present configuration, the LiSALab system uses a microwave transceiver unit working at Ku band (12–18 GHz) with a licensed central frequency of 17.35 GHz (bandwidth of 100 MHz) and generating a synthetic aperture antenna of about 3 m and illuminating about 50% of the rockslide area and upslope sectors up to a maximum distance of about 4 km, embracing the Cima di Saline ridge (Figure 82). A 1-year (2006–2007), long-range GB-InSAR experiment provided displacement time series (with values exceeding 20 mm/year) which were comparable to satellite InSAR data both for slope debris (sector 1) and rocky outcrops within the DSGSD (sector 2).

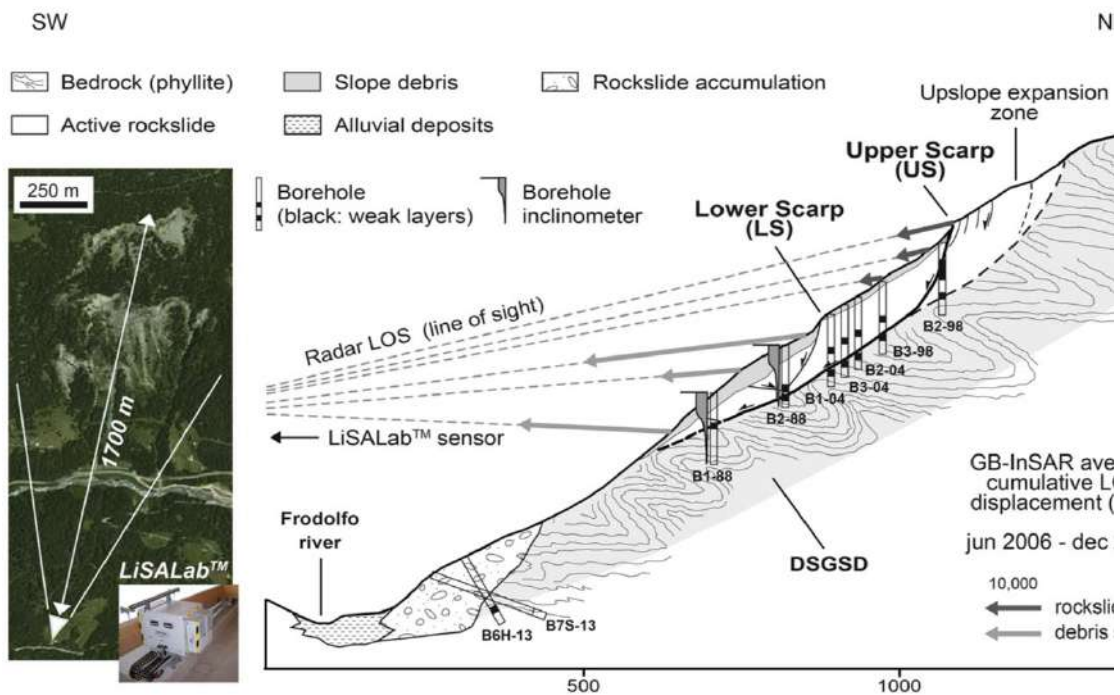


Figure 179 – Point of View of GB-InSAR system and cross-section of Ruinon rockslide (from Crosta et al., 2017)

The permanent monitoring settings of the system allow acquiring radar images and displacement maps with a theoretical range resolution of 1.5 m and a theoretical azimuthal resolution between 2.6 and 5.2 m. The scanning time for each image acquisition and the statistical averaging interval considered to improve the quality of the radar images vary from minutes to hours. During periods of normal landslide activity, the scanning time and the statistical time window are about 14 min (approximately 4–5 images per hour) and 6 h, respectively. These time intervals can be decreased down to 2 min during critical acceleration stages to resolve the possible phase ambiguity and avoid phase wrapping. The accuracy of the system set up under optimal measuring conditions (high scene coherence with high SNR, negligible atmospheric effects, lack of vegetation; Tarchi et al. 2003) amount to a very small fraction of the signal wavelength ( $\lambda$ ) and can reach sub-millimetric values. Of course, limitations to the accuracy and completeness of radar data can derive locally (in space and time) from increased noise due to vegetation, un-resolvable atmospheric effects and line-of-sight obstructions. The system has been equipped with rugged high-speed data transmission connections, redundant power supply, near real-time connection with a weather station and time-lapse webcams. The system now provides the most comprehensive and integrated information about the rockslide behavior, in order to support the risk mitigation actions requested by the civil protection plan. In this perspective, the LiSALab system provides near- and real- time results in terms of (a) geo-referenced pseudo-3D maps of line-of-sight (LOS) displacements, obtained by converting local radar coordinates to global coordinates (X, Y, Z) using a reference digital elevation model and (b) streaming time series of displacement at selected points of interest (POI). Since displacements are resolved only along the radar LOS, the recorded component of the local displacement vector slightly varies at each slope location. This usually implies an underestimation of real displacements,

which is minimized by optimizing system positioning and quantified by ground-truthing. In this case, data from ground-based instrumentation allowed validating the spatially distributed displacement data provided by the GB-InSAR system since 22 July 2006. The comparison between GB-InSAR and wire extensometer data at corresponding locations proved the consistency of radar measurements, with extensometer data often providing upper bounds. GB-InSAR data were also validated through local measurements by total station and optical targets where available.

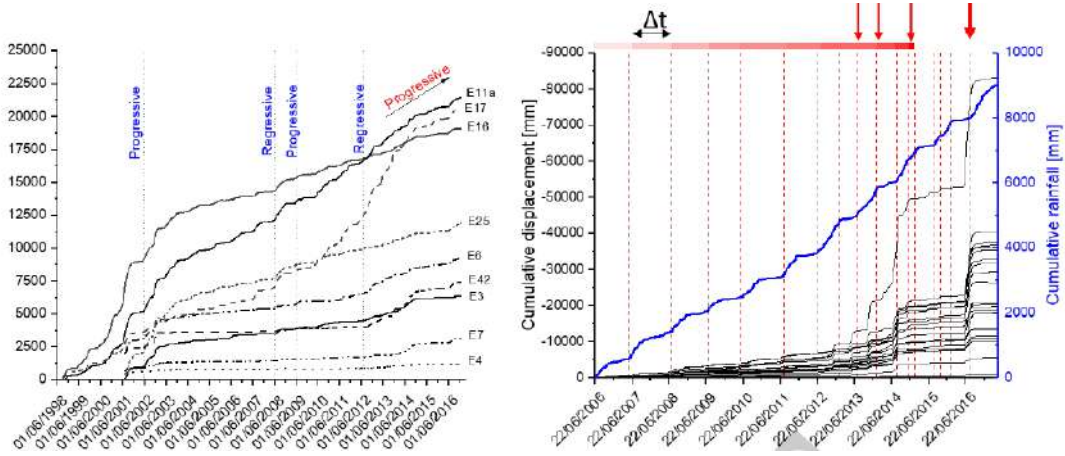


Figure 180 – data provided by extensometers (on left) and ground-based InSAR (on right) network



### 7.1.3 Definition of rockslide sub-areas: early warning domains

The subdivision into sub-areas was refined through geomorphological mapping (Figure 182) based on multi-temporal aerial photointerpretation (on photos taken in 1954, 1976, 1982, 1997, 2000, 2003, 2007, 2010, 2013) and field mapping, aimed at identifying the extent of debris-covered areas and their changes, areas of outcropping rock, major structures and kinematic evidences.

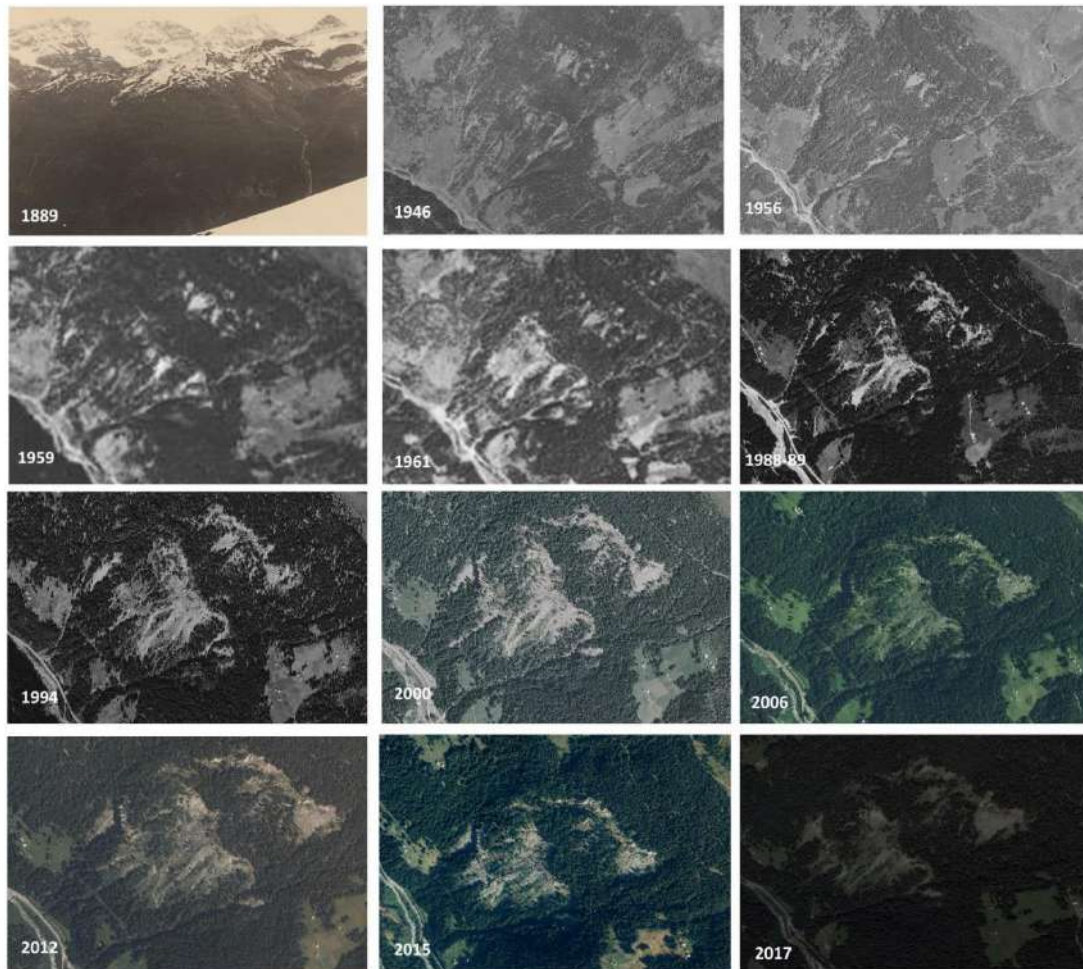


Figure 181 – evolution through time of Ruinon rockslide by photo and orthophoto

This previous analysis identified 13 rockslide sub-areas (Crosta et al., 2017), each one characterized by a homogeneous set of geomorphological features, behavior and style of activity, depending on the affected material (e.g. bedrock, fine or coarse debris) or on local structural controls. Sub-areas have been grouped into seven larger early warning domains (A to G; Figure 182).

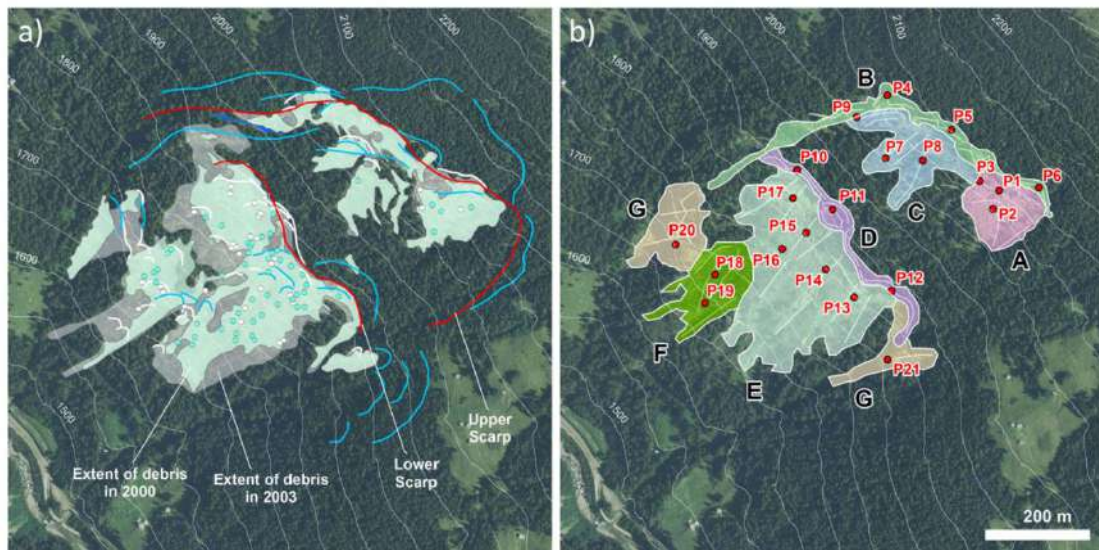


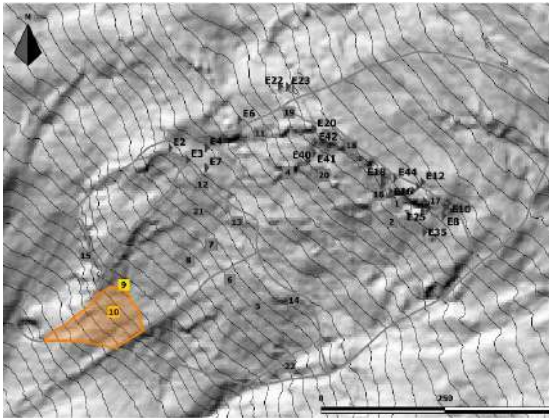
Figure 182 – (a) The subdivision into sub-areas was refined through geomorphological mapping. (b) Sub-areas have been grouped into seven larger early warning domains (A to G) representative of different failure scenarios in a practical early warning perspective (from Crosta et al., 2017)

A further analysis of these sub-areas led to the definition of 7 different scenarios in a practical early warning perspective (Figure 183 and Figure 184), considering the EWD and displacement pattern of each GB-InSAR Points-of-Interest (hereinafter POI). The scenarios are subdivided in small scenarios (Figure 183) and large scenarios (Figure 184), arbitrarily based on volume of involved material ( $> 2\text{Mm}^3$ ).

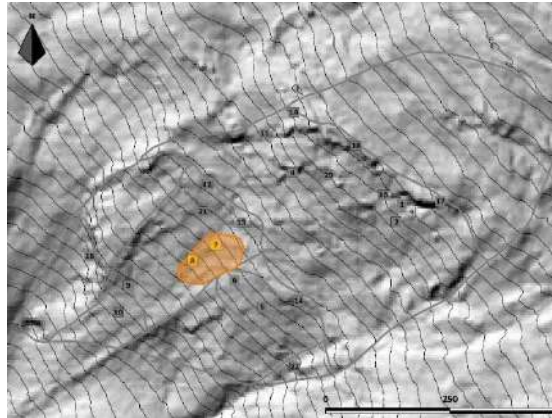
The small scenarios include scenario 1 which is subdivided into 3 sub-scenarios, 1a (almost  $155,000\text{ m}^3$  of material) consists in a large independent debris slide undergoing acceleration stages (EWD F); 1b (about  $65,000\text{ m}^3$ ) involves debris material (EWD E) and the same kinematic behavior; scenario 1c involves the EWD E ( $\approx 70,000\text{ m}^3$ ) and is located close to previous scenario; finally, scenario 2 involves sub-scenarios 1a and 1b (more than  $1.68\text{ Mm}^3$ ) and part of EWD D and E, both rock and debris material.

Large scenarios include scenario 3 (about  $2.89\text{ Mm}^3$ ), partially affecting the steep sector of the lower scarp (LS) formed by both coarse debris and outcropping bedrock (EWD D) and a thick debris covering pre-existing reworked glacial deposits, with masked bedrock outcrops downslope of the LS (EWD E); scenario 4 that involves completely EWD D and E with an estimated volume of about  $3.65\text{ Mm}^3$ ; finally the scenario 5 involves the entire slope from toe to crown of instability with an estimated volume of over  $24\text{ Mm}^3$ .

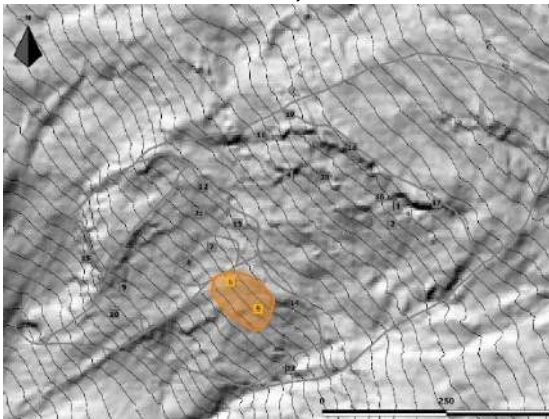
The last two scenarios 6 and 7, refer to the entire slope with complete retrogression (estimated volume of over  $31\text{ Mm}^3$ ) and to the rockfalls along the slope, respectively.



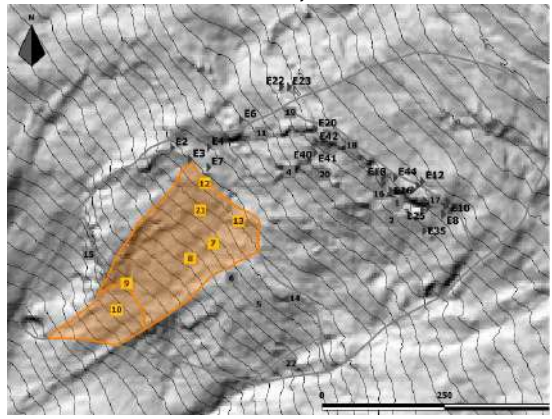
**Scenario 1a – 0,155 Mm<sup>3</sup>**



**Scenario 1b – 0,065 Mm<sup>3</sup>**



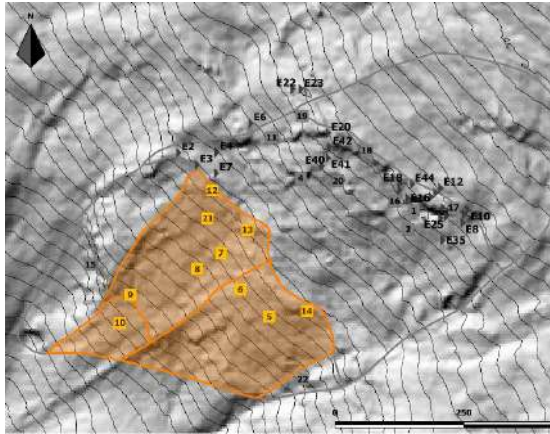
**Scenario 1c – 0,070 Mm<sup>3</sup>**



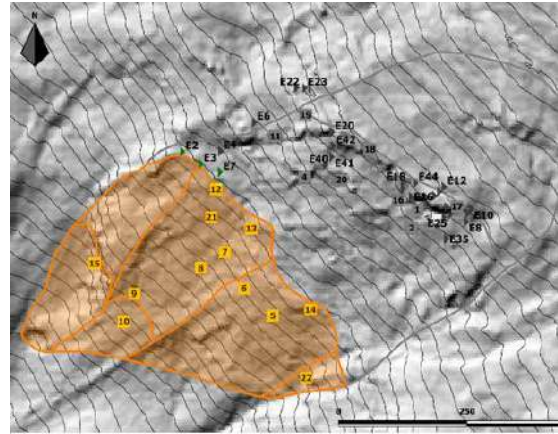
**Scenario 2 – 1,68 Mm<sup>3</sup>**

*Figure 183 – early warning small scenarios (below 2 Mm<sup>3</sup>)*

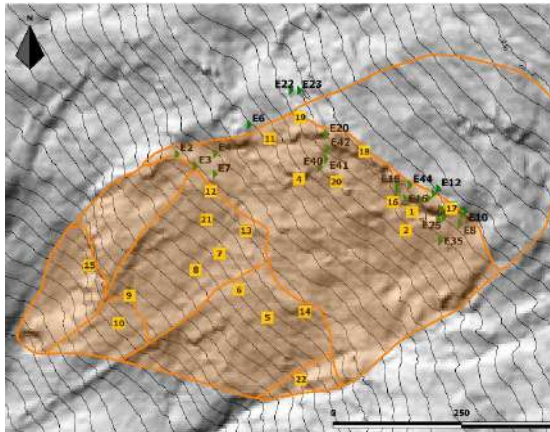




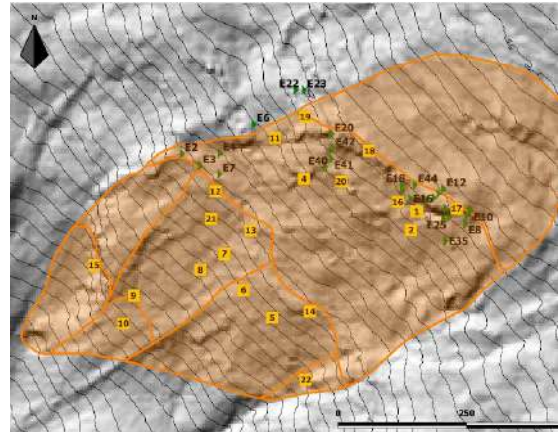
**Scenario 3 – 2,89 Mm<sup>3</sup>**



**Scenario 4 – 3,65 Mm<sup>3</sup>**



**Scenario 5 – 24 Mm<sup>3</sup>**



**Scenario 6 – 31 Mm<sup>3</sup>**

*Figure 184 - early warning large scenarios (more than 2 Mm<sup>3</sup>)*

## **7.2 Objective definition of early warning criteria**

The design of a landslide early warning system (EWS) includes:

- definition of system behavior, mechanisms and sensitivity to triggering actions;
- identification of relevant changes in the system status (e.g. acceleration, failure) and associated probabilities and risk scenarios;
- definition of criteria (thresholds) to detect critical changes in sufficient advance to allow undertaking suitable actions;
- implementation of operational procedures to manage critical changes and the return to ordinary conditions and
- definition of requirements for updating threshold values following changes in system behavior (Crosta and Agliardi 2003; Crosta 2013 and Crosta et al., 2017).

Establishing quantitative early warning thresholds for large rockslides is difficult, due to their complex kinematics, interaction between long-term progressive failure and hydro-mechanical coupling and changing mechanical and hydraulic properties (Crosta et al. 2014). Long-term and seasonal behaviors usually make it difficult to discriminate between long-term creep and hydrologically driven deformation components, and even to clearly identify trigger-response relationships (Bernardie et al. 2015). In fact, large rockslides can respond in different ways to similar triggering actions depending on the season, the cumulative effect of different inputs and the relative contribution of ongoing progressive rock failure processes. We propose a new methodological approach to the evaluation and implementation of different possible early warning approaches on the basis of radar displacement time series.

### **7.2.1 Landslide sensitivity to hydrological triggers: selecting early warning strategies**

Defining suitable early warning criteria for complex rockslides requires assessing relative contributions of long-term creep (e.g. progressive failure) and hydrologically driven failure processes to the measured displacements. This is key to understanding which aspect of landslide behavior (i.e. reactivation/acceleration, triggering of shallow or deep-seated debris slides/debris flows, global rockslide collapse) can be predicted by monitoring a specific slope sector.

The response of the Ruinon rockslide to external inputs varies in intensity and delay. With some exceptions for the snowmelt season (April to June), displacements are recorded during rainy periods (late summer–early fall), with cumulative displacements following cumulative rainfall trends on long, annual and short term. In the dry and cold seasons, the rockslide slowly creeps in most of the sectors, with the slower movements recorded in the rocky sectors at rockslide boundaries (B and G). Snowmelt can explain local displacements in absence of rainfall, whereas the coupling of occasional early snow- fall with intense rainfall events can result in extreme accelerations and cumulative displacements (e.g. October 2012, 2013, 2014). A qualitative evaluation of cumulative rainfall and

cumulative displacement plots suggests that the rockslide sensitivity to rainfall depends on the considered rockslide sector and on the type of rainfall input (i.e. long-term cumulative input, rainy period, close sequence of storms). EW domains A and E (i.e. sectors with thick debris cover) are characterized by large displacements (up to 2 m/year) following well-defined short periods of intense rainfall or snowmelt. The EW domain F (i.e. debris slide downslope of LS) also undergoes large displacements with maximum response associated to longer-duration rainfall. On the opposite, EW domains B and G, embracing the rocky US and rockslide flank, appear less sensitive to rainfall inputs, with total displacements in the monitoring period being less than one tenth of that observed downslope of LS. Along the US (domain B), displacement shows a long-term creep trend, whereas most of the superimposed annual displacements occur until early spring, suggesting that the role of snowmelt is more relevant than rainfall inputs in controlling the deep-seated slide movement. In these sectors, displacements seem to closely follow global rockslide failure scenarios. EW domains C and D, also mirroring deep-seated rockslide movement, follow quite closely the seasonal-scale rainfall patterns but show more complex responses to individual rainfall periods (Figure 185).

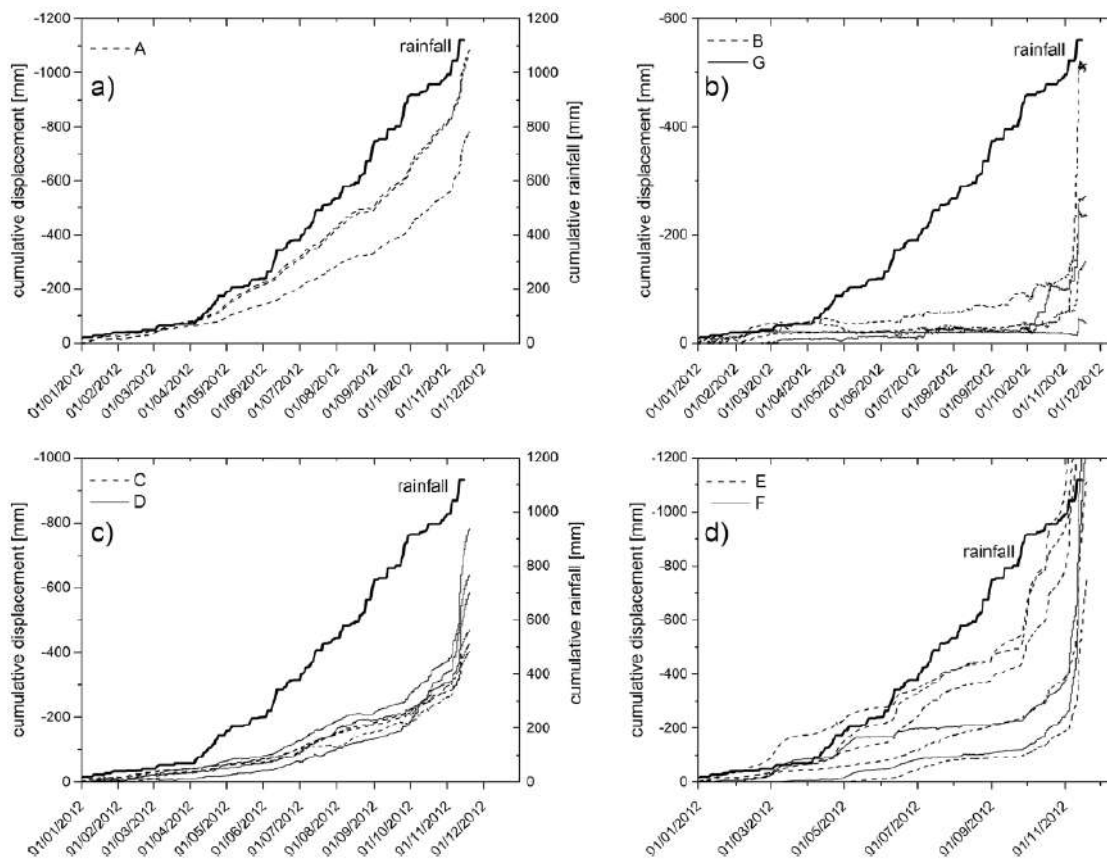


Figure 185 – in the dry and cold seasons, the rockslide slowly creeps in most of the sectors, with the slower movements recorded in the rocky sectors at rockslide boundaries (from Crosta et al., 2017)

We quantitatively assessed the relationship between rainfall and rockslide activity by the analysis of antecedent rainfall. Most published analyses refer to shallow soil slope instabilities and earth slide/flow landslide types (Crosta et al. 2010), whereas very little is available for deep

rockslides. Time series of antecedent rainfall, cumulated over 1, 7, 15, 30, 45, 60, and 90 days, were derived from available datasets and compared to corresponding distributions of displacement rates, measured at each radar streaming point during a training period (June 2006– June 2011). Boxplots representing the distributions of displacement rates for different classes of cumulative antecedent rainfall were prepared for all the streaming points of each EW domain. We selected mean values of displacement rate from boxplots to generate curves of displacement rate versus rainfall, cumulated over different reference periods. The curves obtained in this way for each streaming point (3 curves for EW domains A, B, C and D; 5 curves for domain E; 2 curves for domains F and G) have been averaged considering points within the same rockslide sector. These final curves should represent the average response to rainfall of each rockslide EW domain. In general, we observe a slight increase of displacement rates with the rainfall accumulated in a reference period, until a threshold value, which is different for each EW domain. From then on, a sharp increase in displacement rate is observed with different trends, suggesting that the rockslide response magnitude depends on the rockslide sector and on the rainfall amount- cumulating period.

In particular, EW domain A, involving the continuing failure of coarse-disrupted rock material shows the highest sensitivity to rainfall inputs with sudden and significant short-term responses even to small rainfall inputs. EW domains E and F, involving thick debris material at and below the LS, show significant response to 7 to 15-day cumulative rainfall inputs, suggesting that a certain amount of groundwater recharge is required to trigger acceleration of relatively deep failures affecting thick debris cover. Rockslide domains made of bedrock covered by thin mantling debris (C and D) or by outcropping rocks (B and G) show a low sensitivity to rainfall inputs, which decreases with increased cumulating periods. For rainfall-sensitive domains, 7 and 15 days are the time intervals for which a non-linear relationship between cumulative rainfall input and displacement rate is more evident. The threshold value of cumulative rainfall beyond which displacement rate increases rapidly ranges between 50 and 100 mm. For longer time periods (i.e. 30–60 days), rainfall threshold values rise to about 200 mm.

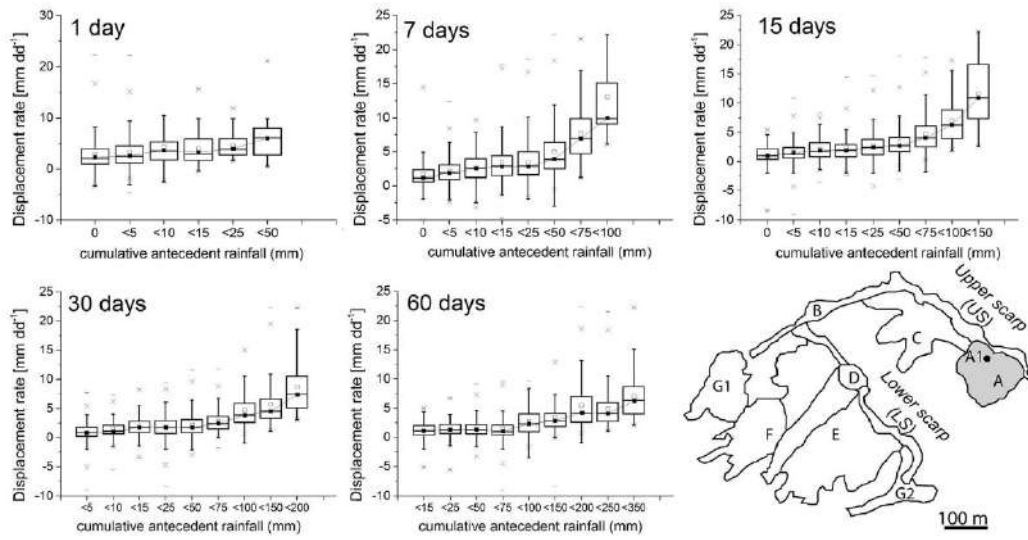


Figure 186 – boxplots representing the distributions of displacement rates for different classes of cumulative antecedent rainfall (from Crosta et al., 2017)

## 7.3 Predicting landslide collapse: early warning velocity thresholds

### 7.3.1 Fukuzono-Voight Approach

Modelling the failure mechanisms of complex rockslides requires a detailed knowledge of rockslide geometry and structure, the constitutive behavior of the involved materials, from initial failure to rapid collapse, as well as the boundary conditions and related variations in space and time (e.g. internal fracturing, shear zone development and relative changes in properties, Crosta et al. 2014). This is usually unfeasible for real-time early warning applications, because of the large dataset required, the time required by model running and calibration tasks and the uncertainties underlying modelling assumptions and the modelling. Several empirical/ phenomenological approaches exploiting the analysis of time series of monitoring data, based on the accelerating slope creep theory (Saito and Uezawa 1961; Fukuzono 1985; Voight 1988; Rose and Hungr 2007), were proposed to overcome some of the abovementioned difficulties. For large landslides with complex kinematics, displacement trends and response to external triggers, Crosta and Agliardi (2003) proposed a methodology to obtain physically based alert velocity thresholds. The method, based on the Fukuzono-Voight equation (Voight 1988), establishes a non-linear relationship between acceleration and displacement rate. The proposed equation provides a description of accelerating (i.e. tertiary) creep:

$$\Omega = \frac{1}{A(\alpha - 2)} \left\{ [A(\alpha - 1)t_f + \dot{\Omega}_f^{1-\alpha}]^{(2-\alpha)/(1-\alpha)} - [A(\alpha - 1)(t_f - t) + \dot{\Omega}_f^{1-\alpha}]^{(2-\alpha)/(1-\alpha)} \right\}$$

with  $\alpha > 1$ ,  $A \neq 2$ ,  $A > 0$  and  $t_f > t$ ,  $t_f$  is the failure time associated to the assumed failure rate (i.e. infinite or having a specific high value), and  $\alpha$  and  $A$  are dimensionless constants controlling the sensitivity of accelerating activity and the curve shape (Crosta and Agliardi 2003). The equation applies under the assumptions of (a) continuous acceleration and (b) constant stress. These conditions are not satisfied in unstable real slopes but are more easily met for fast-evolving single collapses in mining environments, where the inverse velocity approach has been successfully used (Fukuzono 1985; Rose and Hungr 2007). Large landslides are frequently characterized by significant changes in geometry and loading conditions (i.e. non-constant stress), changing rheology (i.e.  $A$  and  $\alpha$  are not constants) and hydrologically controlled seasonal displacement patterns superimposed on long-term slope creep (i.e. landslide is not continuously accelerating). These issues usually hamper a realistic or reliable estimation of the time to failure of complex rockslides.

Crosta and Agliardi (2003) used the Voight's equation, integrated to a power law of displacements versus time, to fit the Ruinon time series of measured cumulative displacements and derive model parameters (namely  $A$ ,  $\alpha$  and  $t_f$ ). Also, Sornette et al. (2004), after observing that some



of the parameters in their slider-block friction model were poorly constrained by inversion process, proposed to fit cumulative displacement data. From the estimated parameters, synthetic velocity-time curves can be derived, providing a quantitative basis to establish alert velocity threshold values. These correspond to different time intervals before expected failure (irrespective of the real, unpredictable time of failure) and can be useful for early warning. Seasonality can be described analytically adding a periodic component to previous equation. This shows that the superimposed periodic acceleration/deceleration is relevant far from the final collapse. Getting closer to the final acceleration phase, the step-like trend disappears with shorter plateau portions as the curve evolves progressively into the asymptotic trend. This decoupling could become more evident for changes in material properties occurring at increasing displacement or velocity.

The method of Crosta and Agliardi (2003) was originally based on data from ground-based instrumentation (e.g. distometer baselines, wire extensometers, total station measurements). Nevertheless, GB-InSAR monitoring approach appears even more suitable to apply this forecasting approach to both debris and deep-seated rock instabilities by providing (a) high coverage spatially distributed data; (b) real-time measurements; (c) high-frequency measurements providing nearly instantaneous velocity estimates; (d) acquisition also in difficult environmental conditions. For the Ruinon rockslide, we fitted time series of cumulative displacement corresponding either to the entire monitoring period or specific critical accelerating periods (e.g. April–July 2008 and October–November 2012) at the 21 representative virtual sensors spread over the 7 EW domains using previous equation. Early warning is enforced by the regional authority at each virtual sensor by the real-time comparison between measured displacement rates (averaged over 6 h) and three velocity thresholds corresponding to pre-alert, alert and emergency conditions. EW thresholds need to be updated as landslide geometry and rheology progressively change due to accumulation of deformation and damage, and to the seasonal effects which strongly modify the applied stresses and available strength. These changes in landslide behavior (and corresponding critical conditions) have been partly accounted for by adapting the reference time intervals before failure to different combinations of intensity of triggering events and rockslide sensitivity. Periods of 7, 15 and 30 days before failure were used until 2012 for the high, moderate and attention warning levels, respectively (see Crosta and Agliardi, 2003). After 2012, they became unsuitable to forecast shallow sliding scenarios in debris-covered areas, especially following rapid snowmelt and rainfall. In these cases, reference time periods were reduced to 2, 3 and 5 days. And a period of 10 and 14 days are implemented to early warning purpose (Figure 188).

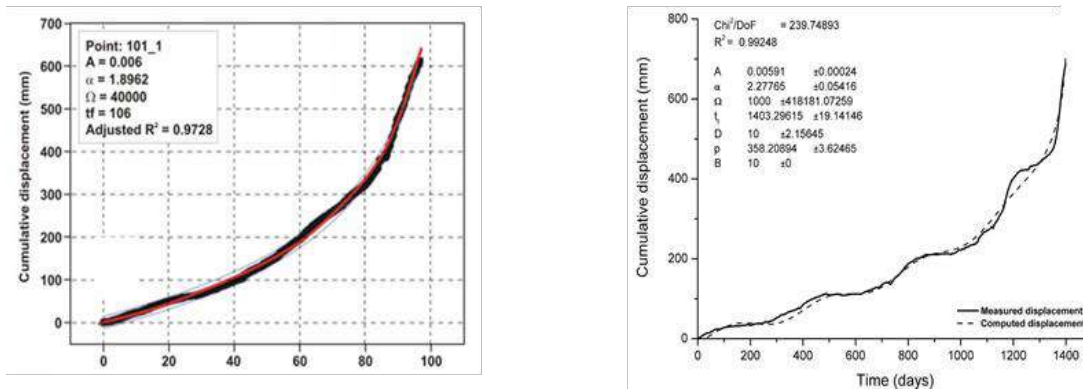


Figure 187 – on left, Ruinon time series of measured cumulative displacements. On right, Seasonality can be described analytically adding a periodic component

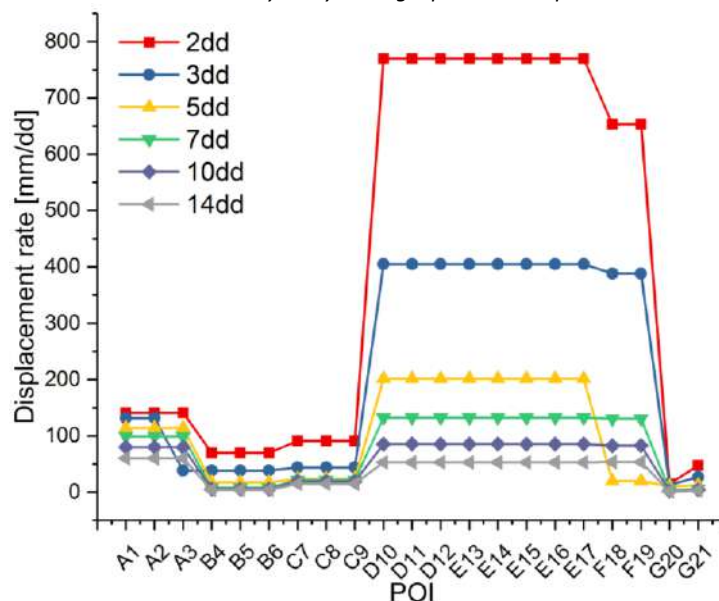


Figure 188 -early warning thresholds concerning GB-InSAR POIs

### 7.3.2 The Statistical Approach

A different statistical method for analysis of monitoring data have been introduced (see section 6.1), this approach results more suitable to understand the evolution of phenomena through time, even if not consider the possible changes for material and process behavior.

For the analyzes of our interest, the data used are the POI (Point-Of-Interest) velocity monitored continuously by the ground interferometric radar system and by extensometers, reported on a daily average. This was possible by compiling a MATLAB routine that allows adding the displacements obtained with different acquisition times and meanings. The data were then analyzed both divided by year and divided by homogeneous areas (Early Warning Domains).

The idea behind the here method presented is the possibility of defining alert thresholds based on the probability of exceedance or not exceedance. Percentile is a measure used in statistics indicating the value below which a given percentage of observations in a group of observations fall, this means that at 90<sup>th</sup> percentile, most of data are below this value, and 10% are above it.

For each POI point, the probability distribution of the displacement rate values for the entire measurement time interval was analyzed. In this way it is possible to define displacement rate values with the probability of not exceeding 75, 90, 95, 99%. Such threshold values thus identified can then be compared with those used in the past or derived from other approaches such as Fukuzono-Voight.

The following graph show some examples of application of the method and the following tables summarize the main results.

It is noted that for the thresholds calculated for GB-InSAR POIs, the values of the 99th percentile are always higher than the thresholds determined with the semi-empirical method at Fukuzono-Voight. At the same time, it is observed that the values corresponding to the 90th and 75th percentiles approximate well the values calculated with the semi-empirical method at 3 and 5 days from the possible collapse.

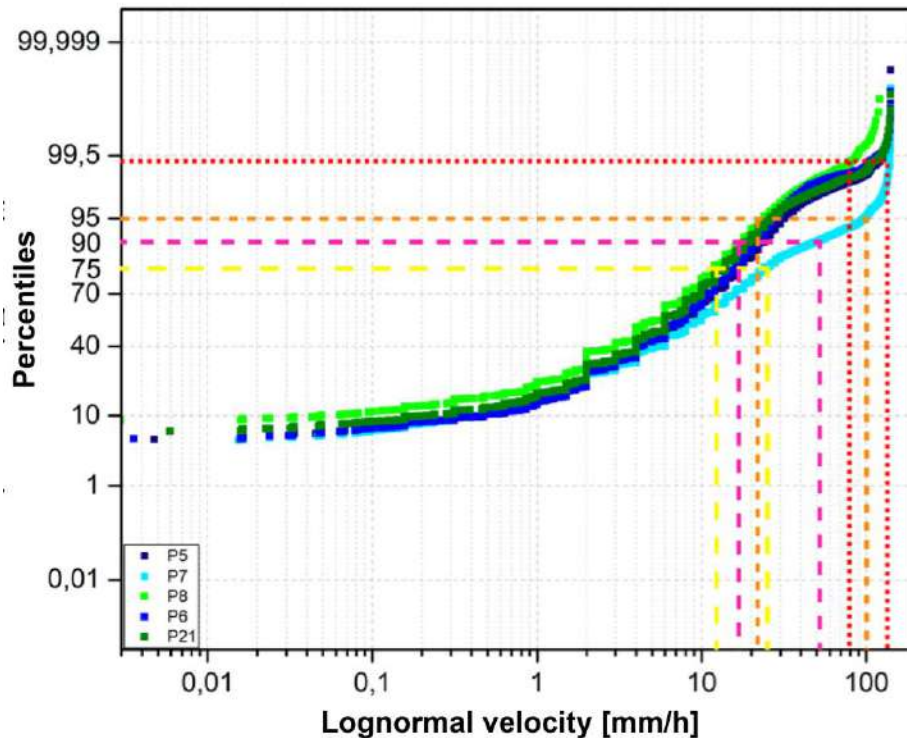


Figure 189 – example of Normal Probability Plot (NPP) with Logarithmic scale applied to GB-InSAR POI velocity data

This kind of approach has been used also on extensometers (Figure 192 and Figure 193) data where typically, the displacement pattern is characterized by stick-slip movement and the Fukuzono-Voight approach is not easily applicable.

This statistical approach has been applied on data that cover the entire monitoring period (since 1998), and the last period of four years (since 2013 to 2017). Arbitrarily, it has been decided to use the thresholds obtained from last period, because representative of an evolution of landslide behavior to large displacement without failure.

The new statistical thresholds have been drawn, and adopted on early warning purpose, 99<sup>th</sup> percentile has been used as highest threshold, 95<sup>th</sup> percentile as moderate threshold and – finally – 90<sup>th</sup> percentile has been used as attention threshold value. These values are close to the thresholds derived by Fukuzono-Voight analyses at 2, 3 and 5 days.

The following Table 15 shows the values for each one extensometer using 99<sup>th</sup>, 95<sup>th</sup> and 90<sup>th</sup> percentiles.

*Table 15 – HL: High Level (99<sup>th</sup> centile); ML: Moderate Level (95<sup>th</sup> centile) and Attention (90<sup>th</sup> centile)*

<b>Extensometers thresholds [mm/day]</b>			
<b>Ext.</b>	<b>HL of critical (P99)</b>	<b>ML of critical (P95)</b>	<b>Attention (P90)</b>
E8	38,4	14,4	9,6
E9	76,6	33,6	24
E10	28,8	14,4	9,6
E11a	57,6	14,4	4,8
E12	19,2	10,8	4,8
E13	9,6	4,8	4,8
E14	9,6	4,8	4,8
E15	24	14,4	9,6
E16	396,6	148,8	76,8
E17	144	57,6	33,6
E18	91,2	52,8	38,4
E25	28,8	9,6	4,8
E33	19,2	4,8	4,8
E35	115,2	19,2	9,6
E44	52,8	14,4	9,6
E3	100,8	38,4	24
E4	129,6	19,2	4,8
E6	91,2	33,6	19,2
E7	134,4	52,8	28,8
E40	168	43,2	19,2
E41	24	9,6	4,8
E42	86,4	14,4	9,6
E20	72	4,8	4,8
E22	14,4	9,6	4,8
E23	57,6	9,6	4,8
E2	67,2	14,4	4,8

#### **7.4 Combining the approaches and minimization of false alarms**

An efficient early warning system (EWS) should in general minimize the rate of false alarms (Crosta et al., 2017), which affect risk perception and pose problems to the technical and decision-making staff in charge of the monitoring network, the population and local administrations affected by the emergency plan and actions. These usually involve costs relative to the alternative transportation of goods and people; the closure of main and sometimes unique roads, and consequently of industrial and commercial activities; the extra hours to be paid to the involved personnel for managing the emergency actions and the monitoring network, and the loss in tourism revenues.

The problem of false alarm reduction can be tackled using different approaches: (a) adopting higher threshold values; (b) increasing redundancy: threshold values must be exceeded for more than one sensor within the same region of interest (in this case early warning domain); (c) introducing pre-alerting thresholds for a step-by-step verification of critical conditions; (d) joint use of different indicators (e.g. displacement, velocity, acceleration, rainfall) for areas with different sensitivity to forcing factors, or areas subjected to different scenarios and (e) threshold adaptation in case of local changes in behavior with consequent change in the representativeness of monitored points.

Considering the abovementioned criteria, new approaches have been introduced to minimize the false alarms. Another key point to take into account is that before this work, to activate the civil protection plan was enough that a single point from GB-InSAR monitoring network exceeded the adopted thresholds (Figure 190). For this reason, the first approach to minimize the false alarms has been to adopt, for POIs into the same EWD, the same thresholds (Figure 191), according to that the kinematic behavior homogeneity of the single POI within the domain. Furthermore, other criteria adopted were that for each EWD at least 2 POIs should exceed the thresholds, simultaneously.

Using this approach and by applying it to the last three years of monitoring data, a relevant decrement of thresholds exceedance is found, up to 85% (EWD G).

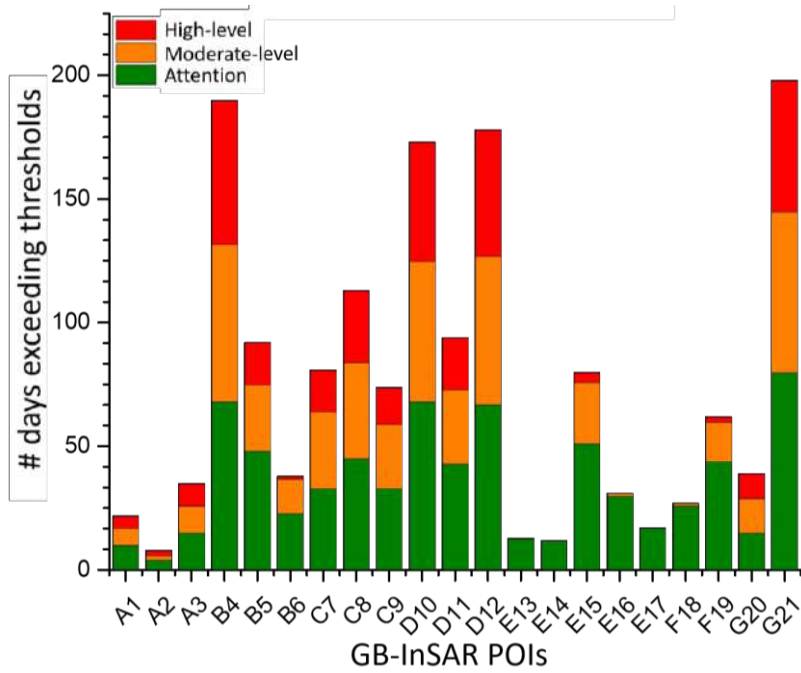


Figure 190 – number of days exceeding thresholds for single POI

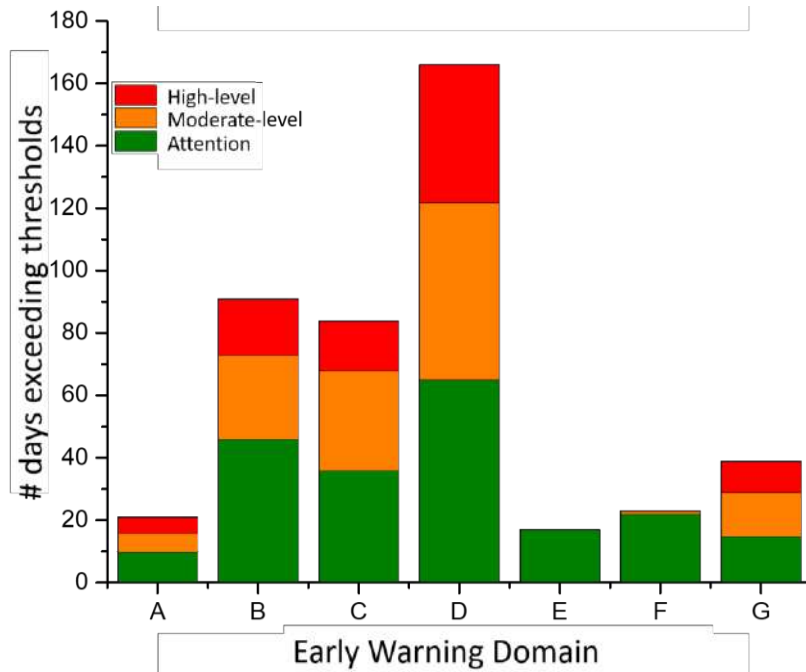


Figure 191 - number of days exceeding thresholds for each Early Warning Domain



Considering the last two years of monitoring and using the Fukuzono-Voight and Statistical approaches an updated version of the thresholds has been released, both for GB-InSAR POIs and extensometers network. Moreover, the extensometers *network* (Figure 192 and Figure 193) has been analyzed and subdivided into 8 different chains, representative of entire phenomenon. The challenge now consists of improving the preexistent early warning strategy combining the new thresholds value and different thresholds from different monitoring systems. To do that, it has been introduced a parameter called *Alert Priority* (hereinafter AP) that represents how much the instrument weights (i.e. is representative) into the event scenario. The extensometers network is characterized by a highest AP because considered more representative of deep instable phenomena (punctual-monitoring) of large and deep fractures in rock than GB-InSAR POIs that are representative of widespread surface displacement (small vs large scenarios).



Figure 192 – distribution of extensometers along the lower scarp of Ruinon rockslide (Chain 1)

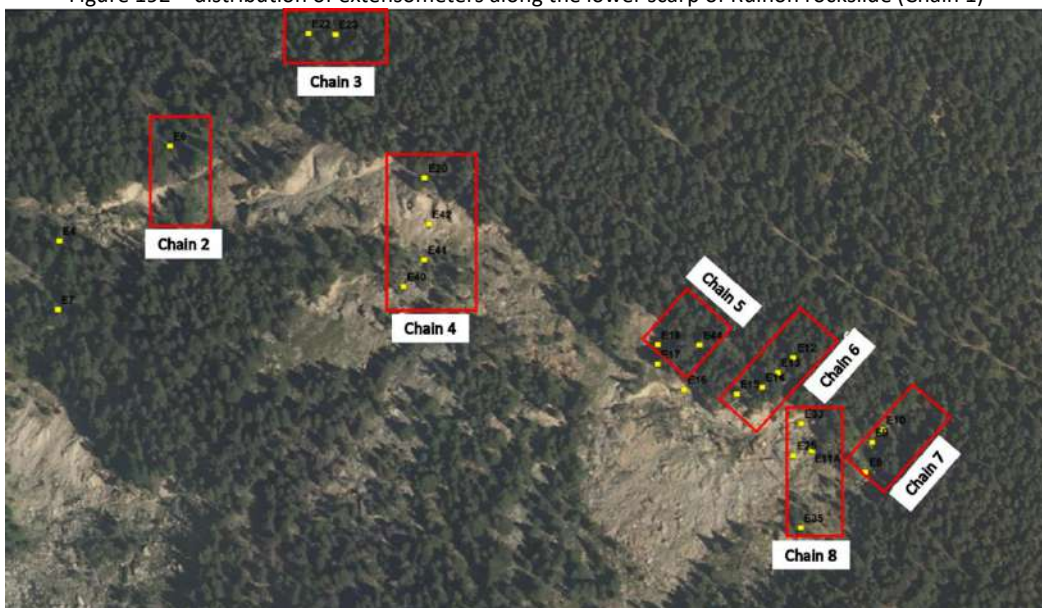


Figure 193 - distribution of extensometers along the upper scarp of Ruinon rockslide (Chain 2 to 8)

Following these criteria, the activation of each different event scenario is subordinate to exceeding of at least two different thresholds simultaneously (Figure 183 and Figure 184).

The application of these new strategies to last two years of monitoring data has been summarized as follow:

*Table 16 – number of days exceeding thresholds for each Event Scenario*

<i># days exceeding thresholds</i>								
<b>Event Scenario</b>	<b>Volume [m<sup>3</sup>]</b>	<b>2dd</b>	<b>3dd</b>	<b>5dd</b>	<b>7dd</b>	<b>10dd</b>	<b>14dd</b>	
<b>SMALL</b>	<b>1a</b>	155,000	0	0	3	21	33	50
	<b>1b</b>	65,000	3	19	34	53	70	101
	<b>1c</b>	70,000	0	0	11	23	35	52
	<b>2</b>	1,680,000	0	0	12	28	48	65
<b>LARGE</b>	<b>3</b>	2,890,000	0	0	15	29	52	67
	<b>4</b>	3,650,000	0	1	17	11	58	71
	<b>5</b>	24,000,000	0	0	0	0	0	0

Table 17 - percentage of days exceeding thresholds for each Event Scenario

<p style="text-align: center;"><b>% exceeding thresholds</b></p>								
	Event Scenario	Volume [m <sup>3</sup> ]	2dd	3dd	5dd	7dd	10dd	14dd
<b>SMALL</b>	<b>1a</b>	155,000	0%	0%	0,5%	3%	5%	8%
	<b>1b</b>	65,000	0,5%	3%	5%	8%	11%	15%
	<b>1c</b>	70,000	0%	0%	2%	3%	5%	8%
	<b>2</b>	1,680,000	0%	0%	2%	4%	7%	10%
<b>LARGE</b>	<b>3</b>	2,890,000	0%	0%	2%	4%	8%	10%
	<b>4</b>	3,650,000	0%	0,2%	3%	5%	9%	11%
	<b>5</b>	24,000,000	0%	0%	0%	0%	0%	0%

Considering the number of exceedances of early warning thresholds in the previous approach (Figure 190 and Figure 191), the here presented novice approach lead to a minimization of false alarms (Table 16 and Table 17). Activation of large scenarios is limited at one day on moderate-level for scenario #4, while the largest scenarios never have been activated. This analysis can be extended also to small scenarios, except to scenario #1b that has been activated until the high-level for 3 days. Considering that for small scenarios are present mitigation measures (i.e. reinforced embankment) to protect the infrastructures (i.e. state national road).

## **7.5 Conclusions**

The long-term records of the Ruinon rockslide allowed testing different early warning threshold enforcement approaches on the recorded rate of false alarms. Velocity thresholds have been applied to verify the number of alerts and false alarms that could have been sent out during more than 10-year-long GB-InSAR monitoring. Furthermore, the recent 2012, 2013, 2014, and 2016 events have been useful to further validate the approach. Exceedance of the threshold value for a single streaming point in a specific EW domain causes a large number of false alarms, whereas exceedance of the maximum threshold value within each EW domain reduces the total number but locally can still generate frequent false alarms. Adoption of threshold values into event scenario, combining data from different monitoring systems in near-real time eliminates most of the false alarms. Another key point concerns the updating of the thresholds, became necessary with the evolution of the rockslide through time and to improve the performance of the warning system, in terms of minimization of the false alarms. For this reason, the proposed statistical approach could be more suitable than Fukuzono-Voight method even if this method cannot allow to take into account for possible changes in material and process behavior.

# CONCLUSIONS

## 8.1 Key findings

This study combined the analysis of landslide monitoring to the results of a series of conventional and unconventional new laboratory tests, which were undertaken to understand the landslide behavior before, during and after the failure conditions. The assessment of this data has been used to (i) study the mechanisms of shear zone development in deep-seated landslides, (ii) analyze how these mechanisms vary in different shear zone materials and evaluate the implications on landslide pre- and post-failure behavior, (iii) use the experimental results in order to develop a simplified visco-plastic model able to describe the potential evolution of landslide.

Regarding the monitoring data, the behavior and the evolution through time of the landslides both on surface and at depth were investigated, especially to analyze the shear zones development. Furthermore, a statistical approach was used, through the use of normal distribution plots, able to describe most of natural phenomena. A new methodology for data analyses and to set the early warning thresholds has been proposed and used for the Ruinon case study. This method clearly does not allow to take into account the possible changes in material behavior and processes but permits to maintain a simplified and faster approach to manage the near-real time monitoring data.

A suite of conventional and unconventional laboratory tests was performed on shear zone samples from different case studies (Mont de La Saxe and Chervaz), characterized by different lithologies. A new type of test has been developed to investigate the creep behavior. The tests performed under drained and undrained conditions indicate that the formation of a slip surface in deep-seated landslides is partially controlled by the properties of the basal shear zone materials. Failure in low-strength metamorphic rock can occur through brittle deformation, as strain localizes - usually - along a singular shear zone. The results have been analyzed to consider the patterns of deformation that are observed in a slope up to final failure. These patterns have been compared with the three-phase creep model.

Furthermore, a mineralogic analysis on shear zone materials was performed, and that point out a main contribution of the mineralogy (especially for phyllosilicates and graphite) on controlling the development and evolution of shear zones.

A simplified model of the progressive development and post-failure behavior of complex landslides has been proposed. The model has been validated using the patterns of landslide movement observed in the Mont de La Saxe rockslide and tested as a potential method of assessing present and potential future landslide behavior. The La Saxe rockslide movement is here interpreted

as the result of two specific mechanisms. The first is ongoing slow displacement, characterized by “creep”-driven movement (dry-conditions, when the water table is either below or close to the failure surface), commonly observed at other landslide sites (e.g. Crosta et al., 2017). A second period of accelerated ground displacement is characterized by seasonal acceleration trend related to water table rise (due to snow-melt).

These results have important implications for understanding the development and post failure behavior of deep-seated landslides, their mechanisms and their relationship to the patterns of movement observed at the ground surface. The results confirm that these relationships could be a powerful tool in the management of future landslide risk.



## 8.2 Limitations

This work has successfully demonstrated the relationship between landslide movement patterns and the mechanisms of shear zone deformation occurring within the basal shear zone of deep-seated landslides. Whilst the results of this investigation demonstrate real progress in the understanding and interpretation of landslide behavior, caution is needed in the application of such techniques to the conditions observed in natural deep-seated landslide conditions. In using this dataset, the limitations of the data presented should be understood.

Both conventional tests are undertaken on relatively small samples which are assumed to be representative of the field conditions. Such small samples may not reflect the potential variability of material conditions across the site and are highly unlikely to reflect any larger scale regional geological or geomorphological features which may be inherent in the landscape. Thus, geomorphological and geological investigations are important in conjunction with the laboratory testing developed in this study if such methods are used to interpret ground behavior at different sites in the future.

The study has benefitted from the continuous monitoring records made available by the Geological Survey of Regione Autonoma Valle d'Aosta. These records are further complimented by a large number of ground movement measurements and observations within the published records. The study has focused largely on the movement patterns of the Mont de La Saxe rockslide. Whilst this provides a reasonable record to analyze ground movement behavior it should be recognized that only one major period of ground acceleration was observed in the records. Although this provided an excellent opportunity to understand the behavior of the landslide, further calibration with future periods of ground acceleration may assist in improving our understanding of ground behavior at the site. Future studies should look to update this investigation with new data from the site when it is made available.

Concerning the here proposed 1D visco-plastic model, taking into account the simplified approach used, some limitations can be listed: (i) GWT is used as punctual, (ii) the interaction between blocks is not considered, (iii) the blocks are considered rigid, which is not true for sectors characterized by debris material and (iv) usually the rockslides are characterized by several shear zones along the profile.

### **8.3 Recommendations for further research**

Whilst this research has provided new knowledge of the mechanisms and processes operating in deep-seated landslide complexes, further research could be considered in order to advance understanding on shear zones.

Movement within pre-existing landslides has been studied using remolded samples in laboratory testing. It is recognized the shear zones in brittle materials presented weakening processes such as polishing, and hardening processes, may occur. Further creep testing would be beneficial to study these processes more accurately, and also investigate the intact material to understand the transition phases toward to development of shear zone. A detailed mineralogic investigation should be considered and should be evaluate their influence on displacement rate, taking into account the studies related to fault zones.

The patterns of movement recorded at Mont de La Saxe provide one of the most detailed monitoring records of a deep-seated landslide. The patterns of movement, however, have revealed two main periods of accelerated displacement during the late winter period of 2014 and 2015. Even if a clear relationship between these events and ground-water oscillation (due to snow-melt and rainfall contribution) has been established at the site it must be recognized that further monitoring may provide additional periods of accelerated ground creep that may assist in refining this relationship.

Finally, combining data from shear zone investigations and monitoring network could be useful to improve the 1D delayed plasticity model proposed here, while retaining the simplified approach suitable to early warning purpose.

This study has demonstrated how a combined method of detailed field monitoring, geomorphological assessment, geotechnical testing and numerical modeling can provide a detailed understanding of complex landslide systems, their mechanisms of movement and their potential future behavior. Furthermore, detailed instrumentation and long-term monitoring would allow the consideration of important parameters, which may be used as hazard warning alert criteria or inform on the design of cost-effective landslide mitigation measures.



*Tutto passa, il resto va.*

*(F. DG)*

## ACKNOWLEDGMENTS

First of all, I would say thank you to Prof. G.B. Crosta, I tried to learn as much as possible from you, and I understood that - as the US veterans say - all give some, some give all. Thank you.

I am a very lucky guy, and I can say that I have three different family. My gratitude goes to my blood family, for supporting me always. Goes to my friends, especially to Gruppo Simpatia, you are blood of my blood. Finally - I would to say thank you Sondrio Rugby family, eagle will come back to fly.

A very special gratitude goes out to all down at research group at second floor of University of Milano – Bicocca., this work would have been not possible without your single contribute. I would mention also Prof. Gonghui Wang at DPRI (Kyoto University) and his research group (Ma Ning, Haibo Miao, Siyuan Zhao and Chengrui Chang), you are a very special people and part of this thesis is your credit.

A special mention goes to my life-coach, PhD Margherita Cecilia Spreafico, to supporting and suffering me, I am sure that without your support this work would have been not possible. Thank you.

Finally, I want to say thank you to all people that I met in this travel, every one of you has left me something, thank you.

Thank you to all and see you down the road, cheers!

## REFERENCES

- Abellán, A., Calvet, J., Vilaplana, J.M., Blanchard, J., (2010). Detection and spatial prediction of rockfalls by means of terrestrial laser scanner monitoring. *Geomorphology* 119 (3-4), 162-171.
- Abellán, A., Jaboyedoff, M., Oppikofer, T., and Vilaplana, J. M. (2009). Detection of millimetric deformation using a terrestrial laser scanner: experiment and application to a rockfall event. *Natural Hazards and Earth System Sciences*, 9(2), 365-372.
- Abramson, L. W., Lee, T. S., Sharma, S., and Boyce, G. M. (2002). *Slope stability and stabilisation methods*. Second edition. Pub. John Wiley & Sons, INC.
- Agliardi, F., Crosta, G., & Zanchi, A. (2001). Structural constraints on deep-seated slope deformation kinematics. *Engineering Geology*, 59(1-2), 83-102.
- Agung, M. W., Sassa, K., Fukuoka, H., & Wang, G. (2004). Evolution of shear-zone structure in undrained ring-shear tests. *Landslides*, 1(2), 101-112.
- Ahnert, F., (2003). *Einführung in die Geomorphologie*. Ulmer, Stuttgart, Germany, 477 p.
- Aladekomo, J. B., & Bragg, R. H. (1990). Structural transformations induced in graphite by grinding: analysis of 002 X-ray diffraction line profiles. *Carbon*, 28(6), 897-906.
- Alexander, E.D. (2002) *Principles of emergency planning and management*. Terra Publishing, Harpenden, 340 p.
- Allison, R. J., & Brunson, D. (1990). Some mudslide movement patterns. *Earth Surface Processes and Landforms*, 15(4), 297-311.
- Ambrosi, C., & Crosta, G. B. (2006). Large sackung along major tectonic features in the Central Italian Alps. *Engineering Geology*, 83(1-3), 183-200.
- and stabilization. 9th International Symposium on Landslides. A.A. Balkema Publishers, Leiden, Rio de Janeiro, Brazil, pp. 541-548.
- Anderson, M.G., Richards, K., (1987). Modelling slope stability: the complementary nature of geotechnical and geomorphological approaches, in: Anderson, M.G. (Ed.), *Slope Stability: Geotechnical Engineering and Geomorphology*. John Wiley & Sons Ltd, pp. 1-9.
- Angeli, M. G., Gasparetto, P., Bromhead, E. (2004). Strength-regain mechanisms in intermittently moving landslides. In: *Proceedings of the 9th International Symposium on Landslides*. Rio de Janeiro. Vol. 1. Taylor and Francis, London (pub). pp. 689 – 696.
- Angeli, M.-G., Gasparetto, P., Menotti, R. M., Pasuto, A., and Silvano, S. (1996). A visco-plastic model for slope analysis applied to a mudslide in Cortina d'Ampezzo, Italy. *Quarterly Journal of Engineering Geology and Hydrogeology*, 29(3):233–240.
- Antoine, P., Pairis, J., and Pairis, B. (1975). Quelques observations nouvelles sur la structure de la couverture sédimentaire interne du massif du mont-blanc, entre le Col du Ferret (frontière Italo-Suisse) et la tête des fours (Savoie, France). *Geologie Alpine*, 51:5–23.
- Antolini, F. (2014). *The use of radar interferometry and finite-discrete modelling for the analysis of rock landslides* (Doctoral dissertation, PhD Thesis, Politecnico di Torino).
- Antolini, F., Barla, M., Gigli, G., Giorgetti, A., Intrieri, E., and Casagli, N. (2016). Combined Finite–Discrete Numerical Modeling of Runout of the Torgiovanetto di Assisi Rockslide in Central Italy. *International Journal of Geomechanics*, 04016019.
- Antonello, G., Casagli, N., Farina, P., Leva, D., Nico, G., Sieber, A. J., & Tarchi, D. (2004). Ground-based SAR interferometry for monitoring mass movements. *Landslides*, 1(1), 21-28.
- Argand, E. (1916). *Sur l'arc des Alpes occidentales*.



- ASTM D3080/D3080M-11(2011). Standard Test Method for Direct Shear Test of Soils Under Consolidated Drained Conditions, ASTM International, West Conshohocken, PA.
- ASTM D4318-17e1 (2017). Standard Test Methods for Liquid Limit, Plastic Limit, and Plasticity Index of Soils, ASTM International, West Conshohocken, PA.
- ASTM D4767-11 (2011) Standard Test Method for Consolidated Undrained Triaxial Compression Test for Cohesive Soils, ASTM International, West Conshohocken, PA
- ASTM D6913/D6913M-17 (2017). Standard Test Methods for Particle-Size Distribution (Gradation) of Soils Using Sieve Analysis, ASTM International, West Conshohocken, PA.
- ASTM D7181-11 (2011) Method for Consolidated Drained Triaxial Compression Test for Soils, ASTM International, West Conshohocken, PA
- Augustesen, A., Liingaard, M., and Lade, P. V. (2004). Evaluation of Time-Dependent Behavior of Soils. *International Journal of Geomechanics*, ASCE, 30 (3): 137 – 156.
- Avian, M., Kellerer-Pirklbauer, A., Bauer, A., (2009). LiDAR for monitoring mass movements in permafrost environments at the cirque Hinteres Langtal, Austria, between (2000) and (2008). *Natural Hazards and Earth System Sciences* 9, 1087–1094.
- Baldo, M., Bicocchi, C., Chiocchini, U., Giordan, D., Lollino, G., (2009). LiDAR monitoring of mass wasting processes: The Radicofani landslide, Province of Siena, Central Italy. *Geomorphology* 105 (3-4), 193–201.
- Banecetti, M., Spreafico, M.C., Elettri, F., Giardino, M., Perotti, L., Borgatti, L., Ghirotti, M., Ratto, S. (2015). *Geomorphological Analyses, Geomatic Surveys and Numerical Modelling for the Characterization of the Chervaz Deep-Seated Gravitational Slope Deformation, Chambave (AO)*. In *Engineering Geology for Society and Territory-Volume 2* (pp. 565-569). Springer, Cham.
- Barla G (2010) Progress in the understanding of deep-seated landslides from massive rock slope failure. In: *ISRM international symposium—6th Asian rock mechanics symposium, October 23–27, (2010), New Delhi, India*, pp 58–72
- Barla, G., Amici, R., Vai, L., Vanni, A., (2004). Investigation, monitoring and modelling of a landslide in porphyry in a public safety perspective, in: Lacerda, W., Ehrlich, M., Fontoura, S.A.B., Sayao, A.S.F. (Eds.), *Landslides: Evaluation and stabilization. 9th International Symposium on Landslides*. A.A. Balkema Publishers, Leiden, Rio de Janeiro, Brazil, pp. 623-628.
- Barla, G., Antolini, F., Barla, M., Mensi, E., & Piovano, G. (2010). Monitoring of the Beaugard landslide (Aosta Valley, Italy) using advanced and conventional techniques. *Engineering Geology*, 116(3-4), 218-235.
- Barla, G., Antolini, F., Mensi, E., and Piovano, G. (2010) Monitoring of the Beaugard landslide (Aosta Valley, Italy) using advanced and conventional techniques." *Engineering Geology* 116.3: 218-235.
- Baum, R.L., Crone, A.J., Escobar, D., Harp, E.L., Major, J.J., Martinez, M., Pullinger, C. and Smith, M.E. (2001) Assessment of landslide hazards resulting from the February 13, (2001), El Salvador earthquake; a report to the government of El Salvador and the U. S. Agency for International Development. U.S. Geological Survey Open-File Report, (2001)-119, 21 p.
- Bell, R., Mayer, J., Pohl, J., Greiving, S., Glade, T. (Eds.), (2010). *Integrative Frühwarnsysteme für Gravitative Massenbewegungen (ILEWS) - Monitoring, Modellierung, Implementierung*. Klartext Verlag, Essen, 272 p.
- Berardi, R., Mercurio, G., Bartolini, P., Cordano, E., (2005). Dynamics of saturation phenomena and landslide triggering by rain infiltration in a slope, in: Hungr, O., Fell, R., Couture, R., Eberhardt, E. (Eds.), *International Conference on Landslide Risk Management*. Taylor & Francis Ltd., Vancouver, Canada, pp. 212-219.

- Bernardie S, Desramaut N, Malet J-P, Gourlay M, Grandjean G (2015) Prediction of changes in landslide rates induced by rainfall. *Landslides* (2015) 12:481–494
- Bertini, T., Cugusi, F., D’Elia, B., Rossi-Doria, M. (1984). Climatic conditions and slow movements of colluvial covers in Central Italy. In: *Proceedings of the IV International Symposium on landslides, Toronto 1984. Vol 1. pp 367 – 376.*
- Binet S, Mudry J, Scavia C, Campus S, Bertrand C, Guglielmi Y (2007) In situ characterization of flows in a fractured unstable slope. *Geomorphology* 86:193–203
- Bishop, A. W. and Henkel, D. J. (1962). Measurement of soil properties in the triaxial test.
- Bishop, A. W. and Lovenbury, H. T. (1969). Creep Characteristics of Two Undisturbed Clays. *Proceedings, 7th International Conference on Soil Mechanics and Foundation Engineering, Mexico, 1: 29 – 37.*
- Bishop, A. W., Green, G. E., Garga, V. K., Andresen, A., & Brown, J. D. (1971). A new ring shear apparatus and its application to the measurement of residual strength. *Geotechnique*, 21(4), 273-328.
- Bjerrum, L. (1973). Problems of soil mechanics and construction on soft clays and structurally unstable soils. In *Proc. 8th ICSMFE (Vol. 3, pp. 111-159).*
- Bjerrum, L. 1967. Engineering Geology of Normally-Consolidated Marine Clays as Related to Settlements of Buildings. *Seventh Rankine Lecture, Geotechnique*, 17(2): 82 – 118
- Blikra, L. H. (2008). The Aknes Rockslide: Monitoring, Threshold Values and Early Warning. In Chen et al. (eds.). *Proceedings, 10th International Symposium on Landslides and Engineered Slopes, Xi’an, China, 2: 1089 – 1094.*
- Blikra, L. H., Braathen, A., Anda, E., Stalsberg, K., & Longva, O. (2002). Rock avalanches, gravitational bedrock fractures and neotectonic faults onshore northern West Norway: Examples, regional distribution and triggering mechanisms. *Geological Survey of Norway Report.*
- Boadu FK (1997) Fractured rock mass characterization parameters and seismic properties: analytical studies. *J Appl Geophys* 36:1–19
- Bogaard, T., (2000). The slope movements within the Mondorès graben (Drôme, France); the interaction between geology, hydrology and typology. *Engineering Geology* 55 (4), 297-312.
- Bonnard, C., (2008). Introduction to Landslide: Mechanisms of Landslides and Specificities of Large Landslides. Presented at the *Landslide Risk Assessment and Mitigation Summerschool (2008) (LARAM), Ravello, Italy.*
- Bonnard, C., Noverraz, F., Dupraz, H., (1996). Long-term movement of substabilized versants and climatic changes in the Swiss Alps, in: Senneset, K. (Ed.), *Landslides. 7th International Symposium on Landslides. Balkema, Rotterdam, Trondheim, Norway, pp. 1525-1530.*
- Bonnard, C., Noverraz, F., Dupraz, H., (1996). Long-term movement of substabilized versants and climatic changes in the Swiss Alps, in: Senneset, K. (Ed.), *Landslides. 7th International Symposium on Landslides. Balkema, Rotterdam, Trondheim, Norway, pp. 1525-1530.*
- Bonzanigo, L. (1999). *Lo slittamento di Campo Vallemaggia (Doctoral dissertation, ETH Zurich) in italian*
- Bonzanigo, L., Eberhardt, E., & Loew, S. (2007). Long-term investigation of a deep-seated creeping landslide in crystalline rock. Part I. Geological and hydromechanical factors controlling the Campo Vallemaggia landslide. *Canadian Geotechnical Journal*, 44(10), 1157-1180.
- Braathen, A., Blikra, L. H., Berg, S. S., & Karlsen, F. (2004). Rock-slope failures in Norway; type, geometry, deformation mechanisms and stability. *Norwegian Journal of Geology/Norsk Geologisk Forening*, 84(1).

- Brace, W. F., & Byerlee, J. D. (1966). Stick-slip as a mechanism for earthquakes. *Science*, 153(3739), 990-992.
- Bracegirdle, A., Vaughn, P. R., Hight, D. W., (1991). Displacement prediction using rate effects on residual strength. In: *Landslides, proceedings from the VI International symposium on Landslides*. Christchurch, New Zealand. Bell (ed). pp 343 – 347.
- Bressani LA, Pinheiro RJB, Bica AVD, Eisenberger CN, Soares JMD (2008) Movements of large urban slope in the town of Santa Cruz do Sul (RGS), Brazil. In: Chen Z, Zhang J, Li Z, Wu F, Ho K (eds) *Landslides and engineered slopes—from the past to the future*, vol 1. CRC Press, Boca Raton, pp 293–298
- Bressani, L. A., Pinheiro, R. J. B., Bica, A. V. D., Eisenberger, C. N., & Soares, J. (2008). Movements of a large urban slope in the town of Santa Cruz do Sul (RGS), Brazil. *Chen, Z.; Zhang, J.; Li, Z*, 293-298.
- Bressani, L.A., Pinheiro, R.J.B., Eisenberger, C.N., Soares, J.M.D., (2008). Movements of a large urban slope in the town of Santa Cruz do Sul (RGS), Brazil. *Landslides and Engineered Slopes. From the Past to the Future 1*, 293-298.
- Broccolato, M., Cancelli, P., Crosta, G. B., Tamburini, A., and Alberto, W. (2011). Tecniche di rilievo e monitoraggio della frana di mont de la saxe (Courmayeur). XXIV Convegno Nazionale di Geotecnica, Innovazione Tecnologica nell'ingegneria Geotecnica, Napoli.
- Bromhead EN, Dixon N (1986) The field residual strength of London clay and its correlation with laboratory measurements, especially ring shear tests. *Geotechnique* 36(4):449–452
- Bromhead, E. N. (1979). A simple ring shear apparatus. *Ground Engineering*, 12(5).
- Bromhead, E., Huggins, M., Ibsen, M.-L., (2000). Shallow Landslides in Wadhurst Clay at Robertsbridge, Sussex, UK, in: Bromhead, E., Dixon, N., Ibsen, M.-L. (Eds.), *Landslides in Research, Theory and Practice*. 8th International Symposium on Landslides. T. Telford, London, Cardiff, Wales, pp. 183-188.
- Bromhead, E.N, and Ibsen, M.-L. (2007). Folkestone warren landslides and the impact of the past rainfall record. In: R McInnes, J Jakeyways, H, Fairbank, and E Mathie (Editors), *Proceedings of the International Conference Landslides and Climate Change*, Ventnor Isle of Wight. Taylor & Francis, London. pp. 17-24.
- Brooks, S.M., Crozier, M.J., Glade, T.W., Anderson, M.G., (2004). Towards Establishing Climatic Thresholds for Slope Instability: Use of a Physically-based Combined Soil Hydrology-slope Stability Model. *Pure and Applied Geophysics* 161 (4), 881-905.
- Brückl E, Brunner FK, Kraus K (2006) Kinematics of a deep-seated landslide derived from photogrammetric, GPS and geophysical data. *Eng Geol* 88:149–159
- Brückl E, Parotidis M (2005) Prediction of slope instabilities due to deep-seated gravitational creep. *Nat Hazards Earth Syst Sci* 5:155–172
- Buffington, J. M., Dietrich, W. E., & Kirchner, J. W. (1992). Friction angle measurements on a naturally formed gravel streambed: Implications for critical boundary shear stress. *Water Resources Research*, 28(2), 411-425.
- Buffington, J. M., Dietrich, W. E., & Kirchner, J. W. (1992). Friction angle measurements on a naturally formed gravel streambed: Implications for critical boundary shear stress. *Water Resources Research*, 28(2), 411-425.
- Buma, J., (2000). Finding the most suitable slope stability model for the assessment of the impact of climate change on a landslide in southeast France. *Earth Surface Processes and Landforms* 25 (6), 565–582.
- Burgi C, Parriaux A, Franciosi G (2001) Geological characterization of weak cataclastic fault rocks with regards to the assessment of their geomechanical properties. *Quart J Eng Geol Hydrogeol* 34:225–232

- Bürgi, C (1999) Cataclastic fault rocks in underground excavations: a geological characterisation In PhD thesis
- Butterfield, R. (2000). A dynamic model of shallow slope motion driven by fluctuating ground water levels. In *Landslides in Research, Theory and Practice: Proceedings of the 8th International Symposium on Landslides held in Cardiff on 26–30 June (2000)*, pages 1–203. Thomas Telford Publishing.
- Byerlee, J., (1978). Friction of rocks. *Pure Appl. Geophys.* 116, 615-626.
- Caine, N., (1980). The Rainfall Intensity: Duration Control of Shallow Landslides and Debris Flows. *Geografiska Annaler. Series A, Physical Geography* 62 (1/2), 23-27.
- Calvello, M., Cascini, L., Sorbino, G., (2008). A numerical procedure for predicting rainfall-induced movements of active landslides along pre-existing slip surfaces. *International Journal for Numerical and Analytical Methods in Geomechanics* 32 (4), 327-351.
- Canutì, P., Casagali, N., Moretti, S., Leva, D., Sieber, A.J., Tarchi, D., (2002). Landslide monitoring by using ground-based radar differential interferometry, in: Rybák J., Stemberk, J., Wagner, P. (Eds.), *First European Conference on Landslides*. Balkema Publishers, Prague, Czech Republic, pp. 523-528.
- Canutì, P., Casagli, N., Moretti, S., Leva, D., Sieber, A. J., & Tarchi, D. (2018). Landslide monitoring by using ground-based radar differential interferometry. In *Landslides* (pp. 523-528). Routledge.
- Cappa F, Gugliemi Y, Soukatchoff VM, Mudry J, Bertrand C, Charmoille A (2004) Hydromechanical modeling of a large moving rock slope inferred from slope levelling coupled to spring long-term hydrochemical monitoring: example of the La Clapière landslide (Southern Alps, France). *J Hydrol* 291:67–90
- Carey, J. (2011) *The Progressive Development and Post-Failure Behavior of Deep-Seated Landslide Complexes*. Doctoral thesis, Durham University
- Carrara, A., Guzzetti, F., Cardinali, M. and Reichenbach, P. (1999) Use of GIS Technology in the Prediction and Monitoring of Landslide Hazard. *Natural Hazards*, 20:2-3 117-135.
- Carson, M. and Kirkby, M., (1972). *Hillslope Form and Process*. University Press, Cambridge, 475 pp.
- Carter, B.J., J, D., Ar, I. & Pa, W., (2000). Simulating fully 3D hydraulic fracturing. *Modeling in geomechanics*, 200, pp.525–557.
- Casagli, N., Catani, F., Del Ventisette, C., & Luzi, G. (2010). Monitoring, prediction, and early warning using ground-based radar interferometry. *Landslides*, 7(3), 291-301.
- Casagli, N., Catani, F., Del Ventisette, C., Luzi, G., (2010). Monitoring, prediction, and early warning using ground-based radar interferometry. *Landslides* 7 (3), 291-301.
- Castellanza, R., Crosta, G. B., Frattini, P., Frigerio, G., Di Prisco, C., Dattola, G., & Bertolo, D. (2015). Modelling of a rapidly evolving rockslide: the Mt. de la Saxe case study. In *IOP Conference Series: Earth and Environmental Science* (Vol. 26, No. 1, p. 012059). IOP Publishing.
- Chambers, John, William Cleveland, Beat Kleiner, and Paul Tukey, (1983), *Graphical Methods for Data Analysis*, Wadsworth.
- Chigira, M. (1992): Long-term gravitational deformation of rocks by mass rock creep.
- Clark, A.R., Fort, D.S., Davis, G.M., (2000). The Strategy, Management and Investigation of Coastal Landslides at Lyme Regis, Dorset, in: Bromhead, E., Dixon, N., Ibsen, M.-L. (Eds.), *Landslides in Research, Theory and Practice*. 8th International Symposium on Landslides. T. Telford, London, Cardiff, Wales, pp. 279-286.
- Cloos, H., (1928). Experimente zur inneren Tectonik. *Centralbl. Mineral. Geol. U Pal.* 1929B, 609-621
- Cnudde, V. and Boone, M. N. (2013). High-resolution x-ray computed tomography in geosciences: A review of the current technology and applications. *Earth-Science Reviews*, 123:1–17.

- Collettini, C., Niemeijer, A., Viti, C., & Marone, C. (2009). Fault zone fabric and fault weakness. *Nature*, 462(7275), 907.
- Collettini, C., Niemeijer, A., Viti, C., Smith, S. A., & Marone, C. (2011). Fault structure, frictional properties and mixed-mode fault slip behavior. *Earth and Planetary Science Letters*, 311(3-4), 316-327.
- Cornelius, R. and Scott, P. (1993). A materials failure relation of accelerating creep as empirical description of damage accumulation. *Rock mechanics and rock engineering*, 26(3):233–252.
- Cornforth, D.H., Mikkelsen, P.E., (1996). Continuous Monitoring of the Slope above an Excavation within a Marginally Stable Landslide, in: Senneset, K. (Ed.), *Landslides. 7th International Symposium on Landslides*. Balkema, Rotterdam, Trondheim, Norway, pp. 1539-1544.
- Corominas, J., Moya, J., Ledesma, A., Lloret, A., and Gili, J. A. (2005). Prediction of ground displacements and velocities from groundwater level changes at the vallcebre landslide (eastern pyrenees, spain). *Landslides*, 2(2):83–96.
- Costa, J.E. and Schuster, R.L. 1987. *The Formation and Failure of Natural Dams*, US Geological Survey Open- File Report. pp. 87-392.
- Coulomb, C.A., (1776). Essai sur une application des regles des maximis et minimis a quelques problemes de statique relatifs a l'architecture. *Memoires de l'Academie Royale pres Divers Savants* 7, 343–387.
- Couperthwaite, S.L. and Marshall, R.G. (1989). Slope instability poses complex problems for pipeline design. *Technology Oil and gas Journal*, 85.
- Coussot, P. (1995). Structural similarity and transition from Newtonian to non-Newtonian behavior for clay-water suspensions. *Physical review letters*, 74(20), 3971.
- Craig, R.F., (1997). *Soil Mechanics*. Spon Press, London. pp. 485.
- Craw, D. (2002). Geochemistry of late metamorphic hydrothermal alteration and graphitisation of host rock, Macraes gold mine, Otago Schist, New Zealand. *Chemical Geology*, 191(4), 257-275.
- Crawford, B., Faulkner, D., Rutter, E., (2008). Strength, porosity, and permeability development during hydrostatic and shear loading of synthetic quartz-clay fault gouge. *J. Geophys. Res. B* 113. [http://dx.doi.org/10.1029/\(2006\)JB004634](http://dx.doi.org/10.1029/(2006)JB004634)
- Cristescu, N., 1989. *Rock rheology*. Springer, 350 p.
- Cristescu, N., (1994). Viscoplasticity of geomaterials, in: *Visco-Plastic Behavior of Geomaterials*. Springer-Verlag, New York, pp. 103–207.
- Cristescu, N., Cazacu, O., (2000). Viscoplasticity of geomaterials, in: *Modeling in Geomechanics*. Wiley, Sussex, pp. 129–154
- Crosta G, Frattini P, Basiricò S, Cancelli P, Alberto W, Tamburini A (2011) Modello idrogeologico del versante di Mont de La Saxe e aggiornamento dello stato delle conoscenze. Regione Valle d'Aosta (unpublished report), 102 pp
- Crosta GB, Agliardi F (2002) How to obtain alert velocity thresholds for large rockslides. *Phys Chem Earth Parts A/B/C* 27(36):1557–1565
- Crosta, G. and Agliardi, F. (2003). Failure forecast for large rock slides by surface displacement measurements. *Canadian Geotechnical Journal*, 40(1):176–191.
- Crosta, G. B. (1989). A study of slope movements caused by heavy rainfall in Valtellina (Italy–July 1987). In *Proc. 6th Int. Conf. and Field Workshop on Landslides ALPS* (Vol. 90, pp. 247-258).
- Crosta, G. B., Agliardi, F., Rivolta, C., Alberti, S., & Dei Cas, L. (2017). Long-term evolution and early warning strategies for complex rockslides by real-time monitoring. *Landslides*, 14(5), 1615-1632.

- Crosta, G. B., Cancelli, P., Tamburini, A., Alberto, W., Broccolato, M., Castellanza, R., Frattini, P., Agliardi, F., Rivolta, C., and Leva, D. (2012). Chasing a complete understanding of a rapid moving rock slide: the la saxe landslide. In EGU General Assembly Conference Abstracts, volume 14, page 11813.
- Crosta, G. B., Chen, H., & Lee, C. F. (2004). Replay of the 1987 Val Pola landslide, Italian alps. *Geomorphology*, 60(1-2), 127-146.
- Crosta, G. B., Di Prisco, C., Frattini, P., Frigerio, G., Castellanza, R., and Agliardi, F. (2014). Chasing a complete understanding of the triggering mechanisms of a large rapidly evolving rockslide. *Landslides*, 11(5):747–764.
- Crosta, G. B., Frattini, P., Valbuzzi, E., & De Blasio, F. V. (2018). Introducing a new inventory of large Martian landslides. *Earth and Space Science*, 5(4), 89-119.
- Crosta, G., (1998). Regionalization of rainfall thresholds: an aid to landslide hazard evaluation. *Environmental Geology* 35 (2), 131–145.
- Crosta, G., Agliardi, F., & Frattini, P. (1999). Convenzione di studio sulla Frana del Ruinon (Valfurva, Sondrio). Technical report, Regione Lombardia–Dipartimento di Scienze Geologiche e Geotecnologie, Università degli Studi di Milano-Bicocca.[In Italian.].
- Crosta, G., Chen, H., and Frattini, P. (2006). Forecasting hazard scenarios and implications for the evaluation of countermeasure efficiency for large debris avalanches. *Engineering Geology*, 83(1):236–253.
- Crosta, G.B., Frattini, P., (2003). Distributed modelling of shallow landslides triggered by intense rainfall. *Natural Hazards and Earth System Sciences* 3, 81–93.
- Crosta, G.B., Frattini, P., (2008). Rainfall-induced landslides and debris flows. *Hydrological Processes* 22 (4), 473-477.
- Crozier, M.J. (1986) *Landslides: causes, consequences & environment*. Croom Helm Pub., London.
- Crozier, M.J., 1989. *Landslides: Causes, Consequences and Environment*. Routledge, 272 p.
- Cruden, D.M., (1991). A very simple definition for a landslide. *IAEG Bulletin*, 43 27-29.
- Cruden, D.M., Varnes, D.J., (1996). Landslide types and processes, in: Turner, A.K., Schuster, R.L. (Eds.), *Landslides: Investigation and Mitigation (Special Report)*. National Research Council, Transportation and Research Board Special
- Cundall, P.A., Strack, O.D.L., (1979). A discrete numerical model for granular assemblies. *Géotechnique* 29 (1), 47-65.
- de Boer, G. B., de Weerd, C., Thoenes, D., and Goossens, H. W. (1987). Laser diffraction spectrometry: Fraunhofer diffraction versus mie scattering. *Particle & Particle Systems Characterization*, 4(1-4):14–19.
- De la Cruz-Reyna, S., & Reyes-Dávila, G. A. (2001). A model to describe precursory material-failure phenomena: applications to short-term forecasting at Colima volcano, Mexico. *Bulletin of Volcanology*, 63(5), 297-308.
- Del Ventisette, C. D., Garfagnoli, F., Ciampalini, A., Battistini, A., Gigli, G., Moretti, S., and Casagli, N. (2012). An integrated approach to the study of catastrophic debris-flows: geological hazard and human influence. *Natural Hazards and Earth System Sciences*, 12(9), 2907-2922.
- Delbridge, B. G., Bürgmann, R., Fielding, E., Hensley, S., & Schulz, W. H. (2016). Three-dimensional surface deformation derived from airborne interferometric UAVSAR: Application to the Slumgullion Landslide. *Journal of Geophysical Research: Solid Earth*, 121(5), 3951-3977.



- Derron, M.H., Blikra, L.H., Jaboyedoff, M., (2005). High resolution digital elevation model analysis for landslide hazard assessment (Åkerneset, Norway), in: Senneset, K., Flaate, K., Larsen, J.O. (Eds.), *Landslide and Avalanches*, ICFL (2005), Norway. Taylor & Francis Group, London, UK, pp. 101-106.
- Desai, C.S., Zhang, D., (1987). Viscoplastic models for geologic materials with generalized flow rule. *Int. J. Num. Anal. Meth. Geomech.* 11,
- Dhakal, A.S. and Sidle, R.C. (2004) Distributed simulations of landslides for different rainfall conditions. *Hydrological Processes*, 18:4 757-776.
- Di Maio, C., Onorati, R., (2000). Influence of Pore Liquid Composition on the Shear Strength of an Active Clay, in: Bromhead, E., Dixon, N., Ibsen, M.-L. (Eds.), *Landslides in Research, Theory and Practice*. 8th International Symposium on Landslides. T. Telford, London, Cardiff, Wales, pp. 463-468.
- Di Maio, C., Vassallo, R., & Vallario, M. (2013). Plastic and viscous shear displacements of a deep and very slow landslide in stiff clay formation. *Engineering Geology*, 162, 53-66.
- Di Toro, G., Han, R., Hirose, T., De Paola, N., Nielsen, S., Mizoguchi, K., ... & Shimamoto, T. (2011). Fault lubrication during earthquakes. *Nature*, 471(7339), 494.
- Di Traglia, F., Intrieri, E., Nolesini, T., Bardi, F., Del Ventisette, C., Ferrigno, F., ... and Stefanelli, C. T. (2014). The ground-based InSAR monitoring system at Stromboli volcano: linking changes in displacement rate and intensity of persistent volcanic activity. *Bulletin of volcanology*, 76(2), 1-18.
- Dieterich, J. H. (1978). Time-dependent friction and the mechanics of stick-slip. In *Rock Friction and Earthquake Prediction* (pp. 790-806). Birkhäuser, Basel.
- Dieterich, J. H. (1979). Modeling of rock friction: 1. Experimental results and constitutive equations. *Journal of Geophysical Research: Solid Earth*, 84(B5), 2161-2168.
- Dieterich, J. H. (1981). Constitutive properties of faults with simulated gouge. *Mechanical behavior of crustal rocks: the Handin volume*, 24, 103-120.
- Dikau, R., Brunsden, D., Schrott, L. and Ibsen, M.-L. (eds.) (1996) *Landslide recognition. Identification, movements and causes*. John Wiley & Sons Ltd, Chichester, England, 251 p.
- Dikau, R., Weichselgärtner, J., (2005). *Der unruhige Planet. Der Mensch und die Naturgewalten*, 1st ed. Primus Verlag.
- Dunning, S.A; Rosser, N.J. Petley, D.N. and Massey, C.R. (2006). Formation and failure of the Tsatichhu landslide dam, Bhutan. *Landslides*, 3(2): 107-113.
- Eberhardt, E., Watson, A.D., Loew, S., (2008). Improving the interpretation of slope monitoring and early warning data through better understanding of complex deep-seated landslide failure mechanisms, in: Chen, Z., Zhang, J.-M., Ho, K., Wu, F.-Q., Li, Z.-K. (Eds.), *Landslides and Engineered Slopes: From the Past to the Future*, Proceedings of the 10th International Symposium on Landslides and Engineered Slopes. Taylor & Francis, Xi'an, China, pp. 39-51.
- Eidsvig, U.M., Medina-Cetina, Z., Kvelde, V., Glimsdal, S., Harbitz, C.B., Sandersen, F., (2009). Risk assessment of a tsunamigenic rockslide at Åknes. *Natural Hazards*.
- Eisbacher, G.H. and Clague, J.J. (1980). Urban landslides in the vicinity of Vancouver, British Columbia, with special reference to the December 1979 rainstorm. *Canadian Geotechnical Journal*, 18: 205-216.
- Ekanayake, J.C., Phillips, C.J., (1999). A model for determining thresholds for initiation of shallow landslides under near-saturated conditions in the East Coast region, New Zealand. *Journal of Hydrology (NZ)* 38 (1), 1-28.

- Emery, J. J. (1978). Simulation of slope creep. In *Developments in Geotechnical Engineering* (Vol. 14, pp. 669-691). Elsevier.
- Engineering Geology* 32,157-184.
- Engl DA, Fellin W, Kieffer DS, Zangerl C (2010) A novel approach for assessing the deformation characteristics of a rockslide. In: Williams AL, Pinches GM, Chin CY, McMorran TJ, Massey CI (eds) *Proceedings of the 11th IAEG congress*. Taylor & Francis, Auckland, pp 1530–1545
- Fang, H.-Y., (1990). *Foundation engineering handbook*. Springer, 954 p.
- Favis-Mortlock, D., De Boer, D., (2003). Simple at heart? Landscape as a self-organizing complex system, in: Trudgill, S., Roy, A. (Eds.), *Contemporary meanings in physical geography*. Oxford University Press, USA, p. 127–172.
- Feda, J. (2002). Notes on the effect of grain crushing on the granular soil behavior. *Engineering geology*, 63(1-2), 93-98.
- Fell, R., Hungr, O., Leroueil, S. and Riemer, W., (2000). Keynote lecture - geotechnical engineering of the stability of natural slopes, and cuts and fills. N: *Proceedings of the Geoengineering Conference*, Melbourne, pp. 21-120.
- Fell, R., Hungr, O., Leroueil, S., & Riemer, W. (2000, November). Keynote lecture-geotechnical engineering of the stability of natural slopes, and cuts and fills in soil. In *ISRM International Symposium*. International Society for Rock Mechanics.
- Fernández-Merodo, J. A., García-Davalillo, J. C., Herrera, G., Mira, P., & Pastor, M. (2014). 2D viscoplastic finite element modelling of slow landslides: the Portalet case study (Spain). *Landslides*, 11(1), 29-42.
- Ferri F, Di Toro G, Hirose T, Han R, Noda H, Shimamoto T, de Rossi N (2011) Low-to-high-velocity frictional properties of the clay-rich gouges from the slipping zone of the 1963 Vaiont slide, northern Italy. *J Geophys Res: Solid Earth* 116:B09208. doi: 10.1029/(2011)JB008338
- Ferri, F., Spagnuolo, E., Di Felice, F., & Di Toro, G. (2014, December). New Insights on the Creeping Phase of the Vajont Landslide from Rotary-Shear Experiments. In *AGU Fall Meeting Abstracts*.
- Finno, R., Harris, W., Mooney, M. A., and Viggiani, G. (1997). Shear bands in plane strain compression of loose sand. *Geotechnique*, 47(1):149–165.
- Fischer U, Kulli B, Flühler H (1998) Constitutive relationships and pore structure of undisturbed fracture zone samples with cohesionless fault gouge layers. *Water Resour Res* 34(7):1695–1701
- Fogliano, L., Lovisolo, M., & Della Giusta, A. (2006). Contribution of DMS monitoring systems in the analysis of slide micro-movements for early warning management, risk assessment and evaluation of mitigating actions. In *Geophysical Research Abstracts* (Vol. 8, p. 06122).
- Fossen, H. (2016). *Structural geology*. Cambridge University Press.
- Fossen, H., & Cavalcante, G. C. G. (2017). Shear zones—A review. *Earth-Science Reviews*, 171, 434-455.
- Frattini, P., Crosta, G., Sosio, R., (2009). Approaches for defining thresholds and return periods for rainfall-triggered shallow landslides. *Hydrological Processes* 23 (10), 1444-1460.
- Frigerio, G. (2010). Evoluzione di movimenti franosi lenti: interpretazione dei dati mediante modellazione numerica semplificata.
- Frigerio, G., Castellanza, R., Crosta, G. B., & di Prisco, C. (2014). Modelling rockslide displacements with delayed plasticity. In *Landslide Science for a Safer Geoenvironment* (pp. 291-298). Springer, Cham.

- Frodella, W., Ciampalini, A., Gigli, G., Lombardi, L., Raspini, F., Nocentini, M., Scardigli, C., and Casagli, N. (2016). Synergic use of satellite and ground based remote sensing methods for monitoring the San Leo rock cliff (Northern Italy). *Geomorphology*, 264, 80-94.
- Froese, C.R., Jaboyedoff, M., Pedrazzini, A., Hungr, O., Moreno, F., (2009). Hazard mapping for the eastern face of Turtle Mountain, adjacent to the Frank Slide, Alberta, Canada. *Landslide Processes* 283–289.
- Froese, C.R., Murray, C., Cavers, D.S., Anderson, W.S., Bidwell, A.K., Read, R.S., Cruden, D.M., Langenberg, W., (2005). Development and implementation of a warning system for the South Peak of Turtle Mountain, in: Hungr, O., Fell, R., Couture, R., Eberhardt, E. (Eds.), *International Conference on Landslide Risk Management*. Taylor & Francis Ltd., Vancouver, Canada, pp. 705-12.
- Froude, M. J., & Petley, D. (2018). Global fatal landslide occurrence from (2004) to (2016). *Natural Hazards and Earth System Sciences*, 18, 2161-2181.
- Fukuoka, H., Sassa, K., & Wang, G. (2007). Shear behavior and shear zone structure of granular materials in naturally drained ring shear tests. In *Progress in landslide science* (pp. 99-111). Springer Berlin Heidelberg.
- Fukuoka, H., Sassa, K., Wang, G and Sasaki, R. (2006). Observation of shear zone development in ring-shear apparatus with a transparent shear box. *Landslides* (2006) 3: 239
- Fukuzono T (1989) A simple method for predicting the failure time of slope—using reciprocal of velocity, *Technology for Disaster Prevention*, Science and Technology Agency, Japan. *Int Coop Agency, Japan* 1(13):111–128
- Fukuzono T (1990) Recent studies on time prediction of slope failure. *Landslide News* 4:9–12
- Fukuzono, T. (1985). A method to predict the time of slope failure caused by rainfall using the inverse number of velocity of surface displacement. *Landslides*, 22(2):8–13 1.
- Fusi, N. and Martinez-Martinez, J. (2013). Mercury porosimetry as a tool for improving quality of micro-ct images in low porosity carbonate rocks. *Engineering Geology*, 166:272–282.
- Ganerød, G.V., Grøneng, G., Rønning, J.S., Dalsegg, E., Elvebakk, H., Tønnesen, J.F., Kvelde, V., Eiken, T., Blikra, L.H., Braathen, A., (2008). Geological model of the Aaknes rockslide, western Norway. *Engineering Geology* 102 (1-2), 1–18.
- Gasparetto, P., Mosselman, M., & Van Asch, T. W. (1996). The mobility of the Alvera landslide (Cortina d'Ampezzo, Italy). *Geomorphology*, 15(3-4), 327-335.
- Giardino, M., Giordan, D., & Ambrogio, S. (2004). GIS technologies for data collection, management and visualization of large slope instabilities: two applications in the Western Italian Alps. *Natural Hazards and Earth System Science*, 4(2), 197-211.
- Gilbert, G., (1884). A theory of the earthquakes of the Great Basin, with a practical application. *Am. J. Sci.* XXVII, 49-54.
- Gillon, M., Riley, P., and Haliday, G. (1992). Movement history and infiltration, cairnmuir landslide, nz. In *Proceedings of the Sixth International Symposium on Landslides*, volume 1, pages 103–110.
- Giordan, D., Manconi, A., Allasia, P., & Bertolo, D. (2015). Brief Communication: On the rapid and efficient monitoring results dissemination in landslide emergency scenarios: the Mont de La Saxe case study. *Natural Hazards and Earth System Sciences*, 15(9), (2009-2017).
- Giraud, R.E., (2002). Movement history and preliminary hazard assessment of the Heather Drive Landslides, Layton, Davis County, Utah, *Utah Geological Survey Report of Investigation 251*. Utah Geological Survey. Utah Department of Natural Resources., 27 p.
- Glade, T. and Crozier, M.J. (2005) The nature of landslide hazard impact. In: Glade, T., Anderson, M.G. and Crozier, M.J. (eds.) *Landslide risk assessment*. John Wiley, 43-74.

- Glade, T. and Crozier, M.J. (2005) A review of scale dependency in landslide hazard and risk analysis. In: Glade, T., Anderson, M.G. and Crozier, M.J. (eds.) *Landslide risk assessment*. John Wiley, 75-138.
- Glastonbury, J. and Fell, R. (2010). Geotechnical characteristics of large rapid rock slides. *Canadian Geotechnical Journal*, 47(1):116–132.
- Glawe, U., Lotter, M., (1996). Time prediction of rock slope failures based on monitoring results, in: Senneset, K. (Ed.), *Landslides. 7th International Symposium on Landslides*. Balkema, Rotterdam, Trondheim, Norway, pp. 1551-1555.
- Godt, J.W., Baum, R.L., Chleborad, A.F., (2006). Rainfall characteristics for shallow landsliding in Seattle, Washington, USA. *Earth Surface Processes and Landforms* 31 (1), 97-110.
- Gonzalez, D. A., Ledesma, A., Corominas, J. (2008). The viscous component in slow-moving landslides: A practical case. In: *Landslides and engineering slopes*. Chen et al. (eds). pp 237 – 242.
- Gottardi, G. and Butterfield, R. (2001). Modelling ten years of downhill creep data. In *Proceedings of the International Conference on Soil Mechanics and Geotechnical Engineering*, volume 1, pages 99–104. AA BALKEMA PUBLISHERS.
- Graham, J., (1984). *Methods of Slope Stability Analysis*, in: Brunsden, D., Prior, D.B. (Eds.), *Slope instability*. Wiley and Sons, New York, p. 171–215.
- Greco, R., Guida, A., Damiano, E., Olivares, L., (2010). Soil water content and suction monitoring in model slopes for shallow flowslides early warning applications. *Physics and Chemistry of the Earth* 35 (3-5), 127-136.
- Griffiths, J.S., Hutchinson, J.N., Brunsden, D.N., Petley, D.J and Fookes, P.G. (2004). The reactivation of a landslide during the construction of the Ok Ma tailings dam, Papua New Guinea. *Quarterly Journal of Engineering Geology and Hydrogeology*, 37: 317-325
- Grøneng, G., Christiansen, H.H., Nilsen, B., Blikra, L.H., (2010). Meteorological effects on seasonal displacements of the Åknes rockslide, western Norway. *Landslides* 1 (8), 1-15.
- Guermani, A. and Pennacchioni, G. (1998). Brittle precursors of plastic deformation in a granite: an example from the mont blanc massif (helvetic, western alps). *Journal of Structural Geology*, 20(2-3):135–148.
- Guglielmi Y, Cappa F, Binet S (2005) Coupling between hydrogeology and deformation of mountainous rock slopes: insights from La Clapière area (southern Alps, France). *Compt Rendus Geosci* 337:1154–1163
- Guzzetti, F. (2006) *Landslide hazard and risk assessment: Concepts, methods and tools for the detection and mapping of landslides, for landslide susceptibility zonation and hazard assessment, and for landslide risk evaluation*. Doctoral thesis, University of Bonn, Bonn, Germany
- Guzzetti, F., Peruccacci, S., Rossi, M., & Stark, C. P. (2007). Rainfall thresholds for the initiation of landslides in central and southern Europe. *Meteorology and atmospheric physics*, 98(3-4), 239-267.
- Guzzetti, F., Peruccacci, S., Rossi, M., Stark, C.P., (2008). The rainfall intensity–duration control of shallow landslides and debris flows: an update. *Landslides* 5 (1), 3-17.
- Guzzetti, F., Reichenbach, P., Cardinali, M., Galli, M. and Ardizzone, F. (2005) *Landslide hazard assessment in the Staffora basin, northern Italian Apennines*. *Geomorphology*.
- Haefeli, R. (1953). *Creep problems in soils, snow and ice*.
- Haines, S. H., Kaproth, B., Marone, C., Saffer, D., & van der Pluijm, B. (2013). Shear zones in clay-rich fault gouge: A laboratory study of fabric development and evolution. *Journal of Structural Geology*, 51, 206-225.

- Hancox, G.T., Bishop, D.G., McKellar, I.C., Suggate, R.P., Northey, R.D. (1980). 1979 East Abbotsford Landslide. Engineering geological data and factors related to the cause of the slide. NZ Geological Survey. Report EG 332, 3 March 1980.
- Hancox, G.T., McSaveney, M.J., Manville, V.R. and Davies, T.R. (2005). The October (1999) Mt Adams rock avalanche and subsequent landslide dam-break flood and effects in Poerua River, Westland, New Zealand. *New Zealand Journal of Geology and Geophysics*. 48: 683-705.
- Hart, R.D., (1993). An introduction to Discint Element Modelling for Rock Engineering, in: *Proceedings of the 7th International Congress on Rock Mechanics*. Pergamon Press, Aachen, Germany, pp. 1881-1892.
- Hayashi et al., (1989). On the forecast of time to failure of slope (II): Approximate forecast in early period of tertiary creep. *Journal of Japanese Landslide Society*, 25(3): 11-16.
- Hearn, G. J., & Massey, C. I. (2009). Engineering geology in the management of roadside slope failures: contributions to best practice from Bhutan and Ethiopia. *Quarterly Journal of Engineering Geology and Hydrogeology*, 42(4), 511-528.
- Heeres, O. M., Suiker, A. S., & de Borst, R. (2002). A comparison between the Perzyna viscoplastic model and the consistency viscoplastic model. *European Journal of Mechanics-A/Solids*, 21(1), 1-12.
- Heincke, B., Günther, T., Dalsegg, E., Ronning, J.S., Ganerød, G.V., Elvebakk, H., (2010). Combined three-dimensional electric and seismic tomography study on the Aknes rockslide in western Norway. *Journal of Applied Geophysics* (70), 292-306.
- Helmstetter, A. and Garambois, S. (2010). Seismic monitoring of Sechilienne rockslide (french alps): Analysis of seismic signals and their correlation with rainfalls. *Journal of Geophysical Research: Earth Surface*, 115(F3).
- Helmstetter, A., Sornette, D., Grasso, J. R., Andersen, J. V., Gluzman, S., & Pisarenko, V. (2004). Slider block friction model for landslides: Application to Vaiont and La Clapiere landslides. *Journal of Geophysical Research: Solid Earth*, 109(B2).
- Henderson IHC, Ganerød GV, Braathen A (2010) The relationship between particle characteristics and frictional strength in basal fault breccias: implications for fault-rock evolution and rockslide susceptibility. *Tectonophysics* 486:132–149
- Hoek, E., & Brown, E. T. (1997). Practical estimates of rock mass strength. *International journal of rock mechanics and mining sciences*, 34(8), 1165-1186.
- Hu, W., Xu, Q., Wang, G., Scaringi, G., Mcsaveney, M., & Hicher, P. Y. (2017). Shear Resistance Variations in Experimentally Sheared Mudstone Granules: A Possible Shear-Thinning and Thixotropic Mechanism. *Geophysical Research Letters*, 44(21).
- Hu, W., Xu, Q., Wang, G., Scaringi, G., Mcsaveney, M., & Hicher, P. Y. (2017). Shear Resistance Variations in Experimentally Sheared Mudstone Granules: A Possible Shear-Thinning and Thixotropic Mechanism. *Geophysical Research Letters*, 44(21).
- Hull, J. (1988). Thickness-displacement relationships for deformation zones. *Journal of Structural Geology*, 10(4), 431-435.
- Hungr, O. & McDougall, S., (2009). Two numerical models for landslide dynamic analysis. *Computers and Geosciences*, 35(5), pp.978–992.
- Hungr, O., Corominas, J., & Eberhardt, E. (2005). Estimating landslide motion mechanism, travel distance and velocity. *Landslide risk management*, 1, 99-128.
- Hunt, B. (1994). Newtonian fluid mechanics treatment of debris flows and avalanches. *Journal of Hydraulic Engineering*, 120(12), 1350-1363.

- Hutchinson JN (1969) A reconsideration of the coastal landslides at Folkestone Warren, Kent. *Geotechnique* 19:6–38
- Hutchinson JN (1988) General report: morphological and geotechnical parameters of landslides in relation to geology and hydrogeology. In: *Proceedings of the 5th International Symposium on Landslides, Lausanne*, 1:3–35
- Hutchinson, J. (2001). Landslide risk—to know, to foresee, to prevent. *Geologica Technica & Ambientale*, 9, 3-24.
- Ishihara, K. (1993). Liquefaction and flow failure during earthquakes. *Geotechnique*, 43(3):351–451.
- Iverson, R. M. (1997). The physics of debris flows. *Reviews of geophysics*, 35(3), 245-296.
- Iverson, R. M. (2005). Regulation of landslide motion by dilatancy and pore pressure feedback. *Journal of Geophysical Research: Earth Surface*, 110(F2).
- Iverson, R.M. (2000) Landslide triggering by rain infiltration. *Water Resources Research*, 36:
- Iverson, R.M., (1985). Dynamics of slow landslides: a theory of time dependent behavior. In: Abrahams, A. D. (Ed), *Hillslope processes*. Binghampton Symposium in Geomorphology No. 16. pp. 297 – 317
- Jaboyedoff, M., Baillifard, F., Bardou, E., & Girod, F. (2004). The effect of weathering on Alpine rock instability. *Quarterly Journal of Engineering Geology and Hydrogeology*, 37(2), 95-103.
- Jaboyedoff, M., Baillifard, F., Bardou, E., & Girod, F. (2004). The effect of weathering on Alpine rock instability. *Quarterly Journal of Engineering Geology and Hydrogeology*, 37(2), 95-103.
- Janbu, N., (1996). Slope stability evaluations in engineering practice, in: Senneset, K. (Ed.), *Landslides. 7th International Symposium on Landslides*. Balkema, Rotterdam, Trondheim, Norway, pp. 17-34.
- Jewell, R .A . (1980). Some effects of reinforcement on soils. PhD. Thesis, University of Cambridge.
- Jing, L. & Hudson, J. a., (2002). Numerical methods in rock mechanics. *International Journal of Rock Mechanics and Mining Sciences*, 39, pp.409–427.
- Jing, L., (1998). Formulation of discontinuous deformation analysis (DDA)—an implicit discrete element model for block systems. *Engineering Geology* 49 (3-4), 371–381.
- Johnson, P. L., & Cotton, W. R. (2005). The Santiago landslide and associated ridge-top graben (sackungen): implications for paleoseismic landslide studies. *Environmental and Engineering Geoscience*, 11(1), 5-15.
- Jongmans, D., Renalier, F., Knies, U., Bièvre, G., Schwartz, S., Pathier, E., Orengo, Y., Villemin, T., Delacourt, C., (2008). Characterisation of the Avignonnet landslide (French Alps) using seismic techniques, in: Chen, Z., Zhang, J.-M., Ho, K., Wu, F.-Q., Li, Z.-K. (Eds.), *Landslides and Engineered Slopes: From the Past to the Future*, *Proceedings of the 10th International Symposium on Landslides and Engineered Slopes*. Taylor & Francis, Xi'an, China, pp. 395-401.
- Karampatakis DA, Hatzigogos TN (1999) A model to describe creeping behavior of thin-layer element for interfaces and joints proceedings from COST C7 Workshop in Thessaloniki, 1–2 October (1999), 1–16
- Kato, N., & Tullis, T. E. (2001). A composite rate-and state-dependent law for rock friction. *Geophysical research letters*, 28(6), 1103-1106.
- Keaton, J.R., DeGraff, J.V., (1996). Surface observation and geologic mapping, in: Turner, A.K., Schuster, R.L. (Eds.), *Landslides: Investigation and Mitigation (Special Report)*. National Research Council, Transportation
- Keaton, J.R., Gailing, R.W., (2004). Monitoring Slope Deformation with Quadrilaterals for Pipeline Risk Management, in: *ASME Conference Proceedings, Proceedings of the (2004) International Pipeline Conference (IPC)*. Calgary, Canada, pp. 269-274.



- Kenney, T. C. (1967). The influence of mineral composition on the residual strength of natural soils.
- Ketcham, R. A. and Carlson, W. D. (2001). Acquisition, optimization and interpretation of x-ray computed tomographic imagery: applications to the geosciences. *Computers & Geosciences*, 27(4):381–400.
- Kirsch R (2006) Petrophysical properties of permeable and low-permeable rocks. In: Kirsch R (ed) *Groundwater geophysics. A tool for hydrogeology*. Springer, Berlin. doi:10.1007/3-540-29387-6, 1–22
- Kneale, P.E., (1987). Instrumentation of pore pressure and soil water suction, in: Anderson, M.G. (Ed.), *Slope Stability: Geotechnical Engineering and Geomorphology*. John Wiley & Sons Ltd, pp. 77-112.
- Korup, O. (2005). Geomorphic hazard assessment of landslide dams in South Westland, New Zealand: fundamental problems and approaches. *Geomorphology*, 66, 167-188.
- Kristmannsdóttir, H. (1979). Alteration of Basaltic Rocks by Hydrothermal-Activity at 100-300 C. In *Developments in sedimentology* (Vol. 27, pp. 359-367). Elsevier.
- Kveldsvik, V., Einstein, H.H., Nilsen, B., Blikra, L.H., (2008). Numerical Analysis of the 650,000 m<sup>2</sup> Åknes Rock Slope based on Measured Displacements and Geotechnical Data. *Rock Mechanics and Rock Engineering* 42 (5), 689-728.
- Kveldsvik, V., Kaynia, A.M., Nadim, F., Bhasin, R., Nilsen, B., Einstein, H.H., (2009). Dynamic distinct-element analysis of the 800 m high Aknes rock slope. *International Journal of Rock Mechanics and Mining Sciences* 46 (4), 686–698.
- Lama RD, Vutukuri V (1978) *Handbook on mechanical properties of rocks*. Trans Tech Publ 2
- Larsen, M.C., (2008). Rainfall-triggered landslides, anthropogenic hazards, and mitigation strategies. *Advances in Geosciences* 14, 147–153.
- Larson, A. C. and R. B. Von Dreele. (1994). *General Structure Analysis System (GSAS) Manual*. LANSCE, MS-H805, Los Alamos National Laboratory, Los Alamos, NM.
- Lee, E.M. (2009). Landslide risk assessment: the challenge of estimating the probability of landsliding. *Quarterly Journal of Engineering Geology and Hydrogeology*, 42(4): 445-458.
- Leloup, P., Arnaud, N., Sobel, E., and Lacassin, R. (2005). Alpine thermal and structural evolution of the highest external crystalline massif: The mont blanc. *Tectonics*, 24(4).
- Leroueil, S. (1996). Compressibility of clays: fundamental and practical aspects. *Journal of Geotechnical Engineering*, 122(7), 534-543.
- Leroueil, S., (2004). Geotechnics of slopes before failure, in: Lacerda, W., Ehrlich, M., Fontoura, S.A.B., Sayao, A.S.F. (Eds.), *Landslides: Evaluation and stabilization*. 9th International Symposium on Landslides. A.A. Balkema Publishers, Leiden, Rio de Janeiro, Brazil, pp. 863-884.
- Localization and Size Effects. Elsevier, London, pp. 440–461
- Lollino, G., Arattano, M., Allasia, P., and Giordan, D. (2006). Time response of a landslide to meteorological events. *Natural Hazards and Earth System Science*, 6(2):179–184.
- Lollino, G., Arattano, M., Cuccureddu, M., (2002). The use of the automatic inclinometric system for landslide early warning: the case of Cabella Ligure (North-Western Italy). *Physics and Chemistry of the Earth* 27 (36), 1545–1550.
- Lovisolo, M., Ghirotto, S., Scardia, G., & Battaglio, M. (2003). The use of Differential Monitoring Stability (DMS) for remote monitoring of excavation and landslide movements. In *Proceedings of the Sixth International Symposium on Field Measurements in Geomechanics*, edited by: Myrvol, A., Oslo, Balkema (pp. 519-524).

- Lupini, J. F., Skinner, A. E., & Vaughan, P. R. (1981). The drained residual strength of cohesive soils. *Geotechnique*, 31(2), 181-213.
- Luzi, G., Pieraccini, M., Macaluso, G., Mecatti, D., Noferini, L., Atzeni, C., Galgaro, A., Teza, G., (2005). Ground based microwave interferometry for estimating the movement of landslides, in: Hungr, O., Fell, R., Couture, R., Eberhardt, E. (Eds.), *International Conference on Landslide Risk Management*. Taylor & Francis Ltd., Vancouver, Canada, pp. 309-314.
- Luzzani, L., & MR, C. (2002). On the relationship between particle breakage and the critical state of sands. *Soils and foundations*, 42(2), 71-82.
- Manconi, A., & Giordan, D. (2015). Landslide early warning based on failure forecast models: the example of the Mt. de La Saxe rockslide, northern Italy. *Natural Hazards and Earth System Sciences*, 15(7), 1639-1644.
- Mansour MF, Martin CD, Morgenstern NR (2011) Movement behavior of the little chief slide. *Can Geotech J* 48(4):655–670
- Mansour, M. F. (2009) Characteristic behavior of slow-moving slides. University of Alberta, Canada
- Martel, S. J. (2004). Mechanics of landslide initiation as a shear fracture phenomenon. *Marine Geology*, 203(3-4), 319-339.
- Massey, C., I. (2010) The dynamics of reactivated landslides: Utiku and Taihape, North Island, New Zealand. Doctoral thesis, Doctoral thesis, Durham University
- Massey, C.I.; Petley, D.N.; McSaveney, M.J. (2013) Patterns of movement in reactivated landslides. *Engineering Geology*, 159: 1-19; doi: 10.1016/j.enggeo.(2013).03.011
- Matsushi, Y., Matsukura, Y., (2007). Rainfall thresholds for shallow landsliding derived from pressure-head monitoring: cases with permeable and impermeable bedrocks in Boso Peninsula, Japan. *Earth Surface Processes and Landforms* 32 (9), 1308-1322.
- Matsuura, S., Asano, S., Okamoto, T. (2008) Relationship between rain and/or meltwater, pore-water pressure and displacement of a reactivated landslide. In: *Engineering Geology*. Vol. 101. pp. 49 – 59.
- McCahon, C.P., Carling, P.A., Pascoe, D. (1987). Chemical and ecological effects of a Pennine peat slide. *Environmental Pollution*, 45: 275– 289.
- McCalpin, J. (1984) Preliminary age classification of landslides for inventory mapping. *Proceedings 21st annual Engineering Geology and Soils Engineering Symposium, Moscow, Idaho*, 99-111
- McSaveney, M. J., and Griffiths, G. A. (1987). Drought, rain, and movement of a recurrent earthflow complex in New Zealand. In: *Geology*. Vol. 15. pp. 643 – 646.
- Means, W. D. (1984). Shear zones of types I and II and their significance for reconstruction of rock history. *Geol. Soc. Am. Bull., Abstract Programs*, 16, 50.
- Means, W. D. (1995). Shear zones and rock history. *Tectonophysics*, 247(1-4), 157-160.
- Mihalinec, Z., Ortolan, Ž., (2008). Landslide “Granice” in Zagreb (Croatia), in: Chen, Z., Zhang, J.-M., Ho, K., Wu, F.-Q., Li, Z.-K. (Eds.), *Landslides and Engineered Slopes: From the Past to the Future*, Proceedings of the 10th International Symposium on Landslides and Engineered Slopes. Taylor & Francis, Xi'an, China, p. 1587–1593.
- Mikoš, M., Vidmar, A., Brilly, M., (2005). Using a laser measurement system for monitoring morphological changes on the Strug rock fall, Slovenia. *Natural Hazards and Earth System Sciences* 5, 143–153.
- Mills, A.J., Moore, R., Carey, J.M. and Trinder, S.K. (2007). Recent landslide impacts in Scotland: Possible evidence of climate change? In: R McInnes, J. Jakeways, H, Fairbank and E Mathie

- (Editors) Proceedings of the International Conference Landslides and Climate Change, Ventnor Isle of Wight. Taylor & Francis, London. pp. 99-106.
- Mills, J.P., Buckley, S.J., Mitchell, H.L., Clarke, P.J., Edwards, S.J., (2005). A geomatics data integration technique for coastal change monitoring. *Earth Surface Processes and Landforms* 30 (6), 651-664.
- Monserrat, O., and Crosetto, M. (2008). Deformation measurement using terrestrial laser scanning data and least squares 3D surface matching. *ISPRS Journal of Photogrammetry and Remote Sensing*, 63(1), 142-154.
- Montety, V. de, Marc, V., Emblanch, C., Malet, J.-P., Bertrand, C., Maquaire, O., Bogaard, T.A., (2007). Identifying the origin of groundwater and flow processes in complex landslides affecting black marls: insights from a hydrochemical survey. *Earth Surface Processes and Landforms* 32 (1), 32-48.
- Montrasio, L., Valentino, R., (2007). Experimental analysis and modelling of shallow landslides. *Landslides* 4 (3), 291-296.
- Moore, D. and Imrie, A. (1995). Stabilization of dutchmans ridge. In Proceedings of the 6th International Symposium on Landslides, Christchurch. Edited by DH Bell. AA Balkema, Rotterdam, volume 3, pages 1783–1788.
- Moore, D. E., & Lockner, D. A. (2004). Crystallographic controls on the frictional behavior of dry and water-saturated sheet structure minerals. *Journal of Geophysical Research: Solid Earth*, 109(B3).
- Moore, D. E., & Lockner, D. A. (2011). Frictional strengths of talc-serpentine and talc-quartz mixtures. *Journal of Geophysical Research: Solid Earth*, 116(B1).
- Morgenstern, N., Tchalenko, J., (1967). Microscopic structures in kaolin subject to direct shear. *Géotechnique* 17, 309-328
- Morgenstern, N.R. (1995). Keynote paper: The role of analysis in the evaluation of slope stability. *Landslides*, Bell (ed). Balkema, Rotterdam,
- Morrow, C. A., Moore, D. E., & Lockner, D. A. (2000). The effect of mineral bond strength and adsorbed water on fault gouge frictional strength. *Geophysical research letters*, 27(6), 815-818.
- Morrow, C. A., Moore, D. E., & Lockner, D. A. (2017). Frictional strength of wet and dry montmorillonite. *Journal of Geophysical Research: Solid Earth*, 122(5), 3392-3409.
- Nakamura, H., (2004). Field instrumentation and laboratory investigation, in: Lacerda, W., Ehrlich, M., Fontoura, S.A.B., Sayao, A.S.F. (Eds.), *Landslides: Evaluation*
- Nakamura, Y., Oohashi, K., Toyoshima, T., Satish-Kumar, M., & Akai, J. (2015). Strain-induced amorphization of graphite in fault zones of the Hidaka metamorphic belt, Hokkaido, Japan. *Journal of Structural Geology*, 72, 142-161.
- Nakatani, M., Conceptual and physical clarification of rate and state friction: Frictional sliding as a thermally activated rheology, *J. Geophys. Res.*, **106**, 13347–13380, (2001).
- Nash, D.F.T., (1987). A comparative review of limit equilibrium methods of stability analysis, in: Anderson, M.G. (Ed.), *Slope Stability: Geotechnical Engineering and Geomorphology*. John Wiley & Sons Ltd, pp. 11-75.
- Nemčok, A., Pašek, J. and Rybář, J. (1972) Classification of landslides and other mass movements. *Rock Mechanics*, 4: 71-78.
- Newmark, N. M. (1965). Effects of earthquakes on dams and embankments. *Geotechnique*, 15(2), 139-160.
- Ng, K. Y. (2007). Mechanisms of Shallow Rainfall-induced Landslides in Residual Soils in Humid Tropical Environments (Doctoral dissertation, Durham University).
- Nieuwenhuis, J. D. (1991). Variations in the stability and displacements of a shallow seasonal landslide in varved clays.

- Nishii, R., Matsuoka, N., Daimaru, H., and Yasuda, M. (2013). Precursors and triggers of an alpine rockslide in Japan: the (2004) partial collapse during a snow-melting period. *Landslides*, 10(1):75–82.
- Noverraz, F. (1996). Sagging or Deep Seated Creep: Fiction or Reality?. In VIth International Symposium on Landslides (No. GEOLEP-CONF-(1996)-006).
- Okada, Y., Sassa, K., & Fukuoka, H. (2004). Excess pore pressure and grain crushing of sands by means of undrained and naturally drained ring-shear tests. *Engineering Geology*, 75(3-4), 325-343.
- Okamoto, T., Larsen, J.O., Matsuura, S., Asano, S., Takeuchi, Y., Grande, L., (2004). Displacement properties of landslide masses at the initiation of failure in quick clay deposits and the effects of meteorological and hydrological factors. *Engineering Geology* 72 (3-4), 233–251.
- Olalla, C., (2004). Recent developments in landslide monitoring, in: Lacerda, W., Ehrlich, M., Fontoura, S.A.B., Sayao, A.S.F. (Eds.), *Landslides: Evaluation and stabilization*. 9th International Symposium on Landslides. A.A. Balkema Publishers, Leiden, Rio de Janeiro, Brazil, pp. 549-555.
- Oohashi, K., Hirose, T., & Shimamoto, T. (2011). Shear-induced graphitization of carbonaceous materials during seismic fault motion: Experiments and possible implications for fault mechanics. *Journal of Structural Geology*, 33(6), 1122-1134.
- Oohashi, K., Hirose, T., & Shimamoto, T. (2013). Graphite as a lubricating agent in fault zones: An insight from low-to high-velocity friction experiments on a mixed graphite-quartz gouge. *Journal of Geophysical Research: Solid Earth*, 118(5), 2067-2084.
- Oohashi, K., Hirose, T., Kobayashi, K., & Shimamoto, T. (2012). The occurrence of graphite-bearing fault rocks in the Atotsugawa fault system, Japan: Origins and implications for fault creep. *Journal of Structural Geology*, 38, 39-50.
- Oppikofer, T., Jaboyedoff, M., Blikra, L., Derron, M.H., Metzger, R., (2009). Characterization and monitoring of the Aknes rockslide using terrestrial laser scanning. *Natural Hazards and Earth System Sciences* 9, 1003–1019.
- Orense, R., Farooq, K. and Towhata, I. (2004). Deformation behavior of sandy slopes during rainwater infiltration. *Soils and Foundations*, 44(2): 15-30.
- Pagano, L., Rianna, G., Zingariello, M.C., Urcioli, G., Vinale, F., (2008). An early warning system to predict flowslides in pyroclastic deposits, in: Chen, Z., Zhang, J.-M., Ho, K., Wu, F.-Q., Li, Z.-K. (Eds.), *Landslides and Engineered Slopes: From the Past to the Future*, Proceedings of the 10th International Symposium on Landslides and Engineered Slopes. Taylor & Francis, Xi'an, China, pp. 1259-1264.
- Palmstrom A (1995) Rmi—a rock mass characterization system for rock engineering purposes. PhD thesis, Oslo Univ., 400 pp
- Panet, M. (1969). Discussion of K.W. John's Paper (ASCE Proc. Paper 5865, March 1968). *Journal of the Soil Mechanics and Foundation Division, ASCE*, Vol. 95, No. SM2, pp 685-686.
- Parry, R.H.G. (1960), Triaxial compression and extension tests on remoulded saturated clay. *Geotechnique*, 10: 166-180.
- Perello, P., Piana, F., and Martinotti, G. (1999). Neo-alpine structural features at the boundary between the penninic and helvetic domains (près. didier-entrèves, aosta valley, italy). *Eclogae Geol. Helv*, 92:347–359.
- Perzyna, P. (1963). The constitutive equations for rate sensitive plastic materials. *Quarterly of applied mathematics*, 20(4), 321-332.
- Perzyna, P. (1966). Fundamental problems in viscoplasticity. In *Advances in applied mechanics* (Vol. 9, pp. 243-377). Elsevier.
- Petley, D. J. 1966. The shear strength of soils at large strains. In: PhD thesis, University of London.

- Petley, D. N., Bulmer, M. H., & Murphy, W. (2002). Patterns of movement in rotational and translational landslides. *Geology*, 30(8), 719-722.
- Petley, D., Mantovani, F., Bulmer, M., and Zannoni, A. (2005). The use of surface monitoring data for the interpretation of landslide movement patterns. *Geomorphology*, 66(1):133–147.
- Petley, D.N. and Allison, R.J. (2006). On the movement of landslides. International Conference on Slopes, Malaysia, Special lecture. pp. 115-137.
- Petley, D.N. and Petley, D.J., (2006). On the initiation of large rockslides: perspectives from a new analysis of the Vaiont movement record. In: S.G Evans, G S Mugnozza, A Strom and R.L Hermanns (Editors), *Landslides from Massive Rock Slope Failure*. NATO Science Series IV: Earth and Environmental Sciences. Springer: Dordrecht. pp. 77-84.
- Petley, D.N., Allison, R.J., (1997). The mechanics of deep-seated landslides. *Earth Surface Processes and Landforms* 22 (8), 747–758.
- Petley, D.N., Hearn, G.J., Hart, A., (2005). Towards the Development of a Landslide Risk Assessment for Rural Roads in Nepal, in: Glade, T., Anderson, M., Crozier, M.J. (Eds.), *Landslide hazard and risk*. John Wiley and Sons, pp. 597- 619.
- Petley, D.N., Higuchi, T., Dunning, S., Rosser, N.J., Petley, D.J., Bulmer, M.H., Carey, J., (2005). A new model for the development of movement in progressive land- slides, in: Hungr, O., Fell, R., Couture, R., Eberhardt, E. (Eds.), *International Conference on Landslide Risk Management*. Taylor & Francis Ltd., Vancouver, Canada, pp. 350-358.
- Petley, D.N., Petley, D.J., Allison, R.J., (2008). Temporal prediction in landslides – Understanding the Saito effect, in: Chen, Z., Zhang, J.-M., Ho, K., Wu, F.-Q., Li, Z.-K. (Eds.), *Landslides and Engineered Slopes: From the Past to the Future*. Taylor & Francis, Xi'an, China, pp. 794-800.
- Petley, D.N., Rosser, N.J., Karim, D., Wali, S., Ali, N., Nasab, N. and Shaban, K. (2010). Non-seismic landslide hazards along the Himalayan Arc. In: Williams, A.L., Pinches, G.M., Chin, C.Y., McMorran, T.J. and Massey, C.I. (Editors) *Geologically Active*. CRC Press, London, pp. 143-154..
- Picarelli, L. (2007). Considerations about the mechanics of slow active landslides in clay. In: *Progress in landslide science*. Sassa, K., Fukuoka, H. Wang, F., Wang, G. editors. Chapter 3. pp. 27-57.
- Picarelli, L., Urciuoli, G. and Russo, C. (2004). Effect of Groundwater Regime on the Behavior of Clayey Slopes. *Canadian Geotechnical Journal*, 41: 467 – 484.
- Pisani G, Castelli M, Scavia C (2010) Hydrogeological model and hydraulic behavior of a large landslide in the Italian Western Alps. *Nat Hazards Earth Syst Sci* 10:2391–2406
- Poisel, R., & Preh, A. (2008). 3D landslide run out modelling using the particle flow code PFC3D. na
- Porter, S. C., & Orombelli, G. (1982). Late-glacial ice advances in the western Italian Alps. *Boreas*, 11(2), 125-140.
- Prokop, a. & Panholzer, H., (2009). Assessing the capability of terrestrial laser scanning for monitoring slow moving landslides. *Natural Hazards and Earth System Science*, 9, pp.1921–1928.
- Puzrin AM, Schmid A (2012) Evolution of stabilized creeping landslides. *Geotechnique* 62(6):491–501
- Ranalli, G. (1995). *Rheology of the Earth*. Springer Science & Business Media.
- Ranalli, M., Gottardi, G., Medina-Cetina, Z., and Nadim, F. (2010). Uncertainty quantification in the calibration of a dynamic visco-plastic model of slow slope movements. *Landslides*, 7(1):31–41.
- Ranalli, M., Gottardi, G., Medina-Cetina, Z., Nadim, F. (2009). Uncertainty quantification in the calibration of a dynamic viscoplastic model of slow slope movements. In. *Landslides*. Online first. DOI 10.1007/s10346-009-0185-0.
- Ratto S, Giardino M, Giordan D, Alberto W, Armand M (2007) Carta dei fenomeni franosi della valle d'Aosta, 1:100 000 in scale. Tipografia valdostana, Aosta

- Reches, Z., Lockner, D.A., (1994). Nucleation and growth of faults in brittle rocks. *Journal of Geophysical Research* 99 (B9), 18159-18173.
- Reed, S. J. B. (2005). *Electron microprobe analysis and scanning electron microscopy in geology*. Cambridge University Press.
- Reid, L.M. (1998) Calculation of average landslides frequency using climatic records. *Water Resources Research*, 34:4 869-877.
- Report 247, Washington, D.C., USA, pp. 36-75.
- Riedel, W., (1929). Zur mechanik geologischer Brucherscheinungen. *Centralbl. Mineral. Geol. U Pal.* 1929B, 354-368
- Riedmüller G, Brosch FJ, Klima K, Medley EW (2001) Engineering geological characterization of brittle faults and classification of fault rocks. *Felsbau* 19(4):13–19
- Rinaldi, M., Casagli, N., Dapporto, S., Gargini, A., (2004). Monitoring and modelling of pore water pressure changes and riverbank stability during flow events. *Earth Surface Processes and Landforms* 29 (2), 237-254.
- Rose ND, Hungr O (2007) Forecasting potential rock slope failure in open pit mines using the inverse-velocity method. *Int J Rock Mech Min Sci* 44(2):308–320
- Rosser, N.J., Dunning, S.A., Lim, M., Petley, D.N., (2005). Terrestrial laser scanning for quantitative rockfall hazard assessment, in: Hungr, O., Fell, R., Couture, R., Eberhardt, E. (Eds.), *International Conference on Landslide Risk Management*. Taylor & Francis Ltd., Vancouver, Canada, pp. 359-368.
- Rosser, N.J., Petley, D.N., (2008). Monitoring and modeling of slope movement on rock cliffs prior to failure, in: Chen, Z., Zhang, J.-M., Ho, K., Wu, F.-Q., Li, Z.-K. (Eds.), *Landslides and Engineered Slopes: From the Past to the Future, Proceedings of the 10th International Symposium on Landslides and Engineered Slopes*. Taylor & Francis, Xi'an, China, pp. 1265-1271.
- Ruina, A. (1983). Slip instability and state variable friction laws. *Journal of Geophysical Research: Solid Earth*, 88(B12), 10359-10370.
- Saito M, Uezawa H (1961) Failure of soil due to creep. In: *Proceedings of the 5th International Conference on Soil Mechanics and Foundation Engineering*. 1: 315–31
- Saito, M. (1965). Forecasting the time of occurrence of a slope failure. In *Proceedings of the 6th international conference on soil mechanics and foundation engineering, volume 2, pages 537–541*. Montreal, Que. Pergamon Press, Oxford.
- Sakai, H., (2008). A warning system using chemical sensors and telecommunication technologies to protect railroad operation from landslide disaster, in: Chen, Z., Zhang, J.-M., Ho, K., Wu, F.-Q., Li, Z.-K. (Eds.), *Landslides and Engineered Slopes: From the Past to the Future, Proceedings of the 10th International Symposium on Landslides and Engineered Slopes*. Taylor & Francis, Xi'an, China, pp. 1277-1281.
- Sakai, H., Tarumi, H., (2000). Estimation of the Next Happening of a Landslide by Observing the Change in Groundwater Composition, in: Bromhead, E., Dixon, N., Ibsen, M.-L. (Eds.), *Landslides in Research, Theory and Practice*. 8th International Symposium on Landslides. T. Telford, London, Cardiff, Wales, pp. 1289-1294.
- Salcedo, D. (1983). Macizos Rocosos: Caracterización, resistencia al corte y mecanismos de rotura. In *Conferencia* (Vol. 25, pp. 143-215).
- Salt, G. (1988). Landslide mobility and remedial measures. *Proceedings of the 6th International Conference on Slopes and Landslide*, 1. pp. 757-762.
- Samtani, N.C., Desai, C.S., Vulliet, L., (1996). An interface model to describe viscoplastic behavior. *Int. J. Num. Anal. Meth. Geomech.* 20,



- Sassa, K. (1988). Motion of Landslides and Debris Flows: Prediction of Hazard Area: Report for Grant-in-aid for Scientific Research by Japanese Ministry on Education, Science and Culture (project No. 61480062). Disaster Prevention Research Institute.
- Sassa, K. (1997). A new intelligent-type dynamic loading ring shear apparatus. *Landslide News*, 10:33.
- Sassa, K., Fukuoka, H., Wang, G., & Ishikawa, N. (2004). Undrained dynamic-loading ring-shear apparatus and its application to landslide dynamics. *Landslides*, 1(1), 7-19.
- Sassa, K., Wang, G., & Fukuoka, H. (2003). Performing undrained shear tests on saturated sands in a new intelligent type of ring shear apparatus. *Geotechnical Testing Journal*, 26(3), 257-265.
- Sausgruber T, Brandner R (2003) The relevance of brittle fault zones in tunnel construction—Lower Inn Valley Feeder Line North of the Brenner Base Tunnel, Tyrol, Austria. *Mitt Österr Geol Ges* 0251–7493(94):157–172
- Savage, W. Z., & Morin, R. H. (2002). Topographic stress perturbations in southern Davis Mountains, west Texas 1. Polarity reversal of principal stresses. *Journal of Geophysical Research: Solid Earth*, 107(B12).
- Schäbitz, M., Janssen, C., Wenk, H. R., Wirth, R., Schuck, B., Wetzels, H. U., & Dresen, G. (2018). Microstructures in landslides in northwest China—Implications for creeping displacements?. *Journal of Structural Geology*, 106, 70-85.
- Schaefer, M., Inkpen, R., (2010). Towards a protocol for laser scanning of rock surfaces. *Earth Surface Processes and Landforms* (35), 417–423.
- Schmid, S. M., Fu¨ngenschuh, B., Kissling, E., and Schuster, R. (2004). Tectonic map and overall architecture of the alpine orogen. *Eclogae Geologicae Helveticae*, 97(1):93–117.
- Schofield, A. and Wroth, P. (1968). *Critical State Soil Mechanics*. McGraw –Hill: London. pp. 222-223.
- Scholz, C. H. (1998). Earthquakes and friction laws. *Nature*, 391(6662), 37.
- Schulz, S. S., Mavko, G. M., Burford, R. O., & Stuart, W. D. (1982). Long-term fault creep observations in central California. *Journal of Geophysical Research: Solid Earth*, 87(B8), 6977-69
- Schulz, W. H., & Wang, G. (2014). Residual shear strength variability as a primary control on movement of landslides reactivated by earthquake-induced ground motion: Implications for coastal Oregon, US. *Journal of Geophysical Research: Earth Surface*, 119(7), 1617-1635.
- Schulz, W. H., McKenna, J. P., Kibler, J. D., Biavati, G. (2009) Relations between hydrology and velocity of a continuously moving landslide – evidence of pore=pressure feedback regulating landslide motion? In. *Landslides*. Vol. 6. pp 181
- Schulz, W. H., Kean, J. W., Wang, G. (2009). Landslide movement in southwest Colorado triggered by atmospheric tides. In. *Nature Geoscience*. Vol. 2. pp. 863-866.
- Schulz, W. H., Smith, J. B., Wang, G., Jiang, Y., & Roering, J. J. (2018). Clayey landslide initiation and acceleration strongly modulated by soil swelling. *Geophysical Research Letters*, 45(4), 1888-1896.
- Schulze, D. G. (1994). Differential X-ray diffraction analysis of soil minerals. *Quantitative methods in soil mineralogy, (quantitativemet)*, 412-429.
- Schumm, S. A. (1979). Geomorphic thresholds: the concept and its applications. *Transactions of the Institute of British Geographers*, 485-515.
- Secondi M, Crosta G, Di Prisco C, Frigerio G, Frattini P, Agliardi F (2011) Landslide motion forecasting by a dynamic visco-plastic model. *Proc WLF 2*, paper WLF2-(2011)-0571
- Secondi, M. M., Crosta, G., di Prisco, C., Frigerio, G., Frattini, P., & Agliardi, F. (2013). Landslide motion forecasting by a dynamic visco-plastic model. In *Landslide science and practice* (pp. 151-159). Springer, Berlin, Heidelberg.

- Secondi, M., Crosta, G. B., di Prisco, C., Frigerio, G., Frattini, P., & Agliardi, F. (2011). Forecasting landslide motion by a dynamic elasto-visco-plastic model. In *Geophysical research abstract* (Vol. 13).
- Selby, M.J. (1993) *Hillslope Materials and Processes*, Oxford University Press, Oxford, pp. 1-451
- Selby, M.J. (1993). *Hillslope Materials and Processes; Second Edition*. Oxford University Press, Oxford, England, pp. 270.
- Shimamoto, T., & Logan, J. M. (1981). Effects of simulated fault gouge on the sliding behavior of Tennessee sandstone: nonclay gouges. *Journal of Geophysical Research: Solid Earth*, 86(B4), 2902-2914.
- Shuzui, H. (2001). Process of slip-surface development and formation of slip-surface clay in landslides in Tertiary volcanic rocks, Japan. *Engineering Geology*, 61(4), 199-220.
- Sibson, R., (1977). Fault rocks and fault mechanisms. *J. Geol. Soc. London* 133, 191-213
- Simo, J.C., (1989). Strain softening and dissipation: a unification of approaches, in: Mazars, J., Bazant, Z.P. (Eds.), *Cracking and Damage, Strain*
- Simo, J.C., Hughes, T.J.R., (1998). *Computational Inelasticity*. Springer, New York
- Singh, A. (1966). *Creep phenomena in soils* (Doctoral dissertation, University of California, Berkeley).
- Sjögren B, Øvsthus A, Sandberg L (1979) Seismic classification of rock mass qualities. *Geophys Prospect* 27(2):409–442
- Skempton AW, Petley DJ (1967) The strength along structural discontinuities in stiff clays. In: *Proceedings geotechnology conference on shear strength properties of natural soils and rocks*, NGI, Norwegian Geotechnical Institute, Oslo, Norway, 2, pp 29–47
- Skempton, A. and Bishop, A. W. (1954). *Soils*. North-Holland.
- Skempton, A. W. (1964). Long-term stability of clay slopes. *Geotechnique*, 14(2), 77-102.
- Skempton, A. W. (1985). Residual strength of clays in landslides, folded strata and the laboratory. *Geotechnique*, 35(1), 3-18.
- Sluys, L.J., (1992). *Wave propagation, localization and dispersion in softening solids*. Dissertation, Delft University of Technology.
- Sornette D, Helmstetter A, Andersen JV, Gluzman S, Grasso JR, Pisarenko V (2004) Towards landslide prediction: two case studies. *Physica A* 338:605–632
- Sprefico, M. C., Franci, F., Bitelli, G., Girelli, V. A., Landuzzi, A., Lucente, C. C., ... & Borgatti, L. (2015). Remote sensing techniques in a multidisciplinary approach for the preservation of cultural heritage sites from natural hazard: the case of Valmarecchia Rock Slabs (RN, Italy). In *Engineering Geology for Society and Territory-Volume 8* (pp. 317-321). Springer, Cham.
- Stark, T. D., Choi, H., & McCone, S. (2005). Drained shear strength parameters for analysis of landslides. *Journal of Geotechnical and Geoenvironmental Engineering*, 131(5), 575-588.
- Stark, T.D., Choi, H., (2008). Slope inclinometers for landslides. *Landslides* 5 (3), 339-350.
- Stead, D., Eberhardt, E. & Coggan, J.S., (2006). Developments in the characterization of complex rock slope deformation and failure using numerical modelling techniques. *Engineering Geology*, 83, pp.217–235.
- Stead, D., Eberhardt, E., Coggan, J. & Benko, B., (2001). Advanced numerical techniques in rock slope stability analysis - applications and limitations. In *LANDSLIDES – Causes , Impacts and Countermeasures*. pp. 615–624.
- Storti, F., Billi, A., Salvini, F. (2003). Particle size distributions in natural carbonate fault rocks: insights for non-self-similar cataclasis. *Earth and Planetary Science Letters*; vol. 206, Issues 1-2, 173-186

- Straub, S. (1997). Predictability of long runout landslide motion: implications from granular flow mechanics. *Geologische Rundschau*, 86(2), 415-425.
- Straühal, T., Zangerl, C., Fellin, W., Holzmann, M., Engl, D. A., Brandner, R., & Tessadri, R. (2017). Structure, mineralogy and geomechanical properties of shear zones of deep-seated rockslides in metamorphic rocks (Tyrol, Austria). *Rock Mechanics and Rock Engineering*, 50(2), 419-438.
- Tarchi, D., Casagli, N., Fantì, R., Leva, D. D., Luzi, G., Pasuto, A., & Silvano, S. (2003). Landslide monitoring by using ground-based SAR interferometry: an example of application to the Tessina landslide in Italy. *Engineering geology*, 68(1-2), 15-30.
- Tenschert, E., Das Langzeitverhalten der Sackungshänge im Speicher Gepatsch (Tirol, Österreich), *Felsbau*, 16, 194–200, (1998)
- Tentschert E (1998) Das Langzeitverhalten der Sackungshänge im Speicher Gepatsch (Tirol, Österreich). *Felsbau* 16(3):194–200
- Terlien, M.T.J., (1998). The determination of statistical and deterministic hydrological landslide-triggering thresholds. *Environmental Geology* 35 (2), 124–130.
- Terranova, O., Antronico, L., Gullà, G., (2007). Landslide triggering scenarios in homogeneous geological contexts: The area surrounding Acri (Calabria, Italy). *Geomorphology* 87 (4), 250–267.
- Ter-Stepanian, G. (1980). Creep on natural slopes and cuttings. In 3rd international symposium on landslides, New Delhi, Meerut Publications (pp. 95-108).
- Terzaghi, K. (1953). Fifty years of subsoil exploration. na.
- Terzaghi, K. (1953). Fifty years of subsoil exploration. na.
- Terzaghi, K. and Paige, S. (1950). *Application of Geology to Engineering Practice: Berkeley Volume*. Geological Soc. of America.
- Terzaghi, K., (1925). *Erdbaumechanik auf bodenphysikalischer Grundlage*. F. Deuticke, Vienna, Austria.
- Terzaghi, K., Peck, R.B., Mesri, G., (1996). *Soil mechanics in engineering practice*. Wiley and Sons, 604 p.
- Terzaghi, K., Peck, R. B. (1948). *Soil mechanics in engineering practice*. Second edition 1967. John Wiley and Sons Inc. Chapter 2. pp 112-127.
- Tesei, T., Collettini, C., Carpenter, B. M., Viti, C., & Marone, C. (2012). Frictional strength and healing behavior of phyllosilicate-rich faults. *Journal of Geophysical Research: Solid Earth*, 117(B9).
- Teza, G., Galgaro, A., Zaltron, N., and Genevois, R. (2007). Terrestrial laser scanner to detect landslide displacement fields: a new approach. *International Journal of Remote Sensing*, 28(16), 3425-3446.
- Thiebes, B. (2011) *Landslide analysis and early warning: Local and regional case study in the Swabian Alb, Germany*. University of Vienna, Wien, Austria
- Thierry, Y., Malet, J. P., Sterlacchini, S., Puissant, A., & Maquaire, O. (2007). Landslide susceptibility assessment by bivariate methods at large scales: application to a complex mountainous environment. *Geomorphology*, 92(1-2), 38-59.
- Tika, T. E., & Hutchinson, J. N. (1999). Ring shear tests on soil from the Vaiont landslide slip surface. *Geotechnique*, 49(1), 59-74.
- Tiwari, B., & Marui, H. (2005). A new method for the correlation of residual shear strength of the soil with mineralogical composition. *Journal of Geotechnical and Geoenvironmental Engineering*, 131(9), 1139-1150.
- Topal, T., Akin, M., (2008). Investigation of a landslide along a natural gas pipeline (Karacabey-Turkey), in: Chen, Z., Zhang, J.-M., Ho, K., Wu, F.-Q., Li, Z.-K. (Eds.), *Landslides and Engineered*

- Slopes: From the Past to the Future, Proceedings of the 10th International Symposium on Landslides and Engineered Slopes. Taylor & Francis, Xi'an, China, pp. 1647-1652.
- Trigila, A., Iadanza, C., & Guerrieri, L. (2007). The IFFI Project (Italian Landslide Inventory): methodology and results. Guidelines for Mapping Areas at Risk of Landslides in Europe, 23, 15.
- Tsiambaos G (1991) Correlation of mineralogy and index properties with residual strength of Iraklion marls. *Eng Geol* 30:357–369
- UNISDR, (2006). Compendium of Early Warning Systems, EWC III, Third National Conference on Early Warning. UN/ISDR, Bonn, Germany,
- UNISDR, (2009). ISDR: Terminology [online]. <http://www.unisdr.org/eng/library/lib-terminology-eng%20home.htm>
- Van Asch, T.W., (1984). Creep processes in landslides. *Earth Surface Processes and Landforms*. 9: 573-583.
- Van Asch, Th. W. J., Van Beek, L. P. H., Bogaard. (2007). Problems in predicting the mobility of slow-moving landslides. In: *Engineering Geology*. Vol 91. pp 46 – 55.
- Van Geet, M., Swennen, R., and Wevers, M. (2001). Towards 3-d petrography: application of microfocus computer tomography in geological science. *Computers & Geosciences*, 27(9):1091–1099.
- Van Genuchten, P. M. B., De Rijke, H. 1988. On pore pressure variations causing slide velocities and accelerations in seasonally active landslide. In: *Earth Surface Processes and Landforms*. Vol. 14. Issue 6. pp 577-586.
- Van Westen, C.J., (2007). Mapping landslides: recent developments in the use of digital information., in: Turner, A., Schuster, R.L. (Eds.), *Landslides and society: proceedings of the First North American Conference on Landslides*, Vail, Colorado, U.S.A., June 3-8, (2007). Association of Environmental and Engineering Geologists, Vail Colorado, USA, pp. 221-238.
- Vardoulakis, I. (2002). Dynamic thermo-poro-mechanical analysis of catastrophic landslides. *Geotechnique*, 52(3), 157-171.
- Varnes, D. J. (1958). Landslide types and processes. *Landslides and engineering practice*, 29(3), 20-45.
- Varnes, D. J. (1978). Slope movement types and processes. Special report, 176, 11-33.
- Varnes, D.J., 1984. *Landslide Hazard Zonation: A Review of Principles and Practice*, IAEG Commission on Landslides and other Mass Movements. UNESCO Press, Paris, France, 63 p
- Vitale, S., Mazzoli, S., (2009). Finite strain analysis of a natural ductile shear zone in limestones: insights into 3-D coaxial vs. non-coaxial deformation partitioning. *J. Struct. Geol.* 31 (1), 104–113. [http://dx.doi.org/10.1016/j.jsg.\(2014\).09.010](http://dx.doi.org/10.1016/j.jsg.(2014).09.010).
- Voight, B. (1988). A method for prediction of volcanic eruptions. *Nature*, 332(6160):125–130.
- Voight, B. (1988). A method for prediction of volcanic eruptions. *Nature*, 332(6160), 125.
- Volkman, G., Schubert, W., (2005). The Use of Horizontal Inclinerometers for the Optimization of the Rock Mass–Support Interaction, in: Erdem, Y., Solak, T. (Eds.), *Underground Space Use-Analysis of the past and lessons for the future*. Taylor & Francis, pp. 967-972.
- Von Raumer, J. and Neubauer, F. (1993). Late precambrian and palaeozoic evolution of the alpine basementan overview. In *Pre-Mesozoic geology in the Alps*, pages 625–639. Springer.
- Wan, Y., & Kwong, J. (2002). Shear strength of soils containing amorphous clay-size materials in a slow-moving landslide. *Engineering geology*, 65(4), 293-303.
- Wang, F., & Sassa, K. (2000). Relationship between grain crushing and excess pore pressure generation by sandy soils in ring-shear tests. *Journal of Natural Disaster Science*, 22(2), 87-96.

- Wang, G., & Sassa, K. (2003). Pore-pressure generation and movement of rainfall-induced landslides: effects of grain size and fine-particle content. *Engineering geology*, 69(1-2), 109-125.
- Wang, G., Sassa, K., Fukuoka, H., & Tada, T. (2007). Experimental study on the shearing behavior of saturated silty soils based on ring-shear tests. *Journal of geotechnical and geoenvironmental engineering*, 133(3), 319-333.
- Wang, G., Suemine, A., and Schulz, W. H. (2010). Shear-rate-dependent strength control on the dynamics of rainfall-triggered landslides, tokushima prefecture, japan. *Earth Surface Processes and Landforms*, 35(4):407– 416.
- Wang, W.M., (1997). Stationary and propagative instabilities in metals – a computational point of view. Dissertation, Delft University of Technology
- Wasowski, J., Lollino, P., Limoni, P.P., Del Gaudio, V., Lollino, G., Gostelow, P., (2004). Towards an integrated field and EO-based approach for monitoring periurban slope instability, in: Lacerda, W., Ehrlich, M., Fontoura, S.A.B., Sayao, A.S.F. (Eds.), *Landslides: Evaluation and stabilization*. 9th International Symposium on Landslides. A.A. Balkema Publishers, Leiden, Rio de Janeiro, Brazil, pp. 809-816.
- Watkins JS, Walters LA, Godson RH (1972) Dependence of in-situ compressional-wave velocity on porosity in unsaturated rocks. *Geophysics* 37(1):29–35
- Watts, B. D. (1981). Lateral Creep Deformations in the Foundation of a High Dam. M. Sc. Thesis, Civil Engineering Department, University of Alberta, Edmonton, Canada.
- Webster, T.L., Dias, G., (2006). An automated GIS procedure for comparing GPS and proximal LiDAR elevations. *Computers & Geosciences* 32 (6), 713–726.
- Wen, B. P., Aydin, A., Duzgoren-Aydin, N. S., Li, Y. R., Chen, H. Y., & Xiao, S. D. (2007). Residual strength of slip zones of large landslides in the Three Gorges area, China. *Engineering Geology*, 93(3-4), 82-98.
- Wenk, H.-R., Kanitpanyacharoen, W., and Voltolini, M. (2010). Preferred orientation of phyllosilicates: Comparison of fault gouge, shale and schist. *Journal of Structural Geology*, 32(4):478–489.
- Wibberley, C. A., Yielding, G., & Di Toro, G. (2008). Recent advances in the understanding of fault zone internal structure: a review. *Geological Society, London, Special Publications*, 299(1), 5-33.
- Wieczorek, G.F., (1996). Landslide triggering mechanisms, in: Turner, A.K., Schuster, R.L. (Eds.), *Landslides: Investigation and Mitigation (Special Report)*. National Research Council, Transportation and Research Board Special Report 247, Washington, D.C., USA, p. 76–90.
- Wieczorek, G.F., Glade, T., (2005). Climatic factors influencing occurrence of debris flows, in: Jakob, M., Hungr, O. (Eds.), *Debris-flow hazards and related phenomena*. Springer, Berlin, Germany, p. 325–362.
- Wienhöfer, J., Lindenmaier, (2009). Temporal variability of a slow-moving landslide: the Heumöser case study in Vorarlberg, Austria, in: Malet, J.P., Remaitre, A., Bogaard, T. (Eds.), *Landslide Processes: From geomorphological mapping to dynamic modelling*, Proceedings of the International Conference on Landslide Processes. CERG Editions, Strasbourg, France, pp. 221-226.
- Wilson, R.C., 1989. Rainstorms, pore pressures, and debris flows: A theoretical framework., in: Sadler, P.M., Morton, D.M. (Eds.), *Landslides in Semi-Arid Environment*. Inland Geological Society, Riverside, California, USA, pp. 101-117.
- Wilson, R.C., Wieczorek, G.F., (1995). Rainfall thresholds for the initiation of debris flows at La Honda, California. *Environmental and Engineering Geoscience* 1(1), 11-27.
- Winter, M.G., Shackman, L. and Mcgregor, F. (2007). Landslide management and mitigation on the Scottish road network. In: R McInnes, J Jakeyways., H Fairbank and E Mathie (Editors), *Proceedings of the International Conference*

- Wong, H.N. and Ko, F.W.Y. (2006). Evolution of slope engineering practice and landslide risk management in Hong Kong. International Conference on Slopes, Malaysia, pp. 487-494.
- WP/WLI - International Geotechnical societies' UNESCO Working Party on World Landslide Inventory (1990) A suggested method for reporting a landslide. International Association Engineering Geology Bulletin, 41: 5-12.
- Wu, T.H., (1996). Soil strength properties and their measurement, in: Turner, A.K., Schuster, R.L. (Eds.), Landslides: Investigation and Mitigation (Special Report). National Research Council, Transportation and Research Board Special Report 247, Washington, D.C., USA, pp. 319-336.
- Wyllie MRJ, Gregory AR, Gardner LW (1956) Elastic wave velocities in heterogeneous and porous media. Geophysics 21:41–70
- Wyllie MRJ, Gregory AR, Gardner LW (1958) An experimental investigation of factors affecting elastic wave velocities in porous media. Geophysics 23:459–493
- Yamasaki, S., & Chigira, M. (2011). Weathering mechanisms and their effects on landsliding in pelitic schist. Earth Surface Processes and Landforms, 36(4), 481-494.
- Yamasaki, S., Chigira, M., and Petley, D. N. (2016). The role of graphite layers in gravitational deformation of pelitic schist. Engineering Geology, 208:29–38.
- Yin, J.H., Zhu, H.H., Jin, W., (2008). Monitoring of soil nailed slopes and dams using innovative technologies, in: Chen, Z., Zhang, J.-M., Ho, K., Wu, F.-Q., Li, Z.-K. (Eds.), Landslides and Engineered Slopes: From the Past to the Future, Proceedings of the 10th International Symposium on Landslides and Engineered Slopes. Taylor & Francis, Xi'an, China, pp. 1361-1366.
- Zangerl C, Eberhardt E, Schönlaub H, Anegg J (2007) Deformation behavior of deep-seated rockslides in crystalline rock. In: Eberhardt E, Stead D, Morrison T (eds) Proceeding of the 1st Canada–U.S. rock mechanics symposium, Vancouver, Canada, vol 2, pp 901–908
- Zangerl, C., Eberhardt, E., & Perzlmaier, S. (2010). Kinematic behavior and velocity characteristics of a complex deep-seated crystalline rockslide system in relation to its interaction with a dam reservoir. Engineering Geology, 112(1-4), 53-67.
- Zhang, Q., Wang, L., Zhang, X.Y., Huang, G.W., Ding, X.L., Dai, W.J., Yang, W.T., (2008). Application of multi-antenna GPS technique in the stability monitoring of roadside slopes, in: Chen, Z., Zhang, J.-M., Ho, K., Wu, F.-Q., Li, Z.-K. (Eds.), Landslides and Engineered Slopes: From the Past to the Future, Proceedings of the 10th International Symposium on Landslides and Engineered Slopes. Taylor & Francis, Xi'an, China, pp. 1367-1372.
- Zhu, J.-H. and Anderson, S.A., (1998). Determination of shear strength of Hawaiian residual soil subjected to rainfall-induced landslides. Geotechnique, 48(1): 73- 82.
- Zulauf, G., Kleinschmidt, G., & Oncken, O. (1990). Brittle deformation and graphitic cataclasites in the pilot research well KTB-VB (Oberpfalz, FRG). Geological Society, London, Special Publications, 54(1), 97-103.